



**Felipe Pereira Fleming**

**Fundamental study of wax deposition under real flow conditions.**

**Tese de Doutorado**

Thesis presented to the Programa de Pós-Graduação em Engenharia Mecânica of PUC–Rio in partial fulfillment of the requirements for the degree of Doutor em Ciências - Engenharia Mecânica.

Advisor: Prof. Luis Fernando Alzuguir Azevedo

Co-Advisors: Prof. Jean-Luc Daridon

Prof. Angela Ourivio Nieckele

Dr. Jérôme Pauly

Rio de Janeiro

April 2018



**Felipe Pereira Fleming**

**Fundamental Study of Wax Deposition  
Under Real Flow Conditions**

Thesis presented to the Programa de Pós-Graduação em Engenharia Mecânica of PUC–Rio in partial fulfillment of the requirements for the degree of Doutor em Ciências - Engenharia Mecânica. Approved by the undersigned Examination Committee.

**Prof. Luis Fernando Alzuguir Azevedo**

Advisor

Departamento de Engenharia Mecânica – PUC-Rio

**Dr. Jérôme Pauly**

Co-Advisor

Total S.A.

**Dr. Jean-Luc Daridon**

Co-Advisor

UPPA

**Profa. Angela Ourivio Nieckele**

Co-Advisor

Departamento de Engenharia Mecânica – PUC-Rio

**Prof. Frederico Wanderley Tavares**

Universidade Federal do Rio de Janeiro - UFRJ

**Prof. Papa Matar Ndiaye**

Universidade Federal do Rio de Janeiro - UFRJ

**Dr. Geraldo Afonso Spinelli Martins Ribeiro**

Petróleo Brasileiro

**Dr. Hervé Carrier**

UPPA

**Prof. Márcio da Silveira Carvalho**

Vice Dean of Graduate Studies

Centro Técnico Científico – PUC-Rio

Rio de Janeiro, April 30th, 2018

All rights reserved.

## Felipe Pereira Fleming

Obtained a B.Sc. in Chemistry from the Universidade Federal do Rio de Janeiro in 2005 and obtained a M.Sc. Degree in Chemistry from the Instituto de Química of the same university in 2007.

### Bibliographic data

Fleming, Felipe Pereira

Fundamental study of wax deposition under real flow conditions / Felipe Pereira Fleming ; advisor: Luis Fernando Alzuguir Azevedo ; co-advisors: Jean-Luc Daridon, Angela Ourivio Nieckele, Jérôme Pauly. – 2018.

210 f. : il. color. ; 30 cm

Tese (doutorado)–Pontifícia Universidade Católica do Rio de Janeiro, Departamento de Engenharia Mecânica, 2018.

Inclui bibliografia

1. Engenharia Mecânica – Teses. 2. Deposição de parafinas. 3. Modelo termodinâmico. 4. Modelo de mistura. 5. Condutividade térmica de n-alcanos. I. Azevedo, Luis Fernando Alzuguir. II. Daridon, Jean-Luc. III. Nieckele, Angela Ourivio. IV. Pauly, Jérôme. V. Pontifícia Universidade Católica do Rio de Janeiro. Departamento de Engenharia Mecânica. VI. Título.

CDD: 621

To Isabela, who brought me into this world with her.

## Acknowledgments

This work was only possible thanks to the collaboration and support of innumerable people. In an attempt to avoid any injustices, as my memory keeps betraying me, I extend my deepest appreciation and gratitude to all that directly or indirectly took part in this work. A special thanks to PETROBRAS for all of the support.

I would like to thank Professor Luis Fernando Azevedo, director of this thesis, for given me a chance to meet a human been like him. One of those who the world only sees every now and then. His kindness and dedication are not only inspirational, but capable of changing people, environments, a whole community.

I would like to thank Professor Angela Nieckele for all of the interesting discussions on CFD during the course of this work. She made possible that a chemist could start to understand the beauty of fluid dynamics.

I would like to thank Professor Jean-Luc Daridon, whose dedication to science is really motivating. The deep discussions and all of our debates helped shape this work. Specially during our weekly rock climbing sessions in France.

I would like to thank Dr. Jérôme Pauly, whose experimental skills and insights are really unique. The way of thinking outside the box and coming up with clever solutions to different problems really made a difference in this work and helped with any merit the experimental results present may have.

I would like to thank Professor Fred Tavares for the long scientific discussions and for those not so scientific as well. His help and guidance made this work possible. And Professor Papa Matar, who is relentless in pushing the work forward.

I would like to thank Dr. Luciana Boher for implementing the CFD code and Vinícius da Silva and Rafael do Carmo for implementing the thermodynamic routines at a completely different level, and efficient enough to run the simulations. I would like to thank Dr. Helena Veiga for the invaluable discussions over experimental techniques and expertise.

I would like to thank Rafaela Silva and Dr. Lenise Couto for helping in DSC experiments.

I would like to thank Professor Hércio Orlande, Iasmin Herzog and Paulo Cesar for all the support given over the thermal conductivity measurements.

I would like to thank Professor Iuri Pepe whose incredible drive towards development is contaminating.

I would like to thank Marcelo Gonçalves, who motivated this thesis from day 1, took me to PUC and made all of this possible. His guidance has been invaluable.

I would like to thank Livia Silva, who stood by me during the hard work and long hours at the lab. She also deserves any credit might this work be worth. My friend Guilherme Lima, as without our discussions it would have never been possible to go this far. My friend Felipe Mauro, who offered an interesting counterpoint in every single discussion, and made all possible. And the one and only Rodolfo de Vico. Life is sweeter with you all in it.

I would like to thank Anderson Rouge, Rodrigo Freitas, Carla Bise, Bruno Charles, Rogério Mesquita, Adriano Furani, Rafaela, Leandro Valim, Magno, Bruno Lacava, Minette, Gaspari and everybody in CENPES that helped in any way. Friends at work makes life better.

I would like to thank Hervé Carrier, Guillaume Galiero, Romain Vermorel, Cédric Kouakou, Matthieu Habrioux, Leticia Ligiero, Fernanda Veloso and Jean and baby, Djamel Nasri, Bertrand Guatarbes, Fouad Oulebsir and all others that made the year in Pau the best of them all. The long discussions with Hervé about almost everything, debates over lunch with Guillaume and Romain, the soccer games and beer with most of them, existential debates with Matthieu, rock climbing with Fernanda and Jean, the effort to offer Djamel some ham, too much to thank in such a small space. Thank you all for everything.

I would like to thank Helena Veiga, Igor Braga, Luciana Boher, Paula Farias, Leonardo Pinhal, Roberta, Livia Tardelli, Márcio Pareto, Bruno Andrade (Tiozão), Pedro Taquechel (Cuba), Natália Passos, and everyone else who made the years at PUC-RIO an incredible time. I am sure I never laughed so much, learned so much and worked so hard in my life. Thank you for everything.

I would like to thank Vinícius da Silva, Rafael do Carmo, Fernando and Iuri from ATOMS for all of fruitful debates about everything that should not be debated!!

I would like to thank my family for all the support and to put up with me every day. My uncle, grandmothers, brother and sisters (and in law), niece, father, mother and specially my dear wife.

Last but not least, I would like to thank little Isabela for given me my days in every breath. I did not know life before she presented me with hers. To whom this work is dedicated, to whom my life is dedicated. Thank you very much for extending me the pleasure and the privilege of being your father.

## Abstract

Fleming, Felipe Pereira; Azevedo, Luis Fernando Alzuguir (Advisor); Daridon, Jean-Luc (Co-Advisor); Nieckele, Angela Ourivio (Co-Advisor); Pauly, Jérôme (Co-Advisor). **Fundamental study of wax deposition under real flow conditions**. Rio de Janeiro, 2018. 210p. Tese de Doutorado – Departamento de Engenharia Mecânica, Pontifícia Universidade Católica do Rio de Janeiro.

Since the early 1980's, efforts have been directed towards modeling the complex wax deposition phenomenon. Over the years, the critical evaluation of the wax deposition mechanisms proposed initially through a solid physical background start to make room to flexible codes that could be tuned to different experiment scenarios. In an attempt to investigate the phenomenon in a fundamental way, the current work proposed a research strategy that would evaluate every single part of the complex wax deposition model under well-controlled optimal conditions. To achieve such a goal, a new strategy to evaluate solid-liquid thermodynamic models was developed. Results showed that the model used was robust enough to precisely describe the solid-liquid phase behavior of asymmetric model mixtures at both ordinary and high pressures, as well as to describe the behavior of complex mixture like Diesel fuel samples. To assure the solid physical basis of the models being employed in this work, the thermal conductivity measurement of heavy *n*-alkanes in both liquid and solid phases was carried out and reported for the first time in the literature. At last, a drift flux solid-liquid CFD model was proposed. Coupled with a thermodynamic model to supply the model with phase equilibria and properties data, the model was used to investigate the experimental results available in the literature. The wax deposition mechanism evaluated was based on the viscosity increase due to the appearance of solids. The results showed that although a qualitative agreement between the model and experimental results were obtained, the model underestimated the thickness of the deposit. On the other hand, the thermal conductivity of the deposit matched the recently available experimental data on the thermal conductivity of such a deposit measured under flowing conditions. This fact strengthens the presented conclusions that wax deposition is not a single mechanism phenomenon after all.

## Keywords

Wax deposition; Thermodynamic model; Mixture model; Thermal conductivity of *n*-alkanes

## Resumo

Fleming, Felipe Pereira; Azevedo, Luis Fernando Alzuguir (Orientador); Daridon, Jean-Luc (Co-orientador); Nieckele, Angela Ourivio (Co-orientador); Pauly, Jérôme (Co-orientador). **Estudo fundamental da deposição de parafinas em condição de escoamento**. Rio de Janeiro, 2018. 210p. Tese de Doutorado – Departamento de Engenharia Mecânica, Pontifícia Universidade Católica do Rio de Janeiro.

Desde o início dos anos 1980, esforços foram direcionados para modelar o fenômeno de deposição de parafinas. Ao longo dos anos, a avaliação crítica dos mecanismos da deposição de parafinas vem cedendo espaço ao desenvolvimento de correlações flexíveis capazes de acomodar diferentes situações testadas no laboratório. Numa tentativa de investigar o fenômeno em uma abordagem fundamental, o presente trabalho propôs uma estratégia de pesquisa que envolve avaliar cada pedaço do fenômeno de deposição de parafinas e garantir seus resultados ótimos. Para alcançar tal objetivo, uma nova estratégia para se avaliar modelos termodinâmicos de equilíbrio de fases sólido-líquido foi desenvolvida. Os resultados mostram que o modelo utilizado é robusto e preciso o suficiente para descrever tais fenômenos para misturas assimétricas em pressões ordinárias e altas, assim como descrever o comportamento de misturas complexas como amostras de óleo Diesel. Para garantir uma base física sólida dos resultados, a condutividade térmica de *n*-alcanos pesados foram medidos na fase líquida e na fase sólida e reportados na literatura pela primeira vez. Por fim, um modelo de escoamento de sólido-líquido foi proposto. Acoplado a um modelo termodinâmico capaz de gerar dados de equilíbrio de fases sólido-líquido e propriedades dessas fases, assim como combiná-las em propriedades da mistura, o modelo foi utilizado para descrever os resultados disponíveis na literatura. O mecanismo de deposição de parafinas avaliado se baseia no aumento da viscosidade com a temperatura e concentração de sólidos. Os resultados mostraram que embora houvesse um acordo qualitativo entre os resultados experimentais e os simulados, o modelo subestimou a espessura do depósito de parafinas. Por outro lado, o modelo foi capaz de descrever a condutividade térmica do depósito de acordo com os dados medidos experimentalmente para um depósito similar. Tal fato reforça as conclusões finais e indica que a deposição de parafinas parece não ser um fenômeno regido apenas por um mecanismo.

### Palavras-Chave

Deposição de parafinas; Modelo termodinâmico; Modelo de mistura; Condutividade térmica de *n*-alcanos

## Résumé

Fleming, Felipe Pereira; Azevedo, Luis Fernando Alzuguir (Director); Daridon, Jean-Luc (Co-Director); Nieckele, Angela Ourivio (Co-Director); Pauly, Jérôme (Co-Director). **Étude fondamentale des dépôts des paraffines dans des conditions réelles d'écoulement**. Rio de Janeiro, 2018. 210p. Tese de Doutorado – Departamento de Engenharia Mecânica, Pontifícia Universidade Católica do Rio de Janeiro.

Depuis le début des années 1980, des efforts ont été déployés pour modéliser le phénomène complexe de dépôt de cire. Au fil des années, l'évaluation critique des mécanismes de formation de dépôts de cire limités initialement à la cristallisation des paraffines, a commencé à faire place à des algorithmes flexibles qui peuvent être adaptés à différents scénarios expérimentaux. Dans une tentative d'étudier le phénomène de manière fondamentale, le travail actuel a consisté à proposer une stratégie globale de recherche qui permet d'évaluer les différents mécanismes impliqués dans la formation de dépôts de cire. Pour atteindre cet objectif, une nouvelle stratégie a tout d'abord été proposée pour ajuster les modèles thermodynamiques utilisés pour décrire le comportement de phase solide-liquide. Les résultats de comparaison avec l'expérience ont montré que la démarche proposée était suffisamment robuste pour décrire précisément le comportement de phase solide-liquide des mélanges synthétiques asymétriques aux pressions ordinaires ou très élevées, ainsi que pour représenter le comportement de mélanges complexes réels comme par exemple des carburants pour moteur Diesel. Dans un second temps, des mesures de conductivité thermique dans des *n*-alcanes lourds à l'état liquide mais aussi solide ont été réalisées et rapportées pour la première fois ici afin d'assurer une base physique solide dans les modèles utilisés dans ce travail. Enfin, un modèle CFD solide-liquide a été proposé. Couplé au modèle thermodynamique utilisé pour décrire les équilibres de phase et les propriétés thermophysiques, ce modèle a été utilisé pour étudier les résultats expérimentaux disponibles dans la littérature. Le mécanisme de dépôt de cire évalué était basé sur l'augmentation de la viscosité devenue de l'apparition des solides. Les résultats ont montré un accord qualitatif entre les prédictions du modèle et les observations expérimentales malgré une sous-estimation de l'épaisseur du dépôt formé. D'autre part, la conductivité thermique du dépôt estimée correspondait parfaitement à la conductivité thermique mesurée récemment dans des conditions d'écoulement réelles.

## Mots clés

Dépôt de cire; Modèle Thermodynamique; Modèle de mixture; Conductivité thermique des *n*-alcanes

## Contents

1 INTRODUCTION	24
1.1. Wax Deposition Mechanisms	26
1.1.1. Molecular diffusion	27
1.1.2. Solid wax radial mass transport	31
1.1.3. Other mechanisms	33
1.2. The Physics of Wax Deposition	34
1.3. Fundamental Model of Wax Deposition	35
1.3.1. Premises of the study	35
1.3.2. Thermodynamic model	36
1.3.3. Thermophysical properties	36
1.3.4. CFD model	37
2 DIRECT ADJUSTMENT OF WAX THERMODYNAMIC MODEL PARAMETER TO MICRO DIFFERENTIAL SCANNING CALORIMETRY THERMOGRAMS	38
2.1. Introduction	38
2.2. Method	40
2.3. Experimental	44
2.3.1. Chemicals	44
2.3.2. Micro differential scanning calorimetry (DSC)	45
2.4. Results and Discussions	45
2.5. Conclusions	52
3 PARAFFIN SOLUBILITY AND CALORIMETRIC DATA CALCULATION USING PENG-ROBINSON EOS AND MODIFIED UNIQUAC MODELS	53
3.1. Introduction	53
3.2. Methodology	55
3.2.1. DSC simulation	55
3.2.2. Thermodynamic model	59
3.2.3. Phase equilibrium algorithm	63
3.2.3.1. Flash calculation	64
3.2.3.2. Stability analysis	65
3.3. Data	67
3.4. Results and Discussions	67
3.4.1. DSC simulation, P-R EoS evaluation and parameter estimation	67
3.4.2. Solid Model Evaluation	76
3.5. Conclusion	83
4 PARAFFIN SOLUBILITY CURVES OF DIESEL FUELS FROM THERMODYNAMIC MODEL ADJUSTED THROUGH EXPERIMENTAL DSC THERMOGRAMS	85
4.1. Introduction	85
4.2. Experimental	86
4.2.1. Diesel samples	86

4.2.2. DSC measurements	87
4.2.3. Analysis of the paraffin distributions	87
4.2.4. Analysis of fluid composition and fluid representation	87
4.2.5. Solubility curve and solid deposit composition	88
4.3. Methodology	89
4.3.1. Thermodynamic model	89
4.3.2. DSC thermogram simulation from the thermodynamic model proposed	92
4.3.3. Thermogram fitting	94
4.3.4. Solid-liquid equilibrium prediction	95
4.4. Results and Discussions	95
4.5. Conclusions	103
<b>5 HIGH PRESSURE PHASE EQUILIBRIA OF CARBON DIOXIDE + N-ALKANES MIXTURES: EXPERIMENTAL DATA AND MODELING</b>	<b>104</b>
5.1. Introduction	104
5.2. Experimental	105
5.2.1. Chemicals	105
5.2.2. Experimental procedure	106
5.3. Thermodynamic Model	107
5.4. Results and Discussions	111
5.5. Conclusions	118
<b>6 THERMAL CONDUCTIVITY OF HEAVY EVEN CARBON NUMBER N-ALKANES (C22 TO C32)</b>	<b>119</b>
6.1. Introduction	119
6.2. Experimental	121
6.2.1. Chemicals	121
6.2.2. Measurements	121
6.3. Results and Discussions	124
6.3.1. Results for the DSC measurements	124
6.3.2. Thermal conductivity of the reference materials	125
6.3.3. Thermal conductivity of the liquid samples	127
6.3.4. Thermal conductivity of the solid samples	134
6.4. Conclusions	136
<b>7 WAX DEPOSITION MODELLING</b>	<b>138</b>
7.1. Introduction	138
7.2. Mathematical Model	140
7.2.1. Basic definitions	140
7.2.2. Continuity equation	141
7.2.3. Continuity equations for the species	142
7.2.4. Linear momentum conservation equation	146
7.2.5. Energy conservation equation	147
7.2.6. Drift Velocities	148
7.2.7. Thermodynamic model and properties	149
7.2.7.1. Densities and volume fractions	149
7.2.7.2. Suspension viscosity model	152
7.2.7.3. Thermal conductivity of the liquid and solid phases	154
7.2.7.4. Diffusion coefficients	159
7.3. Domain of Interest	159
7.3.1. Test section	159

7.3.2. Test fluid	162
7.4. Numerical Method	163
7.4.1. Convergence criteria and general procedure of the numerical solution	166
7.4.2. Grid and time step convergence studies	167
7.5. Experimental Data	169
7.5.1. Measured deposition thickness	170
7.6. Results and Discussions	171
7.6.1. Thermodynamic model	171
7.6.2. Flow variables	172
7.6.3. Paraffin deposition from the model	181
7.6.4. Comparison with experimental results	184
7.7. Conclusions	187
8 CONCLUSIONS	189
9 BIBLIOGRAPHY	191
10 APPENDIX A	205
11 APPENDIX B	208
11.1. Drift Flux of Species	208
11.2. Drift Flux of Linear Momentum	209
11.3. Drift Flux of Energy	210

## List of Figures

<b>Figure 1-1.</b> PETROBRAS' records of production fields versus water depth. The OTC Awards won by PETROBRAS for such achievements are also shown.	<b>25</b>
<b>Figure 1-2.</b> Wax concentration profile for both implementations as discussed by Huang et al. (2011).	<b>30</b>
<b>Figure 2-1.</b> Thermodynamic scheme used to calculate the DSC signal from the model.	<b>41</b>
<b>Figure 2-2.</b> DSC thermogram and simulated DSC curve for sample S1.	<b>46</b>
<b>Figure 2-3.</b> DSC thermogram and simulated DSC curve for sample S2.	<b>46</b>
<b>Figure 2-4.</b> DSC thermogram and simulated DSC curve for sample S3.	<b>47</b>
<b>Figure 2-5.</b> DSC thermogram and simulated DSC curve for sample S4.	<b>47</b>
<b>Figure 2-6.</b> DSC thermogram and simulated DSC curve for sample S5.	<b>47</b>
<b>Figure 2-7.</b> Simulated precipitation curves and experimental results obtained by Dauphin et al. (1999) for sample S1.	<b>49</b>
<b>Figure 2-8.</b> Simulated precipitation curves and experimental results obtained by Dauphin et al. (1999) for sample S2.	<b>50</b>
<b>Figure 2-9.</b> Simulated precipitation curves and experimental results obtained by Dauphin et al. (1999) for sample S3.	<b>50</b>
<b>Figure 2-10.</b> Simulated precipitation curves and experimental results obtained by Dauphin et al. (1999) for sample S4.	<b>50</b>
<b>Figure 2-11.</b> Simulated precipitation curves and experimental results obtained by Dauphin et al. (1999) for sample S5.	<b>51</b>
<b>Figure 3-1.</b> Thermodynamic path used to obtain the molar enthalpy of pure paraffins.	<b>56</b>
<b>Figure 3-2.</b> Phase equilibrium strategy scheme.	<b>63</b>
<b>Figure 3-3.</b> Box diagram of the Flash calculation algorithm.	<b>64</b>
<b>Figure 3-4.</b> S1 (a) DSC and (b) Solubility data description using three different approaches: modified UNIQUAC for solid phases and Peng-Robinson EoS for the liquid phase; modified UNIQUAC for solid phases and Flory+UNIFAC for the liquid phase; modified UNIQUAC with estimated $\Delta A$ for solid phases and Peng-Robinson EoS for the liquid phase.	<b>69</b>
<b>Figure 3-5.</b> S2 (a) DSC and (b) Solubility data description using three different approaches: modified UNIQUAC for solid phases and Peng-Robinson EoS for the liquid phase; modified UNIQUAC for solid phases and Flory+UNIFAC for the liquid phase; modified UNIQUAC with estimated $\Delta A$ for solid phases and Peng-Robinson EoS for the liquid phase.	<b>70</b>
<b>Figure 3-6.</b> S3 (a) DSC and (b) Solubility data description using three different approaches: modified UNIQUAC for solid phases and Peng-Robinson EoS for the liquid phase; modified UNIQUAC for solid phases and	

- Flory+UNIFAC for the liquid phase; modified UNIQUAC with estimated  $\Delta A$  for solid phases and Peng-Robinson EoS for the liquid phase. **72**
- Figure 3-7.** S4 (a) DSC and (b) Solubility data description using three different approaches: modified UNIQUAC for solid phases and Peng-Robinson EoS for the liquid phase; modified UNIQUAC for solid phases and Flory+UNIFAC for the liquid phase; modified UNIQUAC with estimated  $\Delta A$  for solid phases and Peng-Robinson EoS for the liquid phase. **73**
- Figure 3-8.** S5 (a) DSC and (b) Solubility data description using three different approaches: modified UNIQUAC for solid phases and Peng-Robinson EoS for the liquid phase; modified UNIQUAC for solid phases and Flory+UNIFAC for the liquid phase; modified UNIQUAC with estimated  $\Delta A$  for solid phases and Peng-Robinson EoS for the liquid phase. **74**
- Figure 3-9.** S1 (a) DSC and (b) Solubility data description using Peng-Robinson EoS for the liquid phase and comparing three different models for solid phases: modified UNIQUAC with estimated  $\Delta A$ , ideal solid solution and multisolid. **78**
- Figure 3-10.** S2 (a) DSC and (b) solubility data description using Peng-Robinson EoS for the liquid phase and comparing three different models for solid phases: modified UNIQUAC with estimated  $\Delta A$ , ideal solid solution and multisolid. **79**
- Figure 3-11.** S3 (a) DSC and (b) Solubility data description using Peng-Robinson EoS for the liquid phase and comparing three different models for solid phases: modified UNIQUAC with estimated  $\Delta A$ , ideal solid solution and multisolid. **80**
- Figure 3-12.** S4 (a) DSC and (b) Solubility data description using Peng-Robinson EoS for the liquid phase and comparing three different models for solid phases: modified UNIQUAC with estimated  $\Delta A$ , ideal solid solution and multisolid. **81**
- Figure 3-13.** S5 (a) DSC and (b) Solubility data description using Peng-Robinson EoS for the liquid phase and comparing three different models for solid phases: modified UNIQUAC with estimated  $\Delta A$ , ideal solid solution and multisolid. **82**
- Figure 4-1.** (a) Concentration of the paraffins in the solid for different temperatures from sample 1. (b) Concentration of the paraffins in the solid for different temperatures from sample 2. **99**
- Figure 4-2.** Experimental and fitted DSC curves for Diesel 1 (a) and Diesel 2 (b). **100**
- Figure 4-3.** Experimental and predicted solubility curves for Diesel 1 (a) and Diesel 2 (b). **100**
- Figure 4-4.** Experimental and predicted compositions of liquid and solid phases at 273.75 K (a), 268.15 K (b) and 263.15 K (c) for Diesel 1. **101**
- Figure 4-5.** Experimental and predicted compositions of liquid and solid phases at 273.75 K (a), 268.15 K (b) and 263.15 K (c) for Diesel 2. **102**
- Figure 5-1.** Experimental and calculated bubble curves (L–VLE transition) using different values of  $k_{CO_2} - alkane$ . (a) Sample 1 (20% CO<sub>2</sub>); (b)

Sample 2 (40% CO <sub>2</sub> ); (c) Sample 3 (60% CO <sub>2</sub> ); (d) Sample 4 (80% CO <sub>2</sub> ).	114
<b>Figure 5-2.</b> Experimental and calculated phase equilibrium diagrams (L to VLE, L to SLE and VLE to SLVE transitions) for sample 1 using <i>kCO2 – alkane</i> = 0.094.	116
<b>Figure 5-3.</b> Experimental and calculated phase equilibrium diagrams (L to VLE, L to SLE and VLE to SLVE transitions) for sample 2 using <i>kCO2 – alkane</i> = 0.094.	116
<b>Figure 5-4.</b> Experimental and calculated phase equilibrium diagrams (L to VLE, L to SLE and VLE to SLVE transitions) for sample 3 using <i>kCO2 – alkane</i> = 0.094.	117
<b>Figure 5-5.</b> Experimental and calculated phase equilibrium diagrams (L to VLE, L to SLE and VLE to SLVE transitions) for sample 4 using <i>kCO2 – alkane</i> = 0.094.	117
<b>Figure 6-1.</b> (a) C-Therm MTPS sensor ( <a href="http://ctherm.com">http://ctherm.com</a> ). (b) Measuring configuration used for liquid samples. (c) Measuring configuration used for solid samples.	123
<b>Figure 6-2.</b> Results for typical DSC tests for each of the <i>n</i> -alkane samples analyzed.	124
<b>Figure 6-3.</b> Measured thermal conductivity of water compared to the values reported by Ramires et al. (1995).	126
<b>Figure 6-4.</b> Measured thermal conductivity of pyrex compared to the values reported by Assael et al. (2008).	126
<b>Figure 6-5.</b> Measured thermal conductivity of <i>n</i> -dodecane ( <i>n</i> -C12) compared to the values reported in the literature (Kashiwagi et al., 1982; Tanaka et al., 1988; Vargaftik et al., 1994).	128
<b>Figure 6-6.</b> Measured thermal conductivity of liquid <i>n</i> -docosane ( <i>n</i> -C22) compared to the values reported by Rastorguev et al. (1974) and Vargaftik et al. (1994).	129
<b>Figure 6-7.</b> Measured thermal conductivity of liquid <i>n</i> -tetracosane ( <i>n</i> -C24) compared to the values reported by Rastorguev et al. (1974) and Vargaftik et al. (1994).	130
<b>Figure 6-8.</b> Measured thermal conductivity of liquid <i>n</i> -hexacosane ( <i>n</i> -C26).	131
<b>Figure 6-9.</b> Measured thermal conductivity of liquid <i>n</i> -octacosane ( <i>n</i> -C28).	131
<b>Figure 6-10.</b> Measured thermal conductivity of liquid <i>n</i> -triacontane ( <i>n</i> -C30).	132
<b>Figure 6-11.</b> Measured thermal conductivity of liquid <i>n</i> -dotriacontane ( <i>n</i> -C32).	132
<b>Figure 6-12.</b> Measured thermal conductivity of liquid <i>n</i> -docosane, <i>n</i> -tetracosane, <i>n</i> -hexacosane, <i>n</i> -octacosane, <i>n</i> -triacontane and <i>n</i> -dotriacontane as a function of temperature.	133
<b>Figure 6-13.</b> Measured thermal conductivity of liquid <i>n</i> -alkane samples for fixed temperature as a function of carbon number.	133

<b>Figure 6-14.</b> Mean value of the thermal conductivity of each solid <i>n</i> -alkane samples investigated as a function of carbon number.	<b>136</b>
<b>Figure 7-1.</b> Experimental results for the mixture used by Veiga (2017) and the model result with $D=200$ and the composition from Veiga (2017). In the detail, the viscosity of the mixture at temperatures above the WAT.	<b>154</b>
<b>Figure 7-2.</b> Thermal conductivity of <i>n</i> -dodecane from Fleming et al. (2018) compared to the model of Paradela et al. (2005).	<b>155</b>
<b>Figure 7-3.</b> Thermal conductivity of <i>n</i> -docosane from Fleming et al. (2018) compared to the model of Paradela et al. (2005).	<b>156</b>
<b>Figure 7-4.</b> Thermal conductivity of <i>n</i> -tetracosane from Fleming et al. (2018) compared to the model of Paradela et al. (2005).	<b>156</b>
<b>Figure 7-5.</b> Thermal conductivity of <i>n</i> -hexacosane from Fleming et al. (2018) compared to the model of Paradela et al. (2005).	<b>157</b>
<b>Figure 7-6.</b> Thermal conductivity of <i>n</i> -octacosane from Fleming et al. (2018) compared to the model of Paradela et al. (2005).	<b>157</b>
<b>Figure 7-7.</b> Thermal conductivity of <i>n</i> -triacontane from Fleming et al. (2018) compared to the model of Paradela et al. (2005).	<b>158</b>
<b>Figure 7-8.</b> Thermal conductivity of <i>n</i> -dotriacontane from Fleming et al. (2018) compared to the model of Paradela et al. (2005).	<b>158</b>
<b>Figure 7-9.</b> Schematic representation of the test section reported by Veiga (2017). (a) Front view. (b) Cut view.	<b>160</b>
<b>Figure 7-10.</b> Schematic representation of the test section immersed in the temperature controlled water bath by Veiga (2017).	<b>160</b>
<b>Figure 7-11.</b> Temperature of the inner cooper wall ( <i>T<sub>cold</sub></i> ) (Veiga, 2017).	<b>161</b>
<b>Figure 7-12.</b> Chromatogram of the fluid used by Veiga (2017) in the experiments.	<b>163</b>
<b>Figure 7-13.</b> Experimental deposition thickness profile at different times measured by Veiga (2017).	<b>170</b>
<b>Figure 7-14.</b> Solubility curves calculated from the original multisolid model (MS Orig), the adjusted multisolid model (MS Adjust) and the solid solution model (Solsol). The experimental solid-liquid equilibrium temperature is marked in the circle (Exp).	<b>172</b>
<b>Figure 7-15.</b> Temperature fields in times (a) 10 s, (b) 1 min, (c) 3 min, (d) 10 min, (e) 30 min and (f) 1 h.	<b>173</b>
<b>Figure 7-16.</b> Temperature profiles at dimensionless lengths of 0.3, 0.6 and 0.9 in 1 h.	<b>174</b>
<b>Figure 7-17.</b> Solid mass fraction fields in times (a) 10 s, (b) 1 min, (c) 3 min, (d) 10 min, (e) 30 min and (f) 1 h.	<b>175</b>
<b>Figure 7-18.</b> Solid mass fraction profiles at dimensionless lengths of 0.3, 0.6 and 0.9 in 1 h.	<b>176</b>
<b>Figure 7-19.</b> Axial mixture viscosity profiles at dimensionless lengths of 0.3,	

0.6 and 0.9 in 60 min.	176
<b>Figure 7-20.</b> Viscosity fields in times (a) 10 s, (b) 1 min, (c) 3 min, (d) 10 min, (e) 30 min and (f) 1 h.	177
<b>Figure 7-21.</b> Mixture density fields in times (a) 10 s, (b) 1 min, (c) 3 min, (d) 10 min, (e) 30 min and (f) 1 h.	178
<b>Figure 7-22.</b> Mixture density profiles at dimensionless lengths of 0.3, 0.6 and 0.9 in 60 min.	179
<b>Figure 7-23.</b> Axial mixture velocity fields in times (a) 10 s, (b) 1 min, (c) 3 min, (d) 10 min, (e) 30 min and (f) 1 h.	180
<b>Figure 7-24.</b> Axial mixture velocity profiles at dimensionless lengths of 0.3, 0.6 and 0.9 in times (a) 10 s, (b) 10 min, (c) 30 min and (d) 1 h. The velocity is expressed in $\text{m}\cdot\text{s}^{-1}$ .	182
<b>Figure 7-25.</b> Profiles of the axial mixture velocity of $1.0\times 10^{-4} \text{ m}\cdot\text{s}^{-1}$ at different times.	183
<b>Figure 7-26.</b> Thickness of the paraffin deposit at 10 min and the solid mass fraction profile for the values of 0.00, 0.02, 0.05 and 0.10.	183
<b>Figure 7-27.</b> Thickness of the paraffin deposit at 1 h and the solid mass fraction profile for the values of 0.00, 0.02, 0.05 and 0.10.	184
<b>Figure 7-28.</b> Experimental thickness of the paraffin deposit (Veiga, 2017) and the thickness obtained from the proposed model at times 1 min, 3 min, 10 min, 30 min and 1 h.	184
<b>Figure 7-29.</b> Effective thermal conductivity profiles in times (a) 10 s, (b) 1 min, (c) 3 min, (d) 10 min, (e) 30 min and (f) 1 h.	186
<b>Figure 7-30.</b> Effective thermal conductivity profiles at dimensionless lengths of 0.3, 0.6 and 0.9 in 60 min.	187
<b>Figure 10-1.</b> Heating and cooling curves from 0.2 k/min $\mu\text{DSC}$ for sample S1.	206
<b>Figure 10-2.</b> Heating and cooling curves from 0.2 k/min $\mu\text{DSC}$ for sample S2.	206
<b>Figure 10-3.</b> Heating and cooling curves from 0.2 k/min $\mu\text{DSC}$ for sample S3.	206
<b>Figure 10-4.</b> Heating and cooling curves from 0.2 k/min $\mu\text{DSC}$ for sample S4.	207
<b>Figure 10-5.</b> Heating and cooling curves from 0.2 k/min $\mu\text{DSC}$ for sample S5.	207

## List of Tables

<b>Table 2-1.</b> Composition of the samples (mass %) analyzed. Supplier and purity of the standards (mass %) are informed in the last two columns.	<b>44</b>
<b>Table 2-2.</b> Optimized <i>fadjust</i> parameter and highest temperature evaluated for the analyzed samples.	<b>46</b>
<b>Table 2-3.</b> Experimental wax disappearance temperature (WDT) from Dauphin et al. (1999) (Experimental), SLE temperature calculated through the adjusted thermodynamic model (Wax model) and the wax appearance temperature (WAT) measured by DSC (DSC). The uncertainty of the WAT measured by DSC for all samples is $u(\text{WAT})=\pm 1$ °C.	<b>51</b>
<b>Table 3-1.</b> Parameter estimation results (PR)	<b>68</b>
<b>Table 3-2.</b> Experimental and calculated wax disappearance temperatures (WDT)	<b>75</b>
<b>Table 3-3.</b> Deviations between experimental and calculated wax disappearance temperatures (WDT)	<b>75</b>
<b>Table 3-4.</b> Average absolute deviations, Dev, between experimental and calculated solubilities	<b>76</b>
<b>Table 4-1.</b> Density, Flash Point and Sulfur content of the two samples studied.	<b>86</b>
<b>Table 4-2.</b> Feed compositions of both Diesel fuel samples divided into paraffins and other components lumped into pseudocomponents in mass fractions (%) and average MW ( $\text{g}\cdot\text{mol}^{-1}$ ). The relative expanded uncertainty of the composition is under 2% for the paraffin components and under 3% for the pseudocomponents of the reported value. The relative expanded uncertainty of the average molecular mass is 3%.	<b>96</b>
<b>Table 4-3.</b> Amount of solid paraffin for samples 1 and 2 for each temperature measured (mass %). The relative expanded uncertainty is 5% of the presented value.	<b>97</b>
<b>Table 4-4.</b> Compositions of solid paraffins of sample 1 in mass fractions for each temperature evaluated. The relative expanded uncertainty is 5% of the presented value.	<b>97</b>
<b>Table 4-5.</b> Compositions of solid paraffins of sample 2 in mass fractions for each temperature evaluated. The relative expanded uncertainty is 5% of the presented value.	<b>98</b>
<b>Table 4-6.</b> Parameters obtained that multiply the pseudocomponent molecular weights, $\xi MW$ , boiling, $\xi Tb$ , and critical, $\xi Tc$ , temperatures and the paraffins' pair interaction energies, $\xi \lambda$ .	<b>99</b>
<b>Table 5-1.</b> Compositions of the synthetic mixtures (mass %, standard uncertainties also in mass %)	<b>106</b>
<b>Table 5-2.</b> Experimental phase equilibrium data for the samples analyzed. <sup>a</sup>	<b>112</b>
<b>Table 5-3.</b> <i>kCO2</i> – <i>alkane</i> estimation results	<b>114</b>
<b>Table 6-1.</b> Samples analyzed with supplier and purity.	<b>121</b>

<b>Table 6-2.</b> Measured solid-solid o-d transition temperatures ( $T_{tr}$ ), solid-liquid melting temperatures ( $T_f$ ), solid-solid o-d transition enthalpy ( $\Delta h_{tr}$ ) and solid-liquid melting enthalpy ( $\Delta h_f$ ).	<b>125</b>
<b>Table 6-3.</b> Measured thermal conductivity of liquid <i>n</i> -dodecane ( <i>n</i> -C12).	<b>127</b>
<b>Table 6-4.</b> Measured thermal conductivity of liquid <i>n</i> -docosane ( <i>n</i> -C22).	<b>128</b>
<b>Table 6-5.</b> Measured thermal conductivity of liquid <i>n</i> -tetracosane ( <i>n</i> -C24).	<b>129</b>
<b>Table 6-6.</b> Measured thermal conductivity of liquid <i>n</i> -hexacosane ( <i>n</i> -C26).	<b>130</b>
<b>Table 6-7.</b> Measured thermal conductivity of liquid <i>n</i> -octacosane ( <i>n</i> -C28).	<b>131</b>
<b>Table 6-8.</b> Measured thermal conductivity of liquid <i>n</i> -triacontane ( <i>n</i> -C30).	<b>132</b>
<b>Table 6-9.</b> Measured thermal conductivity of liquid <i>n</i> -dotriacontane ( <i>n</i> -C32).	<b>132</b>
<b>Table 6-10.</b> Measured thermal conductivity of solid <i>n</i> -docosane ( <i>n</i> -C22).	<b>134</b>
<b>Table 6-11.</b> Measured thermal conductivity of solid <i>n</i> -tetracosane ( <i>n</i> -C24).	<b>134</b>
<b>Table 6-12.</b> Measured thermal conductivity of solid <i>n</i> -hexacosane ( <i>n</i> -C26).	<b>134</b>
<b>Table 6-13.</b> Measured thermal conductivity of solid <i>n</i> -octacosane ( <i>n</i> -C28).	<b>134</b>
<b>Table 6-14.</b> Measured thermal conductivity of solid <i>n</i> -triacontane ( <i>n</i> -C30).	<b>135</b>
<b>Table 6-15.</b> Measured thermal conductivity of solid <i>n</i> -dotriacontane ( <i>n</i> -C32).	<b>135</b>
<b>Table 7-1.</b> Coefficients for calculating the density of the reference materials with Equation 7-60.	<b>151</b>
<b>Table 7-2.</b> Coefficients for calculating the viscosity of the reference materials with Equation 7-62.	<b>153</b>
<b>Table 7-3.</b> Coefficients for calculating the viscosity of the reference materials with Equation 7-67.	<b>155</b>
<b>Table 7-4.</b> Fluid composition in % mass.	<b>163</b>
<b>Table 7-5.</b> Terms of Equation 7-77 for each conservation equation.	<b>165</b>
<b>Table 7-6.</b> Results for the grid convergence test.	<b>168</b>
<b>Table 7-7.</b> Time steps and respective Courant numbers used in the time step convergence test.	<b>169</b>
<b>Table 7-8.</b> Results for the time step convergence tests.	<b>169</b>
<b>Table 7-9.</b> Dimensionless deposition thickness measured by Veiga (2017) as a function of time.	<b>170</b>
<b>Table 10-1.</b> Composition differences between samples S1 to S5 and Bim 0 to Bim 13 from Dauphin et al. [17] expressed in %.	<b>205</b>

## List of symbols

$B$	mass fraction of the phase
$c$	mass fraction
$CN$	number of carbon atoms
$Cp$	heat capacity ( $\text{J.kg}^{-1}.\text{k}^{-1}$ )
$\mathcal{D}$	binary diffusion coefficient ( $\text{m}^2.\text{s}^{-1}$ )
$f$	fugacity (Pa)
$F$	residuals of the Newton method
$f_{adjust}$	adjust parameter
$G$	Gibbs free energy (J)
$H$	enthalpy (J)
$J$	diffusion flux ( $\text{m}^2.\text{s}^{-1}$ )
$K$	equilibrium ratio
$M, m$	mass (kg)
$MW$	molecular weight ( $\text{kg.mol}^{-1}$ )
$Nc$	number of components
$N_{exp}$	number of experimental data points
$N_{mol}$	number of moles of the mixture (mol)
$Np$	number of phases
$P$	pressure (Pa)
$Pc$	critical pressure (Pa)
$Q$	heat (J)
$r, q$	structural parameters
$R$	universal gas constant ( $\text{J.K}^{-1}.\text{mol}^{-1}$ )
$S$	volume fraction of the phase
$t$	time (s)
$T$	temperature (K)
$Tc$	critical temperature (K)
$tm$	modified tangent plane distance
$u$	velocity vector ( $\text{m.s}^{-1}$ )
$U$	component z of the velocity vector ( $\text{m.s}^{-1}$ )
$V, \mathcal{V}$	volume ( $\text{m}^3$ )
$V$	component r of the velocity vector ( $\text{m.s}^{-1}$ )

$\bar{v}$	diffusion velocity vector (m.s <sup>-1</sup> )
$v$	total velocity vector (m.s <sup>-1</sup> )
$V_c$	critical volume (m <sup>3</sup> .mol <sup>-1</sup> )
$W$	stability variable
$w_t$	weight fraction of solid
$x$	molar fraction
$Z$	coordination number

### Superscripts

$n, m$	phase index
$f$	fusion
$tr$	transition
$ig$	ideal gas
$R$	residual property
$S, s$	solid phase
$L, l$	liquid phase
$V, v$	vapor phase
$E$	excess property
$res$	residual
$comb-fv$	combinatorial-free volume
$sub$	sublimation
$vap$	vaporization

### Subscripts

$i, j, k, w$	component index
$l$	liquid phase
$s$	solid phase
$m$	mixture
$r$	reduced property
$p$	experimental data points index
$0$	ideal gas reference state

### Greek letters

$\Delta$	variation
----------	-----------

$\beta$	phase fraction
$\gamma$	activity coefficient
$\tau, \theta, \Phi$	modified UNIQUAC parameters
$\lambda$	thermal conductivity
$\Lambda$	interaction energy
$\varphi$	fugacity coefficient
$\delta$	kronecker delta
$\tau$	stress tensor
$\mu$	viscosity
$\omega$	acentric factor
$\rho$	density
$\ddot{\rho}$	variable of the general formulation of the conservation equation
$\varepsilon$	Deposit thickness

### Accent

—	molar property
—	vector
^	property in the mixture
=	matrix

### Abbreviations

DSC	differential scanning calorimetry
EGE	excess Gibbs energy
EoS	equation of state
PVT	pressure, volume, temperature
SLE	solid-liquid equilibria
VLE	vapor-liquid equilibria
SLVE	solid-liquid-vapor equilibria
WAT	wax appearance temperature
WDT	wax disappearance temperature
TPD	tangent plane distance
CASRN	CAS registration number

*Our heads are round so our thoughts can change direction*

***Francis Picabia***

# 1 Introduction

The oil industry is in fact a myriad of different segments put together with the mission to find, assess, and drill wells in reservoirs to later produce the fluids, process it, refine it and sell all of the different fractions, modified or not, in the market. As the price of crude oil and of the final derivatives vary freely, it is an international tendency for oil companies to accommodate all of the different segments, leading to big international agglomerates.

One of these segments is responsible for the design and operation of the production installations that transport the oil from the reservoir to the processing units. These production installations are mainly composed of pipelines (tubing, flow lines, risers, etc.), manifolds, connectors and some kind of artificial lift apparatus (gas lift valves, submersible pumps, etc.). As wells can be far from the processing units, these installations can comprise pipelines that are kilometers long, lying a couple of kilometers deep in the ocean bed, through which flows the entire production of the well. The production is completely dependent on the continuity of the operation as any clogging would compromise the production and any intervention to remediate it would cost in the order of tens of millions of dollars.

To guarantee the continuous flow of crude oil through the production installations, a whole segment of the petroleum industry focuses on the subject of fluid behavior to avoid the problems that may disturb the flow. This segment of the industry was named Flow Assurance by PETROBRAS in the early 1990's, and its importance has grown over the following decades as exploration revealed reservoirs at deeper waters (Figure 1-1). Flow assurance major subjects address the formation of solids in both water (scales and hydrates) and oil (asphaltenes and waxes) phases.

Wax deposition, the most important oil phase subject and second only to hydrates in Flow Assurance, consists of an accumulation of waxes over the pipe walls. Wax is a generic name used for organic substances from all different sources that melt around ambient temperature. In petroleum, experience has shown that the molecules that exhibit such a behavior are the *n*-alkanes or paraffins, mostly with

chain lengths larger than 20 carbon atoms. So, whenever dealing with petroleum chemistry and Flow Assurance, the terms wax, *n*-alkanes and paraffin are used as synonyms. Originally soluble in the oil at reservoir conditions, as the fluid cools as it flows through the pipes in cold environments like deep-water seabed, these paraffins may precipitate out of solution and thus deposit over the pipe walls.

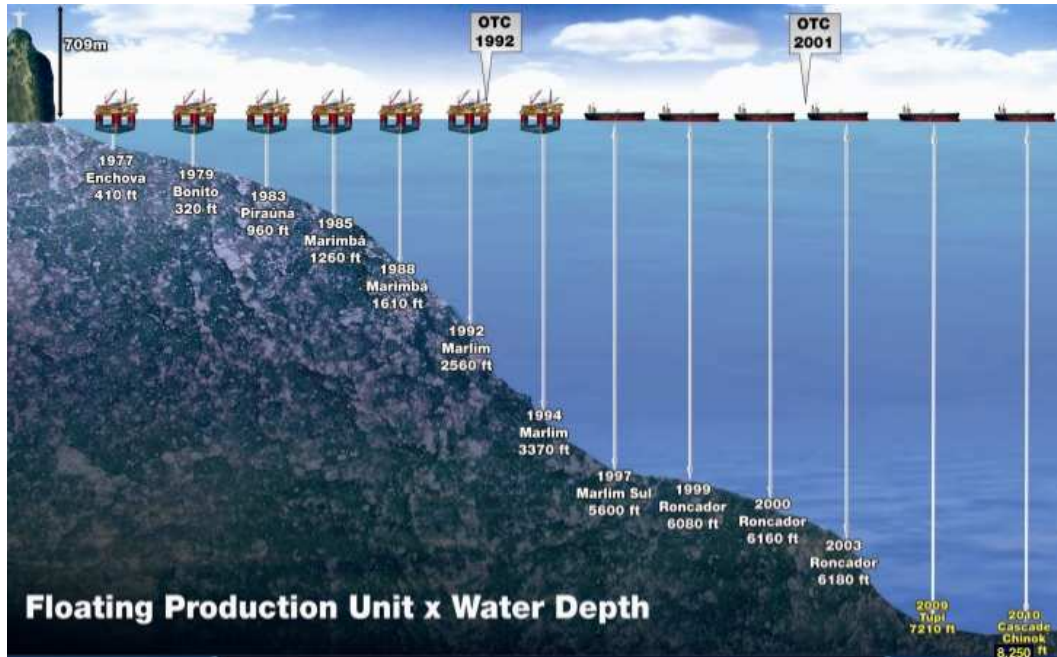


**Figure 1-1.** PETROBRAS' records of production fields versus water depth. The OTC Awards won by PETROBRAS for such achievements are also shown.

When the fluid never experiences temperatures below its solid-liquid equilibrium temperature, there cannot be any wax deposition as the waxes need to crystallize for depositing. This temperature sets a threshold below which wax deposition may occur. In the industry, this solid-liquid equilibrium temperature is known as wax disappearance temperature (WDT). Nevertheless, as the WDT is hard to measure in dark opaque fluids, the temperature usually analyzed by the industry is the wax appearance temperature (WAT). From a thermodynamic perspective these temperatures are not the same due mainly to kinetic reasons, as a supersaturation condition is needed to overcome the excess energy brought by the formation of a solid-liquid interface. The WAT may be measured using different experimental methodologies, like cross-polarized microscopy, differential scanning calorimetry analysis, filtration, light dispersion, etc. Nevertheless, all techniques have shortcomings and the correct measurement of the solid-liquid equilibrium temperature is a challenge (Coutinho and Daridon, 2005).

As for wax deposition, the major focus of Flow Assurance rests in one's ability to predict the precipitation of solids in the fluids being produced as it makes its way through the production system and suffers drastic changes in temperature, pressure and phase composition. The correct modeling of the multiphase flow conditions and the resulting fluid composition throughout the production installation is thus indispensable to any Flow Assurance assessment. With the thermodynamic coordinates at hand (temperature, pressure and phase composition), one evaluates the solid-equilibria behavior over the different phases of the fluid being produced. With such information, one can predict the appearance of solids and use this information in the design of robust production installation that minimizes such issues.

Whenever unavoidable in the design phase of the production installations, the Flow Assurance issues are mitigated by a plethora of available alternatives, among which the continuous injection of substoichiometric inhibitors plays a major role. This solution is particularly efficient for scales and asphaltenes. Just as much, the injection of small chain alcohols and glycols (methanol, ethanol and ethylene glycol) can avoid or remediate hydrate formations. Such an alternative is not available for wax depositions (Chi et al., 2016; Chi et al., 2017; Lima, 2017).

Without an efficient control technology available, the mitigation of wax deposition relies on expensive line cleaning operations with organic solvents or special detergents, or on the mechanical removal using PIGs. All of these processes are laborious and expensive, leading to production losses and risking the production installation itself (Shecaira et al., 2011). For such reasons, on the contrary of other disciplines of Flow Assurance, the study of wax deposition resides on the modeling of the deposition phenomenon itself, not stopping at the thermodynamic evaluation of the solid-liquid phase behavior of the subject. Already in the early 1980's, Burger et al. (1981) conducted a thorough investigation of the wax deposition observed in the Trans Alaska pipeline. The study evaluated different possible deposition mechanisms and set the pace for the subject in the years to come.

## **1.1. Wax Deposition Mechanisms**

Before going into the discussion of the deposition mechanisms themselves, it is important to clarify the use of such mechanisms and how they are actually

evaluated. As mentioned above, on the contrary of other Flow Assurance issues, one cannot easily remediate or avoid wax deposition. As such, the efficient operation of the production installations has to be optimized to accommodate for the mitigation strategy chosen for a given field. This optimization is a strong function of the thickness, position and the mechanical properties of such deposits. For this reason, all of the wax deposition models available or under development focus mainly on the ability of the code to describe accurately the thickness of the deposit over time obtained from lab scale loop experiments, as field data is scarce if available. The discussion often misses completely the physical evaluation of the deposition model itself.

To accumulate over the pipe walls, wax has to be transported from the bulk of the fluid to the walls. The transported wax can either be in solution or already precipitated as a solid in the bulk, depending on the fluid temperature. As such, from the early work of Burger et al. (1981) mass transfer mechanisms for both were proposed. To account for the mass transfer of solid waxes to the pipe wall Burger et al. (1981) suggested Brownian diffusion, shear dispersion and gravitational settling. To account for the mass transfer of the waxes still in solution to the pipe wall, the authors suggested molecular diffusion. Each will be discussed in further detail.

### **1.1.1. Molecular diffusion**

To account for the mass transfer of dissolved wax from the bulk of the fluid to the pipe walls the most relevant alternative is molecular diffusion. When in solution, the state of minimum free energy is achieved when the chemical potential is equal across the system. As such, if for some reason there is a chemical potential gradient, the system will spontaneously rearrange and diffuse molecules over space to reestablish the uniformity of the chemical potential field.

In order to precipitate wax, the fluid has to be cooled. As the fluid flows in pipelines sitting in cold environments, the fluid loses heat through the pipe walls to the environment and the temperature at this point drops. Consequently, as soon as the walls temperature falls below the WAT and waxes start to drop out of solution, a concentration gradient is formed between the first point in the liquid that remains above the WAT and colder points near the pipe walls. The intensity of such a

gradient is directly related to the solubility curve of the system, that is, the amount of solid wax formed as function of temperature, and to the temperature gradient inside the pipe, that is, the heat flux.

Burger et al. (1981) proposed the mass flux of soluble wax molecules towards the pipe walls be modeled according to Equation 1-1, in the form of Fick's law of molecular diffusion.

$$\frac{dm_w}{dt} = -\rho_d \mathcal{D}_w A \frac{dc}{dr} \quad (1-1)$$

where  $m_w$  is the mass of deposited wax,  $\rho_d$  is the density of the deposit,  $\mathcal{D}_w$  is the Fick's diffusion coefficient of wax "w",  $A$  the area of deposition and  $dc/dr$  is the radial concentration gradient of the dissolved wax. Burger et al. (1981) suggested that Equation 1-1 be reformulated as Equation 1-2.

$$\frac{dm_w}{dt} = -\rho_d \mathcal{D}_w A \left( \frac{dc}{dT} \right) \left( \frac{dT}{dr} \right) \quad (1-2)$$

where  $dc/dT$  is the wax concentration gradient with respect to the temperature (solubility curve) and  $dT/dr$  the radial temperature gradient. In this second formulation, the wax mass flux becomes a function only of the fluid properties, as the solubility curve is as much as a fluid property as the WAT, and on the radial temperature gradient obtained from the energy equation. Burger et al. (1981) concluded that this mechanism dominated the wax mass transfer in the presence of high temperatures and high heat fluxes.

To model the diffusion coefficient, Burger et al. (1981) proposed the use of the correlation from Wilke and Chang (1955).

$$\mathcal{D}_w = 7.4 \times 10^{-9} \frac{T(\xi MW_w)^{0.5}}{\mu V^{0.6}} \quad (1-3)$$

where  $T$  is the absolute temperature,  $\xi$  is an association parameter,  $MW_w$  is the molecular weight of the wax,  $\mu$  is the oil viscosity and  $V$  is the wax molecular volume. Burger et al. (1981) proposed a further simplification in the model that reduced the wax diffusion coefficient to a function of only the oil viscosity and an adjustable parameter  $C_1$ .

$$\mathcal{D}_w = \frac{C_1}{\mu} \quad (1-4)$$

Brown et al. (1993) showed that whenever the correlation proposed by Wilke and Chang (1955) was used in the diffusion model, the results were qualitatively correct, but the deposit thickness were significantly underestimated. As such, the simplified model that allowed for a direct adjustment of the diffusion coefficients was preferred, as the model could then be tuned to adjust to experimental data.

Other studies were carried out and concluded that molecular diffusion is the predominant mechanism through which wax deposition occurs (Weingarten and Euchner, 1986; Majeed et al., 1990; Hamouda et al., 1992; Mendes and Braga, 1996; Matzain, 1996; Rygg et al., 1998; Creek et al., 1999; Singh et al., 2000; Apte et al., 2001; Lindeloff and Krejbjerg, 2002; Hernandez-Perez et al., 2004; Huang et al., 2011).

Over the years, the molecular diffusion mechanism received a lot of attention from different research groups. The models got more sophisticated. Singh et al. (2000) showed that the wax deposits age, in a sense that even after they stop growing their wax content continues to increase resulting in a harder deposit. Such a phenomena was modeled as a counter diffusion of light ends from the deposit back to the oil, together with expected diffusion of heavy ends from the oil into the deposit. The threshold that differentiates between the molecules diffusing out of the deposit and those diffusing into it was named Critical Carbon Number (CCN) (Singh et al., 2001a).

Huang et al. (2011) discussed the different hypothesis involved in implementing the molecular diffusion model. One way to implement the method is to make the mass transfer model completely independent of the heat transfer model (Singh et al., 2001b). In this formulation, the temperature of the fluid is calculated ignoring any existence of solid-liquid equilibria in the fluid itself. Then, the concentration gradient ( $dC/dT$ ) when discretized and calculated at the deposit-liquid interface results in the difference between the wax concentration in the bulk,  $C_{bulk}$ , and the wax concentration resulting from the solubility curve calculated at the deposit-liquid interface temperature,  $C_{d-l,int}(T)$ , Equation 1-5. By ignoring the fact that solids might already be precipitated in the liquid, this strategy generates the largest concentration gradient possible and thus is an upper limit of the diffusion mechanism. This implementation was called independent heat and mass transfer (IHMT) by Huang et al. (2011).

$$\frac{dC}{dT} = \frac{C_{d-l,int}(T) - C_{bulk}}{T_{d-l,int} - T_{bulk}} \quad (1-5)$$

Another way to implement the molecular diffusion mechanism is to take into account the solubility of the wax in the liquid as well, resulting in a smoother composition gradient at the deposit-liquid interface (Venkatesan and Fogler, 2004). In this case, the wax concentration in the liquid is also calculated taking into account the solubility curve. This implementation was called solubility model by Huang et al. (2011).

$$\frac{dC}{dT} = \frac{C_{d-l,int}(T) - C_{bulk}(T)}{T_{d-l,int} - T_{bulk}} \quad (1-6)$$

A depiction of the wax concentration profiles for both implementation is show in Figure 1-2.

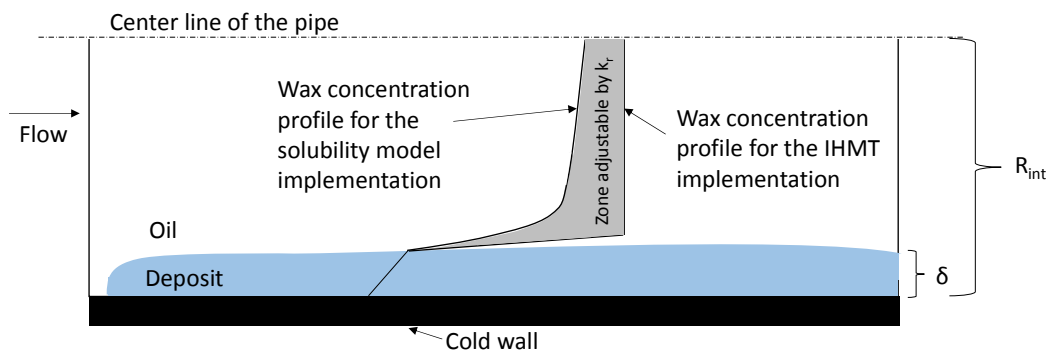


**Figure 1-2.** Wax concentration profile for both implementations as discussed by Huang et al. (2011).

As one might assume, Huang et al. (2011) realized that the lab experimental results fell constantly in between the two scenarios. To accommodate these results, a model that would fall in between was proposed. Huang et al. (2011) assumed that a supersaturated wax solution could be formed in the oil. In this case, the concentration gradient becomes a function of an adjustable parameter  $k_r$  as the wax concentration in the liquid can assume any value between the upper (first implementation) and lower limit (second implementation). This parameter is used as a multiplier in the difference between the wax concentration in the oil and the wax concentration at the deposit-liquid interface.

$$\frac{dC}{dT} = \frac{k_r(C_{d-l,int} - C_{bulk}(T))}{T_{d-l,int} - T_{bulk}} \quad (1-7)$$

Zheng et al. (2017) proposed a model based on molecular diffusion but that also incorporated the non-Newtonian behavior of wax suspensions. As a result, the authors show that the final composition of the deposit is enriched in waxes when one adds the non-Newtonian behavior to the model.

There are several models available in the literature, both commercially available and academic models. The OLGA package, a commercial transient multiphase simulator, offers a module that uses the models proposed by Rygg et al. (1998) and Apte et al. (2001) to simulate wax deposition along with the transient multiphase flow. The PVTsim package, a thermodynamic phase behavior simulator, also offers a module that rests on the work of Lindeloff and Krejbjerg (2002) to simulate wax deposition.

On the academic side, there are mainly two research groups that provide wax deposition simulators to the participants of their Joint Industry Projects (JIP's). The University of Tulsa, that conducts the Tulsa University Paraffin Deposition Projects (TUPDP), that provides the TUWAX simulator. The TUWAX simulator has many versions and has been developed over time with contributions from different graduate work (Matzain, 1996; Lund, 1998; Matzain, 1999; Apte, 1999; Manabe, 2001; Hernandez-Perez, 2002; Couto, 2004; Rodriguez, 2006; Singh, 2013). The Porous Media Research group of the University of Michigan provides the MWP simulator. The MWP is the only available simulator that accounts for the aging of the deposit (evolution of the deposit composition in time). It was also developed over time from the contribution of different graduate works (Singh et al. 2000; Venkatesan, 2004; Lee, 2008; Senra, 2009; Huang, 2011).

All of these simulators are mainly based on the molecular diffusion mechanism.

### **1.1.2. Solid wax radial mass transport**

Burger et al. (1981) proposed three different mechanisms that might lead to mass transfer of solid wax from the bulk to the walls. These were namely Brownian diffusion, shear dispersion and gravity settling. This last mechanism was readily discarded, as the results from experiments at a horizontal deposition section could not be differentiated from those applying a vertical deposition section.

The Brownian diffusion of particles was described by Burger et al. (1981) as presented in Equation 1-8.

$$\frac{dm_w}{dt} = -\rho_d D_b A \frac{dC_w^*}{dr} \quad (1-8)$$

where  $D_b$  is the Brownian diffusion coefficient and  $C_w^*$  is the concentration of wax particles. The shear dispersion of particles was described by Burger et al. (1981) as presented in Equation 1-9.

$$\frac{dm_w}{dt} = -\rho_d D_s A \frac{dC_w^*}{dr} \quad (1-9)$$

where  $D_s$  is the shear dispersion coefficient. As such, the total particle flux into the deposit is represented in Equation 1-10.

$$\frac{dm_p}{dt} = -\rho_d (D_b + D_s) \frac{dC_w^*}{dr} \quad (1-10)$$

Instead of balancing the flux, Burger et al. (1981) suggested the model be simplified and instead of the flux balance, a rate of incorporation of solid particles into the deposit be calculated and directly added to the molecular diffusion model as presented in Equation 1-11.

$$\frac{dm_w}{dt} = -\rho_d D_w A \left( \frac{dC}{dT} \right) \left( \frac{dT}{dr} \right) + k^* C_w^* \gamma A \quad (1-11)$$

where  $\gamma$  is the shear rate at the deposit-liquid interface. Burger et al. (1981) concluded that shear dispersion was the dominant mechanism in experiments at lower temperature and with low heat fluxes. Brownian diffusion was considered to be negligible.

Azevedo and Teixeira (2003) published a critical review of the different wax deposition mechanisms in the literature and pointed out that the conclusions drawn by Burger et al. (1981) and all of the literature after it was misled by a confusion in two figures in Burger et al. (1981) as well as in the conclusion text. When discussing the results of shear dispersion, Burger et al. (1981) was actually evaluating the results from the second term in Equation 1-11. The conclusions were not that shear dispersion dominated under some conditions, but rather the total incorporation of solids from the bulk.

This is an important issue, as shear dispersion is disregarded as a possible mechanism once no deposition is measured in a zero heat flux condition. Nevertheless, as pointed out by Azevedo and Teixeira (2003), this fact does not immediately discard Brownian diffusion.

The mainstream argument used to discard Brownian diffusion relies on the fact that as the temperature at the deposit-liquid interface is lower than the temperature of the fluid, the particle concentration will be higher and Brownian diffusion will actually drive particles away from the wall into the bulk (Huang et al., 2015). Azevedo and Teixeira (2003) pointed out that if these particles near the deposit-liquid interface were trapped in the deposit they would be motionless and thus would not diffuse out but rather induce an inward diffusion of the free particles that are advected in the oil. This discussion was simply ignored and Brownian diffusion was neglected as the models that accounted solely for the wax molecular diffusion could be adjusted to the experimental results. It is thus widely accepted that solid wax do not take part in wax deposition.

### **1.1.3. Other mechanisms**

As the models based on the wax molecular diffusion mechanism could be adjusted to experimental results, there are not many different approaches in the literature.

The group from the University of Calgary led by professor Mehrotra (Bidmus and Mehrotra, 2004; Bhat and Mehrotra, 2005; Bidmus and Mehrotra, 2008a; Bidmus and Mehrotra, 2008b) proposed a heat-transfer analogy model to describe wax deposition. According to their model, solely heat transfer governed the wax deposition phenomena. They were motivated by the fact that from their experiments the deposit-liquid interface was always near the WAT. As such, the phenomena would be thermally driven as there was no room for molecular diffusion

The group from RERI led by professor Firozabaadi (Banki et al., 2008; Hoteit et al., 2008) proposed a model that as soon as the solids would come out of solution, they would be held still in place and no longer be advected by the liquid phase. As such, the deposit would be a porous media through which the liquid could flow according to Darcy's law. The deposit-liquid interface was defined as the position where 2% mass of solids were found. As much as this model allows one to simulate

the entire domain and actually further investigate the physics of the system during a wax deposition event, there is no physical ground for the solids to simply stop where they are formed.

Souza (2014) implemented the model from Banki et al. (2008) and compared it to detailed experimental results available in the literature. The model, especially at the transient regime, overestimated the thickness of the deposits. The results are largely dependent on the thermophysical properties of the fluid and its components.

Singh et al. (1999) rationalized the build of wax deposits over the pipe walls as being a result of the gelation of the oil due to wax precipitation. They investigated the phenomena through a comparison of rheological study and loop experiments. Merino-Garcia et al. (2007) also argued towards the gelation mechanism. Together with a critical discussion about the consequences of adding tuning coefficient to models used to investigate the physics of the wax deposition phenomena, these authors point out that molecular diffusion should be a slow process, incompatible with the high deposition rates observed in lab experiments. As such, they propose that deposition is actually caused by the gelation of the fluid as it cools due to the wax suspension formed. A simple model developed allowed mainly qualitative conclusions, but it was able to describe correctly the deposition experiments carried out. The authors also discuss the asymptotic behavior of the wax deposits and propose that this fact relates directly to shear stress at the deposit-liquid interface as well as the insulation effect caused by the deposit that reaches the WAT at the deposit-liquid interface, ceasing the deposition.

## **1.2. The Physics of Wax Deposition**

As one endeavors through understanding the wax deposition mechanisms presented, the physics under discussion seems clear from the start, as the mechanisms are named after well-known physical processes. Molecular diffusion, for example, is a studied mass transfer mechanism that has an understood physical foundation. Now, if one looks closer into the mathematical formulation presented in the last section, one rapidly raises questions about the validity of the model itself. Fick approximation as formulated is valid for isothermal binary quiescent systems. That is exactly what the subject under study is not. Wax deposition takes place in a multicomponent non-isothermal flowing mixture, whose composition and

temperature are also coupled through phase equilibrium phenomena. This specific issue was raised in the early development of the wax deposition models (Matzain, 1999; Creek et al., 1999). As such, although numbers can always match up in analysis of complex system such as the one under discussion, the truth is that the molecular diffusion mechanism is not modeled with the correct approach to treat molecular diffusion in these systems. In this sense, as one addresses wax deposition using the formulations presented, as they are adjusted to match experimental results, these models should be considered as correlations and thus, cannot be easily extrapolated from lab experimental data to field data.

The same analysis hold for the deposition of solids, for example. The fact that any deposition requires the system to be under particle growing regime imposes the condition that at equilibrium, growth is only achieved locally through Ostwald Ripening mechanism (Coutinho et al., 2003). As such, the fact that no deposition is observed in experiments where no heat flux is present cannot be used to discard a mechanism like Brownian diffusion of solids.

Inasmuch as correlations are useful and the only alternative to address complex system of different sorts, the lack of understanding of the real physical basis of wax deposition limits the evaluation of real scenarios different from those tested in lab experiments and hinders non-intuitive major developments in the field. The search for the physical basis of this complex phenomenon should be pursued.

### **1.3. Fundamental Model of Wax Deposition**

#### **1.3.1. Premises of the study**

To address the physical basis of wax deposition, in this work it is proposed the implementation of a CFD model capable of transporting both liquid and solids. In such a model, the entire domain can be simulated and thus the thermophysical properties of the deposit will be available to be compared with experimental results, not only the deposit thickness. To allow a proper comparison between experiments and simulation, the fluid under analysis should have a well-defined composition and its components should have experimentally determined thermophysical properties. The models used to combine these properties should also be as precise

as possible. At last, the thermodynamic model chosen to describe the solid-liquid phase behavior of the system must render precise phase equilibria data as well as to be general enough so that complex mixtures can be treated the same way in the future.

### **1.3.2. Thermodynamic model**

There are different thermodynamic models available to simulate solid-liquid phase equilibria of wax mixtures (Lira-Galeana et al., 1996; Coutinho et al., 2006). All models, if tuned, are able to present solid-liquid phase equilibrium data that correspond to experimental results. But in a search for a physical coherent description of the phenomena involved in wax deposition, one is pushed to choose a model that can be extrapolated as much as possible.

In this work, a new strategy to evaluate the different thermodynamic models is proposed. The direct simulation of differential scanning calorimetry (DSC) thermograms using the different thermodynamic models is proposed. The methodology not only defines a basis through which the thermodynamic models can be compared, but it also presents an alternative to tune these models more precisely without having to go through the laborious work of measuring the experimental solubility curve of complex mixtures. The proposed strategy and its results are discussed in Chapters 2, 3 and 4.

The thermodynamic model chosen is also pushed to the limit and tested for its ability to correctly describe the phase behavior of a very asymmetric mixture containing CO<sub>2</sub> at high pressures. The results are presented in Chapter 5.

### **1.3.3. Thermophysical properties**

The thermophysical properties of the wax deposits like thermal conductivity reflect directly on its thickness. As such, these properties more often than not are tuned to render the best match between experimental and simulated results. In a search to evaluate the physics governing the complex phenomenon of wax deposition, it is important that these thermophysical properties be modeled as precisely as possible and not tuned at all to adjust the simulation results.

A search in the literature revealed that *n*-alkane thermal conductivity are only available to molecules lighter than *n*-icosane. There is only one measurement available for *n*-docosane and *n*-tetracosane.

To address this lack of thermal conductivity data, an effort to measure the thermal conductivity of heavy *n*-alkanes in both liquid and solid phases is presented in Chapter 6.

#### **1.3.4. CFD model**

To correctly address all of the domain in which wax deposition takes place, one is forced to simulate the advection of solids. Banki et al., (2008) proposed the closest attempt to this proposition available in the literature. Nevertheless, although explicitly treated in the simulation, the authors neglected the solid advection at all.

To improve on this model, a drift flux solid-liquid model (mixture model) is proposed. In such a model, the fluid is treated as a mixture and average properties are used to solve mass, momentum and energy conservation equations. The model is coupled with a thermodynamic routine that feeds back to the model the properties of the different phases and averages them in the mixture.

The wax deposition mechanism investigated is based on the non-Newtonian behavior of wax suspensions. As such, the appearance of solids in the liquid increases the mixture viscosity that, when high enough, renders negligible the velocity of the mixture, thereby forming the liquid-filled, porous wax deposit. The idea that the gelation of the oil could lead to the deposit was already raised in the literature (Singh et al., 1999; Merino-Garcia et al., 2007).

The model itself and the results obtained are presented in Chapter 7.

## 2

# DIRECT ADJUSTMENT OF WAX THERMODYNAMIC MODEL PARAMETER TO MICRO DIFFERENTIAL SCANNING CALORIMETRY THERMOGRAMS

### 2.1.

#### Introduction

Wax deposition is a major issue in oil production. Among the important subjects within the flow assurance, it has received attention from the industry and the academy for years (Huang et al., 2015). The control of wax deposition consists of retarding the oil cooling and mitigating the deposits through pigging operations or chemical interventions. To retard oil cooling, the most used strategies are cold flow, still not an option for the production of deep-water wells, and the implementation of insulated lines, which highly increases the cost of the production installations. The correct dimensioning of the insulation depends majorly on flow modeling and wax deposition simulation (Huang et al., 2015; Banki et al., 2008; Azevedo & Teixeira, 2003).

In order to model wax deposition, it is imperative to predict wax appearance conditions as well as the amount of waxy solids formed as a function of temperature and pressure. These predictions can be carried through sundry thermodynamic models that rest on different assumptions regarding the non-ideality of liquid mixtures and the nature of the solid phase (Banki et al., 2008; Coutinho et al., 2006). The major problem with these models is that most of them cannot be used in a predictive way with crude oils. They depend on empirical parameters that should be tuned to match phase equilibrium data, as these models are extremely dependent on the sample compositional information (Coutinho & Daridon, 2005). The tuning of these parameters is a necessary first step and it has a very strong impact on the models behavior.

The models can be adjusted through different processes. Usually, the wax appearance temperature (WAT) of dead oil samples is used to tune the model parameters. However, it was shown that all current experimental techniques have

shortcomings that preclude effective measurement of the thermodynamic equilibrium point (the point at which a very small crystal of paraffin is in equilibrium with the fluid at the highest possible temperature) (Coutinho & Daridon, 2005). The measurement bias is not only due to the method used but also to the fact that in cooling experiments the WAT measured is affected by the unavoidable supersaturation. On the other hand, the available methods able to quantify waxes in oil, among which the High Temperature Gas Chromatography method, renders high uncertainties for the quantification of heavier waxes, the molecules that dominate the simulated equilibrium temperature in any model (Robustillo et al., 2012). One is then left with a biased reference to adjust the models.

The best experimental curve one might have to adjust the thermodynamic models is the solid build-up curve or solubility curve. It is defined as the amount of waxy solid precipitated versus temperature at a given pressure. It renders real equilibrium data and distributes the error among the entire wax composition. Unfortunately, wax drop out curves are not easily available by direct measurements and take long and laborious experimental efforts to be obtained. It is usually obtained through either filtration or centrifugations methods (Han et al., 2010; Coutinho and Ruffier-Méray, 1997; Coutinho et al., 2000). However, in both methods, trapped liquid prevents the complete separation of solid phase and increases the uncertainties of the experimental results. Therefore, indirect methods are usually preferred by oil companies over direct measurements to generate wax precipitation curves (Coutinho et al., 2006).

The most commonly used indirect method is based on the integration of Differential Scanning Calorimetry (DSC) thermograms (Hansen et al., 1991; Létoffé et al., 1995; Juyal et al., 2011). This procedure rests on several assumptions for converting the area of the thermogram into the amount of solid formed. The main problem with such technique is that the enthalpy of wax crystallization needed to transform the thermogram area in solid mass is empirical. Moreover, as its value changes with wax composition, it cannot be estimated with accuracy before the wax precipitation curve is known.

In order to eliminate this empirical constant, a simple change of strategy is proposed. Instead of converting the thermogram into waxy solid build-up curve, we propose the simulation of the DSC experimental curves from the model itself,

allowing a full curve adjustment without going through the empirical integration of the experimental DSC thermogram. Due to the dynamic nature of the DSC experiments, differences will always be observed (Dumas et al., 2013). But they can be rendered sufficiently small if the DSC experiments are carried out with small temperature rates. Results obtained for complex wax mixtures for which experimental solubility curves are available, are presented and analyzed through the proposed procedure. In this proposed strategy, the thermodynamic model developed by Coutinho et al. (2006) at atmospheric pressure that accounts for the non-ideality of the solid phase was used to simulate the liquid/solid equilibria (SLE) at atmospheric pressure.

## 2.2. Method

DSC experiments are intrinsically transient and its precise modeling requires a heat transfer scheme (Dumas et al., 2013). This heat transfer scheme, on the other hand, needs to be adjusted to experimental results. Since the goal is to use the experimental data to adjust the thermodynamic model, the simultaneous adjustment of a heat transfer model would lead to uncertainties. It is proposed, as an alternative, to use small temperature rates in order to minimize as much as possible the transient effects during the experiment. The rate was established by comparing heating and cooling experiments. It was assumed that the dynamical effects of the experiments were at a minimum, once the only difference between these two experiments was the supersaturation peak in the cooling experiment. As industry standards are the cooling curves, they were used rather than the heating curves.

Supposing a static experiment, the signal calculation becomes straightforward. At a given temperature,  $T$ , the DSC signal ( $DSC_{EXP}$ ) is measured as the enthalpy flux as a function of time ( $\partial h/\partial t$ ), as defined in Equation 2-1. Once the temperature rate is defined ( $dT/dt$ ), the scale may be converted from time to temperature. Since the thermodynamic simulations will give out enthalpy flux as a function of the temperature ( $DSC_{CALC}$ , Equation 2-2), to be compared with the original DSC signal, it has to be multiplied by the temperature rate, as shown in Equation 2-3 (Fleming et al., 2014).

$$DSC_{EXP} = \frac{\partial h}{\partial t} \quad (2-1)$$

$$DSC_{CALC} = \frac{\partial h}{\partial T} \quad (2-2)$$

$$DSC_{EXP} = DSC_{CALC} \frac{dT}{dt} \quad (2-3)$$

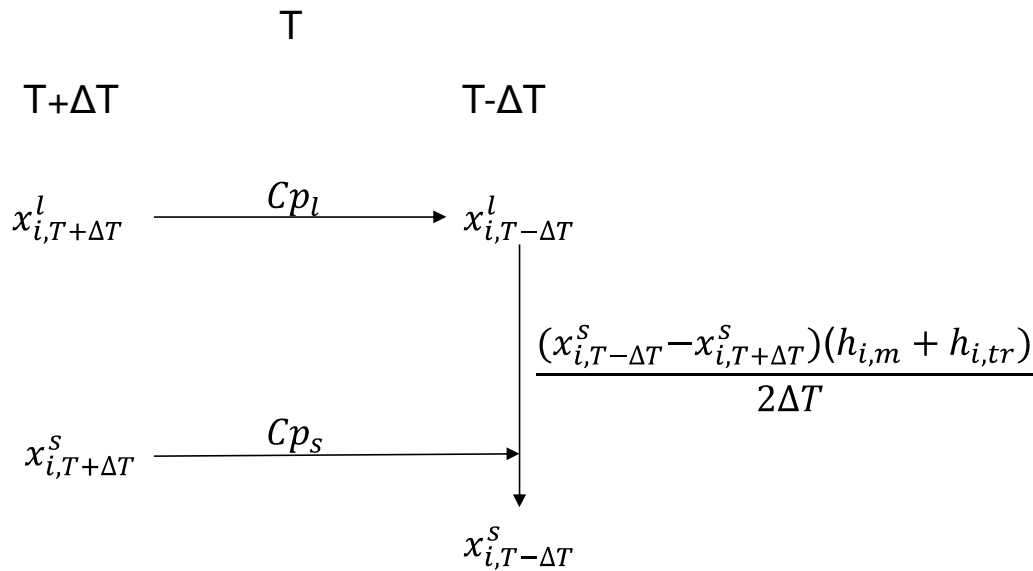


**Figure 2-1.** Thermodynamic scheme used to calculate the DSC signal from the model.

At constant pressure and global composition, the heat variation is equal to the enthalpy variation, and thus can be approximated by Equation 2-4 and the scheme depicted in Figure 2-1. The models will give the compositions of the liquid and solid phases at both temperatures  $T + \Delta T$  and  $T - \Delta T$ . With this information, the proposed equation is solved directly. In equation 2-4,  $x_{i,b}^a$  is the molar composition of component  $i$  in the either liquid or solid phase ( $a=l$  or  $s$ ) and at temperature  $b$  ( $T + \Delta T$  or  $T - \Delta T$ ).  $\Delta \bar{H}_{i,pure}^f$  and  $\Delta \bar{H}_{i,pure}^{tr}$  are respectively the melting enthalpy of component  $i$  and the solid-solid transition enthalpy of component  $i$ .

$$DSC_{CALC} = \sum_i MW_i \left[ x_{i,T+\Delta T}^l Cp_i^l + x_{i,T+\Delta T}^s Cp_i^s + \frac{(x_{i,T-\Delta T}^s - x_{i,T+\Delta T}^s)(\Delta h_{i,m} + \Delta h_{i,tr})}{2\Delta T} \right] \quad (2-4)$$

To evaluate the solid-liquid equilibrium (SLE) in the samples analyzed, a thermodynamic model proposed by Coutinho et al. (2006) was used. Equilibrium state is defined from the equality of fugacity of each component in the liquid and solid phase, as represented in Equation 2-5 (Prausnitz et al., 1999).

$$\hat{f}_i^L(T, P, \underline{x}^L) = \hat{f}_i^S(T, P, \underline{x}^S) \quad (2-5)$$

Equation 2-5 can be further extended to explicitly relate the composition of both liquid and solid phases and the thermophysical properties of their pure compounds (Prausnitz et al., 1999):

$$\ln \left( \frac{f_i^L}{f_i^S} \right) = \frac{\Delta \bar{H}_{i,pure}^f}{RT_i^f} \left( \frac{T_i^f}{T} - 1 \right) + \frac{\Delta \bar{H}_{i,pure}^{tr}}{RT_i^{tr}} \left( \frac{T_i^{tr}}{T} - 1 \right) \quad (2-6)$$

The thermophysical properties were calculated according to Equations 2-7 to 2-11, as proposed by Coutinho et al. (2006) and where developed following Marano and Holder (1997) methods .

$$T_i^f [K] = 421.63 - 1.936412 \times 10^6 \exp[-7.8945(CN_i - 1)^{0.07194}] \quad (2-7)$$

$$T_i^{tr} [K] = 420.42 - 1.34784 \times 10^5 \exp[-4.344(CN_i + 6.592)^{0.14627}] \quad (2-8)$$

$$\Delta \bar{H}_{i,pure}^f [kJ/mol] = 3.7791 CN_i - 12.654 \quad (2-9)$$

$$\Delta \bar{H}_{i,pure}^{tot} [kJ/mol] = 0.00355 CN_i^3 - 0.2376 CN_i^2 + 7.4 CN_i - 34.814 \quad (2-10)$$

$$\Delta \bar{H}_{i,pure}^{tr} [kJ/mol] = \Delta \bar{H}_{i,pure}^{tot} - \Delta \bar{H}_{i,pure}^f \quad (2-11)$$

where  $CN_i$ ,  $T_i^f$  and  $T_i^{tr}$  are respectively the number of carbon atoms, the melting temperature and solid-solid phase transition temperature of  $n$ -alkane  $i$ . This solid phase transition is only expected to occur from  $n$ -nonane to  $n$ -tetracontane.

At low pressure, the non-ideality of the liquid phase is described by an activity coefficient model from Equation 2-12.

$$\ln \gamma_i^L = \ln \gamma_i^{res} + \ln \gamma_i^{comb-fv} \quad (2-12)$$

where  $\gamma_i^{res}$  represents the energetic interactions between molecules and is obtained from the group contribution method, modified UNIFAC (Larsen et al., 1987), as proposed by Coutinho et al. (2006).

The second contribution  $\gamma_i^{comb-fv}$  describes the non-ideality originated from size difference between molecules and free volume effects and is calculated from Equation 2-13.

$$\ln \gamma_i^{comb-fv} = \ln \frac{\phi_i}{x_i} + 1 - \frac{\phi_i}{x_i} \quad (2-13)$$

$$\phi_i = \frac{x_i (V_i^{1/3} - V_{wi}^{1/3})^{3.3}}{\sum_j x_j (V_j^{1/3} - V_{wj}^{1/3})^{3.3}} \quad (2-14)$$

where  $V_i$  and  $V_{wi}$  are respectively de molar volume and the van der Waals volume of  $n$ -alkane  $i$ .

For the solid phase, the activity coefficients,  $\gamma_i^s$ , were described by means of a modified UNIQUAC model proposed by Coutinho et al. (2006) which is defined by:

$$\frac{\bar{G}^E}{RT} = \sum_{i=1}^{Nc} x_i^s \ln \left( \frac{\phi_i}{x_i^s} \right) + \frac{Z}{2} \sum_{i=1}^{Nc} q_i x_i^s \ln \left( \frac{\theta_i}{\phi_i} \right) - \sum_{i=1}^{Nc} q_i x_i^s \ln \left[ \sum_{j=1}^{Nc} \theta_j \tau_{ji} \right] \quad (2-15)$$

$$\tau_{ji} = \exp \left( - \frac{\Lambda_{ji} - \Lambda_{ii}}{q_i RT} \right) \quad (2-16)$$

$\Phi_i$  and  $\theta_i$  represents respectively the fraction of surface and volume of component  $i$  calculated from Equation 2-17 in which the structural parameters of surface  $q_i$  and volume  $r_i$  of the  $n$ -alkane  $i$  are obtained through Equations 2-18 and 2-19.

$$\Phi_i = \frac{x_i^s r_i}{\sum_{j=1}^{Nc} x_j^s r_j} \text{ and } \theta_i = \frac{x_i^s q_i}{\sum_{j=1}^{Nc} x_j^s q_j} \quad (2-17)$$

$$r_i = 0.6744CN_i + 0.4534 \quad (2-18)$$

$$q_i = 0.540CN_i + 0.616 \quad (2-19)$$

The interaction energy,  $\Lambda_{ij}$  can be estimated by means of the local composition concept proposed by the modified UNIQUAC Equation 2-20. The interaction energies between two identical molecules can be estimated from the enthalpy of sublimation of an orthorhombic crystal of the pure component as:

$$\Lambda_{ii} = - \frac{Z}{2} (\Delta \bar{H}_{i,pure}^{sub} - RT) \quad (2-20)$$

where  $Z$  is the coordination number, and  $Z = 6$  will be used for UNIQUAC. The enthalpy of sublimation ( $\Delta \bar{H}_{i,pure}^{sub} = \Delta \bar{H}_{i,pure}^{vap} + \Delta \bar{H}_{i,pure}^f + \Delta \bar{H}_{i,pure}^{tr}$ ) is calculated at the melting temperature of the pure component.  $\Delta \bar{H}_{i,pure}^{vap}$  is calculated using a correlation proposed by Morgan and Kobayashi (1994a,b).

For two different molecules, the interaction parameter  $\Lambda_{ij}$  is related to the contact area between the molecules, which is assumed to be limited by the shorter molecule. Thus, it is considered to be identical to  $\Lambda_{ii}$  of the shorter molecule in the pair. The term  $\Lambda_{ij}$  is also used to tune the model to experimental results, where it is modified according to Equation 2-21 through the parameter  $f_{adjust}$ . This is the only adjustable parameter in the model and is independent of the number of compounds in the solid phases.

$$\Lambda_{ij} = \Lambda_{ij}(1 + f_{adjust}) \quad (2-21)$$

## 2.3. Experimental

### 2.3.1. Chemicals

All of the mixtures used were formulated through the combination of standard single *n*-alkanes. All of the *n*-alkanes were used without further purification. Their origin and purity are listed in Table 2-1, along with its respective amount.

**Table 2-1.** Composition of the samples (mass %) analyzed. Supplier and purity of the standards (mass %) are informed in the last two columns.

	S1	S2	S3	S4	S5	Supplier	Purity (%)
n-C <sub>10</sub>	63.90	64.25	64.65	65.63	66.40	Aldrich	>99
n-C <sub>18</sub>	4.285	4.922	5.362	6.967	10.615	Fluka	99
n-C <sub>19</sub>	3.844	4.419	4.874	6.289	9.651	Fluka	>99
n-C <sub>20</sub>	3.473	3.944	4.388	5.684	8.717	Aldrich	99
n-C <sub>21</sub>	3.116	3.550	4.072	5.103	-	Fluka	>99.5
n-C <sub>22</sub>	2.789	3.213	3.541	4.601	-	Aldrich	99
n-C <sub>23</sub>	2.507	2.883	3.172	-	-	Fluka	>98
n-C <sub>24</sub>	2.254	2.656	2.824	-	-	Aldrich	99
n-C <sub>25</sub>	2.001	2.337	-	-	-	Aldrich	99
n-C <sub>26</sub>	2.006	-	-	-	-	Fluka	>99
n-C <sub>27</sub>	1.595	-	-	-	-	Fluka	>98
n-C <sub>28</sub>	1.442	-	-	-	-	Aldrich	99
n-C <sub>29</sub>	1.263	1.436	-	-	-	Fluka	>99.5
n-C <sub>30</sub>	1.120	1.277	1.442	-	-	Aldrich	99
n-C <sub>31</sub>	0.991	1.145	1.248	-	-	Fluka	>99.5
n-C <sub>32</sub>	0.877	1.000	1.115	1.444	-	Fluka	>95
n-C <sub>33</sub>	0.802	0.887	1.002	1.279	-	Fluka	>97
n-C <sub>34</sub>	0.694	0.787	0.865	1.128	1.723	Aldrich	98
n-C <sub>35</sub>	0.515	0.681	0.760	0.997	1.521	Fluka	>99.5
n-C <sub>36</sub>	0.530	0.617	0.682	0.880	1.377	Aldrich	98

### 2.3.2. Micro differential scanning calorimetry (DSC)

To allow a small temperature rate and a high resolution signal, the experiments were carried out using a SETARAM Micro DSC 7 evo calorimeter. The DSC calibration was performed following the recommended procedure from the manufacturer.

The experiments were carried using samples weighting around 130 mg. The experimental procedure started with a pre-treatment process in which the samples were first heated at a rate of  $1.2 \text{ K}\cdot\text{min}^{-1}$  from ambient temperature to 15 K above their melting point and maintained at this temperature during 30 minutes. The samples were then cooled down to 253.2 K at  $0.2 \text{ K}\cdot\text{min}^{-1}$  and kept at this temperature for 30 min in order to guarantee temperature stabilization. Afterwards the solid samples were heated at a rate of  $0.2 \text{ K}\cdot\text{min}^{-1}$  to achieve the liquid state again. Each run was performed two times with a maximum deviation of 0.1 K. The different curves are available in the Appendix A.

## 2.4. Results and Discussions

The compositions of the samples S1 to S5 are shown in Table 2-1. A comparison between the compositions of the samples used in this work and those of the samples analyzed by Dauphin et al (1999) can be found in the Appendix A. The small differences found should cause a small deviation between the data but the differences in the solubility curves should still be within experimental uncertainties of the original data.

In Figures 2-2 to 2-6 it is shown the experimental DSC cooling thermogram and the simulated curve for samples S1 to S5, respectively. The results are shown only for the optimized  $f_{adjust}$  parameter. This parameter was optimized by calculating the root mean square deviation (rmsd) between the experimental and the simulated results. The optimal parameters and the highest temperature evaluated are displayed in Table 2-2.

**Table 2-2.** Optimized  $f_{adjust}$  parameter and highest temperature evaluated for the analyzed samples.

	S1	S2	S3	S4	S5
$f_{adjust}$	0.008	0.02	0.014	0.012	0.01
Tmax (°C)	33	29	30	32	35

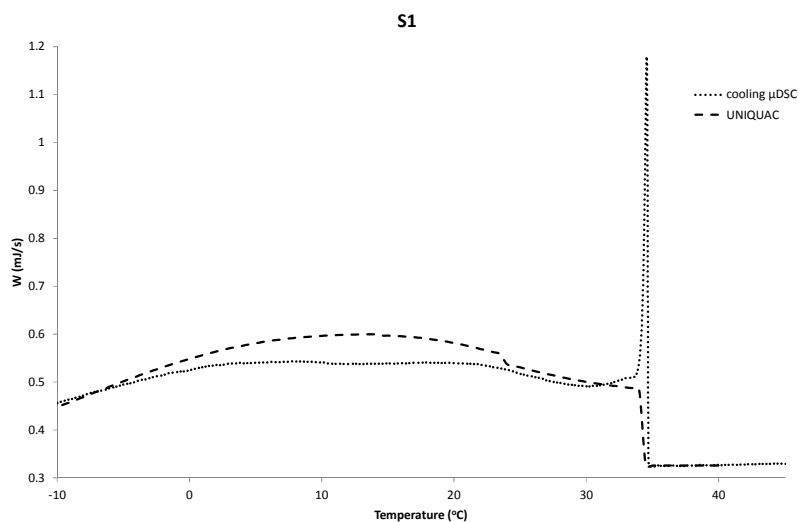


**Figure 2-2.** DSC thermogram and simulated DSC curve for sample S1.

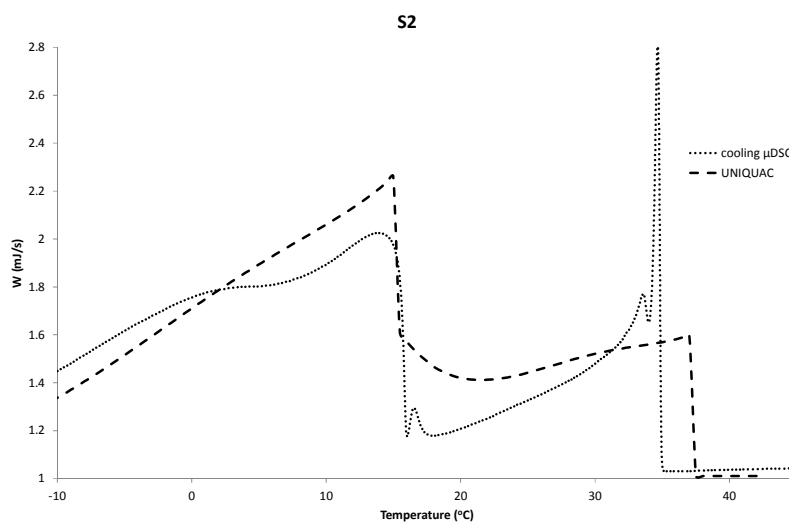


**Figure 2-3.** DSC thermogram and simulated DSC curve for sample S2.

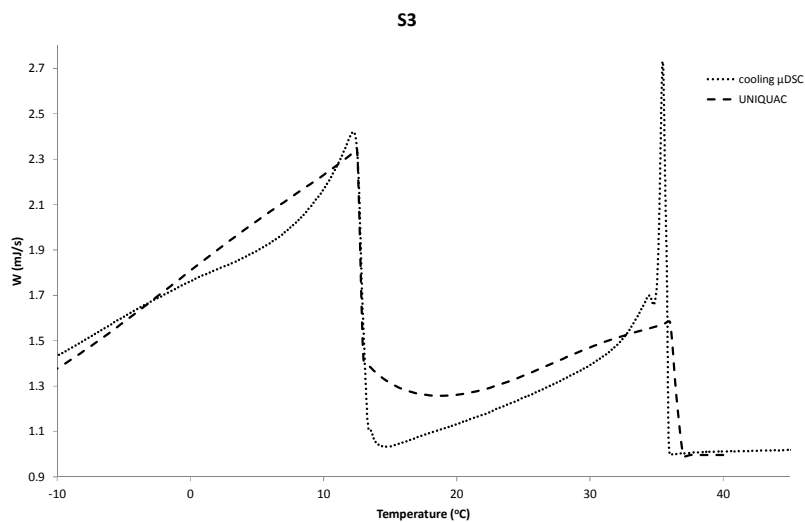


**Figure 2-4.** DSC thermogram and simulated DSC curve for sample S3.

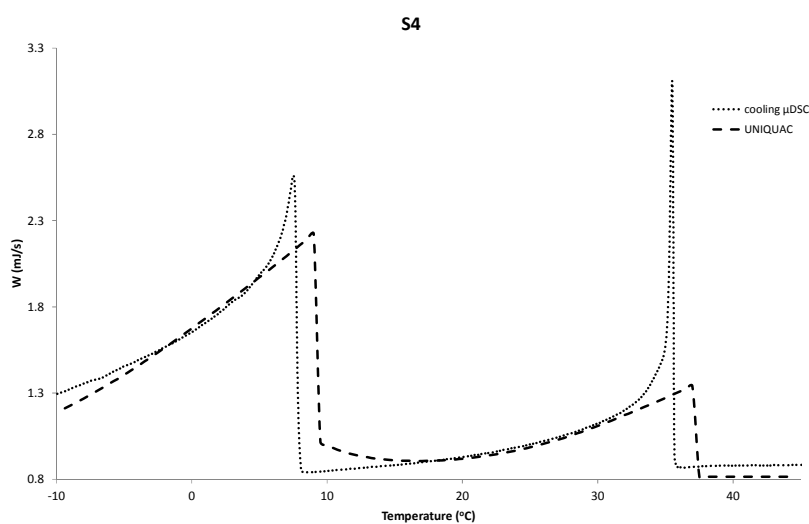


**Figure 2-5.** DSC thermogram and simulated DSC curve for sample S4.

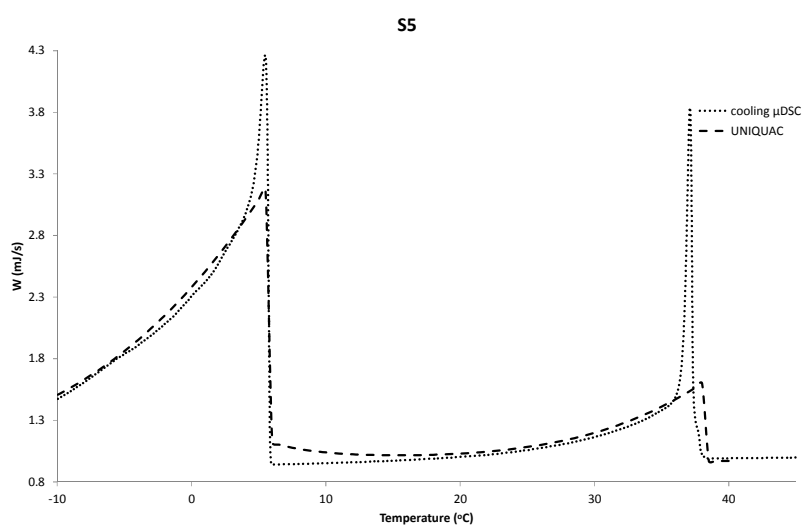


**Figure 2-6.** DSC thermogram and simulated DSC curve for sample S5.

The peak observed in the beginning of the cooling DSC experiments is due to the supersaturation of the wax. This phenomenon is not encompassed in the pure thermodynamic model, requiring kinetics considerations to be properly reproduced. Since this proposed first approach is to model the thermodynamic information encompassed in DSC thermograms, only the points at temperatures below the experimental first peak were considered during the optimization process. The maximum temperatures, below which the optimization process was carried out, are displayed in Table 2-2.

The adjusted parameter changes the interchain interaction energy parameter. So, it is expected that the closer to a continuous is the sample's paraffin distribution the smaller needs to be the adjustments to the original model. As the gap between the bimodal distributions in the samples S2-5 grow, the more the samples behave as a real binary system, rendering a smaller correction in the original parameters. The unbiased adjustment through the proposed method renders the expected trend in the parameter  $f_{adjust}$ .

To estimate the samples specific heat, no temperature dependence was taken into account. The experimental  $C_p$  of the solvent (decane) was obtained from the NIST database ( $313.0 \text{ J}\cdot\text{mol}^{-1}\cdot\text{K}^{-1}$ ). The heat capacity for the other components when in the liquid phase was estimated using the correlation proposed by Marano and Holder (1997) at their melting temperature. The difference  $C_p^L - C_p^S$  for waxy components was estimated using the correlation proposed by Pedersen et al. (1991). Consequently the heat capacity of the mixture was obtained by a linear combination of pure component heat capacities, *i.e.*, the excess heat capacity was negligible in waxy mixtures. From the results displayed in Figures 2-2 to 2-6, it can be seen that the  $C_p$  estimated from this method renders a good agreement between the simulated and experimental DSC signals at temperatures above the WAT.

The second peak observed in the results for samples S2-5 is due to the precipitation of the paraffins from the second modal distribution. This process, as the distance in the two modals grow, may become more susceptible to dynamic variations intrinsic to the DSC experiment. In this sense, as the gap between the modals grows, the same supersaturation phenomena might appear in the second peak. The difference in the intensity of the peak between simulated and

experimental curves might be due to the dynamic behavior of this transition, as it increases continuously from sample S2 to sample S5.

Once the minimization of the rmsd was chosen as the optimization procedure, an immediate consequence is that it will tend to match the temperature of the precipitation of the second modal of the wax distribution. This was the case for all samples except for sample S4.

The solubility curves obtained from the model are displayed in Figures 2-7 to 2-11. They are compared to the experimental data measured by Dauphin et al. (1999). The results are in good agreement, showing that the methodology proposed renders a low cost and low time consuming method to adjust the thermodynamic model to experimental data.

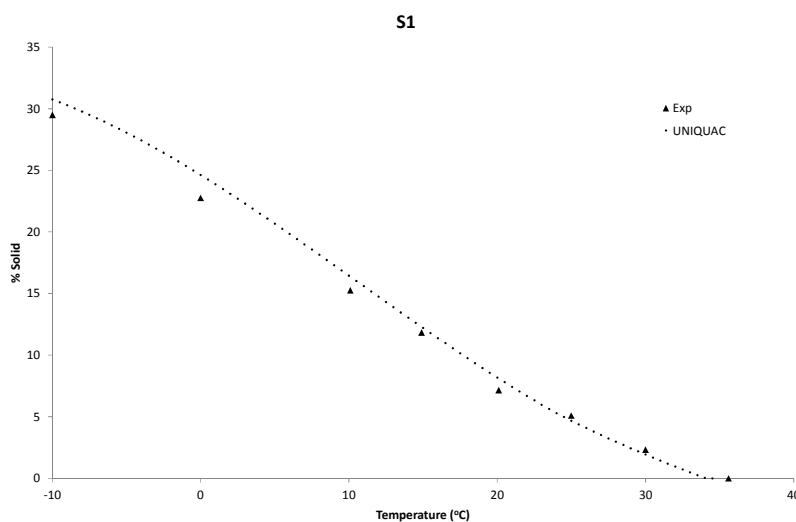


**Figure 2-7.** Simulated precipitation curves and experimental results obtained by Dauphin et al. (1999) for sample S1.

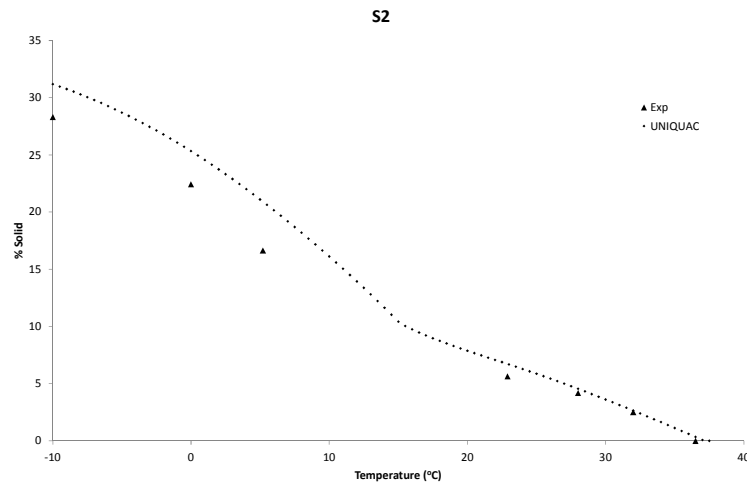


**Figure 2-8.** Simulated precipitation curves and experimental results obtained by Dauphin et al. (1999) for sample S2.

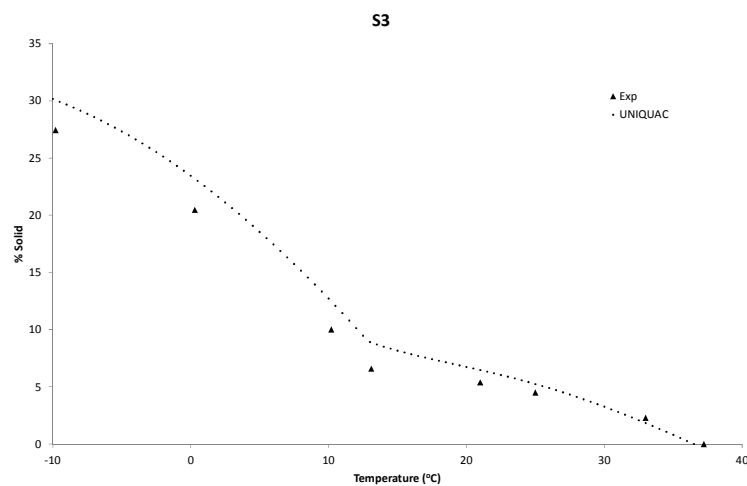


**Figure 2-9.** Simulated precipitation curves and experimental results obtained by Dauphin et al. (1999) for sample S3.

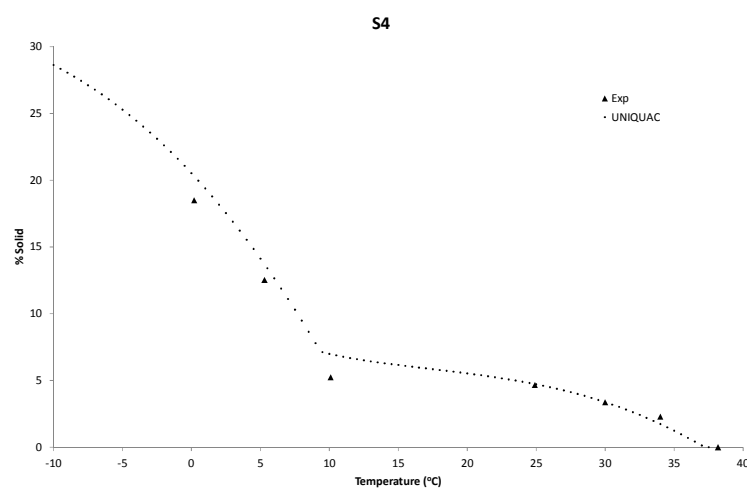


**Figure 2-10.** Simulated precipitation curves and experimental results obtained by Dauphin et al. (1999) for sample S4.

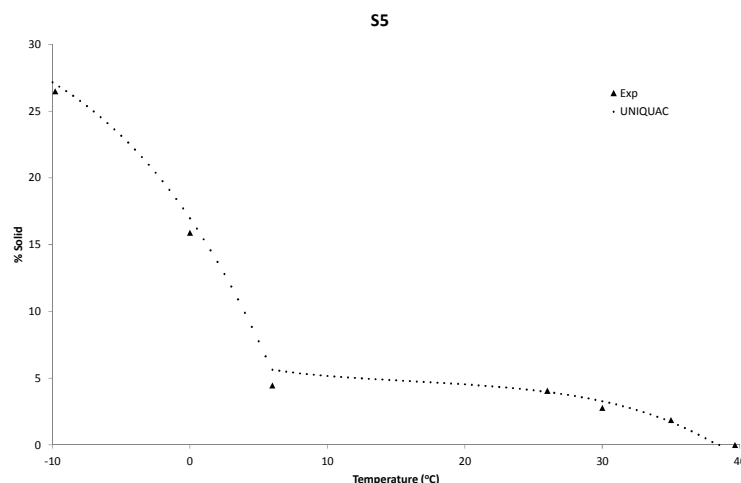


**Figure 2-11.** Simulated precipitation curves and experimental results obtained by Dauphin et al. (1999) for sample S5.

After tuning the model to DSC curve, it is used to estimate liquid-waxy solid phase separation. The comparison between the transition temperatures obtained by this method with those measured by cross polar microscopy during a heating process is presented in Table 2-3. The differences are quite small between the measured and estimated Wax Disappearing Temperatures (WDT), indicating that adjusting the entire DSC curve does not compromise the simulation of the WDT. It is important to note that since a thermodynamic model was used to simulate the wax phase equilibrium, it is the WDT and not the WAT which is calculated. The WDT should be greater than the WAT, indicating that the model cannot be adjusted to DSC measured WAT. But once the solids are present, the rest of the curve is very close to the thermodynamic equilibrium curve, rendering possible its use for the model tuning.

**Table 2-3.** Experimental wax disappearance temperature (WDT) from Dauphin et al. (1999) (Experimental), SLE temperature calculated through the adjusted thermodynamic model (Wax model) and the wax appearance temperature (WAT) measured by DSC (DSC). The uncertainty of the WAT measured by DSC for all samples is  $u(\text{WAT}) = \pm 1$  °C.

	S1	S2	S3	S4	S5
Experimental (°C)	35.5	36.5	37.22	38.18	39.66
Wax model (°C)	34	37	36.5	37	38
DSC (°C)	34.6	34.8	35.8	36.4	37.3

## 2.5. Conclusions

The assessment of wax deposition on oil production system under design depends on the modeling of such phenomenon. These deposition models depend inexorably on the solubility curve. This curve must either be given or has to be calculated through a SLE model. The SLE models depend greatly on the fluid composition and are usually tuned to the experimentally measured WAT, which has unavoidable shortcomings. The experimental alternatives, such as the direct measurement of the solubility curve of dead oil samples are laborious and no viable for many different samples.

To improve the tuning of the SLE methods to experimental results, a new methodology is proposed. Instead of running laborious experiments to measure the wax precipitation curves, or empirically integrating the DSC thermogram, one may simulate the thermogram straight from the model itself. The simulated DSC thermogram can then be compared directly to the experimental DSC curves. These curves are part of the oil characterization, being already available when any oil is studied. They contain all of the wax precipitation curve information. The proposed DSC curve simulation through the thermodynamic models allows a less biased analysis of the DSC results.

The results analyzed suggest that the proposed strategy and method are not only valid but may help to shed light on different solid-liquid equilibrium phenomena. The current applied models are not immediately extrapolated to real fluids, but simple adjustments are under evaluation and development which will allow its broad application by the oil industry with little or no extra effort whatsoever.

### 3

## PARAFFIN SOLUBILITY AND CALORIMETRIC DATA CALCULATION USING PENG-ROBINSON EOS AND MODIFIED UNIQUAC MODELS

### 3.1.

#### Introduction

During production, petroleum is subject to different temperature and pressure conditions, which can lead to precipitation of different solids, such as hydrates, asphaltenes and waxes. Among these flow assurance issues, wax deposition gains importance as the frontier of oil exploration moves towards hostile environments, like deep water and the Arctic (Huang et al., 2015). Wax deposition is hard to remediate, as it depends on mechanical removal of the deposits through pigging operations or chemical intervention like solvent soaking. As these different operations lead to production loss, the most cost effective strategy to deal with wax deposition is to avoid it during the design of production installations (Azevedo and Teixeira, 2003). Therefore, one is obliged to use wax deposition models, which depend either on the amount of wax precipitated or on its derivative with respect to temperature. Both can be calculated through thermodynamic models of solid-liquid equilibria (SLE) of waxes and oil (Azevedo and Teixeira, 2003).

Modeling wax behavior in solid phase has been the aim of study of several works in the literature (Banki et al., 2008; Ji et al., 2004). A variety of solid paraffins models have been developed, e.g., the multisolid model, which describes solid paraffins as being multiple pure solid phases, the ideal solid solution model, which describes paraffinic solid phase as being an ideal solution, and other models that describe solid paraffins as one or more non-ideal solid phase solutions, the solid solution models (Lira-Galeana et al., 1996; Won, 1986; Hansen et al., 1988; Coutinho et al., 2006).

Such as solid phases, liquid phases may also be modelled in different ways. Excess Gibbs energy (EGE) models, also called activity coefficient models, as well as cubic equations of state (EoS), are commonly used to describe liquid phases.

Activity coefficient approaches are known for their good agreement to liquid behavior. On the other hand, there is no substantial information about the use of EoS with van der Waals mixing rule along with EGE models for solids. However, since this last liquid model presents many advantages when compared to activity coefficient models, e.g., possibility of tuning the thermodynamic model from PVT data and taking into account pressure effect, making the model applicable to live oils, determining EoS efficiency in modelling liquids is of great interest.

Usually, validation of SLE modelling is carried out by comparing calculated results with wax appearance temperature (WAT) experimental data, and thermodynamic models available in the literature are tuned using this approach. Nevertheless, the WAT cannot be considered a true equilibrium point, since its value has a strong dependency on the experimental procedure used (Ji et al., 2004; Coutinho and Daridon, 2005). The true equilibrium point is, actually, the wax disappearance temperature (WDT), which is the variable calculated from the thermodynamic models. Hence, tuning thermodynamic models based on the WAT turn up to be a questionable strategy (Fleming et al., 2017).

An alternative approach consists in tuning the thermodynamic model directly to DSC (Differential Scanning Calorimetry) thermograms, as proposed in Chapter 2 (Fleming et al., 2017). In this strategy, instead of fitting the model parameters to solubility or WAT data, they are fitted to DSC curves. For this purpose, in Chapter 2, it was investigated the use of a simplified method for the simulation of DSC thermograms, which only takes into consideration the independent transition enthalpies of the different components, neglecting excess enthalpy contributions, and uses an incompressible model for the liquid phase. Aiming at a more accurate and widely applicable approach, non-idealities should also be contemplated in heat calculations used to build up simulated DSC thermograms. As the liquid model used in Chapter 2 is limited to incompressible fluids with known composition, a different liquid model should also be explored.

To assure a rigorous and widely applicable calculation scheme for the DSC thermograms, a complete energy balance of the system, taking into consideration solid and liquid phases, is performed. It is set as reference for all components in all phases the ideal gas state, which makes the energy balance suitable for multiphase systems. For the liquid phase, Peng-Robinson EoS has been used (Peng and Robinson, 1976). It was compared to the Flory free-volume combined with

modified UNIFAC model used by Fleming et al. (2017). Three different solid models, the multisolid, ideal solid solution and solid solution, were also compared. To validate the proposed approach, the results were compared to experimental data of five synthetic mixtures at atmospheric pressure (Fleming et al., 2017; Dauphin et al., 1999).

## 3.2. Methodology

### 3.2.1. DSC simulation

Differential Scanning Calorimetry (DSC) is an experimental method that measures the heat flow related with transitions in materials as a function of time (Chiavaro, 2015). When carried out at a constant temperature rate, one can easily convert the results from a time dependence to a temperature dependence basis.

For simulation purposes, the heat flux measured in the DSC can be calculated taking into consideration that at a constant pressure the heat exchanged is equal to the product between the system molar enthalpy variation,  $\bar{H}$ , and the total number of moles of the sample,  $N_{mol}$ , as in

$$\frac{\delta Q}{\delta t} = \frac{\partial \bar{H}}{\partial t} N_{mol} \quad (3-1)$$

The molar enthalpy derivative with time is related to its derivative with temperature through

$$\frac{\partial \bar{H}}{\partial t} = \frac{\partial \bar{H}}{\partial T} \frac{\partial T}{\partial t} \quad (3-2)$$

To reduce the transient effects in the DSC experiment, as discussed in Chapter 2, a small value of the temperature rate,  $\partial T / \partial t$ , should be adopted (Fleming et al., 2017; Hansen et al., 1991). A rate of 0.2°C/min was used in Chapter 2 for all the DSC experiments studied in this chapter. Therefore, for DSC simulation, it is just necessary the evaluation of the molar enthalpy derivative with the temperature,  $\partial \bar{H} / \partial T$ . This derivative has been calculated numerically as follows:

$$\frac{\partial \bar{H}}{\partial T} = \frac{\bar{H}(T+\Delta T) - \bar{H}(T-\Delta T)}{2\Delta T} \quad (3-3)$$

The total molar enthalpy,  $\bar{H}$ , is obtained from the molar enthalpy of each phase present in the mixture:

$$\bar{H} = \sum_{j=1}^{Np} \beta^j \bar{H}^j \quad (3-4)$$

where  $Np$ ,  $\beta^n$  and  $\bar{H}^n$  are the number of phases, the phase fraction and the molar enthalpy of phase  $n$ , respectively.

A complete thermodynamic path has been proposed in order to calculate the molar enthalpy of each pure component  $i$  in each phase in the mixture, which can then be combined to give the molar enthalpy of the different phases. The path starts at the ideal gas reference state at  $T_0 = 298$  K and  $P_0 = 1$  atm, and ends at solid state at the system's temperature,  $T$ , and pressure,  $P$ , as shown in Figure 3-1. As a wide range of  $n$ -alkanes present solid-solid transitions before melting (Ji et al., 2004; Coutinho et al., 2006; Coutinho et al., 1995), the proposed path also encompasses such a transition.

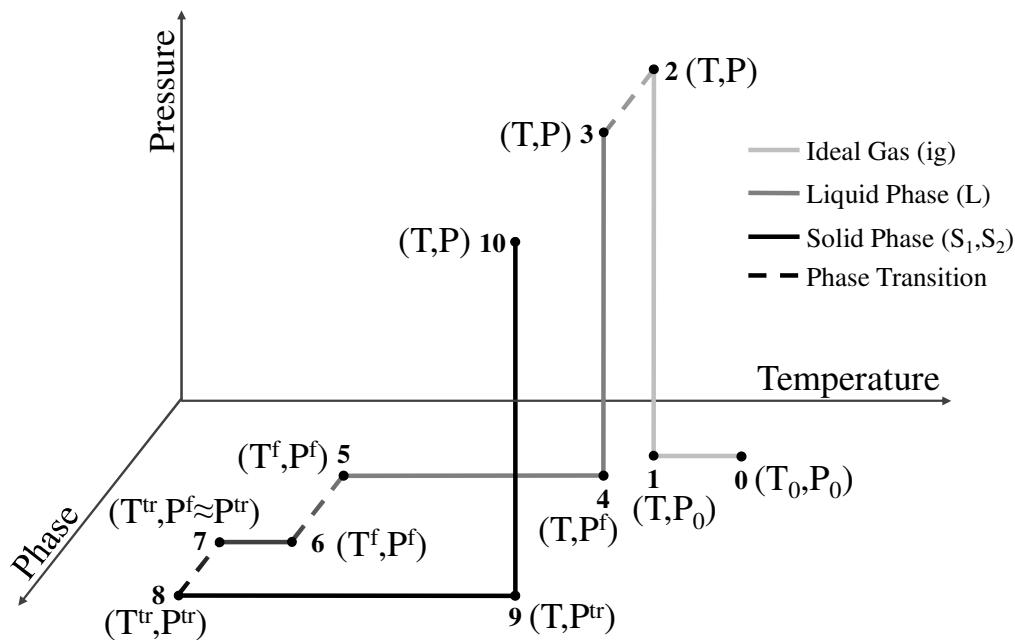


**Figure 3-1.** Thermodynamic path used to obtain the molar enthalpy of pure paraffins.

In Figure 3-1,  $T^f, P^f$ ,  $T^{tr}$  and  $P^{tr}$  are the melting temperature, melting pressure, temperature of crystalline transition and pressure of crystalline transition of pure paraffins, respectively. The different numbers in Figure 3-1 indicate the molar enthalpy of component  $i$  in the different states connected in the proposed path. Equations 3-5 to 3-14 give the molar enthalpy variation that connects the different states, respectively, and are represented as  $\bar{H}_{i,pure}^1 - \bar{H}_{i,pure}^0$ ,  $\bar{H}_{i,pure}^2 - \bar{H}_{i,pure}^1$  and so on.

$$\bar{H}_{i,pure}^1 - \bar{H}_{i,pure}^0 = \int_{T_0}^T C p_{i,pure}^{ig} dT \quad (3-5)$$

$$\bar{H}_{i,pure}^2 - \bar{H}_{i,pure}^1 = \int_{P_0}^P \left[ \bar{V}_{i,pure}^{ig} - T \left( \frac{\partial \bar{V}_{i,pure}^{ig}}{\partial T} \right)_P \right] dP = 0 \quad (3-6)$$

$$\bar{H}_{i,pure}^3 - \bar{H}_{i,pure}^2 = \bar{H}_{i,pure}^L(T, P) - \bar{H}_{i,pure}^{ig}(T, P) = \bar{H}_{i,pure}^R(T, P) \quad (3-7)$$

$$\bar{H}_{i,pure}^4 - \bar{H}_{i,pure}^3 = \int_P^{P_i^f} \left[ \bar{V}_{i,pure}^L - T_i^f \left( \frac{\partial \bar{V}_{i,pure}^L}{\partial T} \right)_P \right] dP \quad (3-8)$$

$$\bar{H}_{i,pure}^5 - \bar{H}_{i,pure}^4 = \int_T^{T_i^f} C p_{i,pure}^L dT \quad (3-9)$$

$$\bar{H}_{i,pure}^6 - \bar{H}_{i,pure}^5 = -\Delta \bar{H}_{i,pure}^f \quad (3-10)$$

$$\bar{H}_{i,pure}^7 - \bar{H}_{i,pure}^6 = \int_{T_i^f}^{T_i^{tr}} C p_{i,pure}^{S_1} dT \quad (3-11)$$

$$\bar{H}_{i,pure}^8 - \bar{H}_{i,pure}^7 = -\Delta \bar{H}_{i,pure}^{tr} \quad (3-12)$$

$$\bar{H}_{i,pure}^9 - \bar{H}_{i,pure}^8 = \int_{T_i^{tr}}^T C p_{i,pure}^{S_2} dT \quad (3-13)$$

$$\bar{H}_{i,pure}^{10} - \bar{H}_{i,pure}^9 = \int_{P_i^{tr}}^P \left[ \bar{V}_{i,pure}^{S_2} - T_i^f \left( \frac{\partial \bar{V}_{i,pure}^{S_2}}{\partial T} \right)_P \right] dP \quad (3-14)$$

In Equations 3-5 to 3-14,  $C p_{i,pure}^{ig}$  and  $\bar{V}_{i,pure}^{ig}$  are the heat capacity and the molar volume of pure component  $i$  as an ideal gas, respectively.  $C p_{i,pure}^L$  is the heat capacity of pure component  $i$  in the liquid phase.  $\bar{H}_{i,pure}^R$  is the molar residual enthalpy of pure component  $i$ , which is calculated from an EoS.  $\bar{V}_{i,pure}^L$  is the molar volume of pure component  $i$  in the liquid phase.  $\Delta \bar{H}_{i,pure}^f$  and  $\Delta \bar{H}_{i,pure}^{tr}$  are the molar melting enthalpy of pure component  $i$  and the molar transition enthalpy between the solid states S1 and S2, respectively.  $\bar{V}_{i,pure}^{S_1}$  and  $\bar{V}_{i,pure}^{S_2}$  are the molar volumes of pure component  $i$  in the solid states S1 and S2, respectively.  $C p_{i,pure}^{S_1}$  and  $C p_{i,pure}^{S_2}$  are the heat capacities of pure component  $i$  in the solid states S1 and S2, respectively.

Considering  $C p_{i,pure}^{S_1}$  and  $C p_{i,pure}^{S_2}$  similar (Ji et al., 2004; Coutinho et al., 1995), one gets:

$$Cp_{i,pure}^{S_1} = Cp_{i,pure}^{S_2} = Cp_{i,pure}^S \quad (3-15)$$

Then, the terms  $\int_{T_i^f}^{T_i^{tr}} Cp_{i,pure}^{S_1} dT$  and  $\int_{T_i^{tr}}^T Cp_{i,pure}^{S_2} dT$  are grouped and added to Equations 3-9, 3-10 and 3-12, resulting in

$$\bar{H}_{i,pure}^g - \bar{H}_{i,pure}^L = \int_{T_i^f}^T (Cp_{i,pure}^S - Cp_{i,pure}^L) dT - \Delta\bar{H}_{i,pure}^f - \Delta\bar{H}_{i,pure}^{tr} \quad (3-16)$$

Since enthalpies of phase transition are many orders of magnitude greater than the integrals of heat capacities difference for the temperatures of interest in petroleum production, the integral in Equation 3-16 has been neglected. Thus, for a pure component  $i$ , the molar enthalpy in the solid phase is

$$\begin{aligned} \bar{H}_{i,pure}^S(T, P) = & \bar{H}_{i,pure}^{ig}(T_0, P_0) + \int_{T_0}^T Cp_{i,pure}^{ig} dT + \bar{H}_{i,pure}^R(T, P) - \Delta\bar{H}_{i,pure}^f - \\ & \Delta\bar{H}_{i,pure}^{tr} + \int_P^{P_i^f} \left[ (\bar{V}_{i,pure}^S - \bar{V}_{i,pure}^L) - T_i^f \left( \frac{\partial(\bar{V}_{i,pure}^S - \bar{V}_{i,pure}^L)}{\partial T} \right) \right] dP \end{aligned} \quad (3-17)$$

Moreover, the term related to pressure variation of condensed phase is very small once  $\bar{V}_i^L \approx \bar{V}_i^S$  and then have also been neglected. Therefore, the molar enthalpy of an ideal solid phase with composition  $\underline{x}^S$  is

$$\begin{aligned} \bar{H}^{S,ideal}(T, P, \underline{x}^S) = & \sum_{i=1}^{Nc} x_i^S \bar{H}_{i,pure}^{ig}(T_0, P_0) + \\ & \sum_{i=1}^{Nc} x_i^S \int_{T_0}^T Cp_{i,pure}^{ig} dT + \bar{H}^R(T, P, \underline{x}^S) - \\ & \sum_{i=1}^{Nc} x_i^S \Delta\bar{H}_{i,pure}^f - \sum_{i=1}^{Nc} x_i^S \Delta\bar{H}_{i,pure}^{tr} \end{aligned} \quad (3-18)$$

The molar enthalpy of the liquid phase is:

$$\begin{aligned} \bar{H}^L(T, P, \underline{x}^L) = & \sum_{i=1}^{Nc} x_i^L \bar{H}_{i,pure}^{ig}(T_0, P_0) + \\ & \sum_{i=1}^{Nc} x_i^L \int_{T_0}^T Cp_{i,pure}^{ig} dT + \bar{H}^R(T, P, \underline{x}^L) \end{aligned} \quad (3-19)$$

where  $\bar{H}^R$  is obtained from the Peng-Robinson EoS. For the ideal gas heat capacities calculation,  $Cp_{i,pure}^{ig}$ , the parameters of the correlation presented by Passut and Danner (1972), originally developed using data from CH<sub>4</sub> to C<sub>20</sub>H<sub>44</sub>, have been correlated and extrapolated for  $n$ -alkanes with longer chains. Here, the ideal gas

molar enthalpy at the reference state for each pure component  $i$ ,  $\bar{H}_{i,pure}^{ig}(T_0, P_0)$ , is set to zero.

Solid phase non-idealities are taken into account through the incorporation of the excess molar enthalpy,  $\bar{H}^E$ :

$$\bar{H}^S(T, P, \underline{x}^S) = \bar{H}^{S,ideal}(T, P, \underline{x}^S) + \bar{H}^E(T, \underline{x}^S) \quad (3-20)$$

where

$$\bar{H}^E(T, \underline{x}^S) = -RT^2 \sum_{i=1}^{Nc} x_i^S \left( \frac{\partial \ln \gamma_i^S}{\partial T} \right)_{P,x} \quad (3-21)$$

In Equation 3-21, the activity coefficient derivative of component  $i$  in the solid phase is obtained analytically from the modified UNIQUAC model (Coutinho et al., 2006).

### 3.2.2. Thermodynamic model

The thermodynamic model used to determinate the amount of paraffins precipitated and the compositions of the phases in the mixture is based on the multiple solid solutions model proposed by Coutinho et al. (2006).

Coutinho's model (Coutinho et al., 2006) employs a combination of modified UNIFAC (Larsen et al., 1987) and Flory free-volume (Coutinho et al., 1995) models to describe the liquid phase non-idealities, and the modified UNIQUAC model to describe the solid phase non-idealities.

The usage of Peng-Robinson EoS to describe liquid phase non-idealities arises as an alternative proposed in this Chapter. In comparison to an activity coefficient model, the Peng-Robinson EoS has the advantage of being already widely used by oil industry, as it can be tuned from PVT data and takes into account pressure effect, making it easier to model live oils. In this work, Peng-Robinson EoS was used together with the classical van der Waals mixing and combining rules, in which the binary interaction coefficient,  $k_{ij}$ , is calculated using the correlation proposed by Pan et al. (1997) and  $l_{ij} = 0$ . The critical properties and acentric factors of all components used in this work are estimated using the correlations suggested by Marano and Holder (1997).

For the solid solution model, if the phases are in equilibrium, the condition of equal fugacities must be satisfied for each component  $i$ :

$$\hat{f}_i^L(T, P, \underline{x}^L) = \hat{f}_i^S(T, P, \underline{x}^S) \quad (3-22)$$

In the model of Coutinho (Coutinho et al., 2006), the liquid and solid fugacities  $\hat{f}_i^L$  and  $\hat{f}_i^S$  are:

$$\hat{f}_i^L(T, P, \underline{x}^L) = x_i^L \gamma_i^L f_i^L \quad (3-23)$$

and

$$\hat{f}_i^S(T, P, \underline{x}^S) = x_i^S \gamma_i^S f_i^S \quad (3-24)$$

in which pure solid fugacity,  $f_i^S$ , is calculated from the pure liquid fugacity,  $f_i^L$ :

$$\ln \left( \frac{f_i^L}{f_i^S} \right) = \frac{\Delta \bar{H}_{i,pure}^f}{RT_i^f} \left( \frac{T_i^f}{T} - 1 \right) + \frac{\Delta \bar{H}_{i,pure}^{tr}}{RT_i^{tr}} \left( \frac{T_i^{tr}}{T} - 1 \right) \quad (3-25)$$

The SLE ratio,  $K_i^{SL}$ , is obtained by:

$$K_i^{SL} = \frac{x_i^S}{x_i^L} = \frac{\gamma_i^L}{\gamma_i^S} \exp \left[ \frac{\Delta \bar{H}_{i,pure}^f}{RT_i^f} \left( \frac{T_i^f}{T} - 1 \right) + \frac{\Delta \bar{H}_{i,pure}^{tr}}{RT_i^{tr}} \left( \frac{T_i^{tr}}{T} - 1 \right) \right] \quad (3-26)$$

The same correlations used by Coutinho et al. (2006) are employed to calculate the transition and fusion properties.

As aforementioned, Coutinho et al. (2006) calculated the liquid activity coefficient,  $\gamma_i^L$ , combining the modified UNIFAC model,  $\gamma_i^{res}$ , with the Flory free-volume model,  $\gamma_i^{comb-fv}$ :

$$\ln \gamma_i^L = \ln \gamma_i^{res} + \ln \gamma_i^{comb-fv} \quad (3-27)$$

The activity coefficient of the solid phase,  $\gamma_i^S$ , is calculated using the modified UNIQUAC model,

$$\frac{\bar{G}^E}{RT} = \sum_{i=1}^{Nc} x_i^S \ln \left( \frac{\Phi_i}{x_i^S} \right) + \frac{Z}{2} \sum_{i=1}^{Nc} q_i x_i^S \ln \left( \frac{\theta_i}{\Phi_i} \right) - \sum_{i=1}^{Nc} q_i x_i^S \ln \left[ \sum_{j=1}^{Nc} \theta_j \tau_{ji} \right] \quad (3-28)$$

in which  $\bar{G}^E$  is the EGE per mole of mixture and  $Nc$  is the number of components in the mixture.

The parameters  $\tau_{ji}$ ,  $\theta_i$  and  $\Phi_i$  are calculated as follow:

$$\tau_{ji} = \exp \left( -\frac{\Lambda_{ji} - \Lambda_{ii}}{q_i RT} \right) \quad (3-29)$$

$$\theta_i = \frac{x_i^S q_i}{\sum_{j=1}^{Nc} x_j^S q_j} \quad (3-30)$$

$$\Phi_i = \frac{x_i^S r_i}{\sum_{j=1}^{Nc} x_j^S r_j} \quad (3-31)$$

The structural parameters of pure components,  $r_i$  and  $q_i$ , are obtained from the parameter table of the original UNIFAC model (Abrams and Prausnitz, 1975):

$$r_i = 0.6744CN_i + 0.4534 \quad (3-32)$$

$$q_i = 0.540CN_i + 0.616 \quad (3-33)$$

where  $CN_i$  is the number of carbon atoms of component  $i$ .

The activity coefficient is defined as

$$RT \ln \gamma_i = \left( \frac{\partial(n_T \bar{G}^E)}{\partial n_i} \right)_{T,P,n_j(j \neq i)} \quad (3-34)$$

then the expression derived for  $\gamma_i^S$  is

$$\ln \gamma_i^S = \ln \left( \frac{\Phi_i}{x_i^S} \right) + 1 - \frac{\Phi_i}{x_i^S} - \frac{Z}{2} q_i \left( \ln \left( \frac{\Phi_i}{\theta_i} \right) + 1 - \frac{\Phi_i}{\theta_i} \right) + q_i - q_i \ln \left( \sum_{j=1}^{Nc} \theta_j \tau_{ji} \right) - q_i \sum_{j=1}^{Nc} \frac{\theta_j \tau_{ij}}{\sum_{w=1}^{Nc} \theta_w \tau_{wj}} \quad (3-35)$$

For two identical paraffins, the pair interaction energies,  $\Lambda_{ii}$ , are (Coutinho et al., 2006):

$$\Lambda_{ii} = -\frac{2}{Z} (\Delta \bar{H}_{i,pure}^{sub} - RT) \quad (3-36)$$

where the coordination number,  $Z$ , is set to 10. The heat of sublimation,  $\Delta \bar{H}_{i,pure}^{sub}$ , for each pure component  $i$  is calculated as (Coutinho et al., 2006)

$$\Delta \bar{H}_{i,pure}^{sub} = \Delta \bar{H}_{i,pure}^{vap} + \Delta \bar{H}_{i,pure}^f + \Delta \bar{H}_{i,pure}^{tr} \quad (3-37)$$

in which the heat of vaporization,  $\Delta \bar{H}_{i,pure}^{vap}$ , is calculated using the correlation proposed by Morgan and Kobayashi (1994a,b)

For two different paraffins, the interaction energy,  $\Lambda_{ij}$ , is defined by Equation 3-38, where the component  $j$  is the  $n$ -alkane with the shorter chain of the pair  $ij$  (Coutinho et al., 1996)

$$\Lambda_{ij} = \Lambda_{ji} = \Lambda_{jj} \quad (3-38)$$

According to the methodology developed by Fleming et al. (2017), the value of  $\Lambda_{ij}$  is used to tune the thermodynamic model in order to make the DSC simulation match the experimental data, as showed in Equation 3-39. The parameter used to tune the thermodynamic model is represented by  $\Delta \Lambda$  and the method of Hook and Jeeves (1961) is employed for the parameter estimation. This parameter will directly affect phase equilibrium by means of the solid activity coefficient, altering equilibrium compositions, phase fractions and, consequently, the system's enthalpy. If  $\Delta \Lambda = 0$ , the model returns the original result and the calculation is completely predictive.

$$\Lambda_{ij}^{adjust} = \Lambda_{ij}(1 + \Delta \Lambda) \quad (3-39)$$

The ideal solid solution method imposes that  $\gamma_i^S$  in Equation 3-24 is unitary, predicting the formation of only one solid phase. Hence, the excess enthalpy is neglected in the solid enthalpy calculation, Equation 3-20, although the effect of the presence of different paraffins in the same phase is accounted by the enthalpy of ideal phase term.

For the multisolid model, each paraffin precipitates in a pure phase. This way, the solid composition will always be unitary and Equation 3-24 will reduce to the pure solid fugacity, being calculated based on the fugacity of pure liquid, Equation 3-25. This model also does not take into consideration the excess enthalpy influence in Equation 3-20. Furthermore, the enthalpy of ideal phase term is calculated by summing the enthalpy of each pure solid phase.

Adopting the Peng-Robinson EoS for liquid phase description, the liquid fugacity is:

$$\hat{f}_i^L(T, P, \underline{x}^L) = x_i^L \hat{\phi}_i^L P \quad (3-40)$$

where  $\hat{\phi}_i^L$  is the fugacity coefficient of component  $i$ . The SLE ratio then becomes:

$$K_i^{SL} = \frac{x_i^S}{x_i^L} = \frac{\hat{\phi}_i^L}{\phi_i^L \gamma_i^S} \exp \left[ \frac{\Delta \bar{H}_{i,pure}^f}{RT_i^f} \left( \frac{T_i^f}{T} - 1 \right) + \frac{\Delta \bar{H}_{i,pure}^{tr}}{RT_i^{tr}} \left( \frac{T_i^{tr}}{T} - 1 \right) \right] \quad (3-41)$$

where  $\phi_i^L$  is the fugacity coefficient of component  $i$  as a pure liquid calculated from the Peng-Robinson EoS.

### 3.2.3. Phase equilibrium algorithm

To calculate DSC and solubility curves, it is first necessary to determine the existing phases in the system and to converge the compositions and fractions of each phase at the given temperature and pressure. Thus, to accomplish this task, it was developed a calculation structure, presented in Figure 3-2.

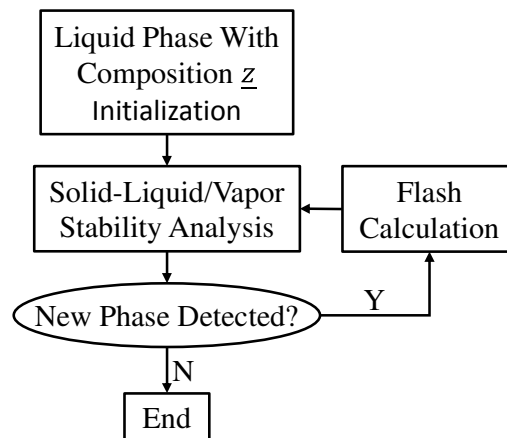


**Figure 3-2.** Phase equilibrium strategy scheme.

Taking the liquid as the reference phase, the algorithm searches for a solid phase by carrying out a stability analysis. If the test points out that there is a new stable solid phase, then a flash calculation is performed to converge the system. These coupled actions are repeated until the stability analysis does not find a new stable solid phase. When it happens, the weight fraction of solid is calculated using

$$wt(\%) = \frac{\sum_{i=1}^{Nc} \sum_{j=1}^{Nps} x_i^j \beta^j MW_i}{\sum_{i=1}^{Nc} \sum_{j=1}^{Nps} x_i^j \beta^j MW_i} \quad (3-42)$$

where  $MW_i$  and  $Nps$  are, respectively, the molecular weight of component  $i$  and the number of solid phases, and the simulation is concluded.

### 3.2.3.1. Flash calculation

To calculate the phase equilibrium with fixed temperature and pressure, the  $Np - 1$  phase fractions and all compositions were calculated using, respectively, Newton's and successive substitution methods.

As shown in Figure 3-3, first the K-factors are obtained by

$$K_i^n = \frac{\hat{\varphi}_i^L}{\phi_i^L \gamma_i^{S_n}} \exp \left[ \frac{\Delta \bar{H}_{i,pure}^f}{RT_i^f} \left( \frac{T_i^f}{T} - 1 \right) + \frac{\Delta \bar{H}_{i,pure}^{tr}}{RT_i^{tr}} \left( \frac{T_i^{tr}}{T} - 1 \right) \right] \quad (3-43)$$

for solid phases. The superscript  $S_n$  represents the  $n$ th solid phase. As we considered that the solvent does not precipitate, its K-factor for solid phases is automatically set to zero.

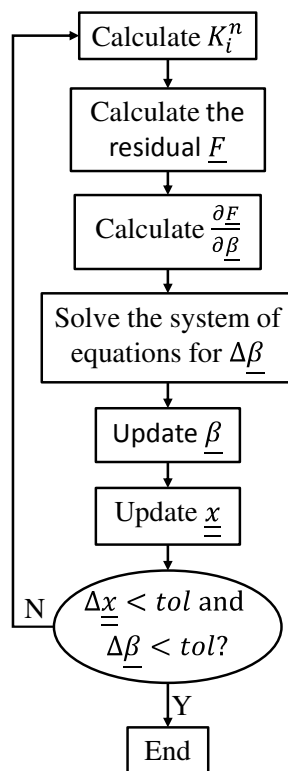


Figure 3-3. Box diagram of the Flash calculation algorithm.

The  $Np - 1$  residuals of the Newton method,  $\underline{F}$ , were calculated by the expression (Ziervogel and Poling, 1983)

$$F^n = \sum_{i=1}^{Nc} x_i^L K_i^n - 1 \quad (3-44)$$

and their derivatives with respect to the  $m^{\text{th}}$  phase fraction by

$$\frac{\partial F^n}{\partial \beta^m} = \sum_{i=1}^{Nc} \frac{x_i^n (x_i^L - x_i^m)}{z_i} \quad (3-45)$$

The system of equations

$$\frac{\partial \underline{F}}{\partial \underline{\beta}} \cdot \Delta \underline{\beta} = \underline{F} \quad (3-46)$$

is then solved, where  $\Delta \underline{\beta}$  is the difference between phase fractions in the current iteration and in the next one. Thus,  $\underline{\beta}$  is updated subtracting it by the step,  $\Delta \underline{\beta}$ , just calculated and, after this, the compositions,  $\underline{x}$ , are updated according to the mass balance:

$$x_i^L = \frac{z_i}{1 + \sum_{n=1}^{Np} \beta^n (K_i^n - 1)} \quad (3-47)$$

and

$$x_i^n = \frac{z_i K_i^n}{1 + \sum_{n=1}^{Np} \beta^n (K_i^n - 1)} \quad (3-48)$$

The convergence criteria is based on the maximum step applied to  $\underline{\beta}$  and  $\underline{x}$ . Unless it's lower than a specified tolerance, the routine is executed again.

### 3.2.3.2. Stability analysis

The tangent plane distance to the Gibbs energy surface criterion (TPD) (Michelsen, 1982) was used to search for solid phases. It was carried out by minimizing the following equation:

$$tm = 1 + \sum_{i=1}^{Nc} W_i \left[ \ln(W_i) + \ln(\gamma_i^S(T, \underline{W})) + \ln(\varphi_i^L(T, P)) - d_i - 1 \right] \quad (3-49)$$

where

$$d_i = \ln(x_i^L) + \ln(\hat{\varphi}_i^L(T, P, \underline{x}^L)) \quad (3-50)$$

$\underline{W}$  is a stability variable that simulates the phase composition and  $tm$  is the modified tangent plane distance, which is an alternative way of expressing the TPD.

The stability analysis begins with the initialization of  $Nc$  trial phases, each one rich in one compound. If it is known that some component certainly will not precipitate, the number of trial phases may be reduced.

Next, the successive substitution method is applied to solve the system of equations (Michelsen, 1982) constituted by the gradient of Equation 3-49, also written as

$$W_i = \exp \left( d_i - \ln(\gamma_i^S(T, \underline{W})) - \ln(\varphi_i^L(T, P)) \right) \quad (3-51)$$

In the end of the method, it should be tested if the trial phases are converging to already existing solid phases, what can be accomplished by testing if

$$\sum_{i=1}^{Nc} |W_i - x_i^L| < tol \quad (3-52)$$

The phases seeming to converge to already existing solid phases are excluded from the search. Whenever the remaining solid trial phases are not converged after the successive substitution method, Newton's method should be utilized (Michelsen, 1982).

The gradient and the Hessian are calculated as follows:

$$\frac{\partial tm}{\partial \varepsilon_i} = \sqrt{W_i} \left[ \ln(W_i) + \ln(\gamma_i^S(T, \underline{W})) + \ln(\varphi_i^L(T, P)) - d_i \right] \quad (3-53)$$

and

$$\frac{\partial^2 tm}{\partial \varepsilon_i \partial \varepsilon_j} = \sqrt{W_i W_j} \frac{\partial \ln(\gamma_i^S(T, \underline{W}))}{\partial W_j} + \delta_{ij} \left[ 1 + \frac{1}{2\varepsilon_i} \frac{\partial tm}{\partial \varepsilon_i} \right] \quad (3-54)$$

where  $\delta_{ij}$  is the kronecker delta and  $\varepsilon_i$  is  $2\sqrt{W_i}$ . After Newton's method, the solid trial phases must be once more compared to the already existing solid phases as it was done after the successive substitution method.

Once the trial phases have converged, the stability variable,  $W_{Total}$ , which is directly connected to the  $tm$ , must be calculated:

$$W_{Total} = \sum_{i=1}^{Nc} W_i \quad (3-55)$$

In case  $W_{Total}$  value is greater than unity, the system is considered unstable, hence the corresponding trial phase must be included in it. Otherwise, the system remains unaltered.

### 3.3. Data

The experimental composition and DSC thermograms for the five synthetic mixtures presented in Chapter 2 were used to simulate the DSC and solubility curves. These mixtures are composed of one continuous series ranging from C<sub>18</sub> to C<sub>36</sub>, and four bimodal distributions obtained by removing a defined number of intermediate paraffins. The WDT and the solubility data of these synthetic mixtures were measured by Dauphin et al. (1999) and are also used. Table 2-1, in the previous Chapter, shows the composition data of the studied mixtures. The name of each mixture is the same given by Dauphin et al. (1999).

### 3.4. Results and Discussions

#### 3.4.1. DSC simulation, P-R EoS evaluation and parameter estimation

All the experimental DSC thermograms discussed in this Chapter are the same discussed in Chapter 2. The first peak presented in all five thermograms is called supersaturation peak, which occur due to kinetic effects (Fleming et al., 2017). Once the focus is only the thermodynamics available in these DSC

thermograms, these peaks will not be taken into consideration. As the experiments have been carried out under cooling regime, the temperature in which the supersaturation peak appears is the measured WAT. The second peak observed in the mixtures S2, S3, S4 and S5 corresponds to the precipitation of a phase rich in the second group of paraffins in the bimodal distributions.

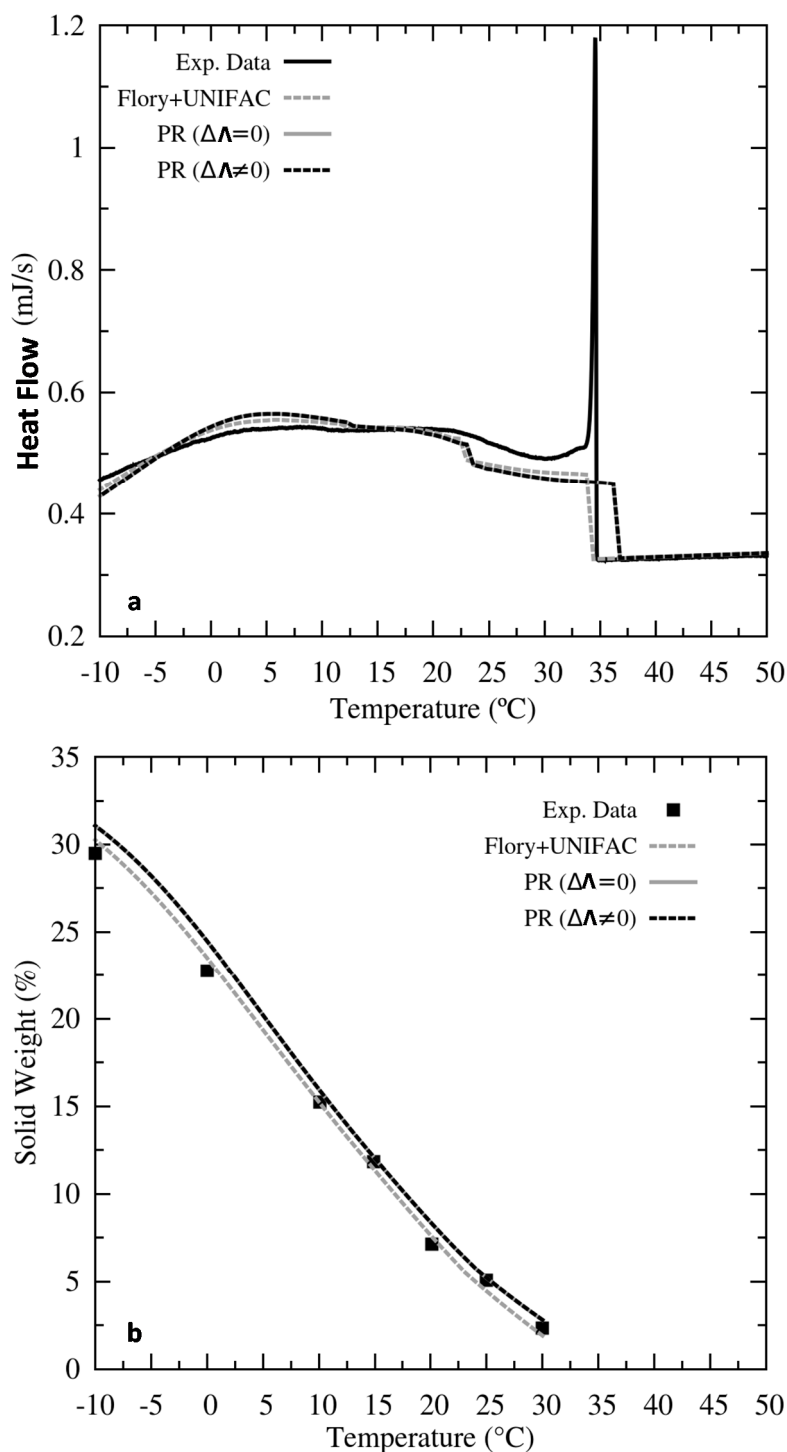
Experimental and calculated DSC thermograms and solubility curves for the five mixtures studied are displayed in Figures 3-4 to 3-8. The results were named Flory+UNIFAC, as studied by Coutinho et al. (2006), which means that the models of Flory free-volume combined with modified UNIFAC are used for the liquid phase, and PR, for the proposed Peng-Robinson EoS for the liquid phase. For the PR results, the curves obtained with the parameter  $\Delta A=0$  and  $\Delta A$  estimated ( $\Delta A \neq 0$ ) are presented. For all cases, the UNIQUAC model has been used for the solid phase.

Parameter  $\Delta A$  was estimated by minimizing the squared error between the experimental and the calculated DSC signals. The results showed that selecting points at indiscriminately lower temperatures than the WAT would most of the times lead to a local minimum, where perfect fit of the thermograms' second peak is achieved. This happens because, since the slope of the curve in this region is greater than in most of the thermogram, a small deviation of a point near there would cause the objective function to sorely increase, while away from there errors would be underrated. To avoid this behavior, only points at least 2.5°C distant from the peaks were used. Parameter estimation was carried out using about forty points, parameter step set to  $10^{-5}$  and the search range fixed between -0.01 and 0.1. Table 3-1 shows the parameter estimation results using the PR EoS for the liquid phase.

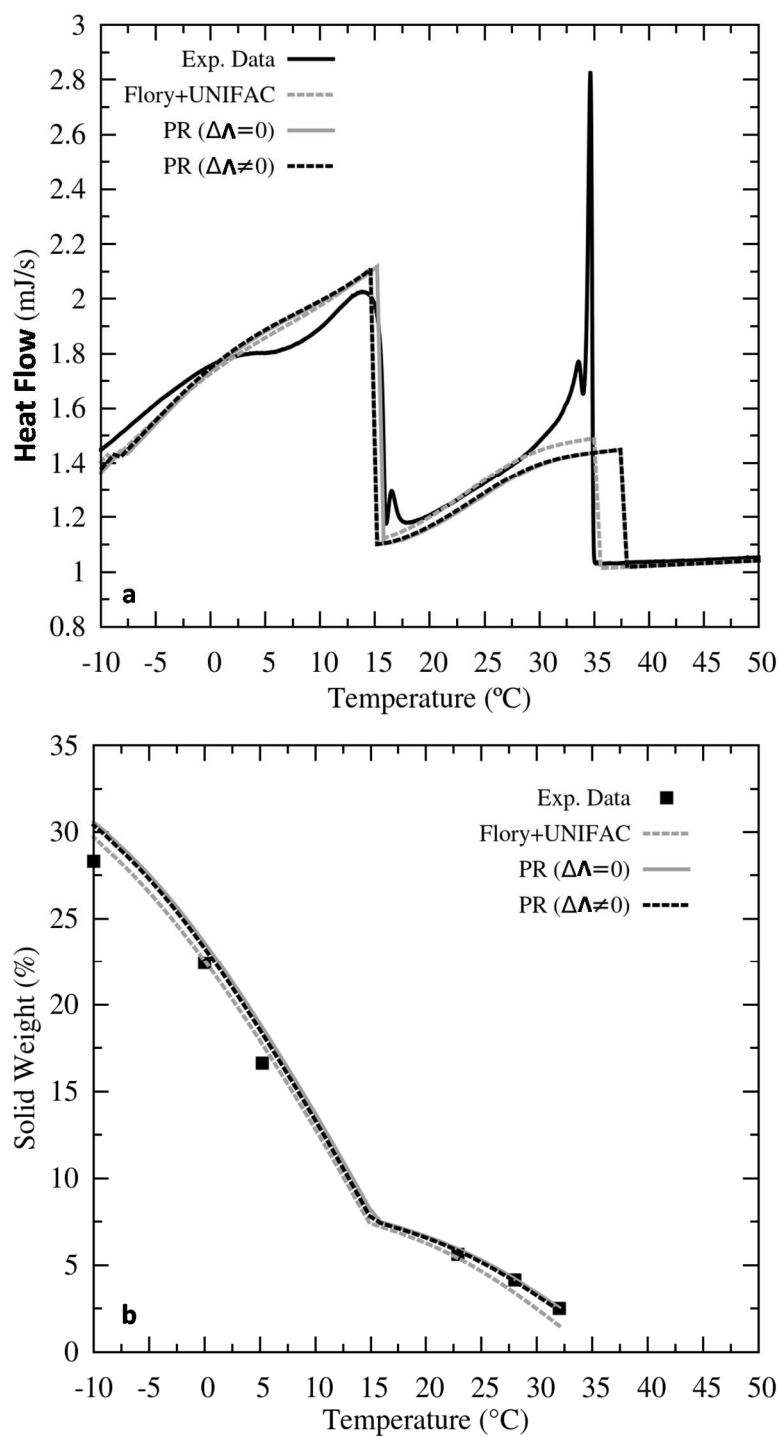
**Table 3-1.** Parameter estimation results (PR)

Mixture	S1	S2	S3	S4	S5
$\Delta A$	0.00014	-0.00245	-0.00207	-0.01294	-0.00477

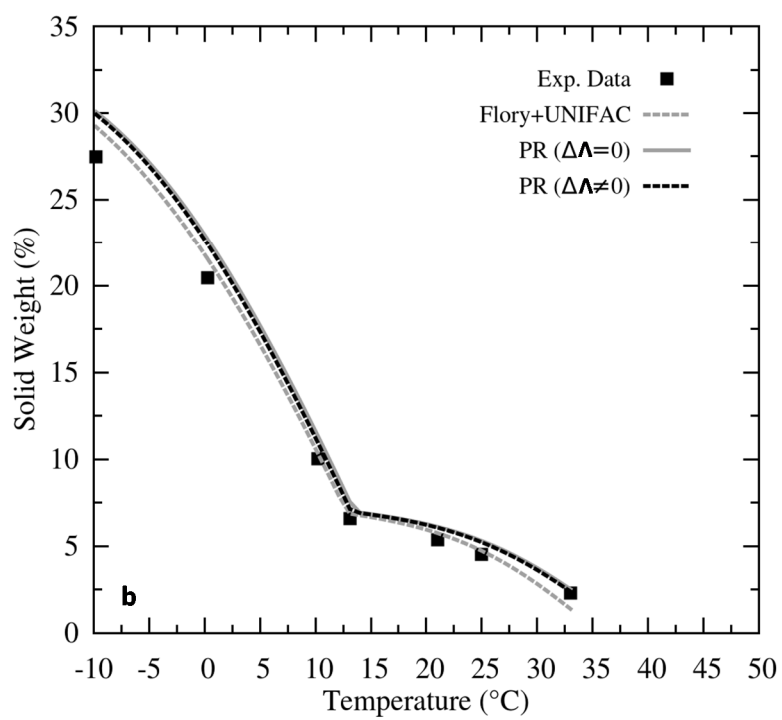
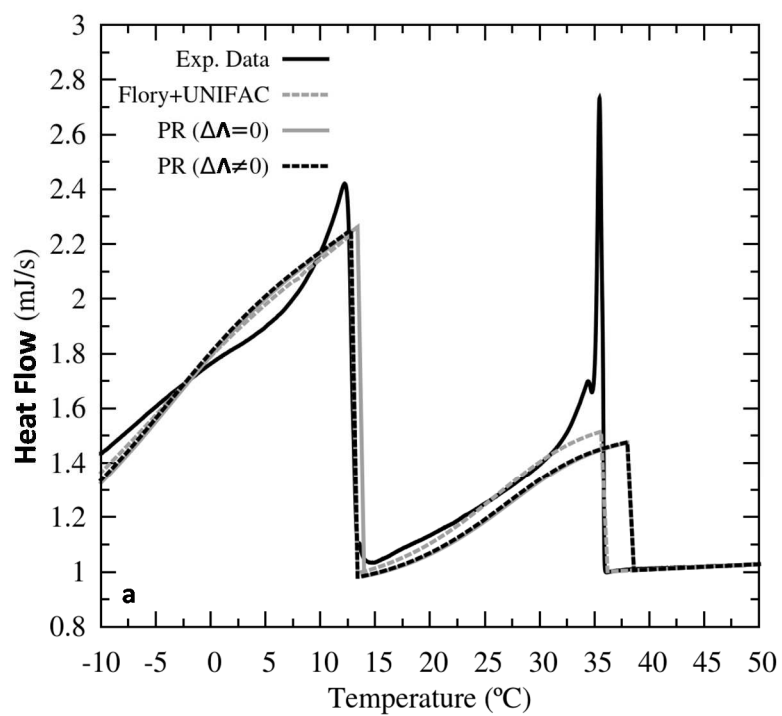
The calculated and experimental values of WDT for the thermodynamic models studied and the deviations between these values are shown in Tables 3-2 and 3-3, respectively.



**Figure 3-4. S1 (a) DSC and (b) Solubility data description using three different approaches: modified UNIQUAC for solid phases and Peng-Robinson EoS for the liquid phase; modified UNIQUAC for solid phases and Flory+UNIFAC for the liquid phase; modified UNIQUAC with estimated  $\Delta\Lambda$  for solid phases and Peng-Robinson EoS for the liquid phase.**



**Figure 3-5.** S2 (a) DSC and (b) Solubility data description using three different approaches: modified UNIQUAC for solid phases and Peng-Robinson EoS for the liquid phase; modified UNIQUAC for solid phases and Flory+UNIFAC for the liquid phase; modified UNIQUAC with estimated  $\Delta A$  for solid phases and Peng-Robinson EoS for the liquid phase.



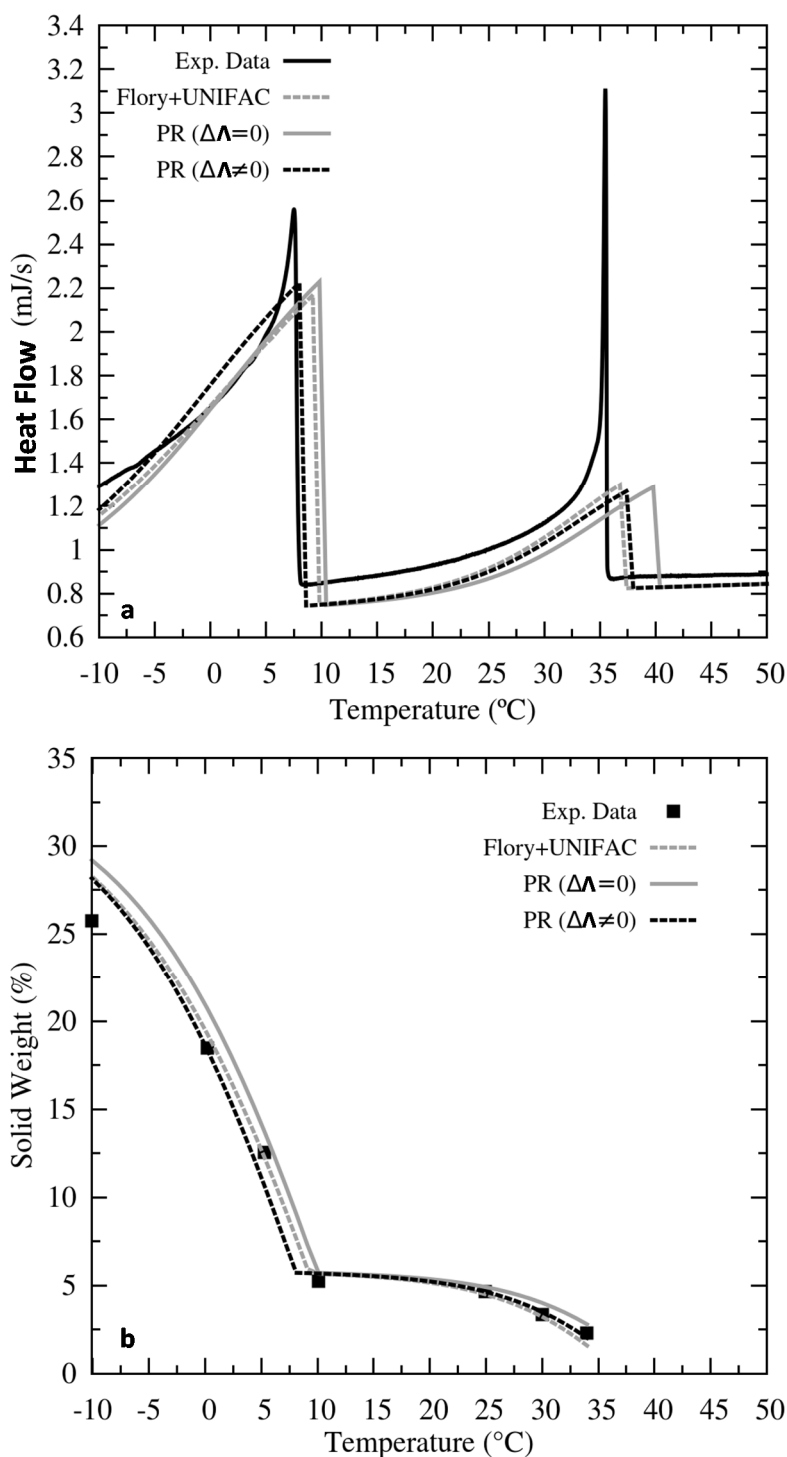


**Figure 3-6. S3 (a) DSC and (b) Solubility data description using three different approaches: modified UNIQUAC for solid phases and Peng-Robinson EoS for the liquid phase; modified UNIQUAC for solid phases and Flory+UNIFAC for the liquid phase; modified UNIQUAC with estimated  $\Delta\Lambda$  for solid phases and Peng-Robinson EoS for the liquid phase.**

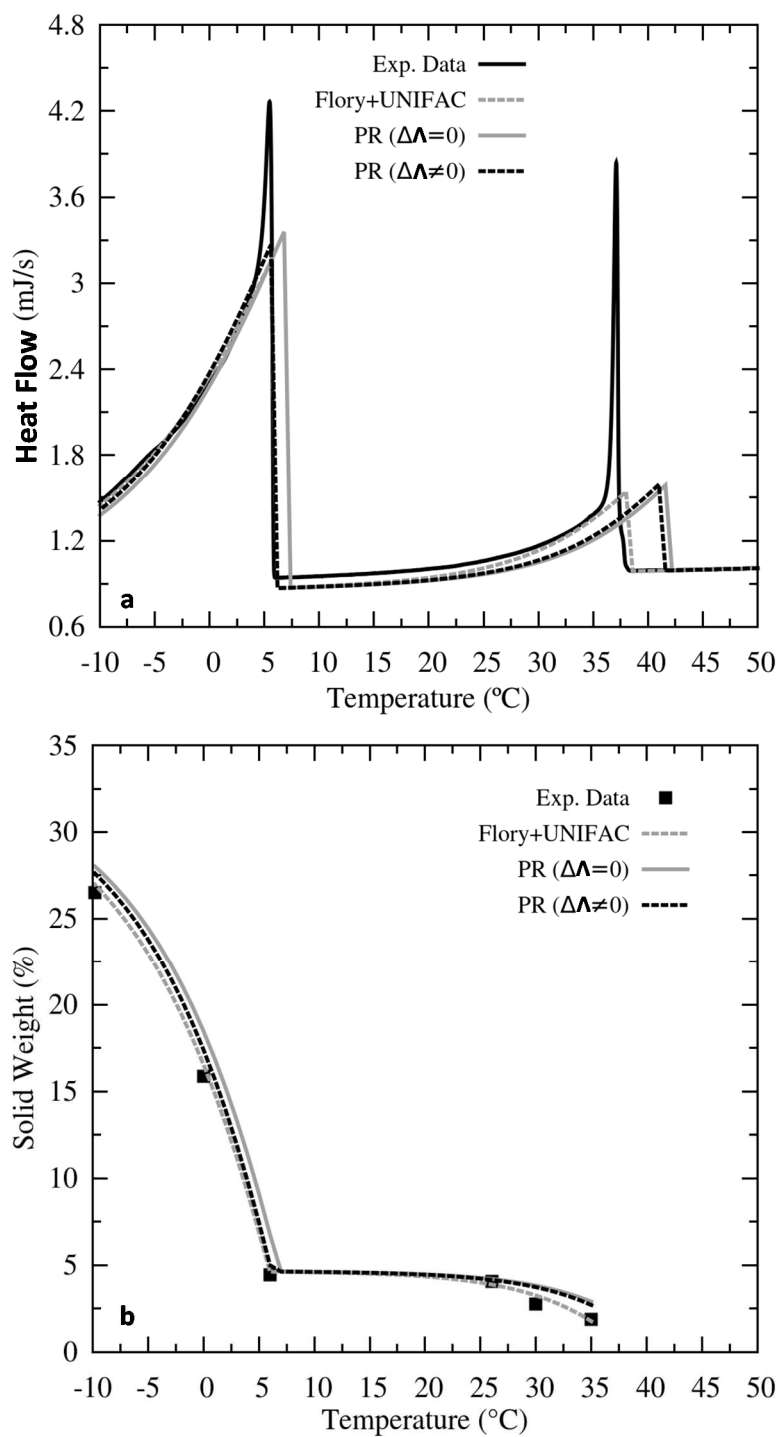


**Figure 3-7. S4** (a) DSC and (b) Solubility data description using three different approaches: modified UNIQUAC for solid phases and Peng-Robinson EoS for the liquid phase; modified UNIQUAC for solid phases and Flory+UNIFAC for the liquid phase; modified UNIQUAC with estimated  $\Delta\Lambda$  for solid phases and Peng-Robinson EoS for the liquid phase.

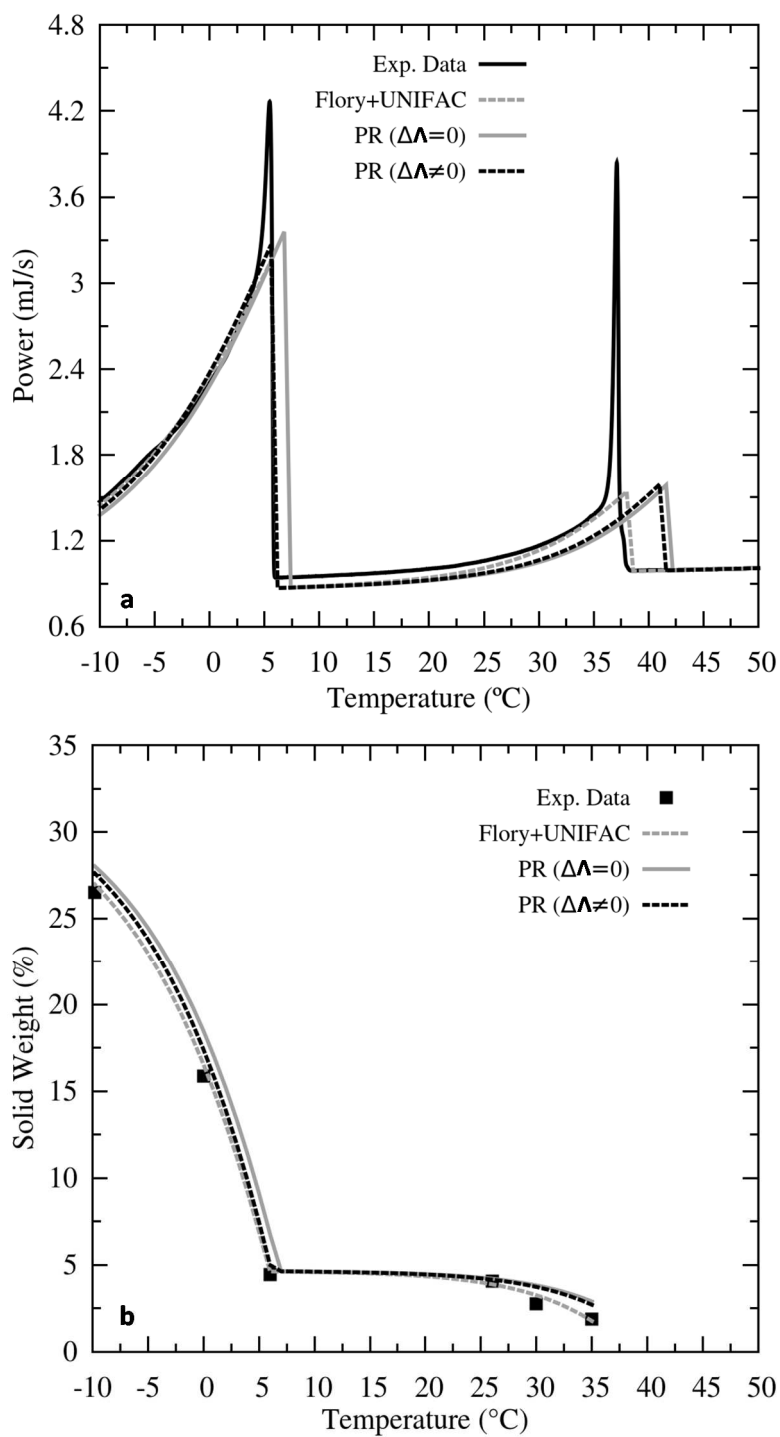


**Table 3-2.** Experimental and calculated wax disappearance temperatures (WDT, in °C)

Mixture	S1	S2	S3	S4	S5
<i>T<sub>exp</sub></i>	35.60	36.50	37.22	38.18	39.66
PR+UNIQUAC ( $\Delta\Lambda=0$ )	36.65	37.77	38.42	39.90	41.87
PR+UNIQUAC ( $\Delta\Lambda\neq 0$ )	36.67	37.41	38.11	37.99	41.16
PR+IdealSolidSolution	42.44	42.83	43.02	43.43	44.05
PR+Multisolid	31.94	32.90	33.53	35.14	38.00
Flory-UNIFAC+UNIQUAC	34.08	35.08	35.65	36.91	38.51

**Table 3-3.** Deviations between experimental and calculated wax disappearance temperatures (WDT, in °C)

Mixture	S1	S2	S3	S4	S5
PR+UNIQUAC ( $\Delta\Lambda=0$ )	1.05	1.27	1.20	1.72	2.21
PR+UNIQUAC ( $\Delta\Lambda\neq 0$ )	1.07	0.91	0.89	-0.19	1.50
PR+IdealSolidSolution	6.84	6.33	5.80	5.25	4.39
PR+Multisolid	-3.66	-3.60	-3.69	-3.04	-1.66
Flory-UNIFAC+UNIQUAC	-1.52	-1.42	-1.57	-1.27	-1.15

The results for S1 displayed in Figure 3-4 show that the models Flory+UNIFAC and PR do not differ considerably, and are in good agreement with the experimental DSC data. Since the estimated parameter  $\Delta\Lambda$  for this mixture was very small, both results for PR model were the same. The Flory+UNIFAC model predicted exactly the value of WAT measured from DSC, whereas the PR model predicted a little higher value. The WAT calculated through thermodynamic models is expected to be higher than the measured WAT as these models calculate indeed the WDT, which is always higher than the WAT (Hansen et al., 1991). Therefore, the PR model gives more realistic results.

The solubility curves displayed in Figure 3-4 confirm the similar prediction observed in DSC using the Flory+UNIFAC and PR models for S1. The average absolute deviations between experimental and calculated solubilities, obtained from Equation 3-56, where  $N_{exp}$  is the number of experimental data points, are shown in Table 3-4.

$$Dev = \sum_{p=1}^{N_{exp}} \frac{|wt_p^{exp} - wt_p^{calc}|}{N_{exp}} \quad (3-56)$$

**Table 3-4.** Average absolute deviations, Dev, between experimental and calculated solubilities

Mixture	<i>Bim 0</i>	<i>Bim 3</i>	<i>Bim 5</i>	<i>Bim 9</i>	<i>Bim 13</i>
PR+UNIQUEAC ( $\Delta\lambda = 0$ )	0.8445	0.9772	1.2716	1.2464	1.4467
PR+UNIQUEAC ( $\Delta\lambda \neq 0$ )	0.8573	0.8475	1.0586	0.7575	0.8495
Flory-UNIFAC+UNIQUEAC	0.4957	0.7767	0.7093	0.7173	0.3425

For the bimodal mixtures, the results displayed in Figures 3-5 to 3-8 also show a good agreement between the experimental and the calculated data. As shown in Table 3-1, the parameter estimation using the PR model resulted in small negative values of the parameter  $\Delta\lambda$ , dislocating the calculated DSC curves to the left side. Moreover, the parameters estimated improved the WDT and the solubility predictions for all bimodal mixtures. The parameter estimation also improved the PR model predictions for the second peak in the mixtures S3, S4 and S5. As observed for S1, the PR model results are quite similar to the Flory+UNIFAC results, indicating that the PR model is able to model the thermodynamic effects in the DSC experiments and provide good descriptions of WDT and solubility curves for the SLE involving paraffins.

These results obtained are very important to predict the paraffin precipitation for real oils because with the use of the Peng-Robinson EoS for describing the liquid phase it is possible to improve the thermodynamic model by tuning the EoS parameters, besides taking the pressure effects into consideration. In addition, the EoS is the approach conventionally used by the petroleum industry.

Concerning the methodology proposed for the DSC simulation, the rigorous thermodynamic path for the enthalpy calculation is showed to be accurate for describing the heat flows and phase transitions measured in the DSC experiments for the mixtures studied in this work.

### 3.4.2. Solid Model Evaluation

DSC simulations and solubility curves calculated with the solid solution, ideal solid solution and multisolid models are compared with experimental data in Figures 3-9 to 3-13. No discussion is held about number of solid phases and their compositions because the corresponding experimental data was not assessed. Besides, the main objective here is to show that the DSC curves can be calculated

through well-established models for well characterized samples. The Peng-Robinson EoS was used to calculate the fugacities of the components in the liquid phase for the three models. For the solid phase, the multisolid model uses the multi-pure-solid approach, the ideal solid solution uses the supposition of an ideal solid phase, and the solid solution model uses the modified UNIQUAC model with the parameter  $\Delta A$  estimated in this work. Because the samples studied here are well characterized, the multisolid model implemented treats each solid phase as a pure paraffin, although Lira-Galeana et al. (1996) and Pan et al. (1997) have suggested the application of the model using pseudo-components. Further work is required to make a complete comparison between the multisolid model (using pseudo-components) and the solid solution model.

Figures 3-9 to 3-13 show that the DSC results are the same at temperatures above the WAT for the three models, where the system is completely in the liquid phase. The good agreement to experimental results indicates that the correlations used to estimate the ideal gas heat capacities,  $Cp_{i,pure}^{ig}$ , are accurate.

The differences in the DSC simulations begin when the WDT's are predicted by each model. As shown in Tables 3-2 and 3-3, the multisolid model underestimated and the ideal solid solution model overestimated the WDT for the five mixtures studied. These models can be adjusted to improve the WDT prediction, however, either the physical properties of the pure paraffins or the composition itself are used to tune the models, which is not physically justifiable. Furthermore, in this case only the WDT will be adjusted, what doesn't ensure good predictions for the entire solubility curve.

Contrary to the solid solution model, the simulated DSC using the multisolid and ideal solid solution models are not in agreement with the trends presented in the experimental data. Moreover, the multisolid model underestimated and the ideal solid solution model overestimated the amount of paraffin precipitated.

Then, taking into consideration the conditions under evaluation, all the results indicate that the assumption of a solid solution is more adequate to model the SLE than the assumptions of neither a multi-pure-solid phase, the way it was implemented here, nor an ideal solid solution. It also becomes evident that the solubility curves alone are not a good comparison to differentiate the solid models.

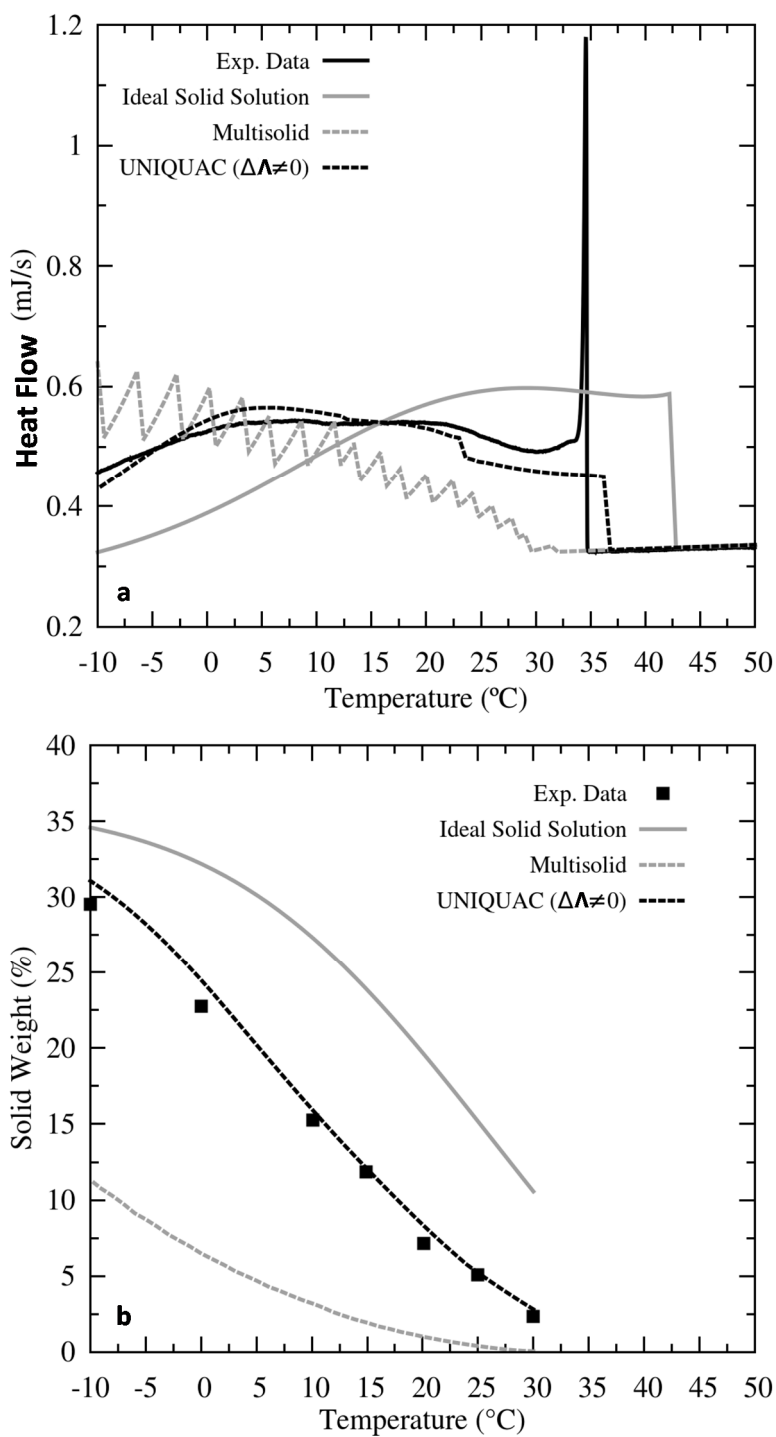


**Figure 3-9. S1** (a) DSC and (b) Solubility data description using Peng-Robinson EoS for the liquid phase and comparing three different models for solid phases: modified UNIQUAC with estimated  $\Delta A$ , ideal solid solution and multisolid.

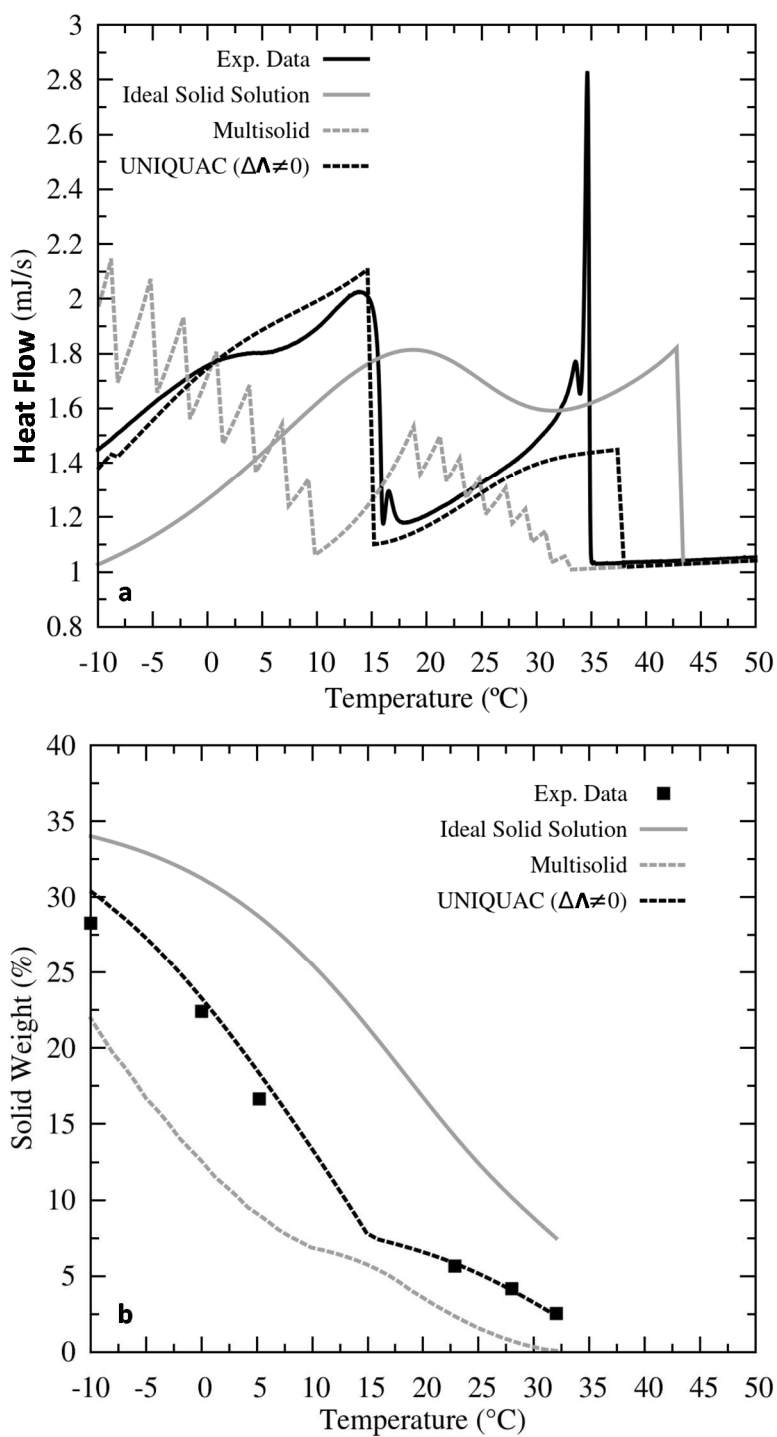


**Figure 3-10.** S2 (a) DSC and (b) solubility data description using Peng-Robinson EoS for the liquid phase and comparing three different models for solid phases: modified UNIQUAC with estimated  $\Delta\Lambda$ , ideal solid solution and multisolid.

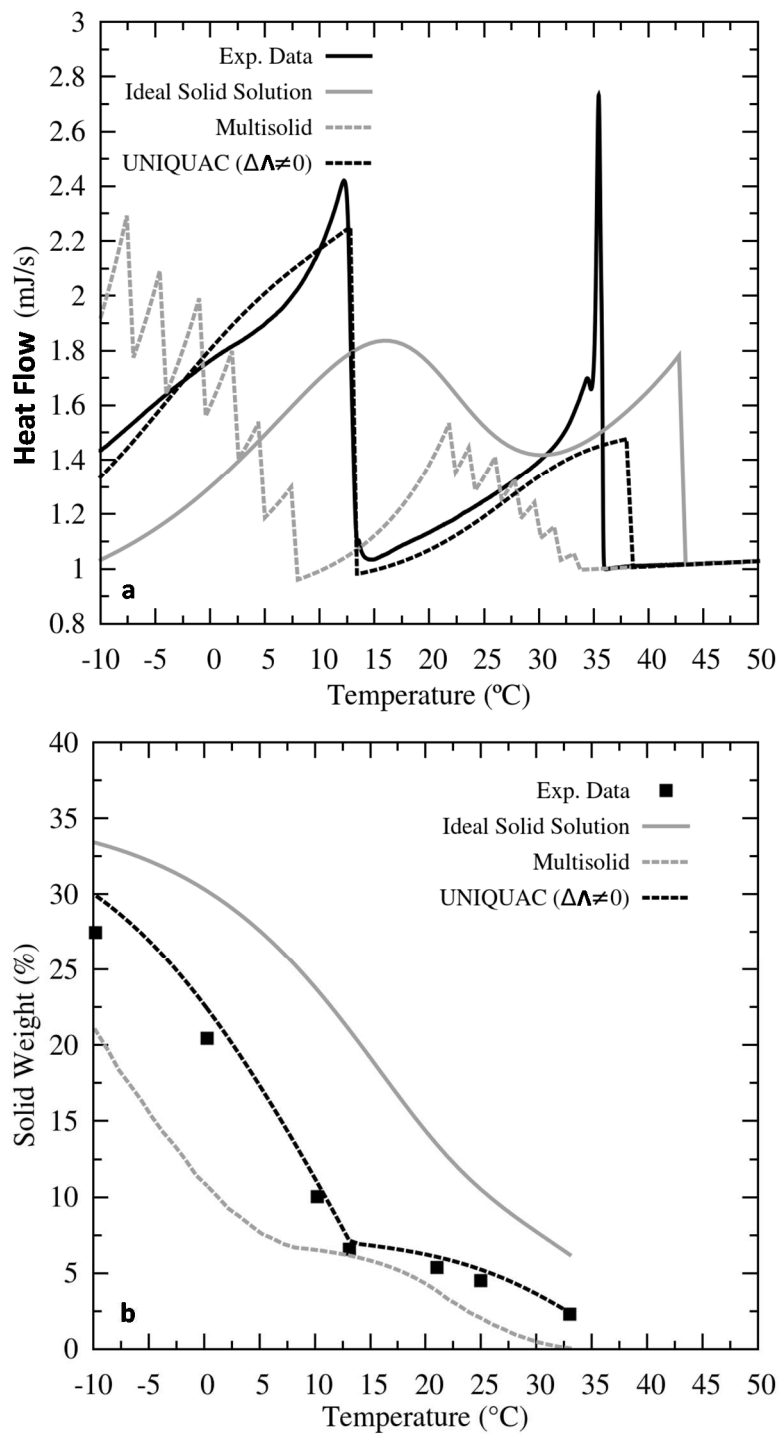


**Figure 3-11.** S3 (a) DSC and (b) Solubility data description using Peng-Robinson EoS for the liquid phase and comparing three different models for solid phases: modified UNIQUAC with estimated  $\Delta\Lambda$ , ideal solid solution and multisolid.

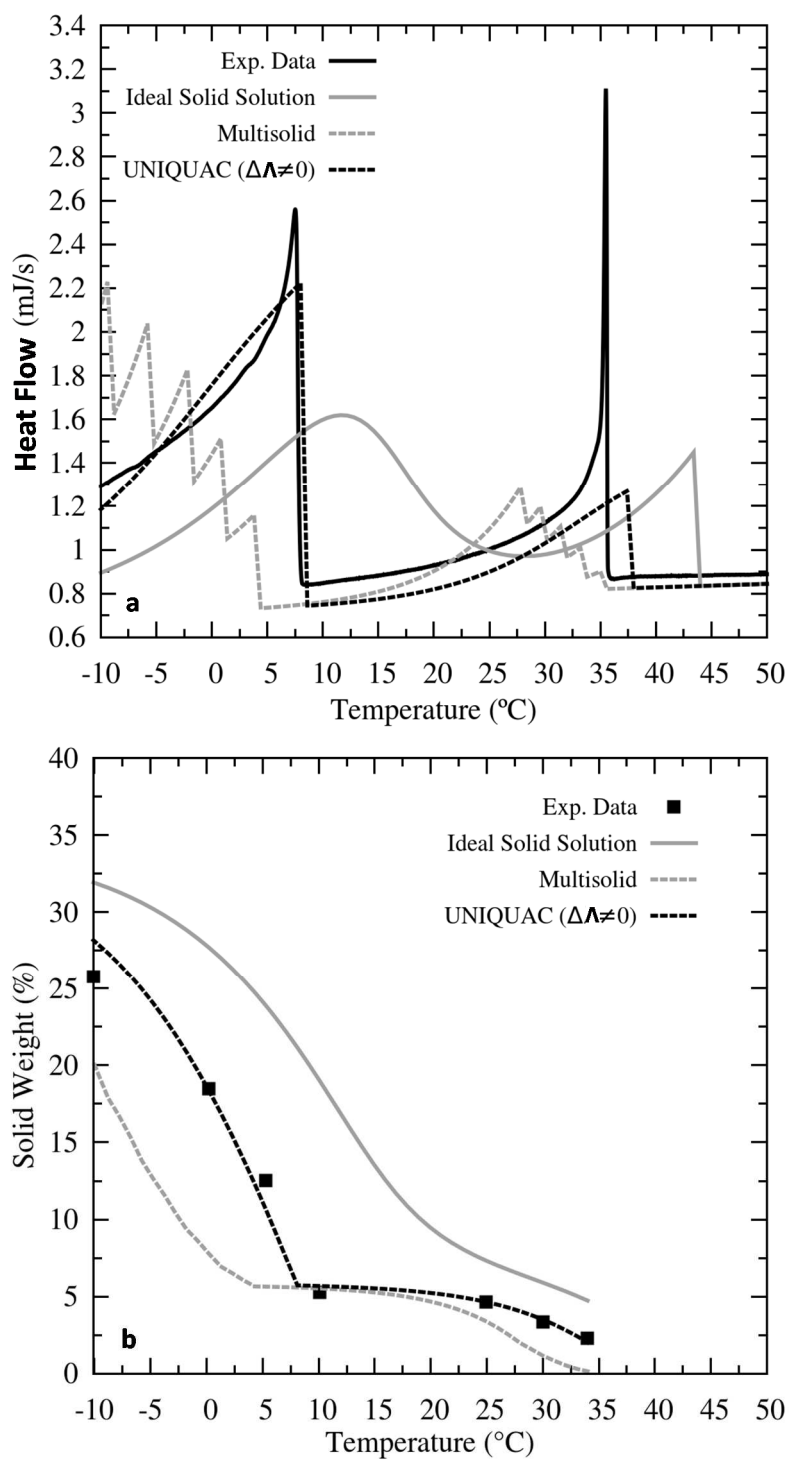


**Figure 3-12. S4 (a) DSC and (b) Solubility data description using Peng-Robinson EoS for the liquid phase and comparing three different models for solid phases: modified UNIQUAC with estimated  $\Delta A$ , ideal solid solution and multisolid.**

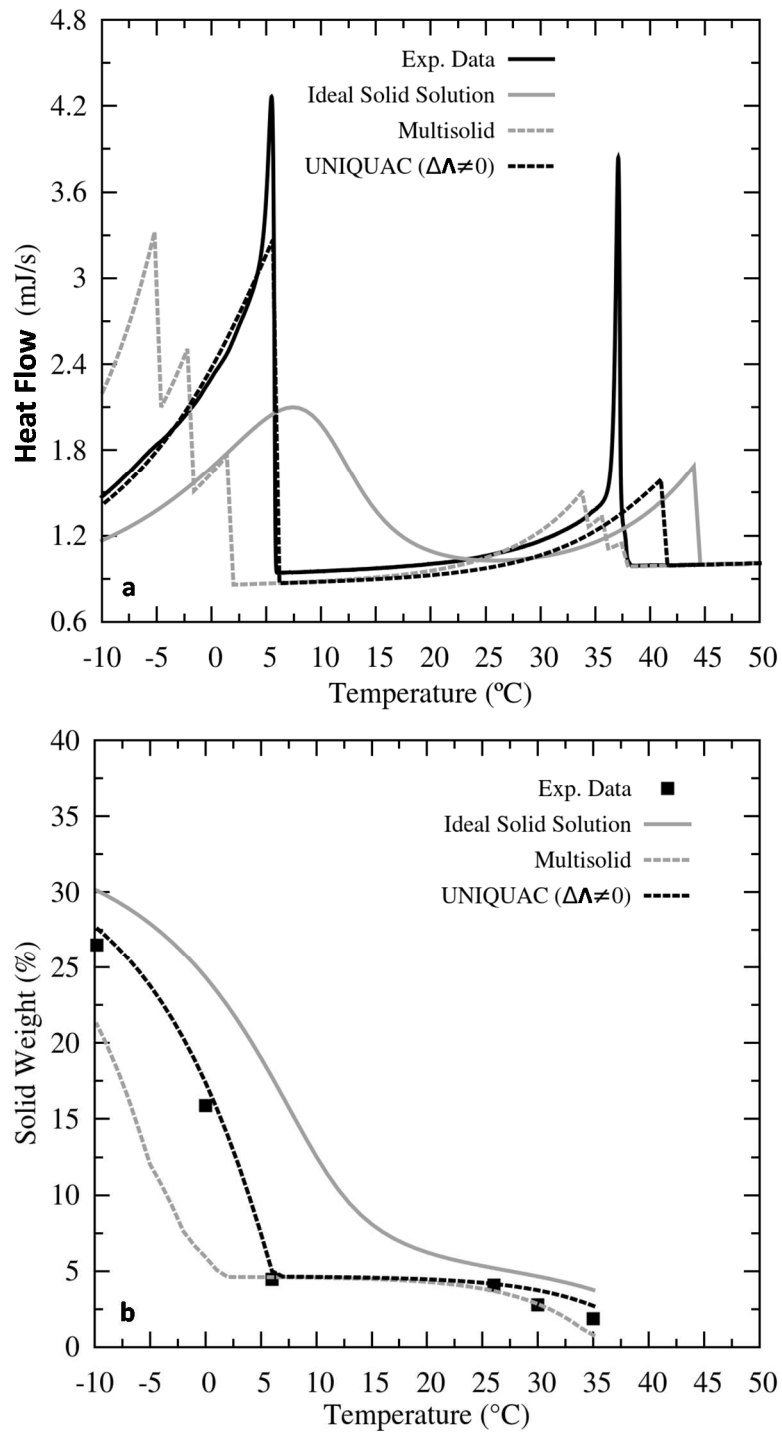


**Figure 3-13.** S5 (a) DSC and (b) Solubility data description using Peng-Robinson EoS for the liquid phase and comparing three different models for solid phases: modified UNIQUAC with estimated  $\Delta\Lambda$ , ideal solid solution and multisolid.

### 3.5. Conclusion

As oil production pushes the boundaries of hostile environments, wax deposition simulation assumes a major role in production system design. These simulations are dependent on an accurate thermodynamic SLE model, which renders the solubility curve. To improve model tuning, a strategy is developed through the evaluation of different models both for liquid and solid phases.

To allow a wide application of this strategy, a new DSC thermogram calculation scheme is proposed, where all of the non-idealities of the different phases are used in the heat flux calculation, as well as an ideal gas reference state was set for all components in all phases. As expected, this result indicates that the non-idealities involved in pure paraffinic systems are small when compared to the heats of phase change. It also points out that DSC experiments at slow enough rates are completely dominated by thermodynamic phenomena, indicating that the proposed strategy represents a significant improvement on relating information from DSC curves to solubility ones. The extrapolation of this new scheme to a multiphase condition is then straightforward.

In order to make the proposed strategy readily applicable to the oil industry, a liquid model based on EoS was evaluated, since this approach is already widely used. The simulation of DSC thermograms was used to compare the performance of the Peng-Robinson EoS in wax precipitation calculations to the Flory and modified UNIFAC models. Results show that the EoS model can be used with little or no losses when compared to the Flory and UNIFAC model. The model tuned to the experimental DSC thermogram renders a solubility curve in agreement with the experimental results within experimental errors.

The proposed strategy also allowed one to compare different solid models. A suitable SLE model should be able to correctly predict the experimental solubility curve as well as the DSC thermogram. The presented results showed that, although the different models evaluated render solubility curves that seem to differ only in values and that might be adjustable, the differences observed in the thermograms allows one to separate these models further. The DSC thermogram is an experimental result directly related to the solubility curve. In this sense, the differences pointed out among the solid models evaluated affect directly their

ability to be used in the current wax deposition model. It is an immediate conclusion that the solid solution model renders more accurate solubility curves, which cannot be tuned in the other models evaluated.

## 4

# PARAFFIN SOLUBILITY CURVES OF DIESEL FUELS FROM THERMODYNAMIC MODEL ADJUSTED THROUGH EXPERIMENTAL DSC THERMOGRAMS

### 4.1.

#### Introduction

Diesel fuels are widely used on road, marine and air transports. These fuels are composed in great part by paraffins, which crystallize and form gels when submitted to low temperatures. Consequently, it reduces the fuel flow by plugging the fuel filters (Coutinho, 2000) and, as the fuel fluid composition is altered by the precipitation, jeopardizes the engine efficiency (Maithufi et al., 2011; Zheng et al., 2014). To avoid these issues, paraffin precipitation is usually controlled by using additives in the fuels (Maithufi et al., 2011; Zheng et al., 2014).

Simulation of the diesel phase behavior may help determining how much additive should be used to avoid paraffin solidification in a desired temperature range. Different models have been used to model solid paraffin solubility curves from diesel fuels, as these curves are extremely laborious to measure experimentally. Coutinho et al. (2006) and Sansot et al. (2005) used an equation of state for the liquid phase and the modified Wilson model for the solid phase. Coutinho et al. (2000) and Coutinho (2000) employed the combination of the UNIFAC model and the Flory free volume equation for the liquid phase and the modified UNIQUAC model for the solid phase. To tune these models, the wax appearance temperature (WAT) was majorly employed. Nevertheless, all current experimental techniques available to measure the WAT have shortcomings that limits an effective measurement of the thermodynamic equilibrium temperature (Coutinho and Daridon, 2005). The supersaturation unavoidable in WAT measurements due to kinetic effects also imposes limitations to its use in model tuning.

To avoid such interferences, a different approach has been proposed in the previous Chapters (Fleming et al. 2017; da Silva et al., 2017). In this new approach,

the single WAT point commonly used to tune the thermodynamic model is substituted by an entire DSC thermogram, that provides phase equilibria information over a large temperature range. Using an appropriate cooling rate in the DSC experiments, solid-liquid equilibrium data is indirectly provided via the enthalpy variation of the system and can thus be directly calculated through an appropriate thermodynamic model. Nevertheless, this approach has only been applied so far to synthetic systems where the composition was controlled and well known. The aim of the present Chapter is to extend the method do Diesel fuels and improve the reliability of paraffin solubility curves obtained from thermodynamic models.

For that purpose, experimental DSC and experimental solubility data were measured for two different Diesel fuel samples. These samples compositions were then analyzed and characterized by their full paraffin distributions whereas non-paraffinic components were lumped into pseudocomponents. The Peng-Robinson equation of state (PR-EoS) was used to model the liquid phase, as it can be readily applied to high pressures systems and complex fluids like crude oil. For the solid phase, the modified UNIQUAC model was used. The models were tuned using the calorimetric data and the predictions obtained for the solubility and compositional data were analyzed.

## 4.2. Experimental

### 4.2.1. Diesel samples

The two samples used in this study were supplied by PETROBRAS and used without any further treatment. Density, flash point and sulfur content of the two samples are presented in Table 4-1.

**Table 4-1.** Density, flash point and sulfur content of the two samples studied.

Sample	Density (kg.m <sup>-3</sup> )	Flash Point (°C)	Sulfur content (ppm)
1	828.2	68.0	1.6
2	824.5	69.0	0.9

#### **4.2.2. DSC measurements**

The calorimetric experiments were carried out using a SETARAM Micro DSC 7 evo calorimeter. All experiments were performed using a temperature rate of  $0.2 \text{ K}\cdot\text{min}^{-1}$  in, at least, triplicates. Samples of around 450 mg were weighted with a precision of 0.01 mg. The experiments were conducted at temperatures from 248.15 K to 303.15 K. The equipment was calibrated using Gallium. This reference compound was acquired from Fluka as an ultrapure sample (purity of 99.999%).

#### **4.2.3. Analysis of the paraffin distributions**

The paraffin distribution within the samples were analyzed using gas chromatography. An Agilent 6890 chromatograph equipped with a split/splitless injector, a flame ionization detector (FID) and HP-1 50 meters capillary column with an internal diameter of 0.20 mm and a film width of  $0.11 \mu\text{m}$  was used. The carrier gas used was hydrogen at a constant pressure of 25 psi. The injector temperature was kept constant at 573.15 K and a split ratio of 128:1 was used. The detector was kept at a constant temperature of 573.15 K with constant flow of air ( $450 \text{ mL}\cdot\text{min}^{-1}$ ). The column temperature was raised from 313.15 K to 573.15 K at  $2 \text{ K}\cdot\text{min}^{-1}$  and from there raised to 653 K at  $4 \text{ K}\cdot\text{min}^{-1}$ . The sample was diluted in CS<sub>2</sub> and 1  $\mu\text{L}$  of the solution was injected using an automatic injection system. The retention time of the different *n*-alkanes were calibrated using a standard mixture Polywax 655 from Supelco. Each sample was injected in at least triplicates. The uncertainties calculated from two standard deviations of the results were smaller than 2% for all cases. *n*-alkanes up to C<sub>35</sub> were identified.

#### **4.2.4. Analysis of fluid composition and fluid representation**

The total composition of the sample was represented by discretizing the original samples into pseudocomponents characterized by their average carbon number and subtracting from each of them the corresponding concentration of paraffin analyzed.

The method used is based on the ASTM standard 7169. An Agilent 6890N chromatograph equipped with an on-column injector, a FID detector and 5 meters steel capillary column with an internal diameter of 0.53 mm and a film width of 0.09  $\mu\text{m}$  was used. The carrier gas used was helium at 25  $\text{mL}\cdot\text{min}^{-1}$ . The injector temperature was raised from 373.15 K to 703.15 K at 15  $\text{K}\cdot\text{min}^{-1}$  and is then kept constant for 26 minutes. The detector was kept at a constant temperature of 703.15 K with constant flows of hydrogen (35  $\text{mL}\cdot\text{min}^{-1}$ ) and air (350  $\text{mL}\cdot\text{min}^{-1}$ ). The column temperature was raised from 308.15 K to 703.15 K at 10  $\text{K}\cdot\text{min}^{-1}$  and is then kept constant for 5 minutes. The sample was diluted in  $\text{CS}_2$  and 0.5  $\mu\text{L}$  were injected using an automatic injection system. The retention time of the different *n*-alkanes were calibrated using a standard mixture Polywax 655 from Supelco. Each sample was injected in at least triplicates. The uncertainties calculated from two standard deviations of the results were smaller than 3% for all cases. *n*-alkanes up to C35 were identified.

#### **4.2.5. Solubility curve and solid deposit composition**

In addition to the calorimetric measurements used for tuning the model, solid liquid phase behavior was studied below the onset of wax crystallization by measuring both the solubility curve and the composition of the waxy solid deposit as a function of temperature. These measurements which are not needed for the implementation of the method were used in the present work only to test the predictive capacity of the proposed method. The solubility curve of both Diesel fuels were measured using a centrifugation method similar to the one proposed by Han et al. (2010). The method consists of cooling the sample to a controlled temperature of interest and proceed a centrifugation at that temperature. The centrifuged sample is then separated in two fractions. The first fraction contains only liquid without the presence of any solids whatsoever. The second fraction contains all of the precipitated solid paraffin and some of the liquid. If one ignores the effect of the centrifugation field on the phase equilibrium of the system, one may assume that the fractions are in equilibria, and consequently the liquid in the first fraction has the same composition of the liquid that remained in the second fraction. Each of these fractions were only analyzed for their paraffin distributions following the method detailed above.

Assuming that the solids are only composed by paraffins, one can use the paraffin distribution of the first fraction and subtract the paraffins that are present on the second fraction due to the presence of the liquid phase and calculate the paraffin composition of the solid wax and consequently its mass. The calculations were carried out as described by Han et al. (2010) and Coutinho et al. (2000).

The centrifugations were performed in a THERMO Heraeus Megafuge 40R centrifuge. The samples were disposed in small flasks containing 1 g of sample each. For each temperature and each Diesel sample, three flasks were centrifuged. Together with the samples flasks, an extra flask holding kerosene was added and before the samples were fractionated the temperature of the kerosene flask was measured with a 0.1 K precision thermometer and reported as the equilibrium temperature.

Mass losses at the fractionation step were always smaller than 0.1% of the total mass of the sample. Combined with the uncertainties from the chromatographic analyzes, the expanded uncertainties of each solubility curve point measured are estimated as 5% of the mass of the solid paraffin.

### 4.3. Methodology

#### 4.3.1. Thermodynamic model

The solid-liquid equilibrium was calculated by means of the following equation

$$x_i^L \hat{\varphi}_i^L P = x_i^S \gamma_i^S f_i^S \quad (4-1)$$

which represents, for each component  $i$ , the equality between its fugacity in the liquid phase,  $\hat{f}_i^L$ , and in the solid phase,  $\hat{f}_i^S$ . In Equation 4-1,  $x$ ,  $f$ ,  $\hat{\varphi}$  and  $\gamma$  are the composition, the fugacity of pure component, the fugacity coefficient in a mixture and the activity coefficient. It was considered that only the paraffins can precipitate, that is, the pseudocomponents are present only in the liquid phase.

The fugacity coefficients in the liquid phase were calculated using the Peng-Robinson equation of state with the classical van der Waals combining rules, in which all the binary interaction parameters,  $k_{ij}$ , were set to zero. The critical

temperature,  $T_c$ , critical pressure,  $P_c$ , and acentric factor,  $\omega$ , were obtained for each paraffin  $i$  through the correlations proposed by Marano and Holder (1997), presented in Equations 4-2, 4-3 and 4-4, respectively.

$$T_{c_i}(K) = 1020.71 - (1020.71 - 127.89)\exp(-0.1981(CN_i - 0.896021)^{0.629752}) \quad (4-2)$$

$$P_{c_i}(bar) = 1336.74\exp(-2.111827(CN_i + 3.625581)^{0.258439}) \quad (4-3)$$

$$\omega_i = -6.5597 + 3.383261(CN_i + 23.608415)^{0.20877} \quad (4-4)$$

For each pseudocomponent  $l$ ,  $T_c$ ,  $P_c$  and  $\omega$  were calculated using the correlations proposed by Pedersen and Christensen (2007), presented in Equations 4-5, 4-6, 4-7 and 4-8 respectively. The densities of the pseudocomponents,  $\rho$ , and their molecular weights, MW, were obtained from Katz and Firoozabadi (1978).

$$T_{c_l}(K) = 73.4043\rho_l + 97.3562\ln MW_l + 0.618744MW_l + \frac{-2059.32}{MW_l} \quad (4-5)$$

$$\ln P_{c_l}(bar) = 0.0728462\rho_l + 2.18811\rho_l^{0.25} + \frac{163.910}{MW_l} + \frac{-4043.23}{MW_l^2} \quad (4-6)$$

$$m_l = 0.373765 + 0.00549269MW_l + 0.017934\rho_l + 0.00000493049MW_l^2 \quad (4-7)$$

$$m_l = 0.37464 + 1.54226\omega_l - 0.26992\omega_l^2 \quad (4-8)$$

The activity coefficients of the components in the solid phase were calculated using the modified UNIQUAC model, proposed by Coutinho et al. (2006), as shown in Equation 4-9., in which  $\Phi$ ,  $\theta$  and  $\tau$  are obtained through Equations 4-10, 4-11 and 4-12, respectively.

$$\ln \gamma_i^S = \ln \left( \frac{\Phi_i}{x_i^S} \right) + 1 - \frac{\Phi_i}{x_i^S} - \frac{Z}{2} q_i \left( \ln \left( \frac{\Phi_i}{\theta_i} \right) + 1 - \frac{\Phi_i}{\theta_i} \right) + q_i - q_i \ln \left( \sum_{j=1}^{N_c} \theta_j \tau_{ji} \right) - q_i \sum_{j=1}^{N_c} \frac{\theta_j \tau_{ij}}{\sum_{k=1}^{N_c} \theta_k \tau_{kj}} \quad (4-9)$$

$$\Phi_i = \frac{x_i^S r_i}{\sum_{j=1}^{N_c} x_j^S r_j} \quad (4-10)$$

$$\theta_i = \frac{x_i^S q_i}{\sum_{j=1}^{N_c} x_j^S q_j} \quad (4-11)$$

$$\tau_{ji} = \exp \left( -\frac{\Lambda_{ji} - \Lambda_{ii}}{q_i RT} \right) \quad (4-12)$$

The parameters  $r_i$ ,  $q_i$  and  $\Lambda_{ii}$  (pair interaction energy) are calculated according to Equations 4-13, 4-14 and 4-15.

$$r_i = 0.6744\text{CN}_i + 0.4534 \quad (4-13)$$

$$q_i = 0.540\text{CN}_i + 0.616 \quad (4-14)$$

$$\Lambda_{ii} = -\frac{2}{z}(\Delta h_i^{\text{sub}} - RT) \quad (4-15)$$

The parameter  $\Lambda_{ij}$  assumes the value of pair interaction energy of the paraffin with the lower Carbon Number (CN) in the pair  $ij$ . In Equation 4-15,  $\Delta h_i^{\text{sub}}$  is the molar enthalpy of sublimation of paraffin  $i$ , calculated via Equation 4-16, in which  $\Delta h_i^{\text{tr}}$ ,  $\Delta h_i^{\text{fus}}$  and  $\Delta h_i^{\text{vap}}$  are the molar enthalpies of crystalline transition, fusion and vaporization of paraffin  $i$ . The latter is obtained according to the correlation proposed by Morgan and Kobayashi (1994a,b) and  $\Delta h_i^{\text{tr}}$  and  $\Delta h_i^{\text{fus}}$  are obtained as suggested by Coutinho et al. (2006).

$$\Delta h_i^{\text{sub}} = \Delta h_i^{\text{vap}} + \Delta h_i^{\text{fus}} + \Delta h_i^{\text{tr}} \quad (4-16)$$

The fugacity of the pure paraffin  $i$  in the solid phase,  $f_i^{\text{S}}$ , is calculated using Equation 4-17, in which  $f_i^{\text{L}}$  is the fugacity of pure paraffin  $i$  in the liquid phase, obtained via the PR-EoS.  $T_i^{\text{fus}}$  and  $T_i^{\text{tr}}$  are the temperatures of fusion and solid-solid (ordered-disordered) transition of paraffin  $i$ , calculated through the correlations suggested by Coutinho et al. (2006).  $\Delta C p_i^{\text{LS}}$  is the difference between the heat capacities of paraffin  $i$  in the liquid and solid phases, calculated using the correlation proposed by Pedersen et al. (1991).

$$f_i^{\text{S}} = f_i^{\text{L}} \exp \left[ \frac{\Delta h_i^{\text{fus}}}{RT_i^{\text{fus}}} \left( 1 - \frac{T_i^{\text{fus}}}{T} \right) + \frac{\Delta h_i^{\text{tr}}}{RT_i^{\text{tr}}} \left( 1 - \frac{T_i^{\text{tr}}}{T} \right) - \frac{1}{RT} \int_{T_i^{\text{fus}}}^T \Delta C p_i^{\text{LS}} dT + \frac{1}{R} \int_{T_i^{\text{fus}}}^T \frac{\Delta C p_i^{\text{LS}}}{T} dT \right] \quad (4-17)$$

The Poynting factor was neglected in the calculation of  $f_i^{\text{S}}$ , as can be observed in Equation 4-17, since the pressure was held equal to 1 bar during all experiments.

### 4.3.2. DSC thermogram simulation from the thermodynamic model proposed

The DSC thermograms were calculated according to the methodology proposed in Chapter 3 (da Silva et al.; 2017). The liquid phase molar enthalpy,  $h^L$ , was obtained through Equation 4-18, that describes a thermodynamic path starting at an ideal gas (ig) reference system at  $T_0$  and  $P_0$ , changing its temperature using the ideal gas heat capacities and adding the residual enthalpy at the desired  $T$  and  $P$ . The enthalpy of the ideal gas system at the reference conditions  $T_0$  and  $P_0$ ,  $h^{ig}(T_0, P_0)$ , is considered equal to zero.

$$h^L(T, P, \underline{x}^L) = \sum_{i=1}^{N_c} x_i^L \int_{T_0}^T C p_i^{ig} dT + h^R(T, P, \underline{x}^L) \quad (4-18)$$

The ideal gas heat capacities of the paraffins were obtained through the correlation of Passut and Danner (1972) modified by in Chapter 3, and the residual enthalpy is calculated from the PR-EoS.

$$C p_i^{ig} = 251.996[B_i + 2C_i T + 3D_i T^2 + 4E_i T^3 + 5F_i T^4] \quad (4-19)$$

in which the coefficients B, C, D, E and F are calculated using Equations 4-20 to 4-24.

$$B_i = -7.100555 \times 10^{-4} C N_i - 1.201093 \times 10^{-4} \quad (4-20)$$

$$C_i = 1.416221 \times 10^{-5} C N_i + 2.669830 \times 10^{-6} \quad (4-21)$$

$$D_i = -3.149971 \times 10^{-9} C N_i + 4.003664 \times 10^{-10} \quad (4-22)$$

$$E_i = 3.489865 \times 10^{-13} C N_i - 1.321624 \times 10^{-13} \quad (4-23)$$

$$F_i = -1.105366 \times 10^{-17} C N_i + 8.714208 \times 10^{-18} \quad (4-24)$$

The ideal gas heat capacities of the pseudocomponents were calculated using Equation 4-25, proposed by Kesler and Lee (1976)

$$C p_i^{ig} = \frac{MW_i [A_0 + A_1 T + A_2 T^2 - B_3 (B_0 + B_1 T + B_2 T^2)]}{4.19002} \quad (4-25)$$

in which the coefficients  $A_0$ ,  $A_1$ ,  $A_2$ ,  $B_0$ ,  $B_1$ ,  $B_2$  and  $C$  are obtained by means of Equations 4-26 to 4-32.

$$A_{0l} = -1.41779 + 0.11828Kw_l \quad (4-26)$$

$$A_{1l} = -(6.99724 - 8.69326Kw_l + 0.27715Kw_l^2) \times 10^{-4} \quad (4-27)$$

$$A_{2l} = -2.2582 \times 10^{-6} \quad (4-28)$$

$$B_{0l} = 1.09223 - 2.48245\omega_l \quad (4-29)$$

$$B_{1l} = -(3.434 - 7.14\omega_l) \times 10^{-3} \quad (4-30)$$

$$B_{2l} = -(7.2661 - 9.2561\omega_l) \times 10^{-7} \quad (4-31)$$

$$C_l = \left[ \frac{(12.8 - Kw_l)(10 - Kw_l)}{10\omega_l} \right]^2 \quad (4-32)$$

$Kw$  is the Watson factor (Kesler and Lee, 1976), defined by Equation 33, in which the boiling temperatures of the pseudocomponents,  $T_b$ , were obtained from the work of Katz and Firoozabadi (1978). The specific mass at 15.5 °C,  $SG$ , is approximately equal to the density,  $\rho$ , of the component, which is also obtained from Katz and Firoozabadi (1978).

$$Kw_l = \frac{\sqrt[3]{1.8T_{bl}}}{SG_l} \quad (4-33)$$

For the solid phases, the thermodynamic path used to calculate the molar enthalpy goes through the liquid phase, for which the description above holds. It then proceeds by taking into consideration the effect of the heat capacities of the liquid, the solidification of the liquid, the solid-solid phase transition, the effect of the heat capacities of the solid and, finally, the excess enthalpy,  $h^E$ , so that a solid phase mixture is considered. As such, neglecting the effects of pressure changes, Equation 4-34 is used to calculate the molar enthalpies of solid phases,  $h^S$ .

$$h^S(T, P, \underline{x}^S) = \sum_{i=1}^{N_c} x_i^S \left[ \int_{T_0}^T Cp_i^{ig} dT - \int_{T_i^{fus}}^T \Delta Cp_i^{LS} dT - \Delta h_i^{fus} - \Delta h_i^{tr} \right] + h^R(T, P, \underline{x}^S) + h^E(T, \underline{x}^S) \quad (4-34)$$

The total molar enthalpy of the system is calculated by summing over the number of phases,  $N_p$ , the product between the molar enthalpy of the phase and its respective molar phase fraction,  $\beta$ , as presented in Equation 4-35.

$$h = \sum_{j=1}^{N_p} \beta^j h^j \quad (4-35)$$

The heat flow,  $\delta Q/\delta t$ , is obtained using Equation 4-36, in which the number of moles of the sample,  $N_{mol}$ , and the variation of  $T$  with time,  $\partial T/\partial t$ , are similar to the experimental ones. The variation of the total molar enthalpy of the system with the temperature,  $\partial h/\partial T$ , is calculated numerically.

$$\frac{\delta Q}{\delta t} = \frac{\partial h}{\partial T} \frac{\partial T}{\partial t} N_{mol} \quad (4-36)$$

### 4.3.3. Thermogram fitting

To adjust the model to the experimental DSC thermograms, the pseudocomponents properties, ideal gas heat capacities and molecular weights were tuned, as well as the pair interaction energy parameter,  $\Lambda_{ij}$ , from the solid model. The initial guesses of all pseudocomponent properties were obtained from Katz and Firoozabadi (1978).

To limit the number of tuning parameters, instead of adjusting each property of each pseudocomponent, a single multiplier was used to adjust simultaneously each of the properties for all pseudocomponents. In this way, only four multipliers were tuned to fit the calculated thermogram to the experimental thermogram.

The molecular weights of the pseudocomponents were the first parameters adjusted using a multiplier,  $\xi_{MW}$ . The molecular mass of the sample was tuned to its measured average molecular weight, presented in Table 4-2.

The other pseudocomponent properties were adjusted by fitting the simulated thermogram to the experimental DSC thermogram in three steps. The first step was to estimate the parameter  $\xi_{T_b}$  that multiplies the pseudocomponents boiling temperatures. These boiling temperatures are used to calculate their ideal gas heat capacities by Equations 4-25 to 4-27, 4-32 and 4-33. As the thermogram recorded at temperatures higher than the WAT are only a function of the heat capacity of the sample and thus a direct function of the ideal gas heat capacities of the samples components, this region was used to tune  $\xi_{T_b}$ .

The second step was to estimate the parameter  $\xi_{T_c}$  that multiplies the pseudocomponents critical temperatures. This parameter was estimated using the

thermogram region ranging from 5 °C below the WAT to the lowest temperature measured.

A final adjustment to the solid-liquid equilibrium curve, the third step, was performed by estimating a parameter  $\xi_A$  that modifies the paraffin pair interaction energies, as proposed in Chapter 3. In this Chapter,  $\xi_A$  is equal to  $(1+\Delta A)$  from Chapter 3. This estimation was carried out using the same region used in step 2. Tests showed that iteration of this sequential parameter estimation is not necessary, since its computational cost is very high and a minor accuracy gain is achieved.

In all three steps described, the optimization parameter was the RMSD between the simulated and the experimental thermograms for each of the regions of interest.

#### **4.3.4. Solid-liquid equilibrium prediction**

From the model with the tuned parameters, the so-called wax appearance temperature that correspond in fact to the wax disappearance temperature can be predicted by calculating the Solid-Liquid phase transition temperature at fixed pressure. This temperature cannot be determined by calorimetric measurements due to subcooling effects. In addition, the model allows calculating of solid-liquid phase equilibrium condition below the wax appearance temperature by solving Equation 4-1. This phase equilibrium calculation provide the amount of solid deposit as well as its composition as a function of temperature.

#### **4.4. Results and Discussions**

The feed compositions of both samples 1 and 2 in terms of paraffins and pseudocomponents are presented in Table 4-2.

The amounts of solids measured at various temperatures below the wax appearance temperature in order to build the solubility curve are presented in Table 4-3. The compositions of the solid paraffin at each temperature for sample 1 are presented in Table 4-4 and those for sample 2, Table 4-5.

**Table 4-2.** Feed compositions of both Diesel fuel samples divided into paraffins and other components lumped into pseudocomponents in mass fractions (%) and average MW ( $\text{g}\cdot\text{mol}^{-1}$ ). The relative expanded uncertainty of the composition is under 2% for the paraffin components and under 3% for the pseudocomponents of the reported value. The relative expanded uncertainty of the average molecular mass is 3%.

Carbon Number	1		2	
	Paraffin	Pseudocomp.	Paraffin	Pseudocomp.
7	0.0425	0.1648	0.0381	-
8	0.2675	0.3501	0.2739	0.6361
9	0.6065	1.8255	0.6904	2.0678
10	0.8774	3.6571	1.0023	4.2041
11	1.1587	5.5495	1.4262	5.9890
12	1.4446	6.5777	1.8173	7.3054
13	1.7070	8.2085	2.0958	9.0891
14	2.1668	7.9017	2.4777	8.9089
15	2.4542	7.8873	2.7530	7.6142
16	2.0144	5.9382	2.2158	5.7477
17	1.8993	6.5838	2.0610	6.5043
18	1.4592	5.2393	1.4776	4.7995
19	1.2696	3.9245	1.2305	3.4036
20	0.9988	2.9136	0.9250	2.3690
21	0.8265	2.2486	0.7235	1.7022
22	0.6255	1.9275	0.5303	1.4064
23	0.4629	1.5370	0.3918	1.0958
24	0.3227	1.1219	0.2712	0.7386
25	0.2451	0.8569	0.2176	0.5743
26	0.1707	0.7733	0.1600	0.4999
27	0.1368	0.6165	0.1296	0.4275
28	0.0937	0.6079	0.0980	0.3745
29	0.0625	0.4312	0.0658	0.3048
30	0.0428	0.4356	0.0461	0.2410
31	0.0253	0.3958	0.0310	0.2329
32	0.0159	0.3053	0.0182	0.1759
33	0.0085	0.2830	0.0106	0.1595
34	0.0070	0.3259	0.0054	0.1325
35	0.0425	0.1648	0.0033	0.1384
MW	202.9		201.3	

**Table 4-3.** Amount of solid paraffin for samples 1 and 2 for each temperature measured (mass %). The relative expanded uncertainty is 5% of the presented value.

Temperature (K)	Sample 1	Sample 2
273.75	0.29	0.26
268.15	0.68	0.52
263.15	1.37	1.14

**Table 4-4.** Compositions of solid paraffins of sample 1 in mass fractions for each temperature evaluated. The relative expanded uncertainty is 5% of the presented value.

Carbon Number	Temperature (K)		
	273.75	268.15	263.15
19	-	0.009	0.018
20	-	0.011	0.050
21	-	0.034	0.087
22	0.017	0.061	0.128
23	0.043	0.108	0.154
24	0.077	0.131	0.137
25	0.118	0.147	0.120
26	0.140	0.132	0.092
27	0.151	0.115	0.072
28	0.132	0.084	0.049
29	0.116	0.068	0.038
30	0.073	0.038	0.021
31	0.054	0.027	0.015
32	0.031	0.014	0.008
33	0.020	0.009	0.005
34	0.012	0.006	0.003
35	0.016	0.006	0.003

**Table 4-5.** Compositions of solid paraffins of sample 2 in mass fractions for each temperature evaluated. The relative expanded uncertainty is 5% of the presented value.

Carbon Number	Temperature (K)		
	273.75	268.15	263.15
19	-	-	0.013
20	-	-	0.051
21	-	0.011	0.073
22	0.010	0.024	0.097
23	0.022	0.079	0.134
24	0.040	0.093	0.125
25	0.081	0.128	0.123
26	0.117	0.143	0.099
27	0.151	0.141	0.086
28	0.148	0.117	0.063
29	0.144	0.100	0.053
30	0.097	0.059	0.030
31	0.076	0.044	0.022
32	0.045	0.024	0.013
33	0.029	0.016	0.008
34	0.018	0.010	0.005
35	0.022	0.011	0.005

The compositions of the solid phases with respect to the original sample mass for both samples are shown in Figure 4-1. As can be seen, at higher temperatures, the solids are composed majorly by the heavy paraffins. As temperature decreases, the lighter paraffins start to incorporate into the solid. Nevertheless, even at the highest temperature, the composition spreads over a big number of paraffins, suggesting that the solid consists of a solid solution of paraffins rather than a simple mixture of pure single paraffin solids.

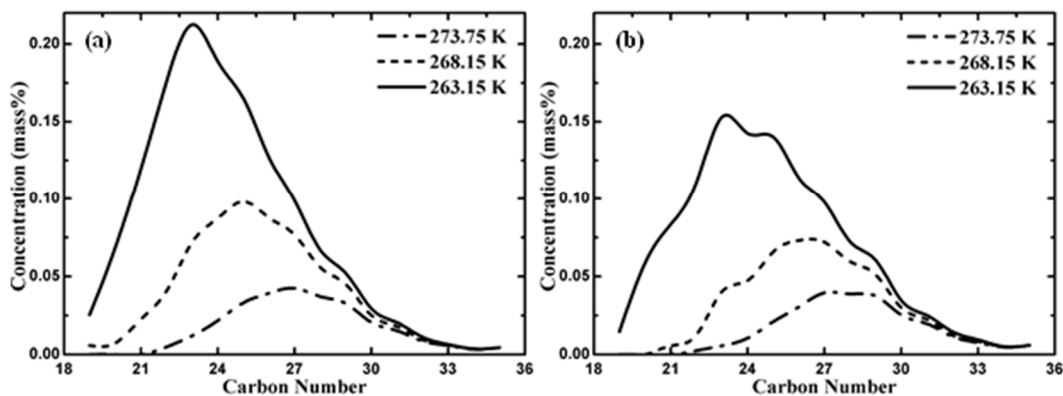


**Figure 4-1.** (a) Concentration of the paraffins in the solid for different temperatures from sample 1. (b) Concentration of the paraffins in the solid for different temperatures from sample 2.

The results obtained for the tuning multipliers are depicted in Table 4-6. The molecular weight multiplier,  $\xi_{MW}$ , corrects the pseudocomponents molecular weight by just 2.6% at most. This correction is within the experimental uncertainty of the measured molecular weight. Moreover, the parameters  $\xi_{\lambda}$  modify the pair interaction energies in less than 1%, what is in agreement with results presented in Chapter 3.

**Table 4-6.** Parameters obtained that multiply the pseudocomponent molecular weights,  $\xi_{MW}$ , boiling,  $\xi_{T_b}$ , and critical,  $\xi_{T_c}$ , temperatures and the paraffins' pair interaction energies,  $\xi_{\lambda}$ .

Diesel	$\xi_{MW}$	$\xi_{T_b}$	$\xi_{T_c}$	$\xi_{\lambda}$
1	0.9932	1.126	0.7372	0.9935
2	1.026	1.139	0.8011	0.9906

The results for the calculated thermogram for both samples after the tuning are presented in Figure 4-2. As can be seen, by tuning the model to the rest of the thermogram instead of just the WAT leads to a difference between the experimental DSC WAT and the solid-liquid equilibrium temperature calculated. The experimental limitations lead to an experimental WAT lower than the crystallization temperature predict by the model, as shown in Figure 4-2. Actually, due to subcooling of paraffins and kinetic effects during experiments carried out by cooling, scanning calorimetry experiment do not give access to the real WAT. The proposed methodology based on fitting the full thermogram provide a more realistic WAT value by correcting this drawback.

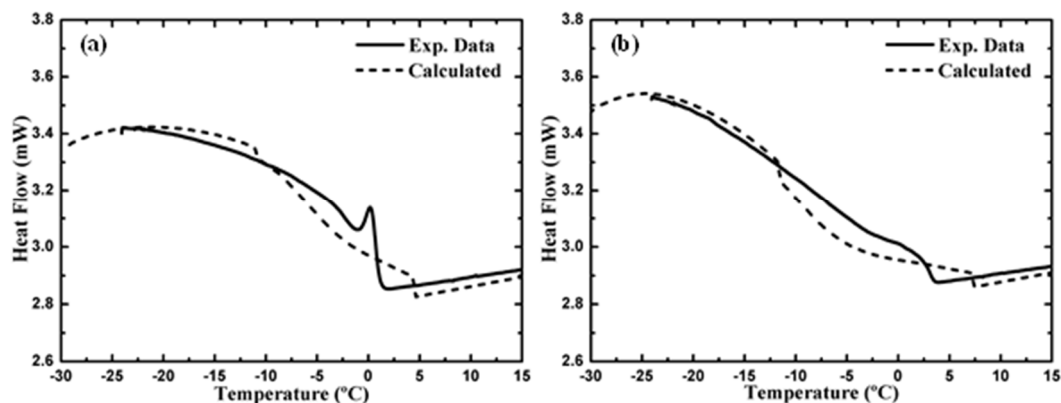


**Figure 4-2.** Experimental and fitted DSC curves for Diesel 1 (a) and Diesel 2 (b).

The experimental solubility curves for both samples as well as the calculated curves are presented in Figure 4-3. As can be seen, the differences are smaller than the experimental uncertainties. To further compare experimental results and the model, the solid and liquid phases compositions for each sample at each temperature are shown in Figures 4-4 and 4-5. Again, the simulated results are in very good agreement with the experimental data for all cases analyzed.

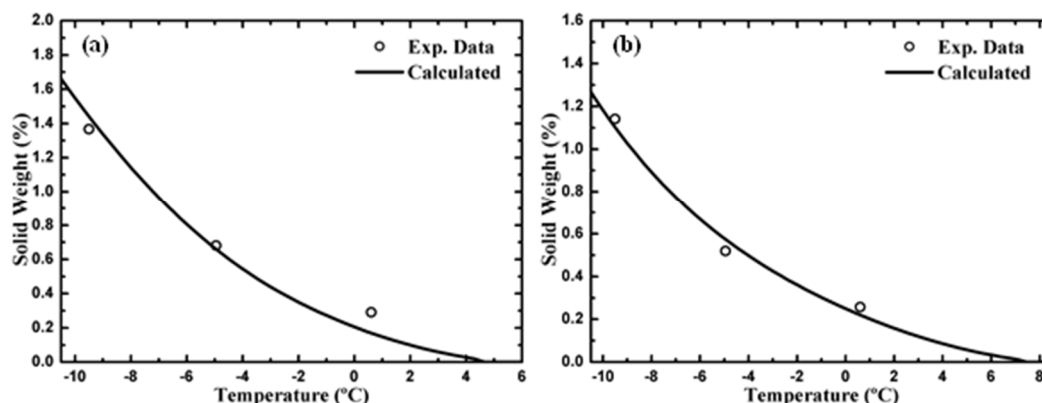


**Figure 4-3.** Experimental and predicted solubility curves for Diesel 1 (a) and Diesel 2 (b).

It seems natural that the solubility curves were well represented by the proposed methodology based on fitting DSC measurements as the area of the thermogram peaks are directly related to the amount waxy solid formed. In contrast, no composition information of the liquid and solid phases measured were used to fit the model and yet the comparison between them and their predictions agree to within experimental uncertainties. This last result, above all, indicates the soundness of the model and clearly shows the predictive capacity of the developed fitting procedure.

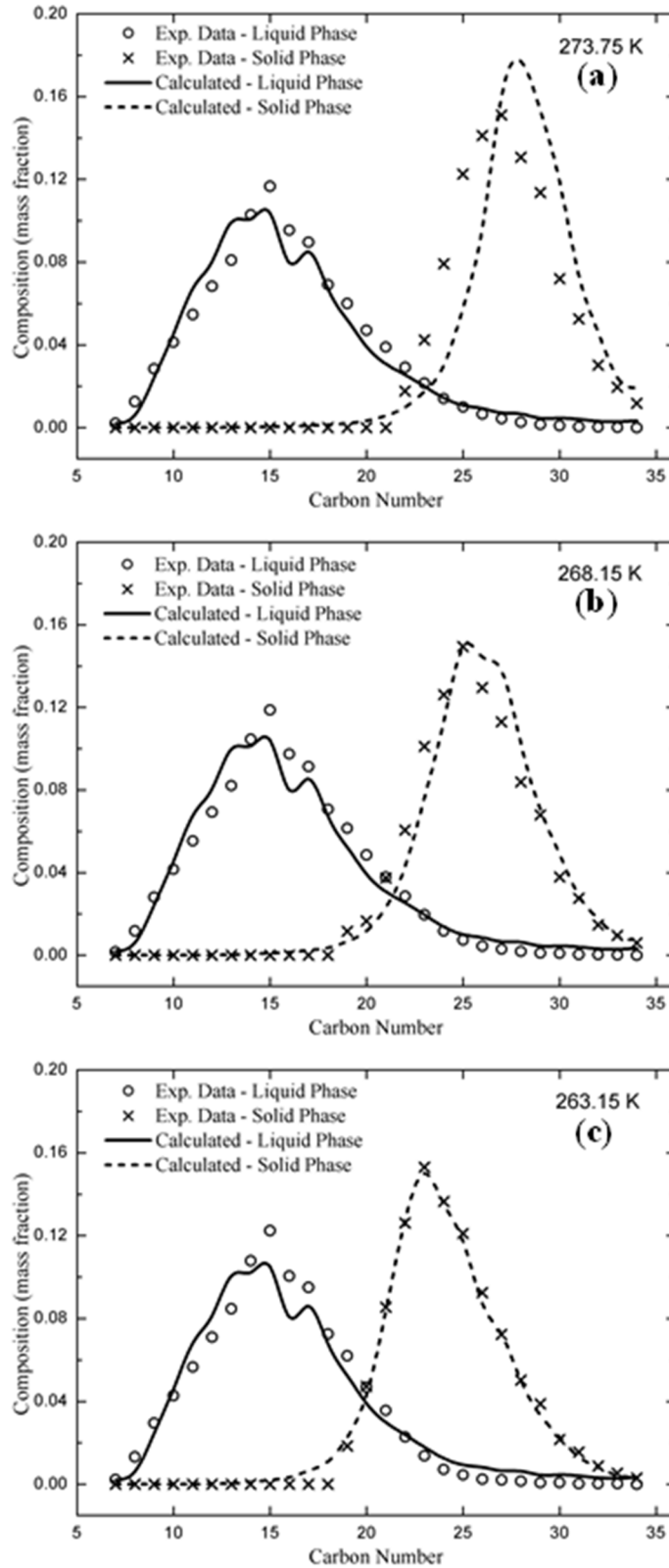


**Figure 4-4.** Experimental and predicted compositions of liquid and solid phases at 273.75 K (a), 268.15 K (b) and 263.15 K (c) for Diesel 1.

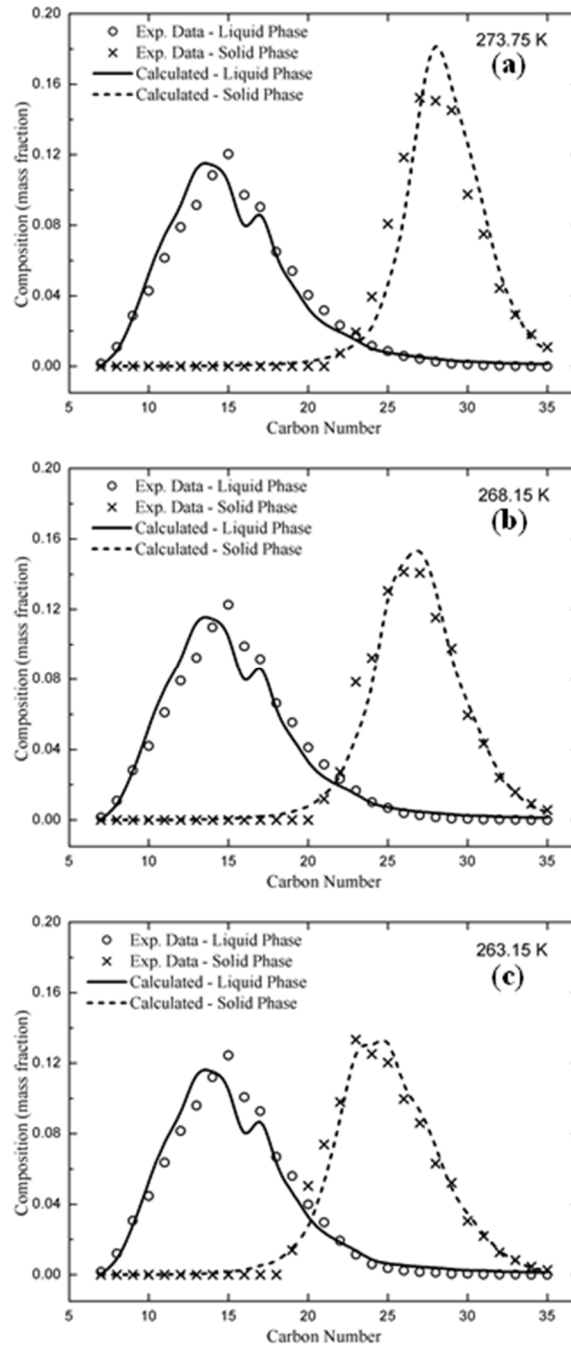


**Figure 4-5.** Experimental and predicted compositions of liquid and solid phases at 273.75 K (a), 268.15 K (b) and 263.15 K (c) for Diesel 2.

The proposed methodology presents itself as a robust alternative to tune thermodynamic solid-liquid equilibria models. The final uncertainty is smaller when compared to the alternative of tuning the model to one temperature alone, the WAT. It also allows the tuning of models to more complex fluids, like crude oil, as long as DSC thermogram at a slow enough rate is available, as discussed in the previous Chapters (Fleming et al., 2017; da Silva et al., 2017).

## 4.5. Conclusions

Solid precipitation in Diesel fluids driven by low temperatures is at the heart of many problems regarding systems that run on this fuel. To assess the risks of a given sample, thermodynamic solid-liquid equilibria models are employed. These thermodynamic models are tuned using the wax appearance temperature, WAT, the highest temperature at which a first crystal of paraffin is spotted in a cooling experiment.

A new strategy to tune thermodynamic solid-liquid equilibria models has been proposed in Chapters 2 and 3 (Fleming et al., 2017; da Silva et al., 2017)). It consists of using DSC thermograms instead of the WAT to adjust the model to experimental data. The strategy has been tested for standard mixtures with well known composition and in this work it is tested against real mixtures where the whole composition is not available. Two different Diesel fuel samples supplied by PETROBRAS are analyzed and their phase behavior assessed by a thermodynamic model.

Calorimetric data ranging from 248.15 K to 303.15 K and solubility data at 273.75 K, 268.15 K and 263.15 K were measured for the two samples. The solid-liquid phase equilibria behavior of these samples were modeled using the PR-EoS for the liquid phase and the modified UNIQUAC model for the solid phase. The models were fitted to the DSC data aiming to correctly reproduce the solubility data and, to do that, the simulated heat flows were calculated according to the methodology proposed in Chapter 3. A parameter estimation was employed, in which the pseudocomponents molecular weights are tuned to the average molecular weight of the samples, followed by the fitting of the simulated thermograms to the DSC experimental results by tuning the pseudocomponents boiling and critical temperatures and the paraffin pair interaction energies, in this order.

The results were in agreement to both the DSC and solubility experimental data for both samples. The solid phase simulated and experimental compositions were in very good agreement for the two samples. The same holds for liquid phases. This way, the developed methodology proves to perform very well for real complex samples.

# 5 HIGH PRESSURE PHASE EQUILIBRIA OF CARBON DIOXIDE + *n*-ALKANES MIXTURES: EXPERIMENTAL DATA AND MODELING

## 5.1. Introduction

Paraffin precipitation is one of the main concerns of oil production in deep-water environments. In equilibrium under reservoir conditions, the paraffin fraction may precipitate and deposit during production majorly due to the cooling of the fluid. Mitigation of these deposits requires use of mechanical methods (Pigging, etc.) or chemical methods (solvents, detergents, etc.) that lead to important production losses. Operators design the production systems to avoid this problem by optimizing thermal insulation and the layout of production facilities. Such a task requires information about phase behavior of paraffinic mixtures and accurate deposition models. In this sense, the study about the influence of light components, as CO<sub>2</sub> and CH<sub>4</sub>, becomes very important, since they may change the conditions under which the paraffins precipitate. Thus, the use of reliable experimental phase equilibrium data, which should cover a broad range of pressure, temperature and composition, is fundamental for the development and validation of thermodynamic models for these systems (Pan et al., 1997; Pauly et al., 2000; Pauly et al., 2012).

To address the thermodynamic behavior of such asymmetric mixtures, experimental phase equilibrium data for four synthetic mixtures constituted by a light component, CO<sub>2</sub>, and the normal alkanes C<sub>12</sub>H<sub>26</sub>, C<sub>22</sub>H<sub>46</sub>, C<sub>23</sub>H<sub>48</sub> and C<sub>24</sub>H<sub>50</sub> is presented. The experiments were carried out at pressures ranging from 0,1 to 70 MPa.

The phase behavior of mixtures made up of CO<sub>2</sub> + *n*-alkanes has been studied in the literature (Nichita et al., 2001; Kariznovi et al., 2013; Nieuwoudt and Rand, 2002). Pan and collaborators(1997) have studied the pressure effect and the influence of CO<sub>2</sub> on wax precipitation for real crude oil systems. They presented experimental data and a thermodynamic approach based on the multisolid model

(Lira-Galeana et al., 1996), where it was observed that dissolving CO<sub>2</sub> in a crude oil results in a reduction of the wax appearance temperature. The work of Rodriguez-Reartes and collaborators (2009) reported experimental high-pressure phase equilibrium data for the system CO<sub>2</sub> + *n*-eicosane. They proposed a modeling approach for the solid-liquid equilibrium and used the Peng-Robinson EoS (Peng and Robinson, 1976) to represent the fluid phases in the liquid-liquid, solid-liquid, liquid-liquid-vapor and solid-liquid-liquid phase equilibria.

To model the phase equilibria of the mixtures investigated, the approach described in Chapter 3 (da Silva et al., 2017) was used. The multiple solid solution model developed by Coutinho and collaborators (2006) was employed to calculate the solid phase non-idealities and the Peng-Robinson EoS with the van der Waals mixing rule and classical combining rules were used to describe the vapor and the liquid phases. As the experimental solid-liquid phase transitions were measured at high pressures, the Poynting correction factor, which was neglected in Chapter 3, was taken into consideration. A correlation for the difference between the components' molar volumes in the liquid and solid phases was estimated using the experimental solid-liquid transition data of the mixtures analyzed. For improving the model predictions, the binary interaction parameters between CO<sub>2</sub> and *n*-alkanes for the Peng-Robinson EoS were fitted using the measured vapor-liquid transition curve of one sample investigated and applied to all other samples. In addition, a comparison between the experimental and predicted phase envelopes was carried out.

## **5.2. Experimental**

### **5.2.1. Chemicals**

The mixture was formulated by combining the appropriate mass of the different standard *n*-alkanes. The composition as well as its uncertainties, origin and purity of the used products are listed in Table 5-1. All chemicals were used without any further purification.

**Table 5-1.** Compositions of the synthetic mixtures (mass %, standard uncertainties also in mass %)

<i>Comp.</i>	<i>Suppl.</i>	<i>Pur.(%)</i>	<i>Sample 1</i>	<i>Sample 2</i>	<i>Sample 3</i>	<i>Sample 4</i>
CO <sub>2</sub>	Messer	99.99	5.23 ± 0.11	12.87 ± 0.13	24.29 ± 0.12	46.12 ± 0.08
C <sub>12</sub> H <sub>26</sub>	Aldrich	99	72.91 ± 0.10	67.03 ± 0.11	58.25 ± 0.11	41.45 ± 0.08
C <sub>22</sub> H <sub>46</sub>	Aldrich	99	8.63 ± 0.03	7.93 ± 0.02	6.89 ± 0.02	4.90 ± 0.01
C <sub>23</sub> H <sub>48</sub>	Fluka	>98	7.21 ± 0.02	6.63 ± 0.02	5.76 ± 0.02	4.10 ± 0.01
C <sub>24</sub> H <sub>50</sub>	Aldrich	99	6.02 ± 0.02	5.53 ± 0.02	4.81 ± 0.01	3.42 ± 0.01

### 5.2.2. Experimental procedure

The phase equilibrium data was obtained by means of direct visual inspection of the entire sample in different temperatures and pressures. The experimental apparatus described in details in a previous work (Pauly et al., 2007) consisted of a stainless steel manual displacement pump with a working pressure limit of 100 MPa, equipped with a full view sapphire window in one end and another smaller sapphire window on the side for illumination. Visualization was possible through the use of an endoscope placed before a full view sapphire window. The circulation of a heat-carrier fluid thermo-regulated by a thermostatic bath (Huber) through the body of the pump itself controlled the temperature and allowed a stability of 0.1 K. The temperature of the system was measured using a calibrated high precision platinum resistance probe placed on the cylinder. To avoid the increase in the cell's dead volume, a piezo resistive silicon pressure transducer (Kulite) was adapted directly in contact with the sample inside the cell. Calibration of such pressure transducer is then required, since it will be exposed to the experimental temperature. To measure a reference pressure, a high precision dead weight gauge (Bundenberg) was attached to the system through an extension capillary tube. An accuracy better than 0.02% was achieved over the entire temperature and pressure ranges with such a calibration procedure.

To reduce uncertainties in the composition and avoid the chemical characterization of the sample, a synthetic method was used (van der Kooi et al., 1995). The previously prepared *n*-alkane mixture was heated and the liquid introduced in the measuring cell through a capillary tube while the container was weighted using a high precision balance (Sartorius) with an accuracy of 0.1 mg. The gas was introduced next using a similar strategy. CO<sub>2</sub> was conditioned in a light

weight recipient and placed on a high precision balance (Sartorius) with an accuracy of 1 mg. The connection with the cell was done using a high pressure flexible capillary tube and the mass of transferred gas was measured. From this procedure, the standard uncertainties in mass introduced were estimated to be better than 0.01 g for liquid mixture and 0.005 g for CO<sub>2</sub>. The composition of the sample was calculated from the masses of the gas and the *n*-alkane mixture transferred.

The phase equilibria boundaries were determined through visualization of the disappearance of the last remaining, bubble, drop or crystal, of a given phase as response to a small step change in either the pressure or the temperature. The composition was kept uniform through the intensive stirring of a magnetic stirrer placed inside the measuring cell. The stirring was interrupted once equilibrium was achieved for visual inspection of phase distribution. The disappearance of the heterogeneous phase was used to avoid uncertainties arising from supersaturation effects. The experimental procedure as proposed allowed measurement of bubble point pressure with an uncertainty of  $\pm 0.05$  MPa whereas L-S temperature transitions at fixed pressure are measured with an uncertainty of 0.3 K.

### 5.3. Thermodynamic Model

For the calculation of the VLE, SLE and SLVE, it is necessary that the fugacity of each component *i* in all phases,  $\hat{f}_i$ , are equal, as shown in Equation 5-1, in which  $\underline{x}^V$ ,  $\underline{x}^L$  and  $\underline{x}^S$  are the composition vectors of the vapor, liquid and solid phases, respectively. *T* and *P* are the temperature and the pressure at equilibrium.

$$\hat{f}_i^L(T, P, \underline{x}^L) = \hat{f}_i^V(T, P, \underline{x}^V) = \hat{f}_i^S(T, P, \underline{x}^S) \quad (5-1)$$

The liquid and vapor fugacities of component *i* in the mixture are evaluated using the following expressions:

$$\hat{f}_i^L(T, P, \underline{x}^L) = x_i^L \hat{\phi}_i^L P \quad (5-2)$$

$$\hat{f}_i^V(T, P, \underline{x}^V) = x_i^V \hat{\phi}_i^V P \quad (5-3)$$

The fugacity coefficients of component *i* in the liquid and vapor phases ( $\hat{\phi}_i^L$  and  $\hat{\phi}_i^V$ ) are obtained from the Peng-Robinson EoS with the classical mixing rules.

The binary interaction coefficients,  $k_{ij}$  between two  $n$ -alkanes were set to zero whereas the  $k_{ij}$  between CO<sub>2</sub> and  $n$ -alkanes was evaluated independently for each mixture using the VLE experimental data (bubble curve) and a constant value that minimizes the deviations for all experimental data was chosen.

The critical properties and acentric factors of  $n$ -alkanes were calculated using the correlations proposed by Marano and Holder(1997), according to Equations 5-4 to 5-6. For CO<sub>2</sub>, these properties were obtained from Poling and collaborators (2001).

$$T_{ci}[K] = 1020.71 - (1020.71 - 127.89)\exp(-0.1981(CN_i - 0.896021)^{0.629752}) \quad (5-4)$$

$$P_{ci}[bar] = 1336.74\exp(-2.111827(CN_i + 3.625581)^{0.258439}) \quad (5-5)$$

$$\omega_i = -6.5597 + 3.383261(CN_i + 23.608415)^{0.20877} \quad (5-6)$$

For the solid phase, the fugacity of component  $i$  in the mixture is calculated from Equation 5-7:

$$\hat{f}_i^S(T, P, \underline{x}^S) = x_i^S \gamma_i^S f_{i,pure}^S \quad (5-7)$$

in which the activity coefficient of each component  $i$  in the solid phase,  $\gamma_i^S$ , is calculated using the modified UNIQUAC model, as presented in Equation 5-8 (Kontogeorgis and Gani, 2004):

$$\ln \gamma_i^S = \ln \left( \frac{\Phi_i}{x_i^S} \right) + 1 - \frac{\Phi_i}{x_i^S} - \frac{Z}{2} q_i \left( \ln \left( \frac{\Phi_i}{\theta_i} \right) + 1 - \frac{\Phi_i}{\theta_i} \right) + q_i - q_i \ln \left( \sum_{j=1}^{Nc} \theta_j \tau_{ji} \right) - q_i \sum_{j=1}^{Nc} \frac{\theta_j \tau_{ij}}{\sum_{k=1}^{Nc} \theta_k \tau_{kj}} \quad (5-8)$$

The parameters  $\tau_{ji}$ ,  $\theta_i$  and  $\Phi_i$  are obtained, respectively, through

$$\tau_{ji} = \exp \left( - \frac{A_{ji} - A_{ii}}{q_i RT} \right) \quad (5-9)$$

$$\theta_i = \frac{x_i^S q_i}{\sum_{j=1}^{Nc} x_j^S q_j} \quad (5-10)$$

$$\Phi_i = \frac{x_i^S r_i}{\sum_{j=1}^{Nc} x_j^S r_j} \quad (5-11)$$

where  $Nc$  is the number of components in the mixture and  $r_i$  and  $q_i$  are the structural parameters of each component, calculated from Equations 5-12 and 5-13 (Coutinho et al., 2006), in which  $CN_i$  is the number of carbon atoms of component  $i$ .

$$r_i = 0.6744CN_i + 0.4534 \quad (5-12)$$

$$q_i = 0.540CN_i + 0.616 \quad (5-13)$$

The pair interaction energies for two identical paraffins,  $\Lambda_{ii}$ , are (Coutinho et al., 2006)

$$\Lambda_{ii} = -\frac{2}{Z}(\Delta\bar{H}_{i,pure}^{sub} - RT) \quad (5-14)$$

where  $Z$  is the coordination number, which is set to 10.

For two different paraffins, as suggested by Coutinho and collaborators (2006), the interaction energy ( $\Lambda_{ij}$ ) is equal to the interaction energy of the  $n$ -alkane with the shorter chain of the pair  $ij$ .

The heat of sublimation,  $\Delta\bar{H}_{i,pure}^{sub}$ , is obtained from Equation 5-15(Coutinho et al., 2006),

$$\Delta\bar{H}_{i,pure}^{sub} = \Delta\bar{H}_{i,pure}^{vap} + \Delta\bar{H}_{i,pure}^f + \Delta\bar{H}_{i,pure}^{tr} \quad (5-15)$$

where the heat of vaporization,  $\Delta\bar{H}_{i,pure}^{vap}$ , is calculated from the correlation proposed by Morgan and Kobayashi (1994a,b).

In Equation 5-7, the fugacity of each paraffin  $i$  as a pure solid,  $f_{i,pure}^S$ , is evaluated following the methodology described by Prausnitz and collaborators (1999) and Firoozabadi (1999), in which the pure solid fugacity is calculated from the pure liquid fugacity and thermophysical properties. Furthermore, the crystalline transition of the solid phase is taken into consideration (Coutinho et al., 2006; Ji et al., 2004), as expressed below.

$$f_{i,pure}^S = f_{i,pure}^L \exp \left[ \frac{\Delta\bar{H}_{i,pure}^f}{RT_i^f} \left( 1 - \frac{T_i^f}{T} \right) + \frac{\Delta\bar{H}_{i,pure}^{tr}}{RT_i^{tr}} \left( 1 - \frac{T_i^{tr}}{T} \right) - \frac{1}{RT} \int_{T_i^f}^T \Delta Cp_i^{LS} dT + \frac{1}{R} \int_{T_i^f}^T \frac{\Delta Cp_i^{LS}}{T} dT - \frac{1}{RT} \int_{P_i^f}^P \Delta\bar{V}_i^{LS} dP \right] \quad (5-16)$$

In Equation 5-16,  $T_i^f$ ,  $P_i^f$  and  $T_i^{tr}$  are, respectively, the melting temperature, the melting pressure and the solid phase crystalline transition temperature of paraffin  $i$ .  $\Delta\bar{H}_{i,pure}^f$  and  $\Delta\bar{H}_{i,pure}^{tr}$  are, respectively, the molar enthalpies of melting and of solid phase crystalline transition of paraffin  $i$ .  $\Delta Cp_i^{LS}$  and  $\Delta\bar{V}_i^{LS}$  are,

respectively, the differences between the heat capacities and the molar volumes of paraffin  $i$  in liquid and solid phases.

The correlations suggested by Coutinho and collaborators (2006) shown in Equations 5-17 to 5-21 were employed to calculate the melting temperature, melting pressure, solid phase crystalline transition temperature, molar melting enthalpy and the molar solid phase crystalline transition enthalpy of paraffin  $i$ .

$$T_i^f [K] = 421.63 - 1936412 \exp(-7.8945(CN_i - 1)^{0.07194}) \quad (5-17)$$

$$T_i^{tr} [K] = 420.42 - 134784 \exp(-4.344(CN_i + 6.5292)^{0.14627}) \quad (5-18)$$

$$\Delta \bar{H}_{i,pure}^{tot} \left[ \frac{kJ}{mol} \right] = 3.7791 CN_i - 12.654 \quad (5-19)$$

$$\Delta \bar{H}_{i,pure}^f \left[ \frac{kJ}{mol} \right] = 0.00355 CN_i^3 - 0.2376 CN_i^2 + 7.40 CN_i - 34.814 \quad (5-20)$$

$$\Delta \bar{H}_{i,pure}^{tr} = \Delta \bar{H}_{i,pure}^{tot} - \Delta \bar{H}_{i,pure}^f \quad (5-21)$$

Since the correlations in Equations 5-17 to 5-21 were developed based on data at 1 bar (Ji et al., 2004; Broadhurst, 1962; Coutinho and Daridon, 2001), this value is adopted in this work for the melting pressure ( $P_i^f$ ).

The heat capacities difference between the liquid and solid phases were obtained from the correlation proposed by Pedersen and collaborators (1991), as in

$$\Delta C p_i^{LS} \left[ \frac{cal}{molK} \right] = 0.3033 MW_i - 4.635 \times 10^{-4} MW_i T \quad (5-22)$$

The last term in Equation 5-16 is the Poynting correction term, which should be taken into consideration when modeling high pressure SLE (Nichita et al., 2001; Ji et al., 2004). This term is a function of the difference between liquid ( $\bar{V}_i^L$ ) and solid ( $\bar{V}_i^S$ ) molar volumes of the crystalizing paraffins. This difference,  $\Delta \bar{V}_i^{LS}$ , can be estimated directly by fitting simultaneously the experimental SLE data of all the mixtures studied here. Following previous studies (da Silva et al., 2017; Pauly et al., 2007), a correlation for  $\Delta \bar{V}_i^{LS}$  is presented in Equation 5-23:

$$\Delta \bar{V}_i^{LS} \left[ \frac{cm^3}{mol} \right] = 1.842 \times 10^{-3} MW_i T - 0.426 MW_i \quad (5-23)$$

where  $T$  is the temperature in Kelvin and  $MW_i$  is the molecular weight in grams/mole of paraffin  $i$ .

Taking the liquid as the reference phase and using the Equations 5-1, 5-2, 5-3, 5-7 and 5-16, we can deduce the expressions for the vapor-liquid ( $K_i^{VL}$ ) and the solid-liquid ( $K_i^{SL}$ ) ratios, presented in Equations 5-24 and 5-25, respectively.

$$K_i^{VL} = \frac{x_i^V}{x_i^L} = \frac{\hat{\phi}_i^L}{\hat{\phi}_i^V} \quad (5-24)$$

$$K_i^{SL} = \frac{x_i^S}{x_i^L} = \frac{\hat{\phi}_i^L}{\hat{\phi}_i^L \gamma_i^S} \exp \left[ \frac{\Delta \bar{H}_{i,pure}^f}{RT_i^f} \left( \frac{T_i^f}{T} - 1 \right) + \frac{\Delta \bar{H}_{i,pure}^{tr}}{RT_i^{tr}} \left( \frac{T_i^{tr}}{T} - 1 \right) + \frac{1}{RT} \int_{T_i^f}^T \Delta C p_i^{LS} dT - \right. \\ \left. \frac{1}{R} \int_{T_i^f}^T \frac{\Delta C p_i^{LS}}{T} dT + \frac{1}{RT} \int_{P_i^f}^P \Delta \bar{V}_i^{LS} dP \right] \quad (5-25)$$

To calculate the phase transitions observed in the experimental data, a flash algorithm, which uses the Newton's and successive substitution methods, was developed. The algorithm also has a stability analysis based on the tangent plane distance to the Gibbs energy surface criterion (Michelsen, 1982), used to determine the solid phase appearance temperature.

#### 5.4. Results and Discussions

The phase equilibrium boundaries obtained experimentally are depicted in Table 5-2.

The binary interaction parameters between CO<sub>2</sub> and *n*-alkanes ( $k_{CO_2-alkane}$ ), employed in the Peng-Robinson EoS, were fitted using the experimental VLE data. Pan and collaborators (1997) suggested a constant value of 0.15 for the interaction parameter between CO<sub>2</sub> and *n*-alkanes longer than six carbon atoms. This value was used as a starting point for the estimation of parameters. As the samples prepared in this work have different amounts of CO<sub>2</sub>, the estimations were carried out for each sample independently, so that we can study the influence of the amount of CO<sub>2</sub> on the binary interaction parameters values, and thus the validity of the model.

**Table 5-2.** Experimental phase equilibrium data for the samples analyzed.<sup>a</sup>

<i>L - VLE transitions</i>		<i>L - SLE transitions</i>		<i>VLE - SLVE transitions</i>	
T (K)	P(MPa)	T (K)	P(MPa)	T (K)	P(MPa)
<b>Sample 1</b>					
293.1	1.73	292.6	2.113	295.2	0.177
302.0	1.91	292.9	2.608	293.0	1.109
313.7	2.12	294.3	10.079	292.5	1.615
323.2	2.30	298.3	30.033		
332.8	2.49	304.3	59.901		
343.3	2.66				
352.8	2.83				
<b>Sample 2</b>					
290.7	3.20	290.6	3.84	295.2	0.18
293.1	3.32	290.7	4.34	291.7	1.85
302.9	3.77	290.9	5.14	291.2	2.34
312.8	4.22	291.9	10.12	290.5	2.86
322.8	4.69	293.9	20.10	290.4	3.35
332.8	5.16	295.9	30.09		
343.4	5.65	297.8	40.08		
352.9	6.07	301.9	59.97		
<b>Sample 3</b>					
289.7	4.52	289.0	4.67	295.2	0.18
292.8	4.77	290.0	10.16	290.2	3.05
303.0	5.61	291.9	20.14	289.4	3.56
312.6	6.45	295.8	40.13	288.9	4.07
322.8	7.37	297.7	50.11	288.8	4.37
332.9	8.29	299.5	60.05		
342.8	9.17				
352.2	9.96				
<b>Sample 4</b>					
289.0	5.14	289.6	5.66	295.2	0.18
289.6	5.20	289.7	6.16	288.6	4.83
293.2	5.65	290.4	10.15	288.8	4.87
303.1	6.97	292.0	20.14	289.2	5.07
312.7	8.47	295.6	40.14		
322.3	10.25	299.2	60.06		
332.2	12.05	300.9	69.93		
342.2	13.78				
351.9	15.31				

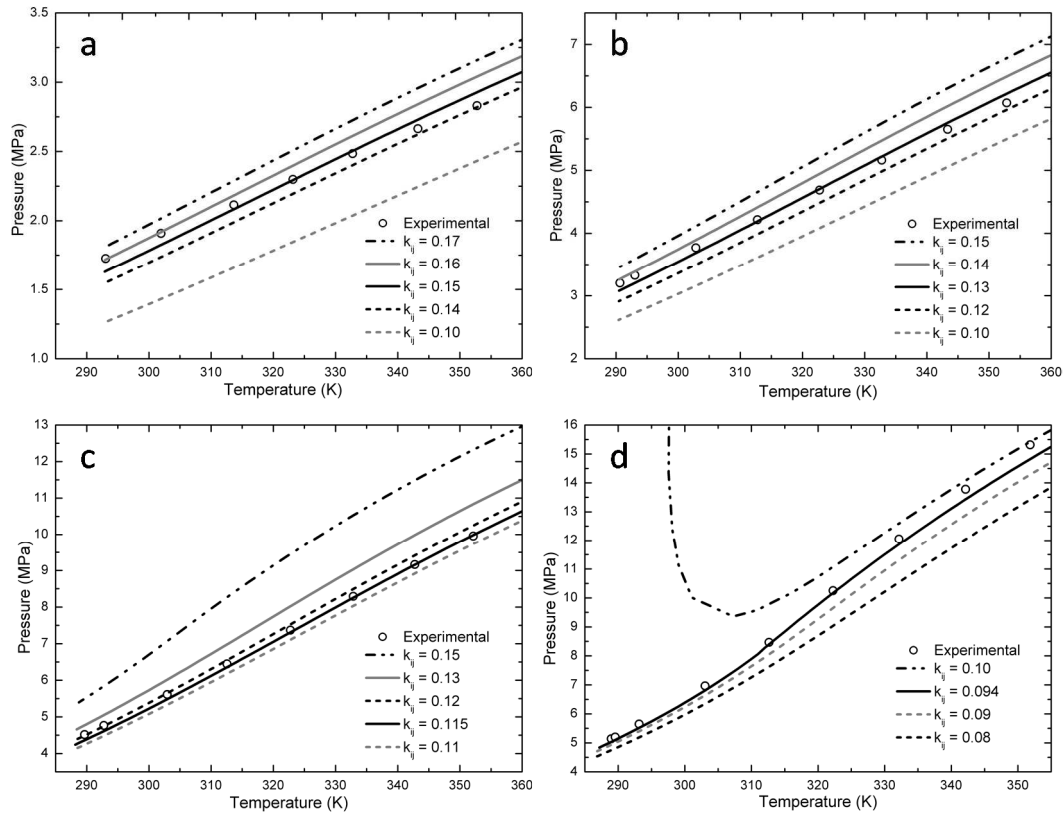
<sup>a</sup>Standard uncertainties  $u$  are  $u(T) = 0.1$  K,  $u(p) = 0.02$  MPa and the combined expanded uncertainties  $U_c$  (level of confidence = 0.95,  $k = 2$ ) are  $U_c(T) = 0.6$  K for L-S temperature transitions at fixed pressure and  $U_c(p) = 0.1$  MPa for bubble point pressures at fixed temperature.

Figure 5-1a shows the experimental and calculated bubble point curve for sample 1, that contains approximately 20% mole CO<sub>2</sub>, using different values of  $k_{CO_2-alkane}$ . The results indicate that for lower temperatures (between 290 K and 305 K), that is a short range in Figure 5-1a, the value of 0.16 better fitted the experimental points. Although, for temperatures greater than 305 K, the value of 0.15, as suggested by Pan and collaborators(1997), presents the best predictions and, in general, represents the best value of the binary interaction parameter between CO<sub>2</sub> and *n*-alkanes for sample 1.

For sample 2, that contains approximately 40% mole CO<sub>2</sub>, the results displayed in Figure 5-1b show that the best agreement with experimental bubble point curve was obtained using  $k_{CO_2-alkane} = 0.13$ . In this case, the value suggested by Pan and collaborators (1997) predicted higher values for the bubble point pressure in comparison with experimental data.

Figure 5-1c shows that the best fit to the experimental data for sample 3, that contains approximately 60% mole CO<sub>2</sub>, was achieved with  $k_{CO_2-alkane} = 0.115$ . According to the results presented for samples 1, 2 and 3, one suggests that as the amount of CO<sub>2</sub> is increased in the sample,  $k_{CO_2-alkane}$  should be reduced in order to obtain the best description of VLE for systems constituted by CO<sub>2</sub> and *n*-alkanes.

The results for sample 4, that contains approximately 80% mole CO<sub>2</sub>, follow exactly the trend aforementioned. The value of  $k_{CO_2-alkane} = 0.094$  presented the best description of the VLE, that is lower than the one obtained for sample 3. However, for values of  $k_{CO_2-alkane}$  greater than 0.094, the model predicts a liquid-liquid equilibrium region delimited by a curve that evolves to high pressures, as shown in Figure 5-1d for  $k_{CO_2-alkane} = 0.10$ , instead of lower pressures, as observed for  $k_{CO_2-alkane}$  equal or lower than 0.094. Such liquid-liquid equilibrium was not found experimentally.



**Figure 5-1.** Experimental and calculated bubble curves (L–VLE transition) using different values of  $k_{CO_2-alkane}$ . **(a)** Sample 1 (20% CO<sub>2</sub>); **(b)** Sample 2 (40% CO<sub>2</sub>); **(c)** Sample 3 (60% CO<sub>2</sub>); **(d)** Sample 4 (80% CO<sub>2</sub>).

Table 5-3 summarizes the results for the  $k_{CO_2-alkane}$  estimation.

**Table 5-3.**  $k_{CO_2-alkane}$  estimation results

Sample	$k_{CO_2-alkane}$
1	0.15
2	0.13
3	0.115
4	0.094

The CO<sub>2</sub> concentration dependency of the binary interaction parameter implies that the use of classical PR EOS with classical mixing rule for such a high asymmetric mixture is testing the model's limits. Nevertheless, as this is thermodynamic model implemented in many reservoir simulators, its applicability was tested for all mixtures using  $k_{CO_2-alkane} = 0.094$ . This value was chosen since, although the best  $k_{CO_2-alkane}$  fits for samples 1, 2 and 3 were greater than

0.094, this is the largest value capable of qualitatively predicting sample 4 behavior according to the experimental data.

Figures 5-2 to 5-5 show the experimental and calculated phase diagrams for all four samples. The region in the diagrams indicated by the letter L is the liquid region, L+V is the VLE region and S+L is the SLE region. For the sake of visualization of the experimental data around the three-phase point for all samples, Figures 5-2 to 5-5 are added with a smaller graph depicting this region in more detail.

For samples 1 and 2, the results for all phase transitions, presented in Figures 5-2 and 5-3, respectively, are in good agreement with experimental data. It can also be pointed out that the correlation proposed for  $\Delta\bar{V}_i^{LS}$  calculate accurately the slope of the high-pressure liquid to SLE transition line.

For sample 3, the results presented in Figure 5-4 are also in agreement with the experimental data. However, the prediction of the SLE and SLVE curves and the three-phase point is displaced towards lower temperatures in comparison with the results for samples 1 and 2. This displacement arises more intensely for sample 4, as shown in Figure 5-5. This result indicates that, as the amount of CO<sub>2</sub> in the sample increases, the predictions of the thermodynamic model with a fixed  $k_{CO_2-alkane}$  deteriorates. Nevertheless, the calculated phase diagrams for samples with higher amount of CO<sub>2</sub> (samples 3 and 4, up to 80% of CO<sub>2</sub>) are still in acceptable agreement with experimental data using the Peng-Robinson EoS with van der Waals mixing rules.

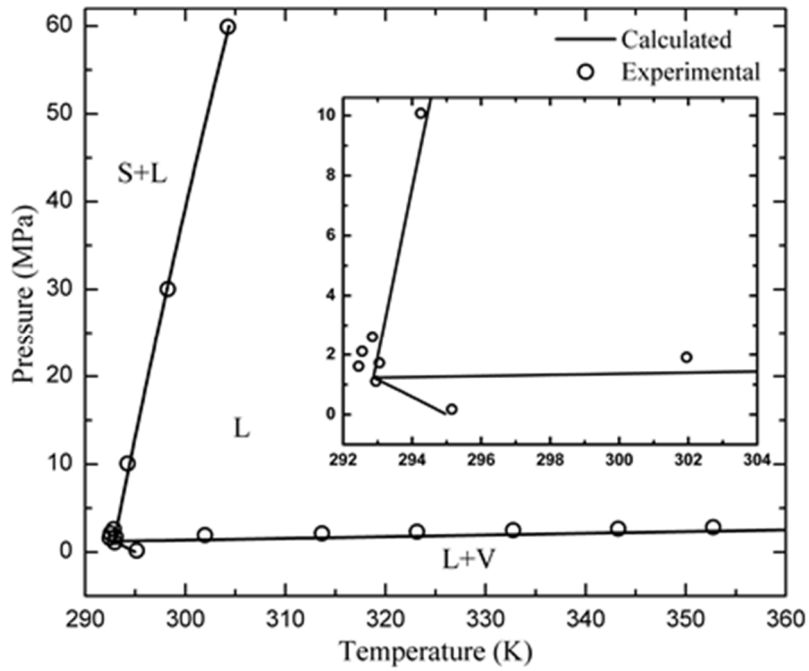


**Figure 5-2.** Experimental and calculated phase equilibrium diagrams (L to VLE, L to SLE and VLE to SLVE transitions) for sample 1 using  $k_{CO_2-alkane} = 0.094$ .

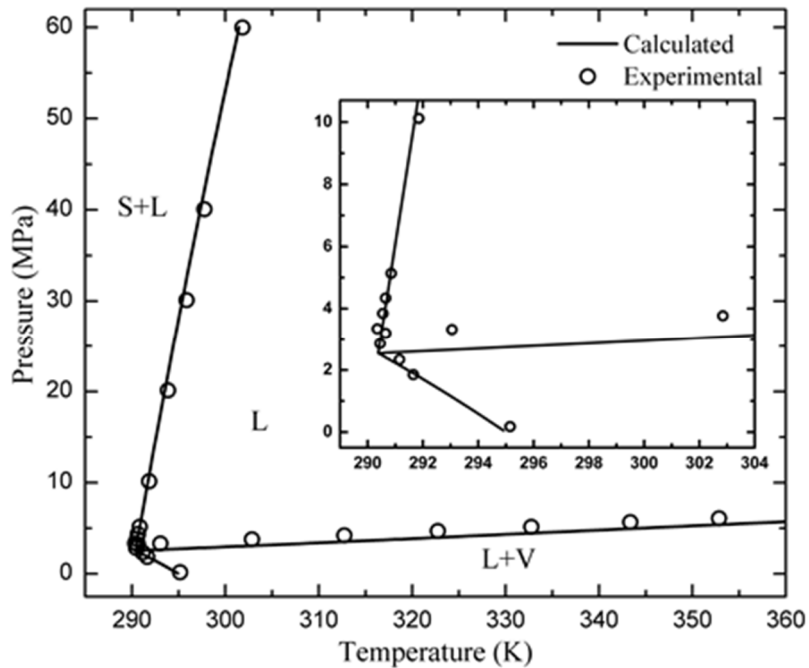


**Figure 5-3.** Experimental and calculated phase equilibrium diagrams (L to VLE, L to SLE and VLE to SLVE transitions) for sample 2 using  $k_{CO_2-alkane} = 0.094$ .

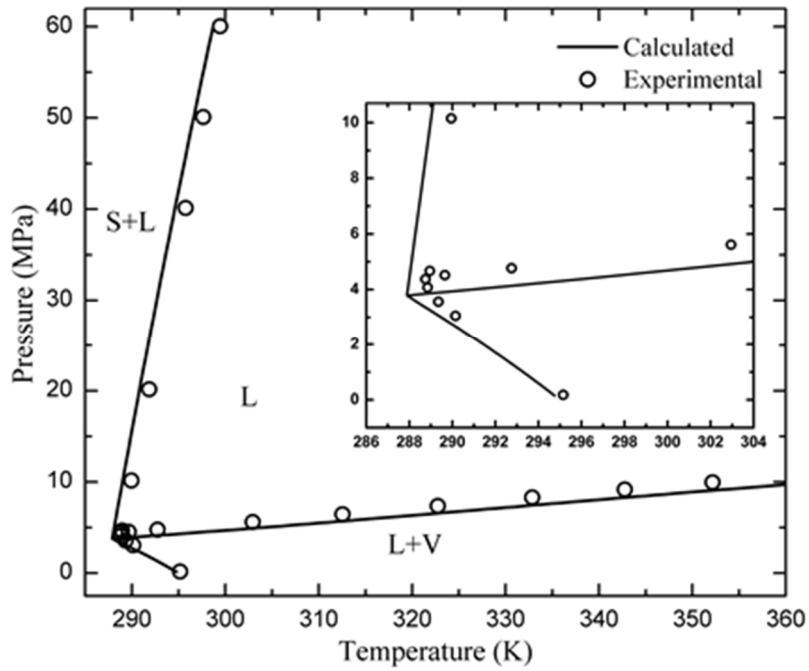


**Figure 5-4.** Experimental and calculated phase equilibrium diagrams (L to VLE, L to SLE and VLE to SLVE transitions) for sample 3 using  $k_{CO_2-alkane} = 0.094$ .

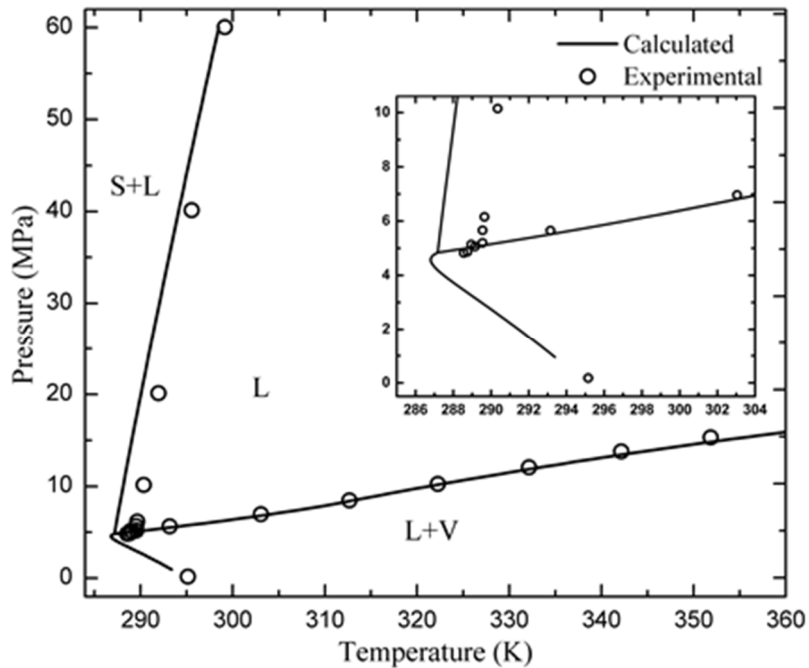


**Figure 5-5.** Experimental and calculated phase equilibrium diagrams (L to VLE, L to SLE and VLE to SLVE transitions) for sample 4 using  $k_{CO_2-alkane} = 0.094$ .

## 5.5. Conclusions

Experimental high pressure (up to 70 MPa) phase equilibrium data for four synthetic samples formed by different amounts of CO<sub>2</sub> and a mixture of the *n*-alkanes C<sub>12</sub>H<sub>26</sub>, C<sub>22</sub>H<sub>46</sub>, C<sub>23</sub>H<sub>48</sub> and C<sub>24</sub>H<sub>50</sub> were measured through an accurate method. For all samples investigated, the measured data presented VLE, SLE and SLVE regions. The phase diagrams were calculated using the Peng-Robinson EoS for the liquid and vapor phases, and the multiple solid solution approach, that employs the modified UNIQUAC equation, to model the solid phase. Also, the Poynting correction term was taken into consideration in the SLE modeling.

The results show that the thermodynamic model represents well the phase envelopes for the samples studied.

The binary interaction parameters from the classical combining rules between CO<sub>2</sub> and *n*-alkanes displayed a CO<sub>2</sub> concentration dependency. Nevertheless, the use of a single value corresponding to the lower value estimated for high CO<sub>2</sub> content allowed for accurate predictions of the phase behavior of all other samples. The results clearly indicate that the PR EoS with classical mixing rule can be used to describe phase equilibria of mixtures up to 80% molar CO<sub>2</sub>. However, the study shows a high sensitivity of the model to the interaction parameter for CO<sub>2</sub>-hydrocarbon binary interactions. An overestimation of this parameter can produce a significant change in the phase envelope. Consequently, the use of such model to live crude oil in presence of CO<sub>2</sub> must be performed with great care, mainly for interpolation of experimental data by tuning  $k_{ij}$  parameters.

## 6

# THERMAL CONDUCTIVITY OF HEAVY EVEN CARBON NUMBER *n*-ALKANES (C22 TO C32)

### 6.1.

#### Introduction

The design, improvement and modeling of different industrial processes are directly linked to the availability of accurate thermophysical properties of different compounds and their mixtures. Among these compounds, linear alkanes play an important role. Efforts towards the design of Phase Change Materials (PCM) solutions for enhancing the energy efficiency of different processes are abundant in the literature (Sharma et al., 2009; Oró et al., 2012; Kenisarin, 2014; Akeiber et al., 2016). *n*-alkanes play a central role in PCM studies as the most investigated material.

Thermophysical properties of *n*-alkanes also play a central role in the modeling of wax deposition in oil production systems (Huang et al., 2015). Intimately related to heat losses through the pipe walls to the environment, wax deposition modeling relies on the thermodynamic simulation of the appearance of solids in the media, as well as on the description of the thermal insulation brought about by the formation of the deposits themselves (Veiga et al., 2017)).

Different groups (Kashiwagi et al., 1982; Mustafa et al., 1982; Menashe and Wakeham, 1982; Nieto de Castro et al., 1983; Calado et al., 1983; Prasad and Venart, 1984; Li et al., 1984; Wada et al., 1985; Assael et al., 1987; Tanaka et al., 1988; Prasad et al., 1989; Friend and Ingham, 1991; Vesovic et al., 1994; Watanabe and Seong, 2002; Perkins et al., 2002; Holmen et al., 2002; Sun et al., 2002; Huber and Perkins, 2005; Assael et al., 2013a; Assael et al., 2013b; Le Neindre et al., 2014; Vassiliou et al., 2015; Vélez et al., 2015a; Vélez et al., 2015b; Le Neindre, 2017; Le Neindre et al., 2018) have measured thermal conductivity of liquid and gas *n*-alkanes from methane to *n*-eicosane at different temperatures and pressures, mostly by the transient hot wire method. On the other hand, experimental results are scarce for heavier *n*-alkanes. Results from *n*-docosane to *n*-tetracosane (C<sub>22</sub>H<sub>46</sub> to C<sub>24</sub>H<sub>50</sub>)

only appear in a handbook organized by Vargaftik et al. (1994) and in the work of Rastorguev et al. (1974). No reported results were found for heavier *n*-alkanes. All of the results for liquid *n*-alkanes clearly exhibited dependence of thermal conductivity on temperature, as well as on molecular mass. Thermal conductivity was shown to increase with the molecular weight of the *n*-alkane and to decrease with temperature.

Experimental results on the thermal conductivity of solid *n*-alkanes are even scarcer in the literature. Forsman and Andersson (1983;1984) reported the thermal conductivity of solid *n*-alkanes with odd carbon numbers from *n*-nonane to *n*-nonadecane ( $C_9H_{20}$  to  $C_{19}H_{40}$ ). They later reported the results for *n*-dodecane ( $C_{12}H_{26}$ ), concluding that the thermal conductivity of the even carbon number *n*-alkane was higher than that of its odd carbon number neighbors, *n*-undecane and *n*-tridecane (Forsman and Andersson, 1986). All measurements were carried out using the transient hot wire method. Griggs and Yarbrough (1978) and Yarbrough and Kuan (1983) published their results on the thermal conductivity of *n*-tetradecane, *n*-pentadecane, *n*-hexadecane, *n*-heptadecane, *n*-octadecane, *n*-nonadecane and *n*-eicosane ( $C_{14}H_{30}$ , to  $C_{20}H_{42}$ ) and used a steady state radial heat-flow apparatus. Irby et al. (1988) measured the thermal conductivity of *n*-octadecane ( $C_{18}H_{38}$ ) through the use of different methods. Holmen et al. (2002) measured the thermal conductivity of *n*-hexadecane to *n*-nonadecane ( $C_{16}H_{34}$ , to  $C_{19}H_{40}$ ) through the use of a steady-state method developed to work at the melting point in the presence of solid and liquid. Solid methane, ethane, propane and *n*-hexane were later investigated using a coaxial-geometry steady state method (Konstantinov et al., 1999; Konstantinov et al., 2006; Konstantinov et al., 2009; Konstantinov et al., 2011). In two different works, Vélez et al. (2015a; 2015b) reported the thermal conductivity of solid *n*-alkanes from *n*-pentadecane to *n*-eicosane ( $C_{15}H_{32}$  to  $C_{20}H_{42}$ ) measured using the transient hot wire method. This last *n*-alkane, *n*-eicosane, was the subject of study of different groups (Stryker and Sparrow, 1990; Fang et al., 2013; Nabil and Khodadadi, 2013). For the solids, results diverge regarding the variation of thermal conductivity with temperature and molecular mass.

To address the lack of experimental results on the thermal conductivity of heavy *n*-alkanes, such thermophysical property was measured in this work for even carbon number *n*-alkanes from *n*-docosane to *n*-dotriacontane ( $C_{22}H_{46}$  to  $C_{32}H_{66}$ ) in

the range from 297.15 to 353.15 K at 0.1 MPa. To assure the purity and determine the solid phase transition boundaries of the different samples during thermal conductivity measurements, the melting point, solid-solid transition temperature and their respective enthalpies were also evaluated.

## 6.2. Experimental

### 6.2.1. Chemicals

All chemicals employed in the measurements were used without any further purification. The information on supplier, as well as on the purity of each *n*-alkane used, can be found in Table 6-1.

**Table 6-1.** Samples analyzed with supplier and purity.

<i>Component</i>	<i>Supplier</i>	<i>Purity(%)</i>	<i>CASRN</i>
<i>n</i> -Dodecane	Sigma-Aldrich	99.99	112-40-3
<i>n</i> -Docosane	Alfa Aesar	>99	629-97-0
<i>n</i> -Tetracosane	Pfaltz & Bauer	>99	646-31-1
<i>n</i> -Hexacosane	Chemos	>99	630-01-3
<i>n</i> -Octacosane	Chemos	>99	630-02-4
<i>n</i> -Triacontane	Sigma-Aldrich	>98	638-68-6
<i>n</i> -Dotriacontane	Sigma-Aldrich	>97	544-85-4

### 6.2.2. Measurements

The melting and solid-solid transition temperatures, as well as the transition enthalpies were measured using an EVO-VII Setaram  $\mu$ DSC. All experiments were performed at a rate of 0.4 K.min<sup>-1</sup> in, at least, triplicates. Samples of around 10 mg were weighted while molten with an uncertainty of 0.01 mg and then added to the sample chamber. All experiments were conducted with temperatures in the range from 293.15 to 353.15 K. The equipment was calibrated using Gallium as a reference, acquired from Fluka as an ultrapure sample (purity of 99.999%). As the melting temperature of the standard presented an uncertainty lower than 0.01 K with a confidence level of 95%, the difference between the measured value and the

value reported by Dirand et al. [48] (0.3 K) was taken as the non-random uncertainty component of the measurement and accounted for in the results [49]. For the transition enthalpies, as the random uncertainty from the standard was similar to that of the samples, the difference between the average value of the melting enthalpy measured for the gallium and that reported in the literature ( $3.0 \times 10^{-3} \text{ J.kg}^{-1}$ ) was taken as the non-random uncertainty component and accounted for in the results (Archer, 2002).

Thermal conductivity measurements were carried out using a C-Therm Technologies TCi Analyzer for all solid and liquid samples (Harris and Levchenko, 2012; Harris et al., 2014). The system is based on a modified transient plane source (MTPS) method (Harris et al., 2014). A photograph of the sensor is presented in Figure 6-1a.

For every temperature in which the thermal conductivity was measured, the system was recalibrated using both a solid and a liquid reference sample. For the liquid reference a water sample was measured and the results compared to the data available in the literature (Ramires et al., 1995). For the solid reference, a standard Pyrex sample, supplied with the equipment was used and its results were also compared to the data available in the literature (Assael et al., 2008). To evaluate the results from these reference materials, at first a non-random uncertainty contribution of 5% was used, as suggested by Harris and collaborators (2014). The non-random component of the expanded uncertainty was evaluated from the results obtained from the reference materials.

The liquid samples were placed in a beaker and the analyzer placed over the glass container allowing the sensor to touch the liquid free surface. In such a configuration, the heat generated by the sensor is transferred to the liquid sample by its top surface, thereby minimizing the disturbances that may arise from natural convection. A simple sketch of this measuring configuration is depicted in Figure 6-1b.

The solid samples were prepared by allowing 30 mL of each *n*-alkane to slowly solidify in a 50 mL beaker. The solid was then removed from the beaker by breaking the glass container. The top and bottom surfaces of the sample were smoothed by heating them to fusion on a petri dish. To improve the thermal contact between the plane source element of the analyzer sensor and the solid samples, 3 droplets of water were placed at the top of the sensor prior to the placement of the

sample. The presence of such a liquid fills the spaces present between the sensor and the sample arising from small imperfections in either surfaces. A 200 g extra weight was placed above the sample to further improve the contact between the sensor and the sample. After all experiments were completed, each solid sample was taken apart and inspected for the presence of any bubbles that might have been trapped in it. None were found. A simple sketch of the measuring configuration used is depicted in Figure 6-1c.

All thermal conductivity measurements were repeated at least ten times for each sample at each tested temperature. The random component of the expanded uncertainty was defined as two standard deviations calculated for each group of measurements. The test temperature was controlled to 0.1 K through the use of a controlled-temperature air bath where the experiments were conducted.

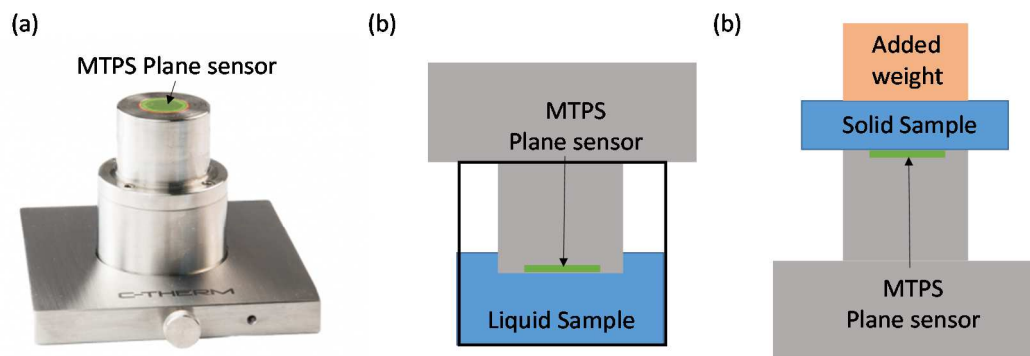


**Figure 6-1.** (a) C-Therm MTPS sensor (<http://ctherm.com>). (b) Measuring configuration used for liquid samples. (c) Measuring configuration used for solid samples.

The expanded uncertainties reported below are associated with a  $k_p=2$  corresponding to a confidence level of 95% were evaluated by combining the random and non-random components for each measurement (BIPM, 2008).

## 6.3. Results and Discussions

### 6.3.1. Results for the DSC measurements

To illustrate the results obtained, a typical DSC run from each *n*-alkane sample analyzed are presented in Figure 6-2. It shows a two-peak profile for all samples analyzed. The peak that appears at a lower temperature level is attributed to a solid-solid transition, from an ordered to a disordered (o-d) solid phase (Dirand et al., 2002). The second peak, the one at a higher temperature level, is attributed to melting (solid-liquid transition). The temperatures at which these transitions occur are defined as the intersection between the baseline and the tangent at the peak inflexion point in the increasing phase. This was calculated with the aid of the AKTS' Calisto software. The enthalpies of each transition were obtained from the integration of each peak associated to its respective transition. The results are summarized in Table 6-2.

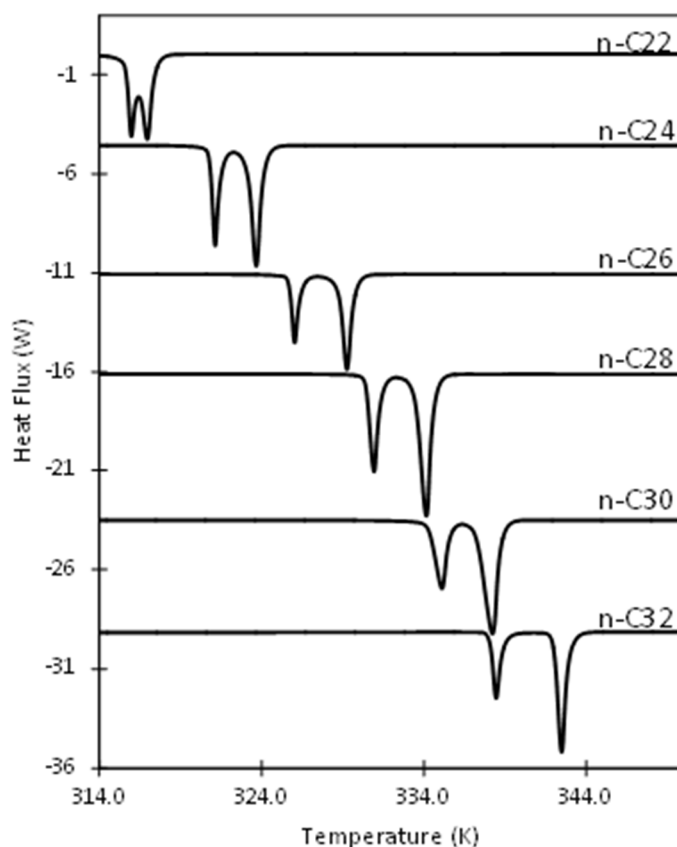


**Figure 6-2.** Results for typical DSC tests for each of the *n*-alkane samples analyzed.

Within the reported uncertainties, all phase transition temperatures and enthalpies are in agreement with the values reported in the literature (Dirand et al., 2002), except for the enthalpy of fusion of the *n*-docosane (*n*-C<sub>22</sub>). As can be seen in Figure 6-2, the thermogram for *n*-docosane did not allow to fully resolve the transition peaks, compromising their direct integration.

**Table 6-2.** Measured solid-solid o-d transition temperatures ( $T_{tr}$ ), solid-liquid melting temperatures ( $T_f$ ), solid-solid o-d transition enthalpy ( $\Delta h_{tr}$ ) and solid-liquid melting enthalpy ( $\Delta h_f$ ).

<i>Component</i>	$T_{tr} (K)^a$	$T_f (K)^a$	$\Delta h_{tr} (10^3 J.kg^{-1})^a$	$\Delta h_f (10^3 J.kg^{-1})^a$
<i>n</i> -C <sub>22</sub>	315.6 ± 0.3	316.6 ± 0.3	93.2 ± 2.8	133.6 ± 4.0
<i>n</i> -C <sub>24</sub>	320.8 ± 0.3	323.1 ± 0.3	91.5 ± 2.9	150.6 ± 5.3
<i>n</i> -C <sub>26</sub>	325.7 ± 0.3	328.8 ± 0.3	84.1 ± 2.5	150.9 ± 4.5
<i>n</i> -C <sub>28</sub>	330.4 ± 0.3	333.4 ± 0.3	88.9 ± 2.7	160.5 ± 4.8
<i>n</i> -C <sub>30</sub>	334.2 ± 0.3	337.1 ± 0.4	89.4 ± 2.7	165.3 ± 5.0
<i>n</i> -C <sub>32</sub>	338.1 ± 0.3	342.0 ± 0.3	86.3 ± 2.6	167.4 ± 5.1

<sup>a</sup>The reported uncertainties are the expended uncertainties (Uc) at 95% confidence level.

### 6.3.2. Thermal conductivity of the reference materials

To evaluate the uncertainties on the thermal conductivity measurements from the C-Therm Technologies TCi Analyzer, especially the non-random component of the uncertainty suggested by the manufacture, two different reference materials were studied prior to the measurements of the samples of interest. The results of the measurements of a deionized water sample are presented in Figure 6-3. The results of the measurements of a sample of Pyrex glass are presented in Figure 6-4. In both figures, the expanded uncertainty displayed was calculated using the non-random component of 5%. Reference data available in the literature are also presented in these figures for comparison with the value measured in this work.

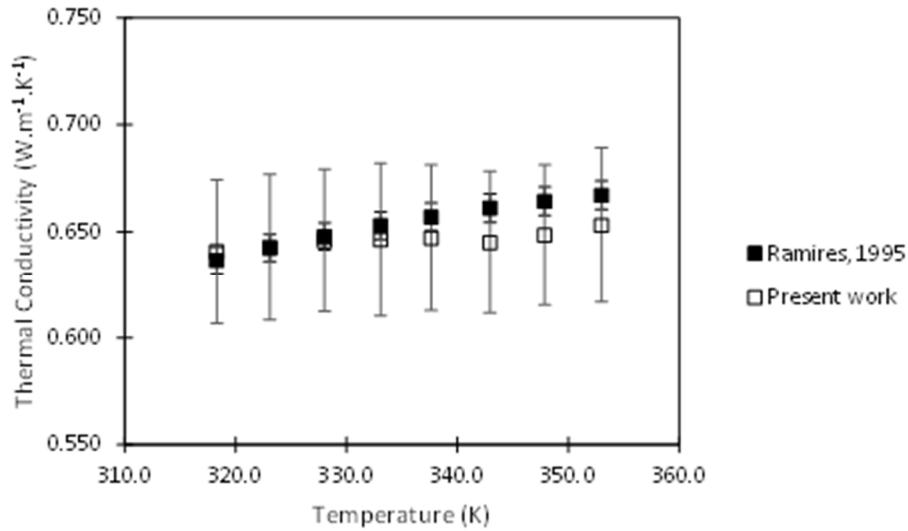


**Figure 6-3.** Measured thermal conductivity of water compared to the values reported by Ramires et al. (1995).

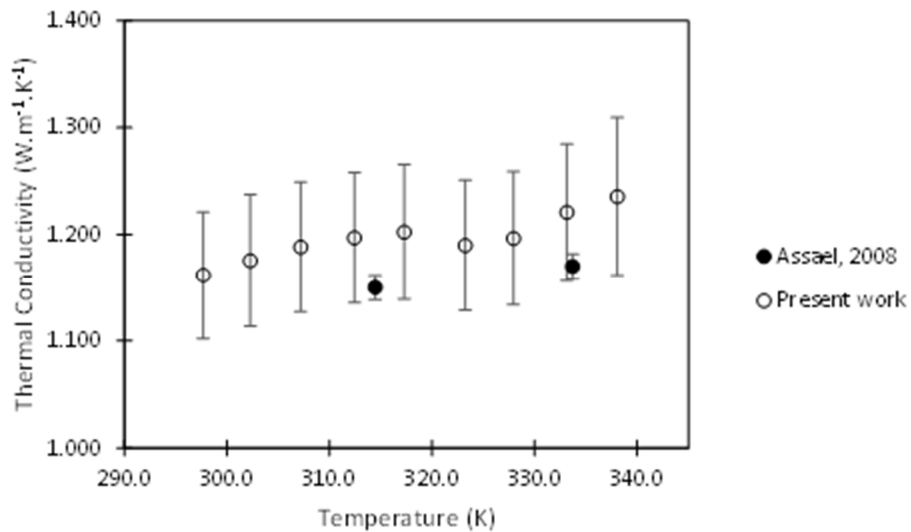


**Figure 6-4.** Measured thermal conductivity of pyrex compared to the values reported by Assael et al. (2008).

A thorough analysis of the results obtained for the reference materials leads to the conclusion that the non-random component of 5% at first suggested was too high, as the random component for each point with  $k_p=2$  was no larger than 2%. So, the measurements carried out for water and pyrex glass were used to establish the non-random uncertainty of the measurements of the liquids and solids samples of interest, respectively, following the published work of the manufactures (Harris et al., 2014). To this end, the largest difference between the reference values

measured and the values from the literature was used as the non-random uncertainty component to calculate the expanded uncertainties of the samples of interest.

### 6.3.3. Thermal conductivity of the liquid samples

The presentation of the thermal conductivity results starts with the measured results for *n*-dodecane shown in Table 6-3. In this table, for each temperature, the value of the thermal conductivity is reported followed by the estimated level of absolute and relative uncertainties associated with the experiments. These uncertainties are reported with a 95% confidence level. Kashiwagi et al. (1982), Tanaka et al. (1988) and Vargaftik et al. (1994) measured the thermal conductivity of *n*-dodecane. Their results are presented in Figure 6-5, together with the results from the present study. As can be observed, there is good agreement between the data of the present work and those from the more recent study of Vargaftik et al. (1994). The data of Tanaka et al. (1988) are lower, although originated from the same group as Kashiwagi et al. (1982).

The measured results for *n*-docosane and *n*-tetracosane are presented, respectively, in Tables 6-4 and 6-5. Rastorguev et al. (1974) and Vargaftik et al. (1994) have reported results for the thermal conductivity of *n*-docosane and *n*-tetradecane. The results from these references are presented together with the results from the present study in Figures 6-6 and 6-7. The measurements obtained in the present study compare well with the results from the literature, considering the levels of uncertainties associated with the experiments and represented as the error bars in the figures.

**Table 6-3.** Measured thermal conductivity of liquid *n*-dodecane (*n*-C12).

<i>Temperature (K)</i>	$\lambda$ ( $W.m^{-1}.K^{-1}$ )	$Uc(\lambda)$ ( $W.m^{-1}.K^{-1}$ )	$Uc(\lambda)$ (%)
318.2	0.135	0.003	2.5
323.2	0.134	0.004	2.7
328.1	0.133	0.004	2.7
333.1	0.131	0.004	2.7
337.7	0.130	0.004	2.9
343.2	0.128	0.004	2.7
347.9	0.127	0.003	2.7
352.8	0.127	0.004	2.9

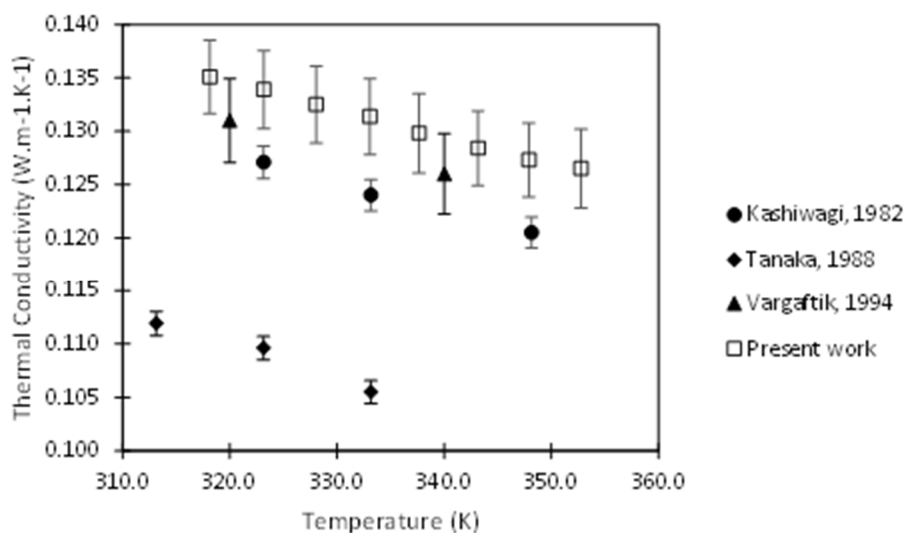


**Figure 6-5.** Measured thermal conductivity of *n*-dodecane (*n*-C12) compared to the values reported in the literature (Kashiwagi et al., 1982; Tanaka et al., 1988; Vargaftik et al., 1994).

**Table 6-4.** Measured thermal conductivity of liquid *n*-docosane (*n*-C22).

Temperature (K)	$\lambda$ (W.m <sup>-1</sup> .K <sup>-1</sup> )	$Uc(\lambda)$ (W.m <sup>-1</sup> .K <sup>-1</sup> )	$Uc(\lambda)$ (%)
318.1	0.151	0.004	2.7
323.0	0.150	0.004	2.6
328.1	0.148	0.004	2.6
333.0	0.146	0.004	2.6
337.7	0.145	0.004	2.8
343.0	0.144	0.004	2.8
347.9	0.143	0.004	2.6
353.0	0.142	0.004	2.7

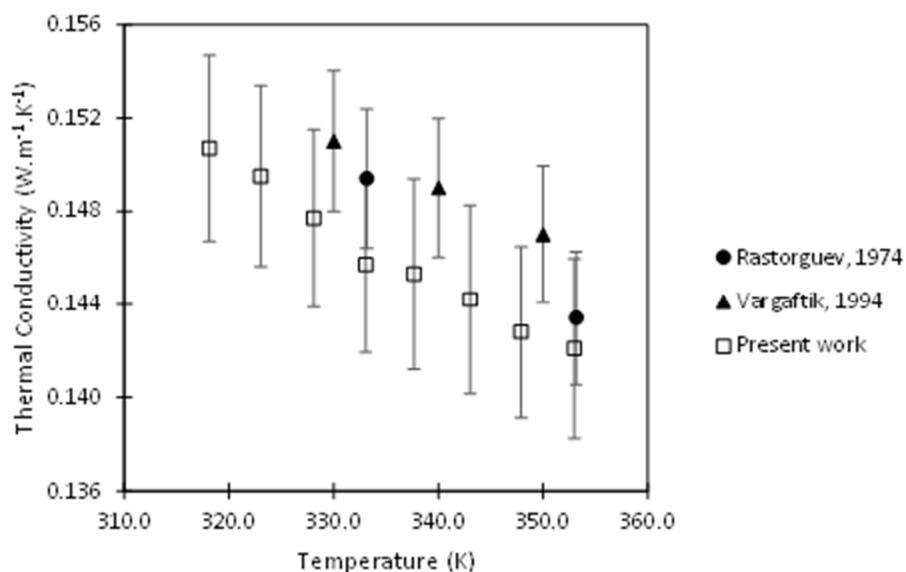


**Figure 6-6.** Measured thermal conductivity of liquid *n*-docosane (*n*-C22) compared to the values reported by Rastorguev et al. (1974) and Vargaftik et al. (1994).

**Table 6-5.** Measured thermal conductivity of liquid *n*-tetracosane (*n*-C24).

Temperature (K)	$\lambda$ (W.m <sup>-1</sup> .K <sup>-1</sup> )	$U_c(\lambda)$ (W.m <sup>-1</sup> .K <sup>-1</sup> )	$U_c(\lambda)$ (%)
323.1	0.152	0.004	2.7
328.0	0.151	0.004	2.8
333.0	0.149	0.004	2.6
337.6	0.148	0.004	2.6
343.1	0.146	0.004	2.6
348.0	0.146	0.004	2.9
353.0	0.145	0.005	3.1

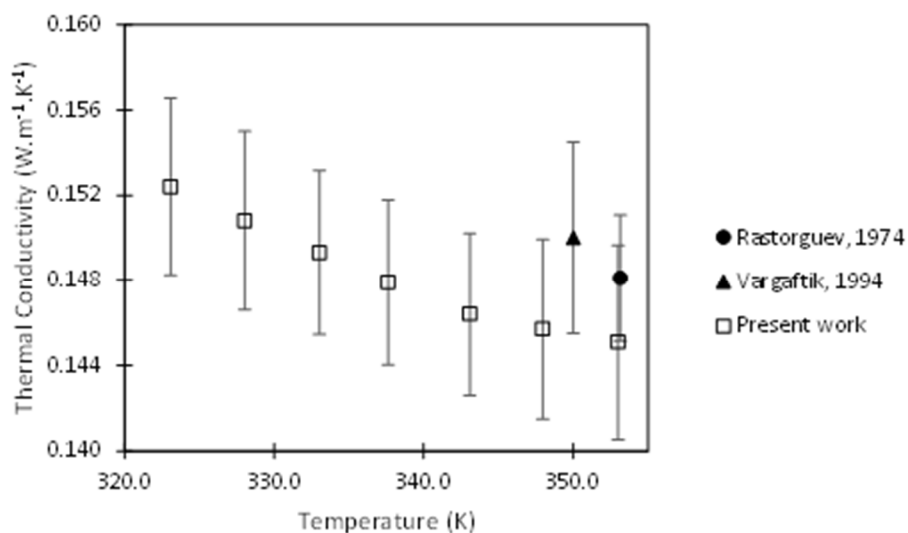
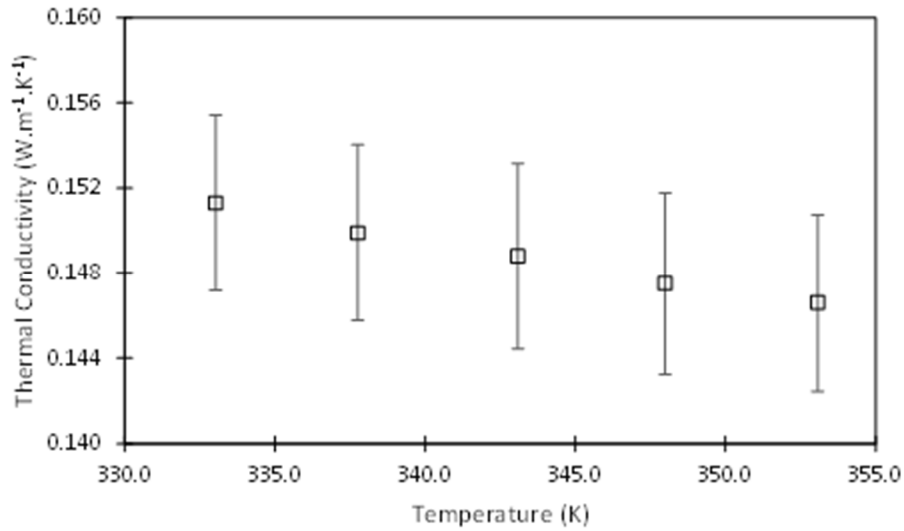


**Figure 6-7.** Measured thermal conductivity of liquid *n*-tetracosane (*n*-C24) compared to the values reported by Rastorguev et al. (1974) and Vargaftik et al. (1994).

For the other samples, namely, *n*-hexacosane (*n*-C26), *n*-octacosane (*n*-C28), *n*-triacontane (*n*-C30) and *n*-dotriacontane (*n*-C32), there are no available thermal conductivity data in the literature. Therefore, the data presented next are, to the best of our knowledge, the first data presented in the literature. The measurements from the present work for these component samples are presented in Tables 6-6 to 6-9 and in Figures 6-8 to 6-11.

**Table 6-6.** Measured thermal conductivity of liquid *n*-hexacosane (*n*-C26).

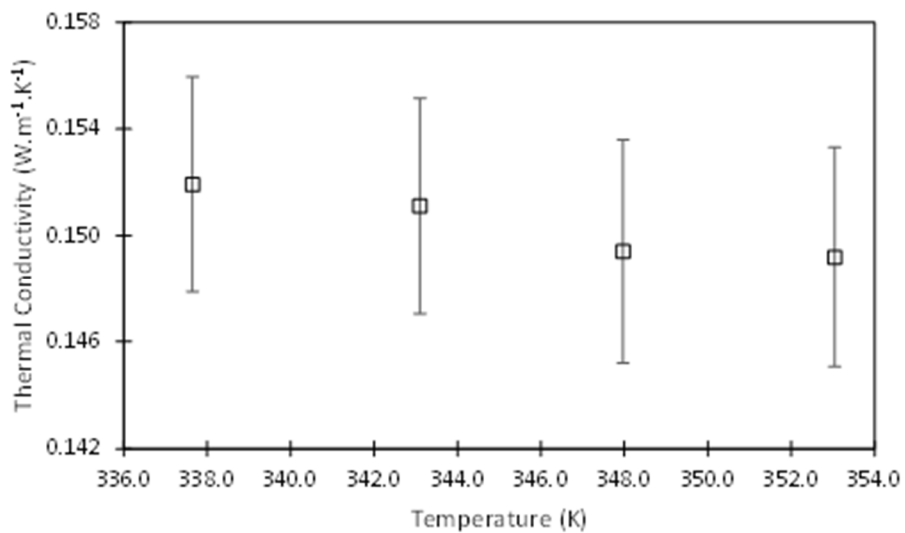
Temperature (K)	$\lambda$ (W.m <sup>-1</sup> .K <sup>-1</sup> )	$U_c(\lambda)$ (W.m <sup>-1</sup> .K <sup>-1</sup> )	$U_c(\lambda)$ (%)
333.0	0.151	0.004	2.7
337.8	0.150	0.004	2.8
343.1	0.149	0.004	2.9
348.0	0.148	0.004	2.9
353.1	0.147	0.004	2.8



**Figure 6-8.** Measured thermal conductivity of liquid *n*-hexacosane (*n*-C26).

**Table 6-7.** Measured thermal conductivity of liquid *n*-octacosane (*n*-C28).

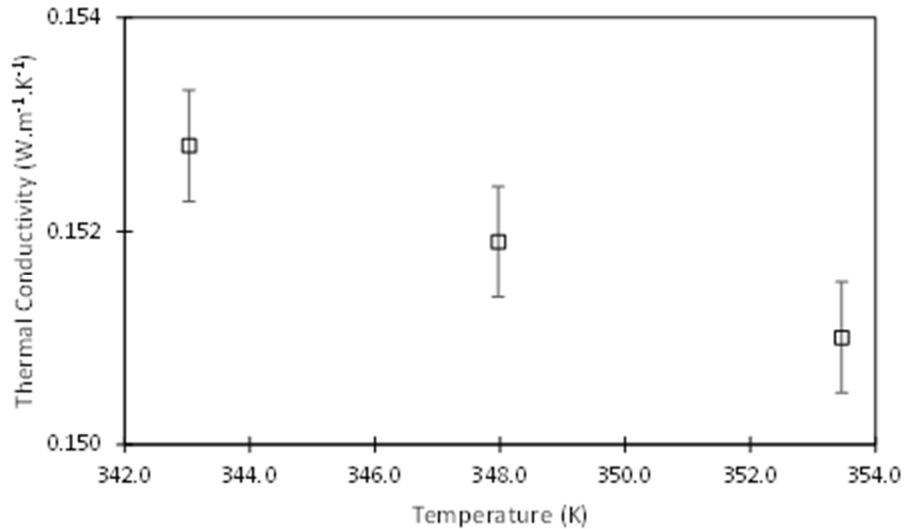
Temperature (K)	$\lambda$ (W.m <sup>-1</sup> .K <sup>-1</sup> )	$Uc(\lambda)$ (W.m <sup>-1</sup> .K <sup>-1</sup> )	$Uc(\lambda)$ (%)
337.7	0.152	0.004	2.7
343.1	0.151	0.004	2.7
348.0	0.149	0.004	2.8
353.0	0.149	0.004	2.8



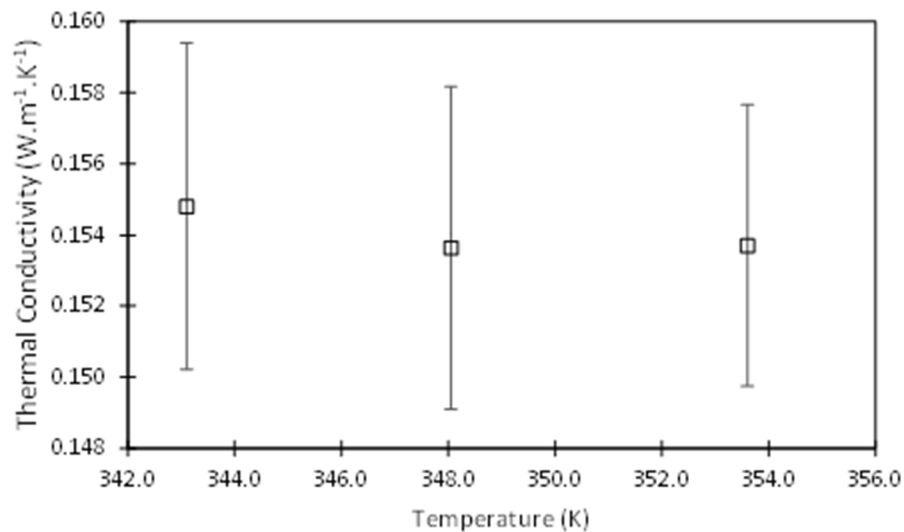
**Figure 6-9.** Measured thermal conductivity of liquid *n*-octacosane (*n*-C28).

**Table 6-8.** Measured thermal conductivity of liquid *n*-triacontane (*n*-C30).

Temperature (K)	$\lambda$ ( $W.m^{-1}.K^{-1}$ )	$Uc(\lambda)$ ( $W.m^{-1}.K^{-1}$ )	$Uc(\lambda)$ (%)
343.1	0.153	0.004	2.8
348.0	0.152	0.004	2.6
353.5	0.151	0.004	2.7

**Figure 6-10.** Measured thermal conductivity of liquid *n*-triacontane (*n*-C30).**Table 6-9.** Measured thermal conductivity of liquid *n*-dotriacontane (*n*-C32).

Temperature (K)	$\lambda$ ( $W.m^{-1}.K^{-1}$ )	$Uc(\lambda)$ ( $W.m^{-1}.K^{-1}$ )	$Uc(\lambda)$ (%)
343.0	0.153	0.005	3.0
348.0	0.152	0.005	3.0
353.1	0.149	0.004	2.6

**Figure 6-11.** Measured thermal conductivity of liquid *n*-dotriacontane (*n*-C32).

A general observation of the data presented indicates a trend of decreasing thermal conductivity with increasing temperature also observed for other *n*-alkanes in the literature. This trend becomes easier to be observed in Figure 6-12 where the data from Figures 6-8 to 6-11 are presented together. Additionally, the results of Figure 6-12 also show a trend already described in the literature of increasing thermal conductivity with increasing molecular mass of the samples (Kashiwagi et al., 1982; Tanaka et al., 1988). Indeed, the results of Figure 6-13 show that, for a fixed temperature, the thermal conductivity of the liquid *n*-alkane samples increases nearly linearly with the sample molecular mass.

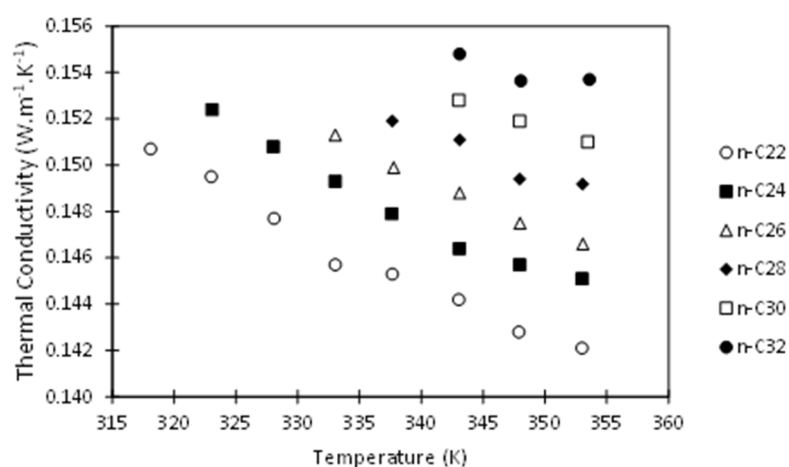


**Figure 6-12.** Measured thermal conductivity of liquid *n*-docosane, *n*-tetracosane, *n*-hexacosane, *n*-octacosane, *n*-triacontane and *n*-dotriacontane as a function of temperature.

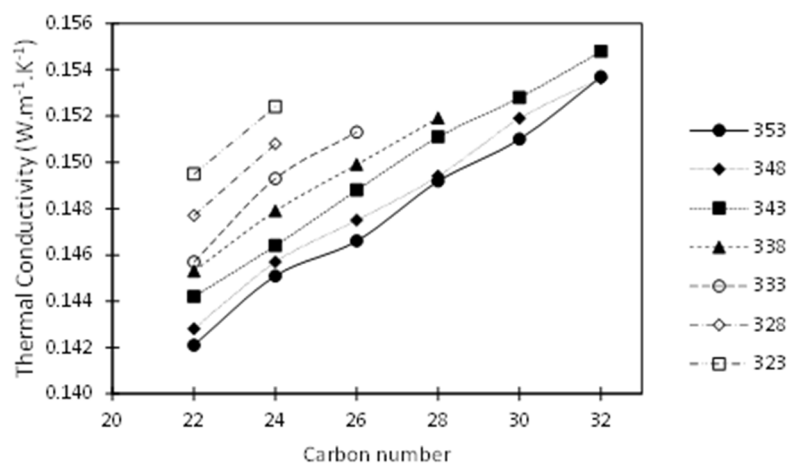


**Figure 6-13.** Measured thermal conductivity of liquid *n*-alkane samples for fixed temperature as a function of carbon number.

### 6.3.4. Thermal conductivity of the solid samples

A literature search conducted did not reveal any data on the thermal conductivity of the solid *n*-alkanes heavier than *n*-eicosane. The results from the present study for these heavier solid *n*-alkane samples are presented in Tables 6-10 to 6-15.

**Table 6-10.** Measured thermal conductivity of solid *n*-docosane (*n*-C22).

Temperature (K)	$\lambda$ (W.m <sup>-1</sup> .K <sup>-1</sup> )	$U_c(\lambda)$ (W.m <sup>-1</sup> .K <sup>-1</sup> )	$U_c(\lambda)$ (%)
297.6	0.624	0.028	4.5
302.4	0.668	0.029	4.3
307.9	0.637	0.030	4.6
Mean value	0.643	-	-

**Table 6-11.** Measured thermal conductivity of solid *n*-tetracosane (*n*-C24).

Temperature (K)	$\lambda$ (W.m <sup>-1</sup> .K <sup>-1</sup> )	$U_c(\lambda)$ (W.m <sup>-1</sup> .K <sup>-1</sup> )	$U_c(\lambda)$ (%)
297.6	0.594	0.025	4.3
302.3	0.545	0.024	4.4
307.7	0.545	0.024	4.4
312.9	0.603	0.026	4.3
Mean value	0.572	-	-

**Table 6-12.** Measured thermal conductivity of solid *n*-hexacosane (*n*-C26).

Temperature (K)	$\lambda$ (W.m <sup>-1</sup> .K <sup>-1</sup> )	$U_c(\lambda)$ (W.m <sup>-1</sup> .K <sup>-1</sup> )	$U_c(\lambda)$ (%)
297.6	0.499	0.022	4.4
302.4	0.524	0.022	4.2
307.8	0.484	0.023	4.7
312.7	0.513	0.023	4.4
318.5	0.574	0.026	4.6
Mean value	0.519	-	-

**Table 6-13.** Measured thermal conductivity of solid *n*-octacosane (*n*-C28).

Temperature (K)	$\lambda$ (W.m <sup>-1</sup> .K <sup>-1</sup> )	$U_c(\lambda)$ (W.m <sup>-1</sup> .K <sup>-1</sup> )	$U_c(\lambda)$ (%)
297.7	0.514	0.022	4.3
302.4	0.489	0.022	4.5
308.0	0.471	0.020	4.3
312.7	0.469	0.020	4.3
318.6	0.473	0.023	5.0
323.4	0.505	0.024	4.7
Mean value	0.487	-	-

**Table 6-14.** Measured thermal conductivity of solid *n*-triacontane (*n*-C30).

<i>Temperature (K)</i>	$\lambda$ ( $W.m^{-1}.K^{-1}$ )	$Uc(\lambda)$ ( $W.m^{-1}.K^{-1}$ )	$Uc(\lambda)$ (%)
297.7	0.616	0.027	4.4
302.3	0.603	0.025	4.2
307.8	0.556	0.024	4.4
312.6	0.612	0.027	4.4
318.5	0.559	0.025	4.5
323.3	0.514	0.025	4.8
328.0	0.536	0.025	4.6
Mean value	0.571	-	-

**Table 6-15.** Measured thermal conductivity of solid *n*-dotriacontane (*n*-C32).

<i>Temperature (K)</i>	$\lambda$ ( $W.m^{-1}.K^{-1}$ )	$Uc(\lambda)$ ( $W.m^{-1}.K^{-1}$ )	$Uc(\lambda)$ (%)
297.7	0.574	0.024	4.3
302.3	0.574	0.026	4.5
307.5	0.585	0.026	4.5
312.8	0.607	0.027	4.5
318.0	0.585	0.027	4.6
323.1	0.561	0.025	4.5
328.0	0.588	0.026	4.4
332.6	0.621	0.028	4.4
Mean value	0.587	-	-

All measurements of the thermal conductivity of the solid samples were performed at temperatures lower than the first phase transition displayed by the sample in order to avoid any interference from this phenomenon in the results. Whenever the measurements were performed at temperatures near the solid-solid transition temperature, the thermal conductivity values were observed to rise, together with the random uncertainty component levels. This rise in thermal conductivity was an expected result, since part of the heat supplied by the probe was absorbed by the sample as latent solid-solid phase transition heat, and misinterpreted in the transient analysis as a higher thermal conductivity value. Nevertheless, these samples may exhibit different solid phases that are not always measurable in the heating curves of regular DSC's (Stryker and Sparrow, 1990; Wang et al., 2003). The fact that the thermal conductivity of the solids did not vary with the temperature beyond the uncertainties, can be interpreted as an evidence that all samples were indeed at the same solid phase during all measurements. As

such, the mean value and its standard uncertainty at 95% confidence level are reported at the bottom of each table.

As mentioned, the thermal conductivity of the solid samples does not vary significantly with the temperature, considering the uncertainty levels of the experiments. When the mean value is plotted against the molecular weight of the sample, a trend different from the one observed for the liquid samples is revealed. While for the liquid samples a monotonic increase of the thermal conductivity with the molecular weight was observed in Figure 6-12, for the solids, no such behavior was observed. In fact, the data presented in Figure 6-14 displays a minimum thermal conductivity value for the *n*-octasane sample. The lightest sample analyzed, *n*-docosane, displayed the highest thermal conductivity and seems to decrease towards *n*-octacosane, where it starts to rise again towards the *n*-dotriacontane. The physical reasoning behind this observed trend needs further investigation.

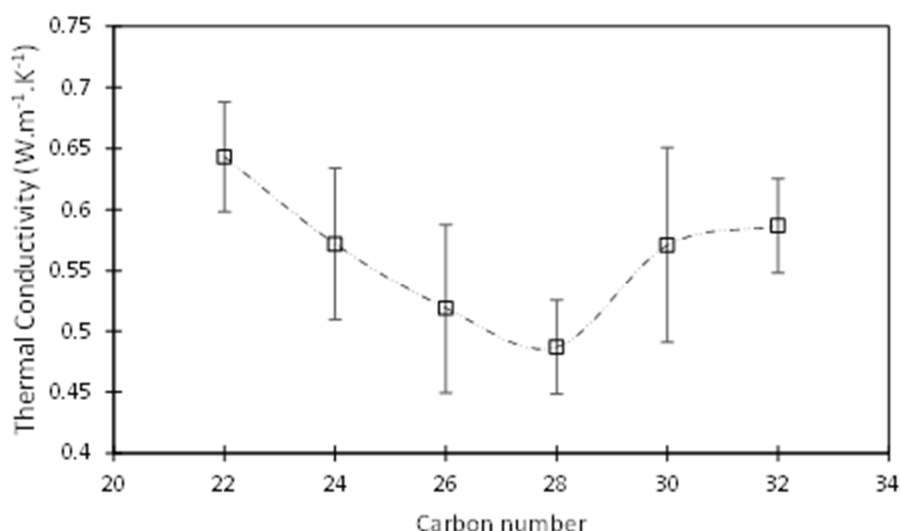


**Figure 6-14.** Mean value of the thermal conductivity of each solid *n*-alkane samples investigated as a function of carbon number.

#### 6.4. Conclusions

Although indispensable in the design, model and maintenance of many processes, thermal conductivity of high molecular weights *n*-alkanes are not available in the literature. To address such an issue, thermal conductivities of samples of *n*-dodecane, *n*-docosane, *n*-tetracosane, *n*-hexacosane, *n*-octacosane, *n*-triacontane and *n*-dotriacontane were measured. The phase transition temperatures

and their respective enthalpies were also measured using a DSC to characterize the samples under analysis.

All the measured results compared well with values available in the literature within the declared uncertainties levels, except for the heat of transition of *n*-docosane. This is most likely caused by the low resolution between the solid-solid phase transition and the melting peaks obtained in the thermograms for this sample. Nevertheless, the phase transition temperatures matched the expected values and all samples were used without any further purification.

The thermal conductivity of the samples, both solid and liquid, were analyzed using the C-Therm Technologies TCi Analyzer in a temperature range from 297.15 to 353.15 K at 0.1 MPa.

The results for the liquid samples displayed well-defined trends between thermal conductivity and temperature, as well as thermal conductivity and molecular mass of the sample. The results for *n*-dodecane, *n*-docosane and *n*-tetracosane, for which results were available in the literature, agreed well with these published results, within the prevailing uncertainty levels. The results for *n*-hexacosane, *n*-octacosane, *n*-triacontane and *n*-dotriacontane are not available in the literature, being an original contribution of the present work.

The results for the solid samples, on the other hand, displayed a higher scatter with temperature. Such scatter is accommodated within experimental uncertainties and did not indicate a variation of the thermal conductivity with temperature, for the range investigated.

For all solid *n*-alkane samples, a rise in thermal conductivity was apparent near the solid-solid phase transition temperature, posing as evidence that all samples were at the most stable solid phase during all measurements. The thermal conductivity of solid *n*-alkanes heavier than *n*-eicosane were not available in the literature and are presented here for the first time.

# 7

## WAX DEPOSITION MODELLING

### 7.1. Introduction

During oil production, fluids flow from the reservoir to processing units through a complex system of different equipment like pipes and valves. Siting originally at equilibrium in reservoir conditions, as the fluid flows through the production system it experiences important variations in both temperature and pressure. The expertise to assure the continuous flow are gathered in a discipline named Flow Assurance. Coined by Petrobras in the 1990's, a big part of flow assurance is petroleum chemistry, more specifically the thermodynamic behavior of the fluid when passing through different temperatures and pressures.

One of the central problems in flow assurance is the appearance of solids as the fluid is cooled during production. These solids, waxes, are mainly composed of heavy paraffin and have been the subject of many studies over the years (Burger et al., 1981; Huang et al., 2015). Despite the different methods and technologies developed to cope with such an issue, the most efficient way to avoid it is through a robust design of the production system. Such a robust design is inevitably dependent on the availability of precise models able to predict wax deposition in flow simulations.

The development of deposition models is the subject of study of different research groups (Burger et al., 1981; Merino-Garcia et al., 2007, Huang et al., 2011, Zheng et al., 2017). The development of such models resides on a physical description of the wax deposition phenomenon. Simple models, strongly based on empirical correlations, are commercially available in packages like Olga and PVTsim.

The physical mechanism responsible for the deposition of paraffin over the pipe's wall is still under debate. Many different mechanisms have been proposed and argued for and against (Azevedo and Teixeira, 2003). So far, the molecular diffusion mechanism has been the most used and lie at the heart of all commercially

available as well as at most of the academic simulators. One major drawback of all available models is that they are built around the molecular diffusion mechanism and accurate results depend on the tuning of different parameters. These parameters can be physical properties of the fluids components or some phenomena associated with these components like crystallization kinetics.

Recently, experimental results of wax deposition in a rig that allows visual inspection of the phenomena under flow conditions have become available (Veiga, 2017). With such rich results, deposition models should take a step further and try to match all of the measured events that accompany wax deposition. Simulators should encompass explicitly the thermodynamics of wax phase equilibria as well as the transport of wax solids over the entire domain. Such endeavor may help to shed light over the complex mechanism responsible for wax deposition.

Banki et al. (2008) made such an attempt by proposing a model in which phase equilibria is explicitly calculated together with the CFD simulation. Nevertheless, the model proposed by Banki et al. (2008) does not encompass the advection of solids. They assume that the solid phase velocity is always zero and once precipitated they rest still in the domain. This approximation is too extreme as there is no physical justification for a particle not to be transported by the moving fluid in the absence of an external force to hold it in place. As such, there is no physical meaning of the deposition itself, as the deposit appearance is a direct result of the frozen particles. A similar model was proposed and analyzed by Souza (2014)

Distant from the molecular diffusion mechanism, it has been proposed in the literature that gelation is actually responsible for the formation of wax deposits (Singh et al., 1999; Merino-Garcia et al., 2007). This mechanism resides on the fact that solid suspensions formed once paraffin precipitate out of solution increase the fluid's viscosity and leads to a solid-like gel. As viscosity increases drastically as the solid content rises, the shear stress imposed by the flow would no longer be capable of deforming such a viscous material. As a result, this process leads to the formation of the deposit. In this mechanism, deposition is a direct consequence of the increase in the viscosity of the mixture, which is itself a thermodynamic property of the composition, temperature and pressure of the system. As such, this mechanism can be investigated using a CFD model that explicitly accounts for the solid advection and the thermodynamic equilibrium of paraffin.

In the present work, a model that relaxes the restriction of zero velocity imposed in the model proposed by Banki et al. (2008) is proposed. A fluid-solid mixture model (Ishii and Hibiki, 2011) is formulated and used to test different thermodynamic models for solid wax and to investigate in more detail the rheological mechanism of wax deposition. The model is compared to the experimental results of Veiga (2017).

## 7.2. Mathematical Model

To determine the velocity field and predict the wax deposition, the flow is modelled as a liquid/solid mixture. The model can be obtained by combining the conservation equations for each phase, as shown in the following sections.

In principle, the liquid and solid phase can move with different velocities, and the relation between the phase velocities must be modeled or empirically defined.

Before presenting the conservation equations, it is convenient to introduce a few definitions of physical properties of the mixture.

### 7.2.1. Basic definitions

To help presenting the mixture model, a few definitions of the mixture physical properties are introduced. Those are: total mass of the mixture ( $M_T$ ), total volume of the mixture ( $\forall$ ), density of the each phase  $k$  ( $\rho_k$ ), where the subscript  $k$  corresponds to either liquid  $l$  or solid  $s$  phases and mass fraction of component “ $i$ ” in the mixture ( $c_i$ ).

$$M_t = m_l + m_s \quad (7-1)$$

$$\forall = \forall_l + \forall_s \quad (7-2)$$

$$\rho_l = \frac{m_l}{\forall_l} \quad ; \quad \rho_s = \frac{m_s}{\forall_s} \quad (7-3)$$

$$c_i = \frac{m_i}{M_t} \quad ; \quad c_{i,l} = \frac{m_{i,l}}{m_l} \quad ; \quad c_{i,s} = \frac{m_{i,s}}{m_s} \quad (7-4)$$

where  $m_k$  and  $\forall_k$  are the mass and volume of each phase  $k$ , respectively;  $m_{i,k}$  is the mass fraction of component  $i$  in phase  $k$  and  $M_t$  is the total mass of the system.

The mass fraction of the components as well as the mass of each phase must obey the following restrictions

$$\sum_{i=1}^N c_i = \sum_{i=1}^N c_{i,l} = \sum_{i=1}^N c_{i,s} = 1 \quad (7-5)$$

$$\sum_{i=1}^N c_i M_t = \sum_{i=1}^N (c_{i,l} m_l + c_{i,s} m_s) = M_t \quad (7-6)$$

From these previous definitions, the mass fraction of phase  $k$  ( $B_k$ ), which is a direct result of the thermodynamic model (Chapter 3), can be defined.

$$B_l = \frac{m_l}{M_t} \quad ; \quad B_s = \frac{m_s}{M_t} \quad (7-7)$$

Further, the volume fraction of each phase  $k$  ( $S_k$ ) as well as the mixture density  $\rho_m$  are

$$S_l = \frac{v_l}{v} = B_l \frac{\rho_m}{\rho_l} = \frac{\frac{B_l}{\rho_l}}{\frac{B_l}{\rho_l} + \frac{B_s}{\rho_s}} \quad ; \quad S_s = \frac{v_s}{v} = B_s \frac{\rho_m}{\rho_s} = \frac{\frac{B_s}{\rho_s}}{\frac{B_l}{\rho_l} + \frac{B_s}{\rho_s}} \quad (7-8)$$

$$\rho_m = \frac{M_t}{v} = \frac{m_l + m_s}{v_l + v_s} = \left( \frac{B_l}{\rho_l} + \frac{B_s}{\rho_s} \right)^{-1} = S_l \rho_l + S_s \rho_s \quad (7-9)$$

These variables are calculated using the thermodynamic model and are a function of  $T$ ,  $p$  and the global composition of the mixture  $c_i$ .

The molar fraction of component  $i$  can be converted to the mass fraction through the following relation:

$$S_l \rho_{l,i} = c_{i,l} S_l \rho_l = x_{i,l} \left( \frac{MM_i}{MM_l} \right) S_l \rho_l \quad (7-10)$$

where  $MM_i$  and  $MM_l$  are respectively the molar mass of component  $i$  and the molar mass of the liquid phase.

### 7.2.2. Continuity equation

For the liquid and solid phases, the continuity equations may be written as:

$$\frac{\partial}{\partial t} (S_l \rho_l) + \nabla \cdot (S_l \rho_l \mathbf{u}_l) = \varphi - \nabla \cdot J_l \quad (7-11)$$

$$\frac{\partial}{\partial t} (S_s \rho_s) + \nabla \cdot (S_s \rho_s \mathbf{u}_s) = -\varphi - \nabla \cdot J_s \quad (7-12)$$

where  $\varphi$  represents the mass transferred between the two phases originating from melting or crystallization and  $\nabla \cdot J_k$  represents the diffusion flux of phase  $k$ . The liquid phase is considered continuum and only its species diffusion are considered. The liquid diffusion in the solid and vice-versa are neglected.

Since there is at most only two phases present, all mass leaving one phase is equal to the mass entering the other phase, i.e., the amount  $\varphi$  is exactly symmetric. The continuity equation for the mixture results from the sum of Equations 7-11 and 7-12 and may then be written as:

$$\frac{\partial}{\partial t} (S_l \rho_l + S_s \rho_s) + \nabla \cdot (S_l \rho_l \mathbf{u}_l + S_s \rho_s \mathbf{u}_s) = 0 \quad (7-13)$$

The mixture velocity ( $\mathbf{u}_m$ ) is defined considering the total mass flux of the mixture

$$\mathbf{u}_m = \frac{S_l \rho_l \mathbf{u}_l + S_s \rho_s \mathbf{u}_s}{\rho_m} \quad (7-14)$$

With the mean definition of density and velocity, the mixture mass conservation equation can be rewritten as

$$\frac{\partial}{\partial t} (\rho_m) + \nabla \cdot (\rho_m \mathbf{u}_m) = 0 \quad (7-15)$$

### 7.2.3. Continuity equations for the species

Each phase and the mixture are composed by  $n$  species, therefore, the continuity equation for each species  $i$  is required

$$\frac{\partial}{\partial t} (c_{i,l} S_l \rho_l + c_{i,s} S_s \rho_s) + \nabla \cdot (c_{i,l} S_l \rho_l \mathbf{v}_{i,l} + c_{i,s} S_s \rho_s \mathbf{v}_{i,s}) = 0 \quad (7-16)$$

The velocity  $\mathbf{v}_{i,k}$  that appears in the convection term is the result of the combination of the purely convective velocity  $\mathbf{u}_k$  and the diffusion velocity of each species in each of the phases  $\bar{\mathbf{v}}_{i,k}$ :

$$\mathbf{v}_{i,l} = \mathbf{u}_l + \bar{\mathbf{v}}_{i,l} \quad ; \quad \mathbf{v}_{i,s} = \mathbf{u}_s + \bar{\mathbf{v}}_{i,s} \quad (7-17)$$

In the model proposed here, the solid diffusion may lead to two different interpretations. If one assumes the solid to be continuous across the domain, then

the diffusion of the species in the solid phase is to be modeled as the relative movement of each species in the solid matrix due to a gradient of its chemical potential. This diffusion has a characteristic time which is orders of magnitude longer than the process being modeled and thus can be neglect. One may also assume the solid to be distributed in particles and thus dispersed in the domain. The diffusion then will have to account the species balance due to the diffusive transport of the particles themselves. A model to describe such dispersion falls beyond the scope of the proposed model and will be neglect for the time being. In this manner, the diffusion velocities for all species in the solid phase will be assumed zero ( $\bar{\mathbf{v}}_{i,s} = 0$ ).

Rewriting the species continuity equations considering the diffusion velocity of the species in the liquid phase explicit, one comes to:

$$\frac{\partial}{\partial t} (c_{i,l}S_l\rho_l + c_{i,s}S_s\rho_s) + \nabla \cdot (c_{i,l}S_l\rho_l\mathbf{u}_l + c_{i,s}S_s\rho_s\mathbf{u}_s + c_{i,l}S_l\rho_l\bar{\mathbf{v}}_{i,l}) = 0 \quad (7-18)$$

Assuming the following relations for the density and diffusive mass flux of the component  $i$

$$\rho_{m,i} = \frac{m_{i,l} + m_{i,s}}{V} = c_{i,l}S_l\rho_l + c_{i,s}S_s\rho_s \quad (7-19)$$

$$c_{i,l}S_l\rho_l\bar{\mathbf{v}}_{i,l} = \mathbf{j}_i \quad (7-20)$$

One comes then to:

$$\frac{\partial}{\partial t} (\rho_{m,i}) + \nabla \cdot (\rho_{m,i}\mathbf{u}_m) = -\nabla \cdot \mathbf{j}_i - \nabla \cdot \left[ \frac{S_l\rho_l S_s\rho_s}{\rho_m} (\mathbf{u}_l - \mathbf{u}_s)(c_{i,l} - c_{i,s}) \right] \quad (7-21)$$

The source term  $[S_l\rho_l S_s\rho_s / \rho_m](\mathbf{u}_l - \mathbf{u}_s)(c_{i,l} - c_{i,s})$  that appears is only a consequence of a variable transformation to base the convective term on “ $\mathbf{u}_m$ ” and it is demonstrated in the Appendix B.

The diffusive flux of a multicomponent mixture may be modeled through the Maxwell-Stefan equations:

$$\frac{\nabla\mu_{i,l}}{RT} = \nabla (\ln a_i) = \sum_{j=1}^N \frac{x_{i,l}x_{j,l}}{D_{i,j}} (\bar{\mathbf{v}}_j - \bar{\mathbf{v}}_i) \quad (7-22)$$

where,  $\mu_{i,l}$  is the chemical potential of species  $i$ ,  $a_i$  the activity of species  $i$ ,  $X_{i,l}$  is the molar fraction of species  $i$  in the liquid phase,  $D_{i,j}$  is the Maxwell-Stefan's

diffusion coefficient of species  $i$  and  $j$ , that differs from the well-known Fick's diffusion coefficient, and  $\bar{v}_i$  is the diffusion velocity of species  $i$ . However, as an approximation, Fick's law may be used to replace Maxwell-Stefan's equations, so the gradient of the molar fraction of species  $i$  can be defined as

$$\nabla X_{i,l} = \sum_{j=1}^N \frac{x_{i,l}x_{j,l}}{\mathcal{D}_{i,j}} (\bar{v}_j - \bar{v}_i) \quad (7-23)$$

Thus, for the sake of simplicity, the diffusive mass flux of the component  $i$ ,  $\mathbf{j}_i$ , can be defined as Fick's law:

$$c_{i,l}S_l\rho_l\bar{v}_{i,l} = \mathbf{j}_i = -\mathcal{D}_i\nabla c_{i,l}S_l\rho_l \quad (7-24)$$

Assuming that one of the species is present in a concentration greater than all others and the advection speed of all species is the same in the liquid phase, the multicomponent Fick's coefficient  $\mathcal{D}_i$  may be defined for all species but that present in higher concentration as:

$$\mathcal{D}_i = \mathcal{D}_{i,N} = \frac{1-x_{i,l}}{\sum_{j=1, j \neq i}^N (x_{j,l} / \mathcal{D}_{ij})} \quad (7-25)$$

and the diffusion coefficient of the species present in higher concentration may be defined as:

$$\mathcal{D}_N = \frac{\sum_{j=1}^{N-1} \mathcal{D}_j \nabla c_{i,l} S_l \rho_l}{\sum_{j=1}^{N-1} \nabla c_{i,l} S_l \rho_l} \quad (7-26)$$

This approximation eliminates the non-linearity that comes from the coupling of all diffusive velocities and guaranties that the following relation holds

$$\sum_{i=1}^N c_{i,l} S_l \rho_l \bar{v}_{i,l} = 0 \quad (7-27)$$

Nevertheless, this approach maintains the non-linearity due to the coupling of the concentration of all of the species. The main objective of the proposed model is to be a first approach where the solids are allowed to be transported by the moving fluid. In this sense, an extra non-linearity may be a numerical challenge and a stronger simplification will be used for the sake of computation effort. The multicomponent effect in the diffusion of the different species will be dropped and the diffusion of each species will be calculated as if it was in a binary mixture with the solvent. The diffusion coefficient then becomes the Fick's binary diffusion

coefficient for the solvent and species  $i$ . To ensure that the total diffusive flux adds to zero, the solvent diffusive flux will be calculated from the summation of the diffusive fluxes of all other species.

For the solutes:

$$c_{i,l}S_l\rho_l\bar{\mathbf{v}}_{i,l} = \mathbf{j}_i = -\mathcal{D}_i\nabla c_{i,l}S_l\rho_l \quad (7-28)$$

For the solvent:

$$c_{N,l}S_l\rho_l\bar{\mathbf{v}}_{N,l} = \mathbf{j}_N = -\sum_{i=1}^{N-1} c_{i,l}S_l\rho_l\bar{\mathbf{v}}_{i,l} \quad (7-29)$$

in a way to guarantee that:

$$\sum_{i=1}^N c_{i,l}S_l\rho_l\bar{\mathbf{v}}_{i,l} = 0 \quad (7-30)$$

The summation of the all of the species continuity equations results in the global continuity equation since:

$$\sum_{i=1}^N \rho_{m,i} = \sum_{i=1}^N (c_{i,l}S_l\rho_l + c_{i,s}S_s\rho_s) = S_l\rho_l + S_s\rho_s = \rho_m \quad (7-31)$$

$$\sum_{i=1}^N -\nabla \cdot \left[ \frac{S_l\rho_l S_s\rho_s}{\rho_m} (\mathbf{u}_l - \mathbf{u}_s)(c_{i,l} - c_{i,s}) \right] =$$

$$-\nabla \cdot \left[ \frac{S_l\rho_l S_s\rho_s}{\rho_m} (\mathbf{u}_l - \mathbf{u}_s)(1 - 1) \right] = 0 \quad (7-32)$$

$$\sum_{i=1}^N c_{i,l}S_l\rho_l\bar{\mathbf{v}}_{i,l} = \sum_{i=1}^N \mathbf{j}_i = 0 \quad (7-33)$$

Consequently:

$$\sum_{i=1}^N \left[ \frac{\partial}{\partial t} (\rho_{m,i}) + \nabla \cdot (\rho_{m,i} \mathbf{u}_m) \right] = \frac{\partial}{\partial t} (\rho_m) + \nabla \cdot (\rho_m \mathbf{u}_m) \quad (7-34)$$

$$\sum_{i=1}^N \left\{ -\nabla \cdot \left[ \frac{S_l\rho_l S_s\rho_s}{\rho_m} (\mathbf{u}_l - \mathbf{u}_s)(c_{i,l} - c_{i,s}) + \mathbf{j}_i \right] \right\} = 0 \quad (7-35)$$

The mass diffusion flux can be written based on density of the component  $i$  as

$$\mathbf{j}_i = -\mathcal{D}_i\nabla c_{i,l}S_l\rho_l \quad (7-36)$$

Thus, the mass conservation of specie  $i$  can be written as

$$\frac{\partial}{\partial t}(\rho_{m,i}) + \nabla \cdot (\rho_{m,i} \mathbf{u}_m) = -\nabla \cdot \left[ \mathbf{j}_i + \frac{S_l \rho_l S_s \rho_s}{\rho_m} (\mathbf{u}_l - \mathbf{u}_s)(c_{i,l} - c_{i,s}) \right] \quad (7-37)$$

#### 7.2.4. Linear momentum conservation equation

The linear momentum conservation equation for each phase are

$$\frac{\partial}{\partial t}(S_l \rho_l \mathbf{u}_l) + \nabla \cdot (S_l \rho_l \mathbf{u}_l \mathbf{u}_l) = -S_l \nabla p + \nabla \cdot (S_l \boldsymbol{\tau}^l) + S_l \rho_l \mathbf{g} + \mathbf{M}_{int} \quad (7-38)$$

$$\frac{\partial}{\partial t}(S_s \rho_s \mathbf{u}_s) + \nabla \cdot (S_s \rho_s \mathbf{u}_s \mathbf{u}_s) = -S_s \nabla p + \nabla \cdot (S_s \boldsymbol{\tau}^s) + S_s \rho_s \mathbf{g} - \mathbf{M}_{int} \quad (7-39)$$

where  $\boldsymbol{\tau}^l$  is the liquid viscous tensor and  $\boldsymbol{\tau}^s$  is the equivalent tensor for a pack of solid particles.  $\mathbf{M}_{int}$  is related to the momentum interfacial transfer.

The mixture momentum equation can be obtained by adding the phase-equation, resulting in

$$\begin{aligned} \frac{\partial}{\partial t}(S_l \rho_l \mathbf{u}_l + S_s \rho_s \mathbf{u}_s) + \nabla \cdot (S_l \rho_l \mathbf{u}_l \mathbf{u}_l + S_s \rho_s \mathbf{u}_s \mathbf{u}_s) = \\ -\nabla p + \nabla \cdot \boldsymbol{\tau}_m + \rho_m \mathbf{g} \end{aligned} \quad (7-40)$$

where the mixture viscous stress tensor is defined as

$$\boldsymbol{\tau}_m = S_l \boldsymbol{\tau}^l + S_s \boldsymbol{\tau}^s \quad (7-41)$$

The mixture viscous stress depends on the definition of a viscous stress tensor for the solid phase, which is not straight forward. As a first approximation the solid will be treated as a fluidized bed, i.e., a pack of solid particles will be modeled assuming that it flows in a similar way as a fluid. The mixture viscous stress tensor then takes the form:

$$\boldsymbol{\tau}_m = S_l \boldsymbol{\tau}^l + S_s \boldsymbol{\tau}^s = \mu_m \left[ \nabla \mathbf{u}_m + (\nabla \mathbf{u}_m)^T - \frac{2}{3} \nabla \cdot \mathbf{u}_m \mathbf{I} \right] \quad (7-42)$$

where  $\mu_m$  is the mixture viscosity, which must depend on the solid concentration.

Rewriting the equation in view of the definitions priory stated one comes to:

$$\frac{\partial}{\partial t}(\rho_m \mathbf{u}_m) + \nabla \cdot (\rho_m \mathbf{u}_m \mathbf{u}_m) =$$

$$-\nabla p + \nabla \cdot \boldsymbol{\tau}_m - \nabla \cdot \left[ \frac{S_l \rho_l S_s \rho_s}{\rho_m} (\mathbf{u}_l - \mathbf{u}_s)^2 \right] \quad (7-43)$$

In the present model, the body force  $\rho_m \mathbf{g}$  is neglected. The source term  $[S_l \rho_l S_s \rho_s / \rho_m] (\mathbf{u}_l - \mathbf{u}_s)^2$  is a consequence of a variable transformation to make the equation dependent on “ $\mathbf{u}_m$ ” and it is demonstrated in the Appendix B.

As a clear improvement over the model proposed by Banki et al. (2008), here the solids are no longer held in place, as soon as they are formed. However, to allow for formation of a deposit, the model needs further assumptions. One should expect that the flow should be different in the deposit region. Different models can be tested for this purpose and thus the physics of the wax deposition can be assessed.

At the present work, the resistance to the flow that characterizes the deposit will be introduced in the form of an increase in the viscosity of the mixture as solids come out of solution. The liquid/solid mixture displays non-Newtonian behavior that is dependent on the concentration of solids and on their shape and size and also on the temperature. As the temperature will be lower near the walls and consequently the solids will be present in a higher concentration, the viscosity will be higher and the fluid will slow down, resulting in a deposit. The transport equations as proposed will allow a diffusion flux in the gelled region even if there is no advection velocity.

### 7.2.5. Energy conservation equation

The mixture energy conservation equation can also be obtained by combining the energy conservation equation of each phase, and it may be defined as:

$$\begin{aligned} \frac{\partial}{\partial t} (S_l \rho_l h_l + S_s \rho_s h_s) + \nabla \cdot (S_l \rho_l h_l \mathbf{u}_l + S_s \rho_s h_s \mathbf{u}_s) = \\ \frac{Dp}{Dt} + \nabla \cdot (\lambda_m \nabla T) - \nabla \cdot (\sum_{i=1}^N \mathbf{j}_i h_{i,l}) + \Phi \end{aligned} \quad (7-44)$$

where “ $h_l$ ” is the enthalpy of the liquid phase, “ $h_s$ ” is the enthalpy of the solid phase, “ $\lambda_m$ ” is thermal conductivity of the mixture and “ $\Phi$ ” is the viscous dissipation. The viscous dissipation is defined as

$$\Phi = \boldsymbol{\tau}_m : \nabla \mathbf{u}_m \quad (7-45)$$

At the present work, the Eckert number is low, i.e., the thermal transfer is significant, therefore, the viscous dissipation can be neglected. For the same reason, it is expected the total pressure variation to be negligible in relation to the heat transfer flux, thus,  $Dp/Dt$  is also neglected.

The enthalpy for the mixture can be defined as:

$$h_m = \frac{S_l \rho_l h_l + S_s \rho_s h_s}{\rho_m} \quad (7-46)$$

resulting in the following form of the energy conservation equation

$$\frac{\partial}{\partial t} (\rho_m h_m) + \nabla \cdot (\rho_m h_m \mathbf{u}_m) = \nabla \cdot (\lambda_m \nabla T) - \nabla \cdot \left( \sum_{i=1}^N \mathbf{j}_i h_{i,l} \right) - \nabla \cdot \left[ \frac{S_l \rho_l S_s \rho_s}{\rho_m} (h_l - h_s) (\mathbf{u}_l - \mathbf{u}_s) \right] \quad (7-47)$$

The source term  $[S_l \rho_l S_s \rho_s / \rho_m] (h_l - h_s) (\mathbf{u}_l - \mathbf{u}_s)$  is a consequence of a variable transformation to make the equation dependent on “ $h_m$ ” and is demonstrated in the Appendix B.

### 7.2.6. Drift Velocities

The difference between the liquid and solid velocities is the relative velocity

$$\mathbf{u}_r = (\mathbf{u}_l - \mathbf{u}_s) \quad (7-48)$$

and leads to the definition of a mass drift flux

$$\mathbf{J}_{drift} = \frac{S_l \rho_l S_s \rho_s}{\rho_m} (\mathbf{u}_l - \mathbf{u}_s) = \frac{S_l \rho_l S_s \rho_s}{\rho_m} \mathbf{u}_r \quad (7-49)$$

The drift of the species, momentum and energy are

$$\mathbf{J}_{i,drift} = \mathbf{J}_{drift} (c_{i,l} - c_{i,s}) \quad (7-50)$$

$$\mathbf{J}_{u,drift} = \mathbf{J}_{drift} (\mathbf{u}_l - \mathbf{u}_s) \quad (7-51)$$

$$\mathbf{J}_{h,drift} = \mathbf{J}_{drift} (h_l - h_s) \quad (7-52)$$

The phase velocities can be obtained from the mean and relative velocities

$$\mathbf{u}_l = \mathbf{u}_m + \frac{S_s \rho_s}{\rho_m} \mathbf{u}_r \quad ; \quad \mathbf{u}_s = \mathbf{u}_m - \frac{S_l \rho_l}{\rho_m} \mathbf{u}_r \quad (7-53)$$

To determine the relative velocity needed to evaluate the drift flux, an additional model is required. Here, as a first approximation for the present methodology, the relative velocity was considered null, i.e., both the liquid and the

solid velocities were kept equal, therefore, the drift flux is null, and the flow is homogeneous. However, the formulation is general, and it does not depend on this restriction.

### 7.2.7. Thermodynamic model and properties

The thermodynamic model used is based on the model described in detail in Chapters 3 and 4. Some simplifications were made aiming at reducing the computation cost. As the fluid under analysis will only be submitted to mild pressure and temperature conditions, the gas-liquid flash calculation and its stability analysis were eliminated. The Newton method step used to converge the multiphase solid flash was also eliminated and convergence is achieved through the successive substitution method. The total number of solid phases available in the modified Uniquac method was reduced to one third of the total number of components.

The thermodynamic model is applied to determine the following properties: mass fraction of each phase ( $B_k$ ), their respective mass ( $c_{i,k}$ ) and molar ( $x_{i,k}$ ) compositions, their specific enthalpy ( $h_k$ ) and the specific enthalpy of each component in the liquid phase ( $h_{i,l}$ ). These quantities are determined based on the temperature, pressure and global mass composition ( $c_i$ ).

The molar composition of all phases are used to calculate their density ( $\rho_l, \rho_s$ ), the viscosity of the liquid phase ( $\mu_l$ ) and the thermal conductivity of the liquid phase ( $\lambda_l$ ) with the methods described in the following sections. Once the densities were calculated, the mass fraction of each phase was used to calculate the volume fraction of each phase ( $S_k$ ), using Equations 7-8.

#### 7.2.7.1. Densities and volume fractions

Although the densities ( $\rho_l, \rho_s$  and  $\rho_m$ ) and, by consequence, the volume fractions of asymmetric  $n$ -paraffin mixtures can be determined from the thermodynamic model, they are not well modeled by the Peng-Robinson equation of state. To overcome this deficiency, a volume translation scheme can be employed as proposed by Peneloux and Rauzy (1982). However, the density would then be a

function of the pressure. This non-linearity would not bring any new information for the present approach and a density model that would be independent from the pressure is preferred.

The density of the liquid phase is obtained through a corresponding state model where the second derivative of the Taylor expansion series ( $D_2$ ) of the reduced property ( $X_r$ ) is taken into account (Queimada et al., 2005). The reduced property is calculated as follows:

$$X_r = X_{r1} + D_1(\omega - \omega_1) + D_2(\omega - \omega_1)(\omega - \omega_2) \quad (7-54)$$

$$D_1 = \frac{X_{r2} - X_{r1}}{\omega_2 - \omega_1} \text{ and } D_2 = \frac{1}{\omega_3 - \omega_2} \left[ \frac{X_{r3} - X_{r1}}{\omega_3 - \omega_1} - \frac{X_{r2} - X_{r1}}{\omega_2 - \omega_1} \right] \quad (7-55)$$

where  $\omega$  is the Pitzer acentric factor of the system and the indexes 1, 2 and 3 refer to the reference materials. The reduced density ( $\rho_r$ ) of any system is calculated from the system's density ( $\rho$ ) as follows

$$\rho_r = Vc \cdot \rho \quad (7-56)$$

where  $Vc$  is the critical volume of the system under evaluation.

To calculate the reduced property of any system through Equation 7-54, one needs only the reduced properties of 3 reference materials at the temperature of interest to calculate the constants of Equation 7-55, and the critical volume of that system to convert the critical property calculated through Equation 7-54 to the property itself.

To be applied to mixtures, a set of mixing rules must be used. These mixing rules allow one to combine the critical properties of the different components of the mixture into a single mixture critical property that may now be used in Equations 7-54 and 7-56. Queimada et al. (2005) presents the following mixing rules, through which the acentric factor and the critical volume of the mixture is obtained.

$$\omega_m = \sum_i x_i \omega_i \quad (7-57)$$

$$Vc_m = \sum_i \sum_j x_i x_j Vc_{ij} \quad (7-58)$$

$$Vc_{ij} = 0.125 \left( Vc_i^{1/3} + Vc_j^{1/3} \right)^3 \quad (7-59)$$

To calculate the density of the liquid mixture,  $\rho_m$ , one should first calculate the density of three reference systems. In their original work, Queimada et al. (2005) proposed as reference materials methane (CH<sub>4</sub>), *n*-pentadecane (C<sub>15</sub>H<sub>32</sub>) and *n*-hexacosane (C<sub>26</sub>H<sub>54</sub>). To avoid temperature restrictions, methane was substituted by butane (C<sub>4</sub>H<sub>10</sub>). The density of the reference materials was calculated as follows:

$$\rho_n [\text{mol. cm}^{-3}] = \frac{A}{10^3 B^{1+[1-(T/C)]^D}} \quad (7-60)$$

where index  $n$  stands for the reference material (1, 2 or 3) and the parameters A, B, C and D are shown in Table 7-1.

**Table 7-1.** Coefficients for calculating the density of the reference materials with Equation 7-60.

	A	B	C	D
<b>C<sub>4</sub>H<sub>10</sub></b>	1.0677	0.27188	425.12	0.28688
<b>C<sub>15</sub>H<sub>32</sub></b>	0.2844	0.25269	708.00	0.30786
<b>C<sub>26</sub>H<sub>54</sub></b>	0.1624	0.24689	819.00	0.34102

With the density of the reference materials at the temperature of interest, one calculates the reduced density for each of them using Equation 7-56. It should be clear at this point that the critical volume and the acentric factor of the reference materials should also be available. One may now obtain  $D_1$  and  $D_2$  as presented in Equation 7-55. Next, one calculates the mixture's critical volume and acentric factor using the set of mixing rules described by Equations 7-57 to 7-59. With the mixture acentric factor, one uses Equation 7-54 to calculate the reduced property of the mixture at the temperature of interest. Finally, using the mixture's critical volume, one may calculate the density of the mixture using Equation 7-56.

In the present model, the density of the solid is calculated by using the density of a liquid with the same composition of the solid and increasing that density by a factor of 10%. This factor is empirical and should be regarded as so.

With the density of both solid and liquid, and with the mass fraction of both calculated through the thermodynamic model, the volume fractions of liquid and solid are calculated.

### 7.2.7.2. Suspension viscosity model

The viscosity of wax suspensions is a function of  $c_i$ ,  $T$  and  $p$ , as well as a function of shear stress once the solids are present. The mixture behaves like a Newtonian fluid while monophasic and as soon as there is solid formation, a non-Newtonian behavior arises. The increase of the viscosity due to solids precipitation is the physical driving force to stop the flow near the cold wall. As viscosity increases with the amount of solids one should expect a threshold where above that given point, advection velocity will be zero.

At the present model, the viscosity of the solid suspension is described as function of the viscosity of the liquid phase and the volume fraction of solids. Although the appearance of solids can induce a non-Newtonian behavior, i.e., a dependence of the viscosity on the shear stress, at the present model, the viscosity was modeled as a function of only the temperature and solid volume fraction.

Following the approach used to model density, the viscosity of the fluid phase was modeled as suggested by Queimada et al (2005). Following the same logic, the reduced viscosity is determined based on critical properties, 3 reference materials with a model to calculate their viscosities in any given temperature, and the critical properties of the system of interest.

The reduced viscosity ( $\mu_r$ ) is calculated from the liquid viscosity ( $\mu_l$ ) as follows:

$$\mu_r = \frac{\mu_l V c^{2/3}}{M M^{1/2} T c^{1/2}} \quad (7-61)$$

where  $Tc$ ,  $Vc$  and  $MM$  are the critical temperature, the critical volume and the molar mass, respectively. As proposed by Queimada et al. (2005), the references used were ethane ( $C_2H_6$ ),  $n$ -octane ( $C_8H_{18}$ ) and  $n$ -octadecane ( $C_{18}H_{38}$ ). The viscosity of the references as a function of temperature can be calculated using the following correlation

$$\mu_n [mPas] = \exp \left( A + \frac{B}{T} + C \ln(T) + DT^E \right) \times 10^3 \quad (7-62)$$

where index  $n$  stands for the reference material (1, 2 or 3) and the parameters A, B, C, D and E are shown in Table 7-2.

**Table 7-2.** Coefficients for calculating the viscosity of the reference materials with Equation 7-62.

	<b>A</b>	<b>B</b>	<b>C</b>	<b>D</b>	<b>E</b>
<b>C<sub>2</sub>H<sub>6</sub></b>	-7.0046	276.380	-0.6087	3.111x10 <sup>-18</sup>	7.0
<b>C<sub>8</sub>H<sub>18</sub></b>	-7.7310	979.376	-0.5460	0	0
<b>C<sub>18</sub>H<sub>38</sub></b>	-2.3884	1280.02	-1.3112	0	0

The critical properties and the molecular mass required to calculate the reduce viscosity of the reference materials are the same used in the thermodynamic modeling.

The reduced viscosity of the liquid can be calculated using the same Equation 7-56 where the critical properties of the mixture should be calculated through Equations 7-53, 7-54, 7-55 and the following.

$$Tc_m Vc_m = \sum_i \sum_j x_i x_j Tc_{ij} Vc_{ij} \quad (7-63)$$

$$Tc_{ij} = \sqrt{Tc_i Tc_j} \left( \frac{\sqrt{Vc_i Vc_j}}{Vc_{ij}} \right)^{(n)-1} \quad (7-64)$$

where the indexes  $i$  and  $j$  represent pure components and  $n$  is a fitting parameter, set to 1 in this work.

Once the viscosity of the liquid was calculated, the viscosity of the mixture (liquid with solid suspension) was calculated as follows:

$$\mu_m = \mu_l \exp(\Omega S_s) \quad (7-65)$$

where  $\mu_l$  and  $\Omega$  are the liquid viscosity and a fitting parameter. To establish  $\Omega$ , the viscosity of the mixture used by Veiga (2017) was measured under a constant shear rate of 120 s<sup>-1</sup>. The shear rate is half way between the maximum and the minimum shear rates experienced by the fluid during the experiment. Results are presented in Figure 7-1 for  $\Omega$  equal to 200. For temperatures above the WAT, the model matches the mixture viscosity to the experimental uncertainties. As solids start to appear, the viscosity rises extremely fast, leading the uncertainty of the viscosity measure to become as big as the data since the probe starts to slip. So the parameter  $\Omega$  was adjusted to reproduce the first two points below the WAT where the results are still reproducible.

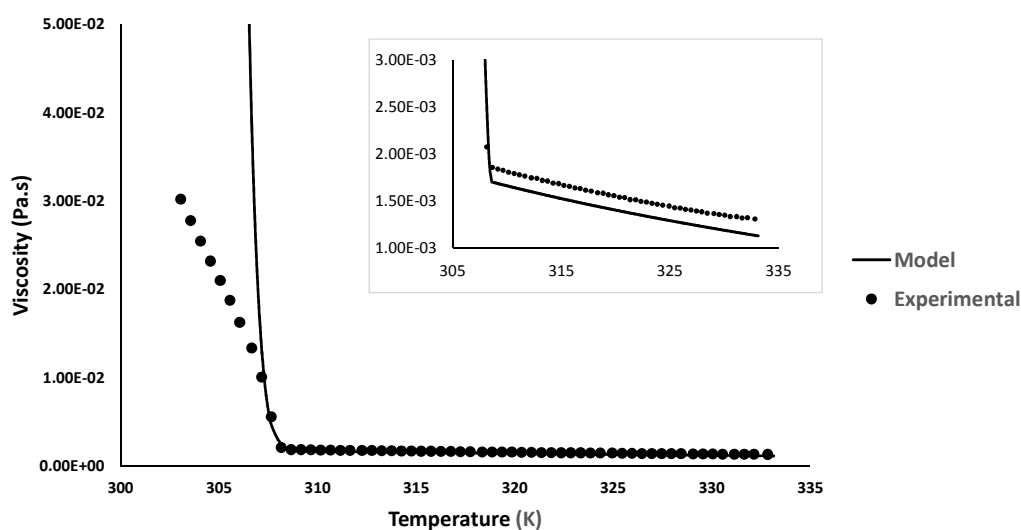


**Figure 7-1.** Experimental results for the mixture used by Veiga (2017) and the model result with  $D=200$  and the composition from Veiga (2017). In the detail, the viscosity of the mixture at temperatures above the WAT.

### 7.2.7.3. Thermal conductivity of the liquid and solid phases

Many correlations are available to calculate the thermal conductivity of *n*-alkanes (Assael et al., 1990; Assael et al., 1992; Civan, 2008; Lashkarbolooki et al., 2016; Latini et al., 2017; Marcías-Salinas, 2018). Nevertheless, the vast majority are focused on light *n*-alkanes with carbon number up to 10 or 12. In part, this is due to the lack of experimental information on the thermal conductivity of higher carbon number *n*-alkanes.

Recently, the thermal conductivity of both liquid and solid *n*-alkanes up to *n*-dotriacontane have been measured. The results can now be used to check the correlations. Following the same model used to calculate both density and liquid viscosity, the thermal conductivity of the liquid phase was calculated using a second order corresponding state model as proposed by Paradela et al. (2005). Once again, it is needed a model to calculate the reduced thermal conductivity based on critical properties, 3 reference materials with a model to calculate their thermal conductivities in any given temperature and the critical properties of the system of interest. The model was first tested against the results of Fleming et al. (2018), presenting a very good performance.

The reduced thermal conductivity of the system can be calculated by using

$$\lambda_r = \frac{\lambda_l V c^{2/3} M M^{1/2}}{T c^{1/2}} \quad (7-66)$$

The thermal conductivity of the references as a function of temperature was calculated using the model and correlation parameter suggested by Yaws (2003). *n*-butane, *n*-decane and *n*-tetracosane were chosen as reference materials and the correlation coefficients are shown in Table 7-3.

$$\lambda_n [W \cdot m^{-1} \cdot K^{-1}] = A + BT + CT^2 \quad (7-67)$$

**Table 7-3.** Coefficients for calculating the viscosity of the reference materials with Equation 7-67.

	A	B x 10 <sup>4</sup>	C x 10 <sup>7</sup>
<b>C<sub>4</sub>H<sub>10</sub></b>	0.2348	-3.7626	-2.5291
<b>C<sub>10</sub>H<sub>22</sub></b>	0.1860	-1.1813	-1.9797
<b>C<sub>24</sub>H<sub>50</sub></b>	0.2399	-3.0556	1.3889

The critical properties needed are the same as those needed for viscosity and were calculated in the same manner.

The comparison between the results of the model and the measurements from Fleming et al. (2018) are depicted in Figures 7-2 to 7-8. The differences are no larger than 3.5%, well within the reported uncertainty. The thermal conductivity of the solids were all estimated to be 0.6 W.m<sup>-1</sup>.K<sup>-1</sup>.

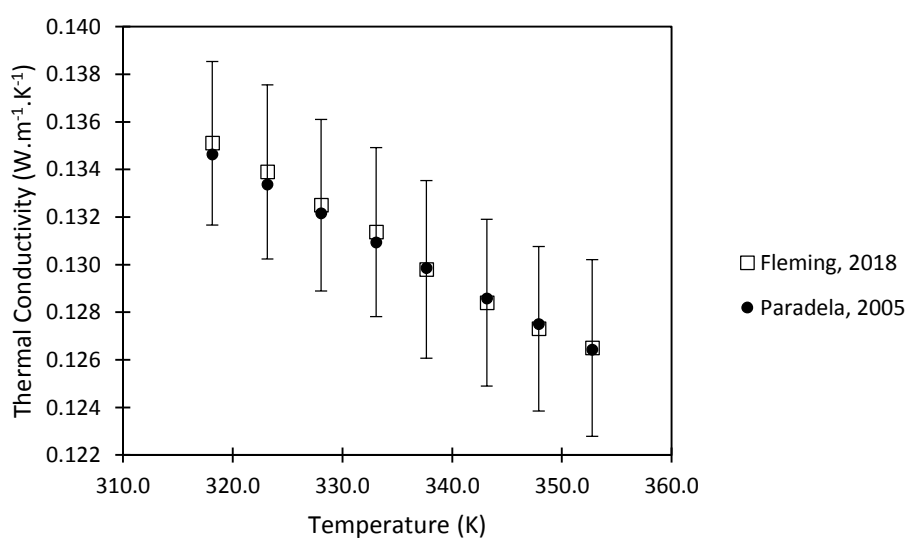


**Figure 7-2.** Thermal conductivity of *n*-dodecane from Fleming et al. (2018) compared to the model of Paradela et al. (2005).

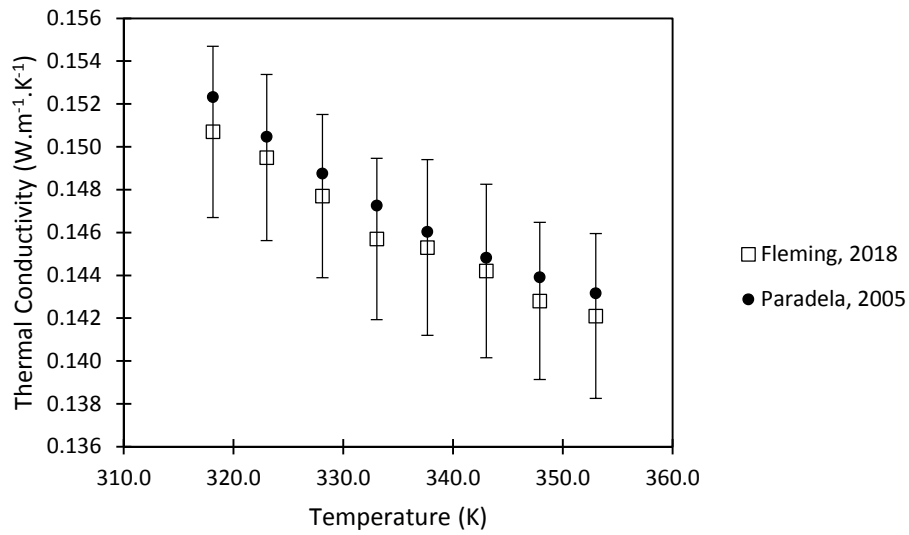


**Figure 7-3.** Thermal conductivity of *n*-docosane from Fleming et al. (2018) compared to the model of Paradela et al. (2005).

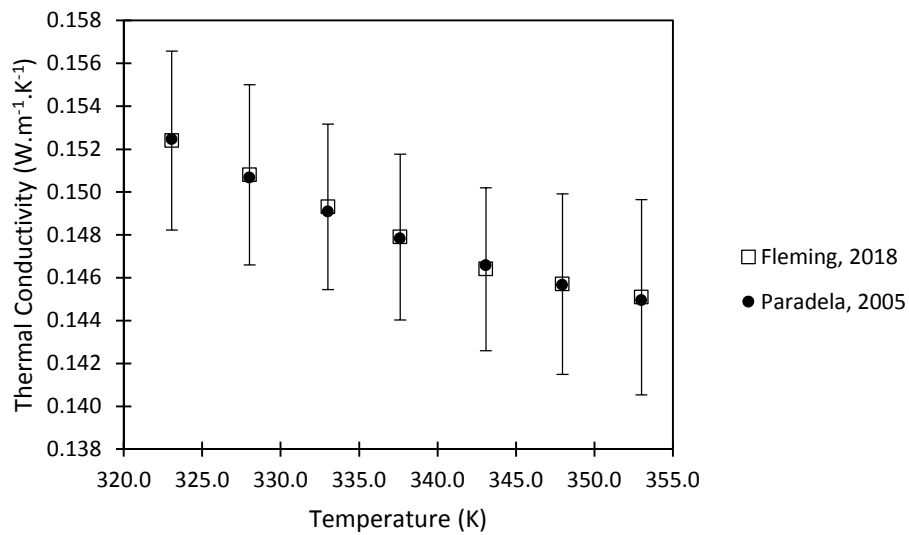


**Figure 7-4.** Thermal conductivity of *n*-tetracosane from Fleming et al. (2018) compared to the model of Paradela et al. (2005).

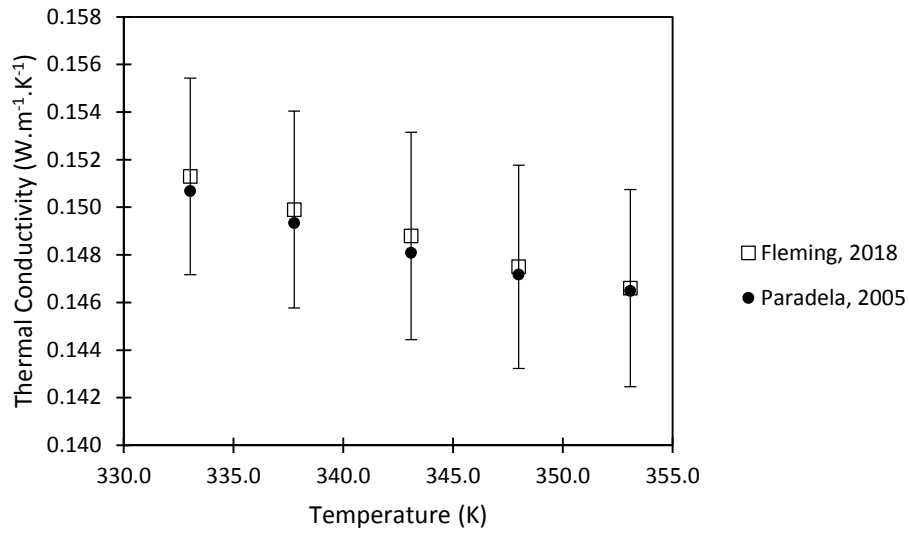


**Figure 7-5.** Thermal conductivity of *n*-hexacosane from Fleming et al. (2018) compared to the model of Paradela et al. (2005).

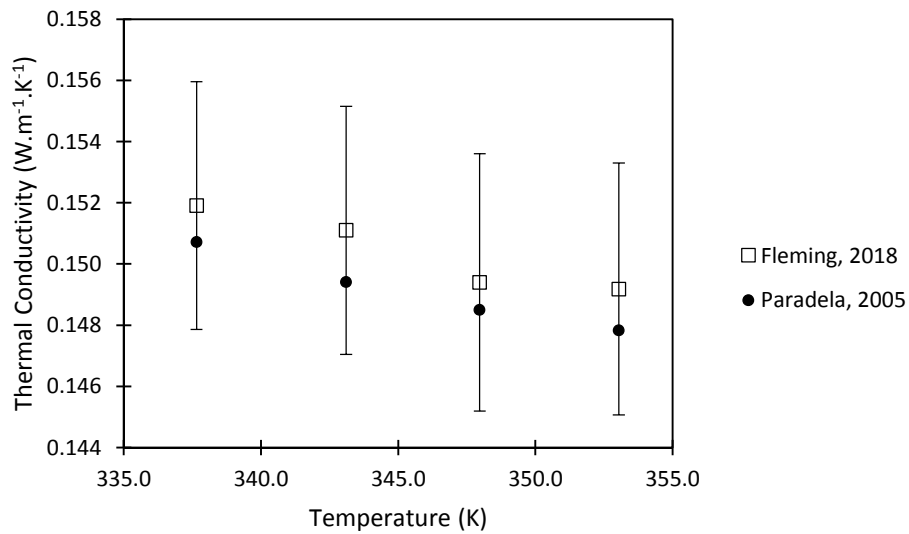


**Figure 7-6.** Thermal conductivity of *n*-octacosane from Fleming et al. (2018) compared to the model of Paradela et al. (2005).

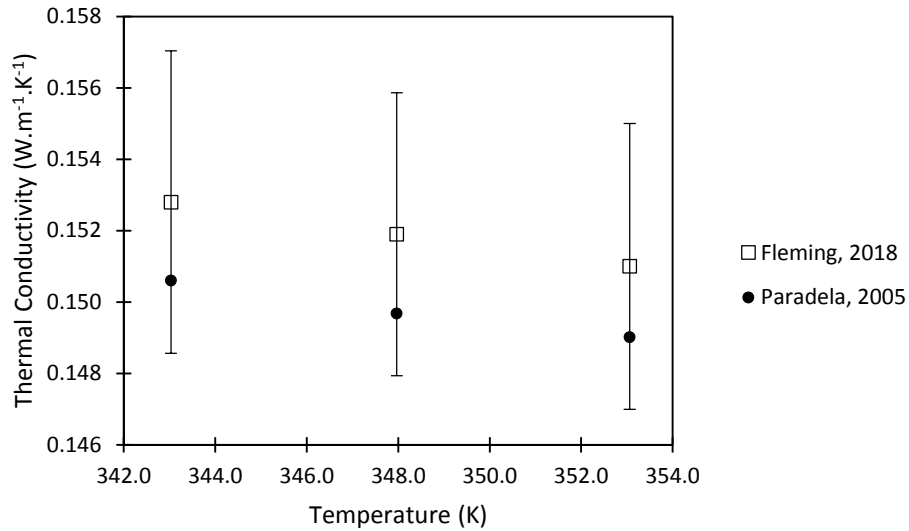


**Figure 7-7.** Thermal conductivity of *n*-triacontane from Fleming et al. (2018) compared to the model of Paradela et al. (2005).

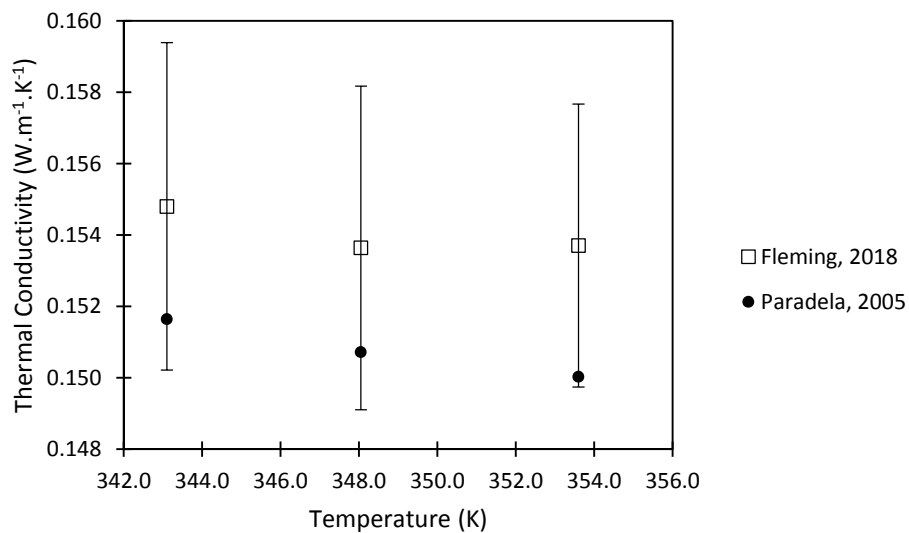


**Figure 7-8.** Thermal conductivity of *n*-dotriacontane from Fleming et al. (2018) compared to the model of Paradela et al. (2005).

The thermal conductivity of the mixture ( $\lambda_m$ ) is calculated through the combination of the thermal conductivities of both phases as

$$\lambda_m = S_l \lambda_l + S_s \lambda_s \quad (7-68)$$

#### 7.2.7.4. Diffusion coefficients

The calculation of the diffusion of the liquid components through the model proposed in section 7.2.3 depends on the binary diffusion coefficients between each component and the solvent *n*-dodecane,  $\mathcal{D}_{AB}$ . For that, the correlation proposed by Hayduk and Minhas (1982) presented below was used.

$$\mathcal{D}_{AB} [cm^2 \cdot s^{-1}] = 13.3 \times 10^{-8} T^{1.47} \mu_m \gamma \bar{V}_A^{-0.71} \quad (7-69)$$

where  $T$  is the temperature in K,  $\mu_m$  is the viscosity of the mixture in mPa.s and  $\bar{V}_A$  is the molar volume of the solute in  $cm^3 \cdot mol^{-1}$ .  $\gamma$  is calculated as follows.

$$\gamma = \frac{10.2}{\bar{V}_A} - 0.791 \quad (7-70)$$

### 7.3. Domain of Interest

Recently, Veiga (2017) presented high quality experimental results of wax deposition collected in an ingenious test rig that allows low uncertainty determination of the transient deposit thickness. A brief description of the test section and conditions is presented.

#### 7.3.1. Test section

The section built by Veiga (2017) consisted of an annulus enclosed between an internal copper tube and a Plexiglas outer tube. The inner tube was connected to a chiller which allowed to control its temperature ( $T_{cold}$ ). The deposition took place over the surface of this copper tube. The transient thickness of the deposit could be directly measured both by visual inspection as well as directly probed by an inserted temperature probe. The inner copper tube had an external diameter of 19.05 mm ( $R_{in}=9.525$  mm) and the outer Plexiglas tube had an internal diameter of 34 mm ( $R_{ex}=17$  mm), leaving an annular space ( $R_{gap} = R_{ex} - R_{in}$ ) of 7.475 mm. The total length of the copper tube and hence the length ( $L$ ) of the deposition section was 1050 mm. An overview of the test section is presented in Figure 7-9.

The temperature of the external wall of the Plexiglas tube ( $T_{hot}$ ) was kept constant over the experiment and equal to the inlet temperature of the fluid ( $T_{in}$ ), at 38 °C. To do so, Veiga placed the apparatus in a temperature controlled water bath, as depicted in Figure 7-10. As such, the tests were run with controlled mass flow of the fluid of interest (constant Reynolds number), constant temperature at the outer wall of the annulus and a known temperature gradient on the inner wall.

The temperature of the copper tube wall ( $T_{cold}$ ) is reduced from the starting temperature (38 °C) as fast as possible to the temperature of interest, 12 °C. Despite the efforts, the time that took the temperature to drop was not negligible and, as such, the transient temperature measured in the experiments was used as boundary condition for the copper tube wall temperature ( $T_{cold}$ ). This temperature is plotted against time in Figure 7-11.

As presented, the test section is axisymmetric. As such, the conservation equations can be solved in a 2-D scheme.

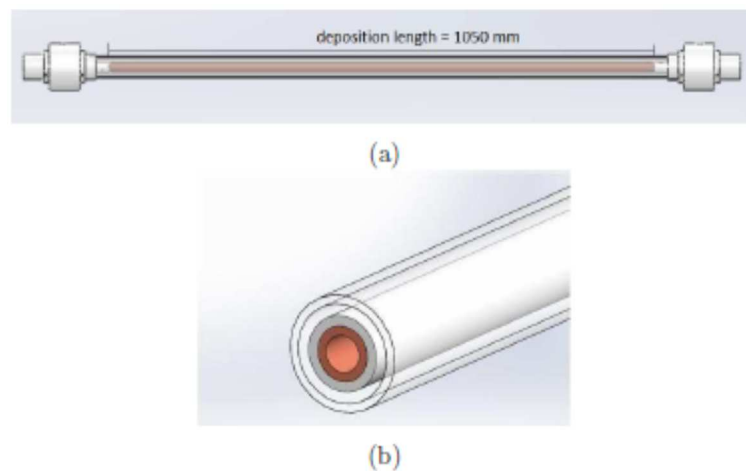


**Figure 7-9.** Schematic representation of the test section reported by Veiga (2017).  
(a) Front view. (b) Cut view.

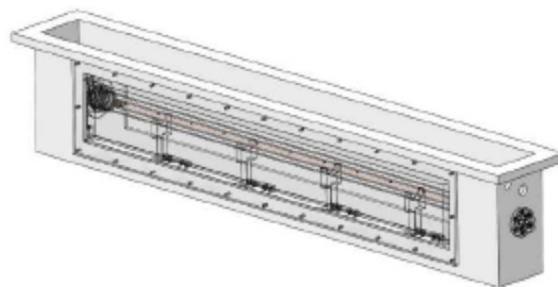


**Figure 7-10.** Schematic representation of the test section immersed in the temperature controlled water bath by Veiga (2017).

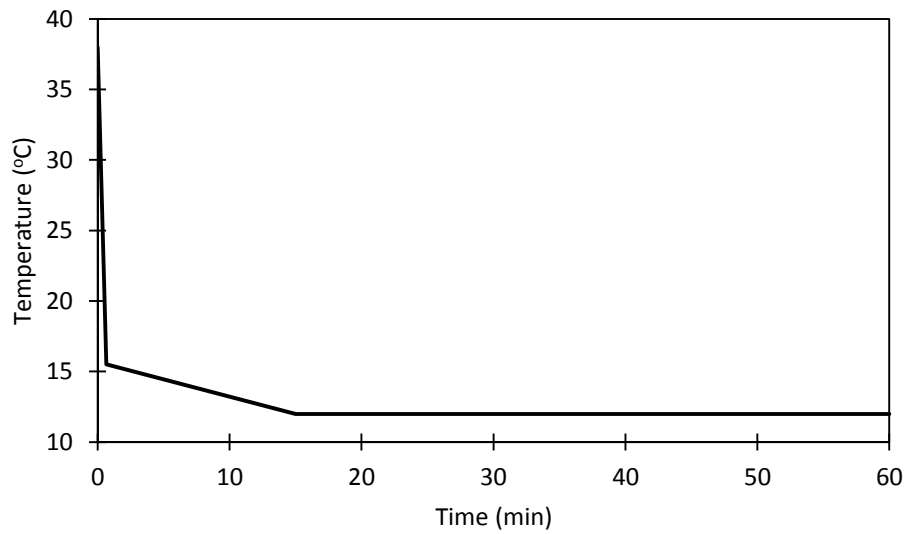


**Figure 7-11.** Temperature of the inner cooper wall ( $T_{cold}$ ) (Veiga, 2017).

The average velocity in the test section is defined as the ratio between the total flow rate and the area of the annulus.

$$U_{avg} = \frac{2 \int_{R_{in}}^{R_{ex}} u_m r dr}{R_{ex}^2 - R_{in}^2} \quad (7-71)$$

The flow problem is governed by the geometric parameters, the fluid parameters, the Reynolds number, Prandtl and Schmidt numbers. The Reynolds number is defined as

$$Re = \frac{2R_{gap} U_{avg} \rho_m}{\mu_m} \quad (7-72)$$

The Prandtl is

$$Pr = \frac{c_p \mu_m}{\lambda_m} \quad (7-73)$$

and the Schmidt number is

$$Sc = \frac{\mu_m}{\rho_m D} \quad (7-74)$$

The section length can become dimensionless by using the total length of the copper pipe ( $z/L$ ). The radius can be normalized by the hydraulic diameter ( $2R_{gap}$ ), and the dimensionless temperature can be defined as follows.

$$\theta = \frac{T - T_{cold}}{T_{hot} - T_{cold}} \quad (7-75)$$

The initial condition of the system is a fully developed flow with the entire domain at  $\theta = 1$ . The boundary conditions are:

$$(1) \frac{R_{in}}{2R_{gap}} = \frac{1}{2\left(\frac{R_{ex}}{R_{in}} - 1\right)} ; \theta = 0$$

$$(2) \frac{R_{ex}}{2R_{gap}} = \frac{\frac{R_{ex}}{R_{in}}}{2\left(\frac{R_{ex}}{R_{in}} - 1\right)} ; \theta = 1$$

$$(3) \frac{z}{L} = 0 ; \theta = 1$$

$$(4) \frac{z}{L} = 1 ; \frac{\partial \theta}{\partial z} = 0$$

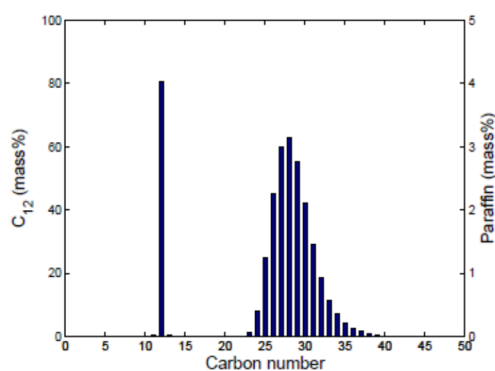
The fluid used in the simulations followed the composition and properties of the fluid used in the experimental results presented by Veiga (2017).

### 7.3.2. Test fluid

The test fluid was designed by Veiga (2017) to assure the greatest possible control over thermophysical properties of the system. As such, the fluid is the result of a mixture of *n*-alkanes with a well-defined total composition. The solvent was chosen as *n*-dodecane and to it was added a mixture of *n*-alkanes ranging from  $C_{22}H_{46}$  to  $C_{39}H_{80}$ . The composition of the fluid is presented in Table 7-4. A chromatogram of the same mixture is shown in Figure 7-12.

**Table 7-4.** Fluid composition in % mass.

Component	% mass
C <sub>12</sub> H <sub>26</sub>	83.32
C <sub>22</sub> H <sub>46</sub>	0.01
C <sub>23</sub> H <sub>48</sub>	0.10
C <sub>24</sub> H <sub>50</sub>	0.50
C <sub>25</sub> H <sub>52</sub>	1.37
C <sub>26</sub> H <sub>54</sub>	2.32
C <sub>27</sub> H <sub>56</sub>	2.84
C <sub>28</sub> H <sub>58</sub>	2.76
C <sub>29</sub> H <sub>60</sub>	2.26
C <sub>30</sub> H <sub>62</sub>	1.64
C <sub>31</sub> H <sub>64</sub>	1.10
C <sub>32</sub> H <sub>66</sub>	0.71
C <sub>33</sub> H <sub>68</sub>	0.45
C <sub>34</sub> H <sub>70</sub>	0.28
C <sub>35</sub> H <sub>72</sub>	0.17
C <sub>36</sub> H <sub>74</sub>	0.10
C <sub>37</sub> H <sub>76</sub>	0.05
C <sub>38</sub> H <sub>78</sub>	0.02
C <sub>39</sub> H <sub>80</sub>	0.01

**Figure 7-12.** Chromatogram of the fluid used by Veiga (2017) in the experiments.

The solid-liquid equilibrium temperature was determined by cross-polarized microscopy to be  $309.45 \pm 0.5$  K.

#### 7.4. Numerical Method

The numerical solution of the proposed mathematical model described in section 7.2 was carried out through the finite volumes method as proposed by Patankar (1980). As suggested, the conservation equations should be written in the following form:

$$\frac{\partial}{\partial t}(\rho_m \Phi) + \nabla \cdot (\rho_m \mathbf{u} \Phi) = \nabla \cdot (\Gamma \nabla \Phi) + S_C + S_P \Phi \quad (7-76)$$

where  $\rho_m$  is the density of the mixture,  $\Phi$  is the variable for which one is solving the equation,  $\mathbf{u}$  is the velocity vector,  $\Gamma$  is the diffusion coefficient of the variable  $\Phi$  and  $S = S_C + S_P \Phi$  is the source term. The inequality  $S_P \leq 0$  must hold to assure numerical stability of the solution.

Since the domain of interest is annular, the flow equations can be written in cylindrical coordinates. Further, the axisymmetric assumption can be employed, resulting in the following form of the general conservation equation.

$$\frac{\partial}{\partial t}(\ddot{\rho} \Phi) + \frac{\partial}{\partial z}(\ddot{\rho} U_m \Phi) + \frac{1}{r} \frac{\partial}{\partial r}(r \ddot{\rho} V_m \Phi) = \frac{\partial}{\partial z} \left[ \Gamma \frac{\partial \Phi}{\partial z} \right] + \frac{1}{r} \frac{\partial}{\partial r} \left[ r \Gamma \frac{\partial \Phi}{\partial r} \right] + S_C + S_P \Phi \quad (7-77)$$

The variables to be used in Equation 7-77 for each conservation equation are shown in Table 7-5. To complete the terms presented in Table 7-5, it is needed to define as well

$$\nabla \cdot \mathbf{u} = \frac{1}{r} \frac{\partial}{\partial r}(rV) + \frac{\partial}{\partial z}(U) \quad (7-78)$$

$$\mathbf{j}_i = -D_i S_l \rho_l \nabla c_{i,l} \quad (7-79)$$

$$\mathbf{j}_N = -\sum_{i=1}^{N-1} c_{i,l} S_l \rho_l \bar{\mathbf{v}}_{i,l} \quad (7-80)$$

The differential equations are discretized in a mesh of finite volumes. Following the recommendation of Patankar (1980; Harlow and Welch, 1965), a staggered mesh was used, in which all scalar variables like temperature, pressure, composition etc. are calculated at a nodal point inside the control volume and the velocities are calculated at the faces of the control volumes.

**Table 7-5.** Terms of Equation 7-77 for each conservation equation.

Conservation Equation	$\Phi$	$\ddot{\rho}$	$\Gamma$	$Sc$	$Sp$
Total Mass	1	$\rho_m$	0	0	0
Species	1	$\rho_{m,i}$	0	$\frac{\partial}{\partial z} \left[ \mathcal{D}_i S_l \rho_l \frac{\partial c_{i,l}}{\partial z} \right]$ $+ \frac{1}{r} \frac{\partial}{\partial r} \left[ r \mathcal{D}_i S_l \rho_l \frac{\partial c_{i,l}}{\partial r} \right]$	0
Axial momentum	$U_m$	$\rho_m$	$\mu_m$	$-\frac{\partial p}{\partial z} - \frac{2}{3} \frac{\partial}{\partial z} [\mu_m \nabla \cdot \mathbf{u}]$ $+ \frac{1}{r} \frac{\partial}{\partial r} \left( r \mu_m \frac{\partial V_m}{\partial z} \right)$ $+ \frac{\partial}{\partial z} \left( \mu_m \frac{\partial U_m}{\partial z} \right)$	0
Radial momentum	$V_m$	$\rho_m$	$\mu_m$	$-\frac{\partial p}{\partial r} - \frac{2}{3} \frac{\partial}{\partial r} [\mu_m \nabla \cdot \mathbf{u}] V_m$ $+ \frac{1}{r} \frac{\partial}{\partial r} \left[ r \mu_m \frac{\partial V_m}{\partial r} \right] + \frac{\partial}{\partial z} \left[ \mu_m \frac{\partial U_m}{\partial r} \right]$	$-2 \frac{\mu_m}{r^2}$
Energy	$T$	0	$\lambda_m$	$-\frac{\partial}{\partial t} (\rho_m h_m) - \frac{\partial}{\partial z} (\rho_m h_m U_m)$ $- \frac{1}{r} \frac{\partial}{\partial r} (r \rho_m h_m V_m)$ $- \sum_{i=1}^N \left[ \frac{\partial}{\partial z} (J_i h_{i,l}) + \frac{1}{r} \frac{\partial}{\partial r} (r J_i h_{i,l}) \right]$	0

The mesh employed was non-uniform, concentrated in the regions of larger gradients are higher to improve accuracy.

The integration of the equations in time was calculated using the first order implicit Euler scheme and the integration in space was calculated using the power-law scheme as suggested by Patankar (1980). The velocity-pressure coupling was treated using the SIMPLEC algorithm (Van Doormaal and Raithby, 1984). The algebraic equation systems were solved using the tridiagonal matrix algorithm (TDMA) coupled with the block-correction acceleration method proposed by Settari and Aziz (1973).

#### 7.4.1.

#### Convergence criteria and general procedure of the numerical solution

The solution was considered converged at each time step when the sum of the residue was lower than  $10^{-8}$ . The same tolerance was used for all conservation equations.

The thermodynamic model used follows the same implementation as described in Chapter 3. Both the multisolid model proposed by Lira-Galeana et al. (1996) and the solid solution model proposed by Coutinho et al. (2006).

The general numerical procedure to solve the proposed model follows briefly.

- Read input data, starting conditions and calculation of all properties that are independent of temperature, pressure and composition;
- Construction of the non-uniform grid;
- Initialization of all variables. For the temperature, the system is initiated with a temperature of 38 °C throughout the entire domain;
- Determination of the properties at the initial time instant, based on the uniform temperature, pressure of the steady state flow and known species concentration, obtained with thermodynamic phase equilibria calculations;
- External iteration in time:
  1. Impose temperature of the cold surface (inner copper tube) following the experimental temperature ramp;
  2. Thermodynamic phase equilibria calculations;
  3. Calculate all properties that are a function of the temperature, pressure and composition;
  4. Prepare post processing data and outputs;
  5. If the logical variable LSTOP is true, the execution is terminated. Otherwise, the calculation will continue in the same time step;

6. If the global composition is converged, the calculation will increase the time step. Otherwise, calculations proceed for the same time step;
7. Solve the linear momentum equations and the continuity equation resulting in the velocity and pressure fields;
8. Solve the energy conservation equation obtaining the temperature field;
9. Solve the species continuity equations, obtaining the density of component  $i$ ;
10. Iteration is incremented. The total simulation time is verified and if it matches the set final simulation time the logical variable LSTOP is set to true;
11. Return to step 1.

#### 7.4.2. Grid and time step convergence studies

To better capture the steep gradients, the grid was defined concentrated near the annulus' walls, with a finer grid near the cold wall where the deposition occurs.

The time step was based on the Courant number, which is a dimensionless number that reflects the number of grid volumes that will be traversed by the property by advection in one time step. According to the literature (Patankar, 1980), the time step should be small enough to assure that the property do not crosses more than one grid volume. The Courant number was defined based on the axial direction flow as follows

$$Co = \frac{U_{avg} \Delta t}{\Delta z_{ref}} \leq 1 \quad (7-81)$$

where  $\Delta z_{ref} = \frac{L}{N_z}$  is the reference grid size in the axial direction, where  $N_z$  is the number of control volumes in the axial direction. Note that as the grid gets thinner, to keep Co unaltered, the time step should be decreased.

The mesh size was defined based on a grid convergence test. Three different grids were evaluated, 47×32, 77×62 and 114×96, named grids 1, 2 and 3, respectively. For each grid, the time step was changed in order to keep the Courant number smaller than one. The time steps used were 0.1 s, 0.05 s and 0.025 s for grids 1, 2 and 3, respectively, resulting in the respective Courant numbers of 0.42, 0.34 and 0.25.

To evaluate the mesh convergence, the amount of solid deposited was selected. To this end, the average thickness of the deposit in the domain was determined. The deposit region was defined as the region with 2% solid mass fraction, as suggested by Souza (2014).

$$\varepsilon_{\text{avg}} = \frac{1}{L_t} \int r|_{B_s \geq 0.02} dz \quad (7-82)$$

The average thickness along the pipe length  $\varepsilon_{\text{avg}}$  was compared for a simulated time of 30 minutes. Only the multisolid themodynamic model was used as it runs 32 faster than the solid solution model. The differences between grids 1 and 2, and grids 2 and 3 are shown in Table 7-6.

**Table 7-6.** Results for the grid convergence test.

Differences	(%)
<b>Grids 1 and 2</b>	1.64
<b>Grids 2 and 3</b>	0.16

As observed, all differences were lower than 2%. The difference between grids 2 and 3 is smaller than the difference between grids 1 and 2. The convergence with the grid indicates the consistency of the implemented numerical solution, and the numerical solution converges to the exact algebraic solution as the grid spacing goes to zero.

As the grid gets thinner, convergence time increases substantially. As such, grid 2 (77×62) was chosen to be used for the numerical solution of the model. For this grid, 1 hour of simulated flow takes approximately 200 h of real CPU time.

Even though the implicit time method used is theoretically always stable, a time step convergence test was performed, to guarantee accuracy of the solution. The time step convergence test was carried out using three different time steps, 0.1 s, 0.05 s and 0.025 s, for tests 1, 2 and 3, respectively. As the grid was already chosen (77×62), the Courant numbers and time steps can be found in Table 7-7.

**Table 7-7.** Time steps and respective Courant numbers used in the time step convergence test.

<b>Test</b>	<b>Time step (s)</b>	<b>Co</b>
<b>1</b>	0.1	0.69
<b>2</b>	0.05	0.34
<b>3</b>	0.025	0.17

As used for the grid convergence test, the 2% solid mass fraction thickness was once again used for the time step convergence test. This test was also performed using the multisolid model. The differences between tests 1 and 2 and tests 2 and 3 were calculated for 2, 5, 10, 20 and 30 minutes of simulation time. The results are shown in Table 7-8.

**Table 7-8.** Results for the time step convergence tests.

<b>Time</b>	<b>Differences between tests (%)</b>	
	<b>1 and 2</b>	<b>2 and 3</b>
<b>2</b>	16.90	15.57
<b>5</b>	13.80	11.16
<b>10</b>	8.13	3.58
<b>20</b>	3.88	2.78
<b>30</b>	2.87	1.06

The differences are high at first, where the solid formation is intense. As time progresses, the differences diminish, becoming inferior to 3%. As observed for the grid convergence tests, the error diminishes as the time step is lowered, another evidence for the consistency of the implemented model. From the results, the time step 2, 0.05 s, was used for all simulations.

## **7.5. Experimental Data**

To evaluate the proposed model, the results were compared to the experimental results obtained by Veiga (2017). To this end, the domain of interest was defined based on Veiga (2017) experimental test section.

### 7.5.1. Measured deposition thickness

The deposition thickness profiles measured by Veiga (2017) for the experiment with a Reynolds number of 746 are presented in Table 7-9 and also shown in Figure 7-13.

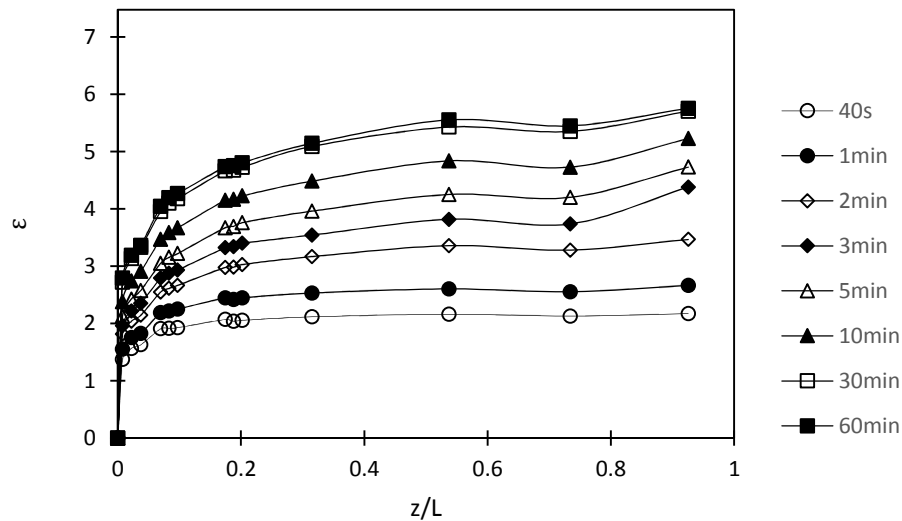


**Figure 7-13.** Experimental deposition thickness profile at different times measured by Veiga (2017).

**Table 7-9.** Dimensionless deposition thickness measured by Veiga (2017) as a function of time.

Pos (mm)	X (z/L)	40s	1min	2min	3min	5min	10min	30min	60min
		$\epsilon/R_{gap}$							
0	0	0	0	0	0	0	0	0	0
8	0.01	1.372	1.554	1.815	1.962	2.127	2.381	2.720	2.792
23	0.02	1.564	1.753	2.039	2.218	2.425	2.740	3.134	3.188
39	0.04	1.628	1.824	2.143	2.351	2.577	2.910	3.327	3.364
73	0.07	1.908	2.190	2.548	2.791	3.052	3.469	3.956	4.045
87	0.08	1.913	2.218	2.611	2.875	3.153	3.588	4.102	4.194
102	0.10	1.927	2.251	2.665	2.934	3.220	3.669	4.178	4.268
183	0.17	2.069	2.446	2.978	3.321	3.672	4.152	4.665	4.737
197	0.19	2.038	2.421	2.981	3.341	3.693	4.166	4.674	4.751
212	0.20	2.054	2.445	3.029	3.399	3.758	4.226	4.725	4.806
331	0.32	2.116	2.530	3.167	3.543	3.960	4.485	5.090	5.143
564	0.54	2.160	2.603	3.358	3.817	4.251	4.837	5.426	5.553
771	0.73	2.129	2.554	3.280	3.738	4.200	4.727	5.351	5.448
972	0.93	2.173	2.663	3.467	4.381	4.730	5.226	5.704	5.754

## 7.6. Results and Discussions

To evaluate the results of the model proposed, initially, the thermodynamic model is analyzed. Then, the flow field variables are presented. In the sequence, the thickness of the deposit is discussed.

### 7.6.1. Thermodynamic model

Two thermodynamic models were developed at the present work: multisolid model and solid solution model. However, the solid solution model coupled with the flow model required an elevated time to run in relation with the multisolid model, which was 32 times faster. Therefore, only the multisolid model was selected to be investigated here, coupled with the flow solution. However, since the solid solution model is more accurate, before combining the multisolid solid with the flow solution, at the present section, both models are compared, to guarantee the quality of the solution.

As shown in previous Chapters, the multisolid model might not be able to describe the solid-liquid phase equilibrium of *n*-alkane mixtures. To evaluate its results, the calculated solid-liquid equilibrium temperature was compared to the experimental result available. The calculated solubility curve is shown in Figure 7-14. As can be clearly seen, the calculated solid-liquid equilibrium temperature is far from the experimental result. The multisolid model cannot be tuned, as it is a direct function of the thermophysical properties of the mixture components. As such, the only way to correct the model and adjust it to match the experimental results is by adjusting the thermophysical properties of the components themselves. As a reference, since the multisolid model cannot reproduce de DSC curve as mentioned in Chapter 3, the solubility curve calculated using the solid solution model was used as a reference for choosing which of the thermophysical properties of the *n*-alkanes to be adjusted. The solubility curve calculated using the solid solution model is presented in Figure 7-14. As both curves are almost parallel, distant only in temperature, the solid-solid transition temperature and the melting temperatures of the *n*-alkanes were chosen as thermophysical properties to be adjusted. A linear value of 11 K was added to both temperatures of each *n*-alkane and the solubility

curve was recalculated, rendering a result close to the solid solution model and matching the experimental solid-liquid equilibrium temperature. The curve calculated from the adjusted curve is also presented in Figure 7-14. Once the model was adjusted, the simulation of the flow was carried out.

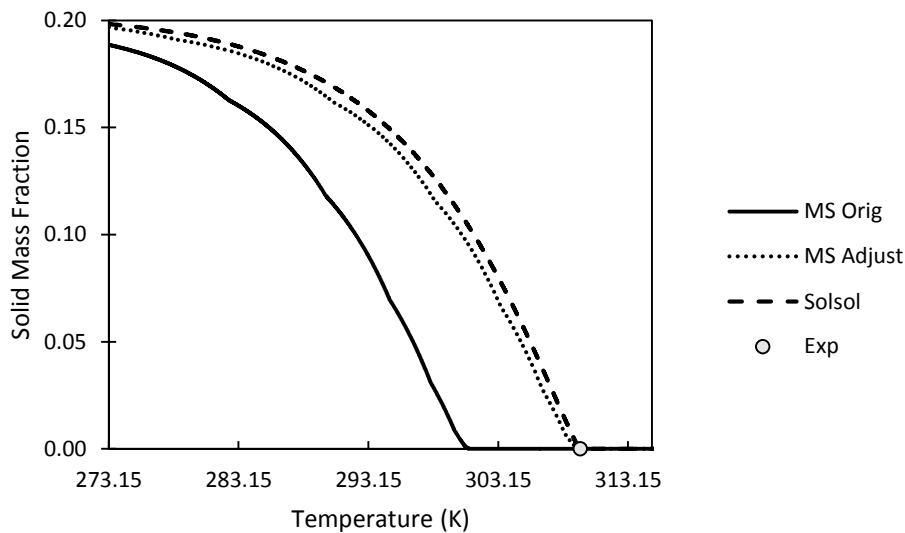


**Figure 7-14.** Solubility curves calculated from the original multisolid model (MS Orig), the adjusted multisolid model (MS Adjust) and the solid solution model (Solsol). The experimental solid-liquid equilibrium temperature is marked in the circle (Exp).

### 7.6.2. Flow variables

The solution of the conservation equations governing the flow field were numerically obtained as described in previous section. As already mentioned, the computational domain was defined to match the experimental apparatus, as an annular pipe with internal radius  $R_{in}$  and external radius  $R_{ex}$ , corresponding to a radial gap  $R_{gap}$ , with length  $L$ . Also as already mentioned, the flow was considered axisymmetric.

The initial condition for the numerical experiment was numerically obtained by solving the conservation equation until steady state condition was attained, for a flow with uniform temperature equal to  $T_{in}$ . The temperature  $T_{in}$  and mass flow rate  $\dot{m}_{in}$  were maintain constant at the inlet, as well as the species concentration. The experimentally measured copper wall temperature  $T_{cold}$  was adjusted by a polynomial as a function of time and it was imposed during the cooling.

Due to the low temperature at the copper wall, at the inner annular radius, the temperature of the fluid close to this wall starts to drop. The temporal evolution of the temperature is shown in Figure 7-15, through isotherm contour maps. To help visualize the flow, the axial coordinate was normalized by the test section length. In the figures,  $y = r - R_{in}$ , in mm. It can be seen the heat diffusing inside the domain, cooling the incoming mixture as time increases. Further, it can be seen a steeper temperature gradient near the inlet. Note also that the temperature distribution 30 minutes after the beginning of the process is very similar to the one obtained after 1 hour, indicating that the temperature is reaching a new equilibrium.

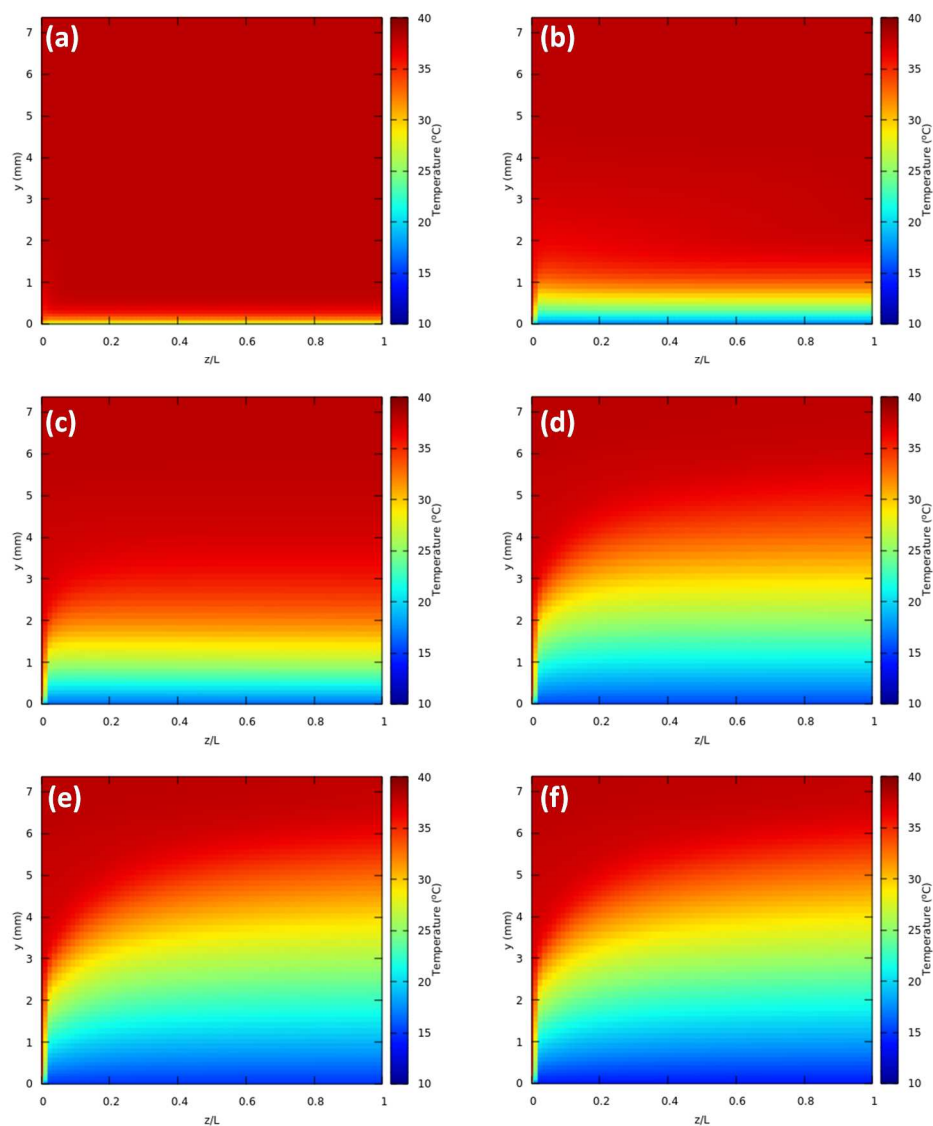


**Figure 7-15.** Temperature fields in times (a) 10 s, (b) 1 min, (c) 3 min, (d) 10 min, (e) 30 min and (f) 1 h.

Figure 7-16 illustrates the temperature profile along the gap at three axial positions ( $z/L=0.3$ ;  $0.6$  and  $0.9$ ), 1 hour after the beginning of the process. Note that the temperature profile inside the deposit indicates a pure conduction profile, with a strong change in the slope at the interface with the moving fluid, where its temperature is almost constant.

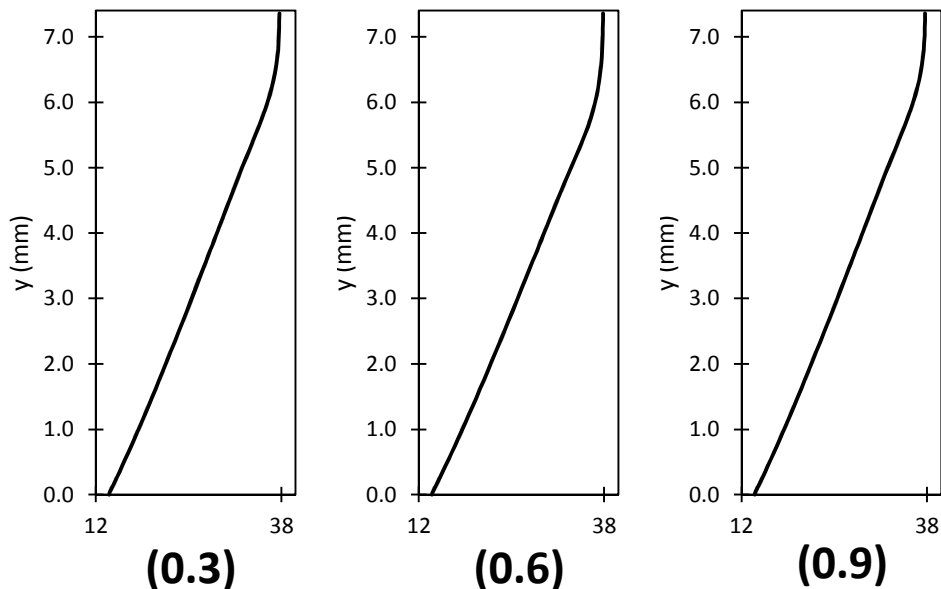


**Figure 7-16.** Temperature profiles at dimensionless lengths of 0.3, 0.6 and 0.9 in 1 h.

When the fluid temperature becomes lower than solid-liquid equilibrium temperature, solids start to come out of solution. The amount of solids are proportional to the temperature in the manner displayed by the solubility curve shown in Figure 7-14. As a result, the mass fraction of solids in the mixture increases as the temperature decreases, as can be seen in Figure 7-17.

The solid mass fraction profiles is shown in Figure 7-18, at the same coordinates selected to illustrate the temperature profile. It can be clearly seen the direct relation between both variables, and the slight increase of the region corresponding to the deposit region.

In turn, as the solid mass fraction increases, the thermophysical properties of the mixture start to be modified by the presence of such solids. The mixture density, its thermal conductivity and specially its viscosity start to increase.

The viscosity field in different times instants are presented in Figure 7-20, while the viscosity profile along the cross section at threes position after 1 hour of

cooling is shown in Figure 7-19. As can be seen, the viscosity very rapidly grows as the solid mass fraction increases. Such a result is expected from the model that imposes an exponential increase in the viscosity with 200 times the solid volume fraction. To avoid numerical instabilities, the viscosity was limited to 1000 mPa.s. After 10 s from the beginning of the cooling process, the viscosity is almost uniform along the test section and equal to the limit value. At time evolves, a more clear dependence of the viscosity in the temperature and solid concentration can be observed, with similar shapes between these three variables.

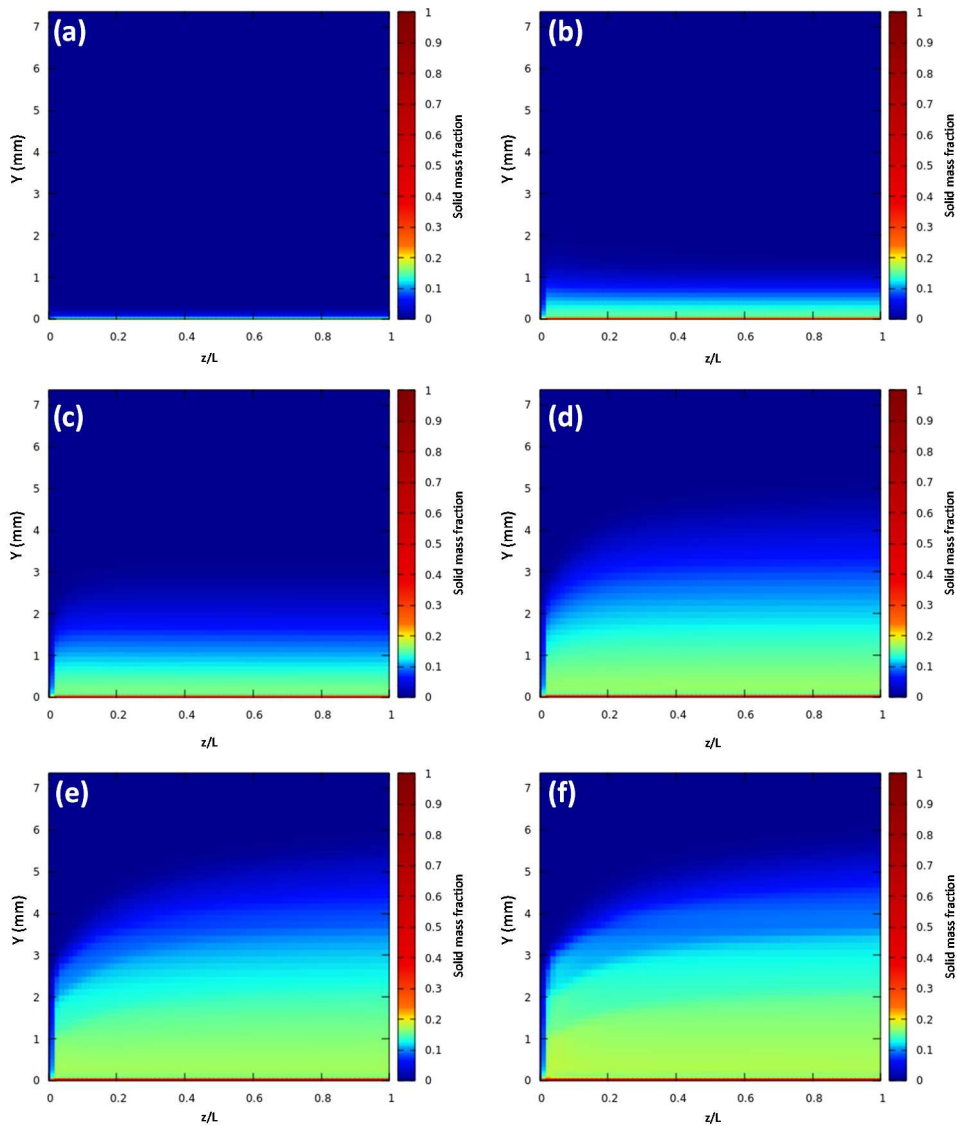


**Figure 7-17.** Solid mass fraction fields in times (a) 10 s, (b) 1 min, (c) 3 min, (d) 10 min, (e) 30 min and (f) 1 h.

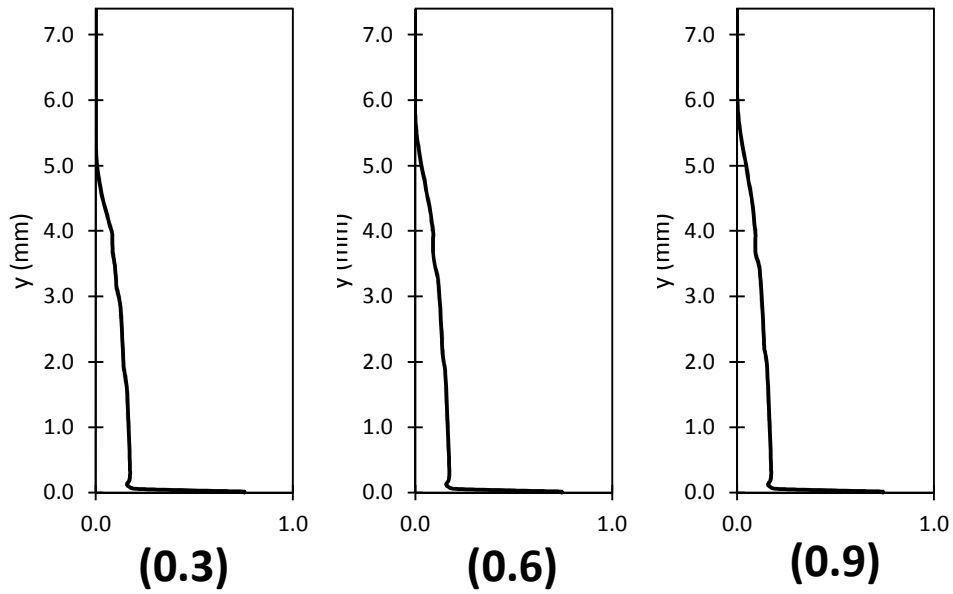


**Figure 7-18.** Solid mass fraction profiles at dimensionless lengths of 0.3, 0.6 and 0.9 in 1 h.

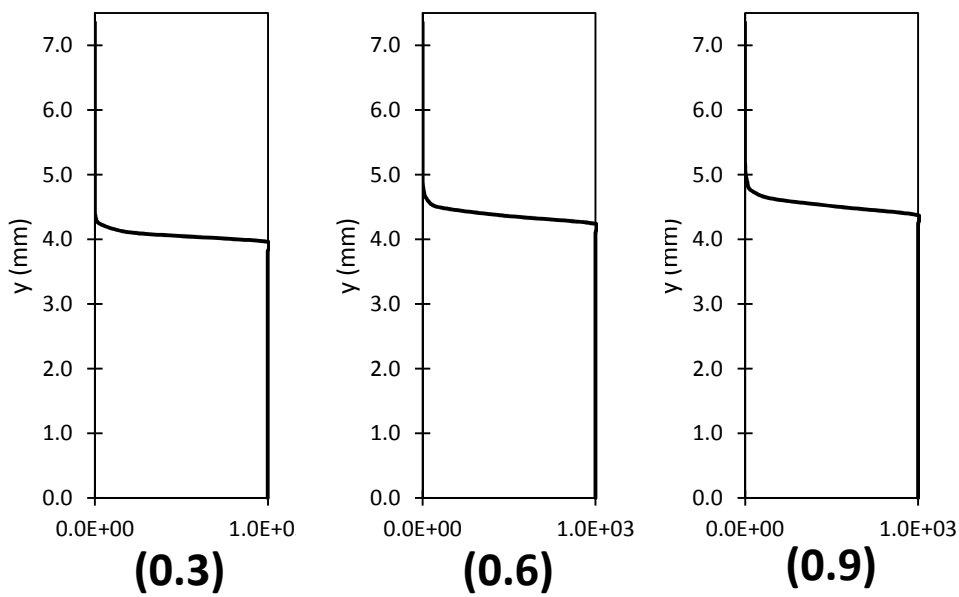


**Figure 7-19.** Axial mixture viscosity profiles at dimensionless lengths of 0.3, 0.6 and 0.9 in 60 min.

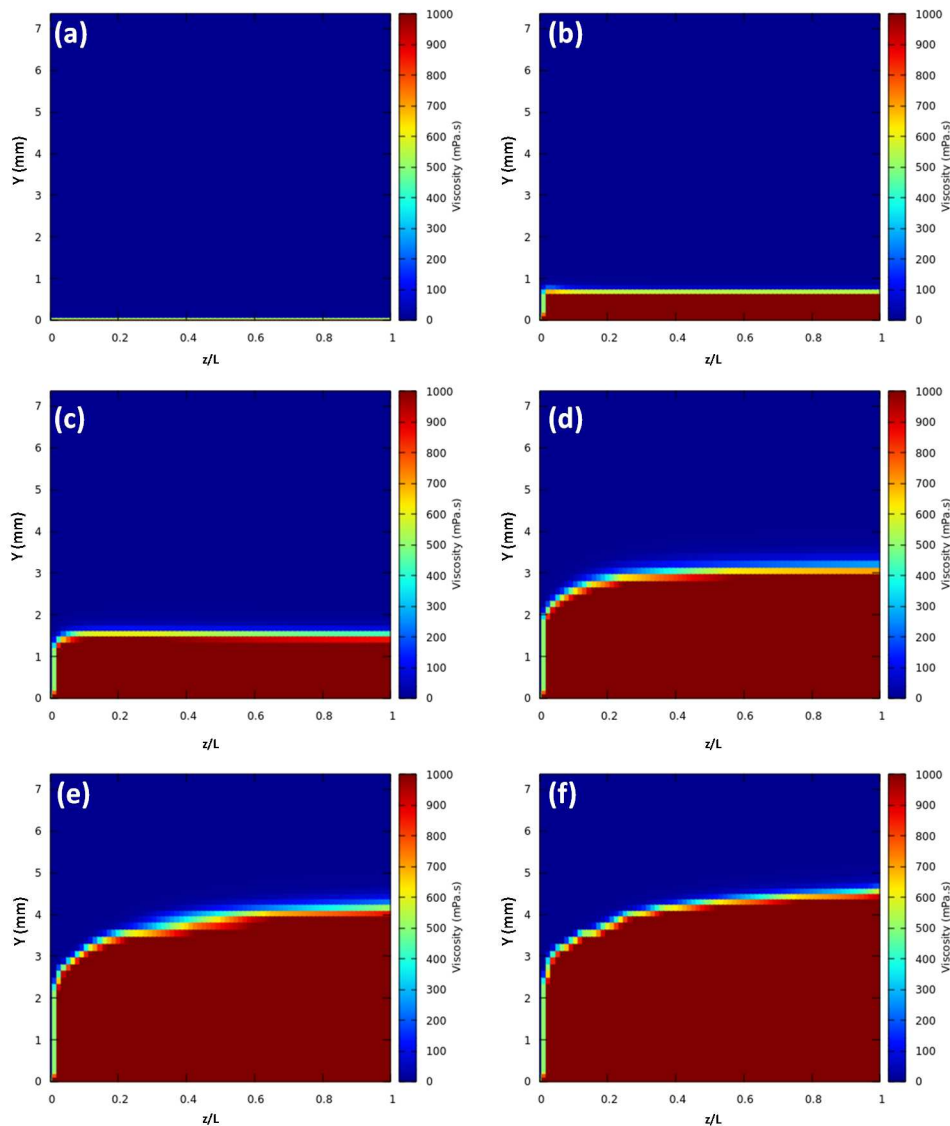


**Figure 7-20.** Viscosity fields in times (a) 10 s, (b) 1 min, (c) 3 min, (d) 10 min, (e) 30 min and (f) 1 h.

The deposit region can also be inferred from Figure 7-20, as the region with large viscosity.

The mixture density also increases as the solid mass fraction rises. Nevertheless, the differences are never very large except for a thin layer near the cold wall, as can be seen in Figure 7-21. This is direct consequence of the small differences between the solid and the liquid densities, in the order of 10 to 20 %.

The density profile along the cross section is illustrate at Figure 7-22, where its variation inside the deposit region can be better observed.

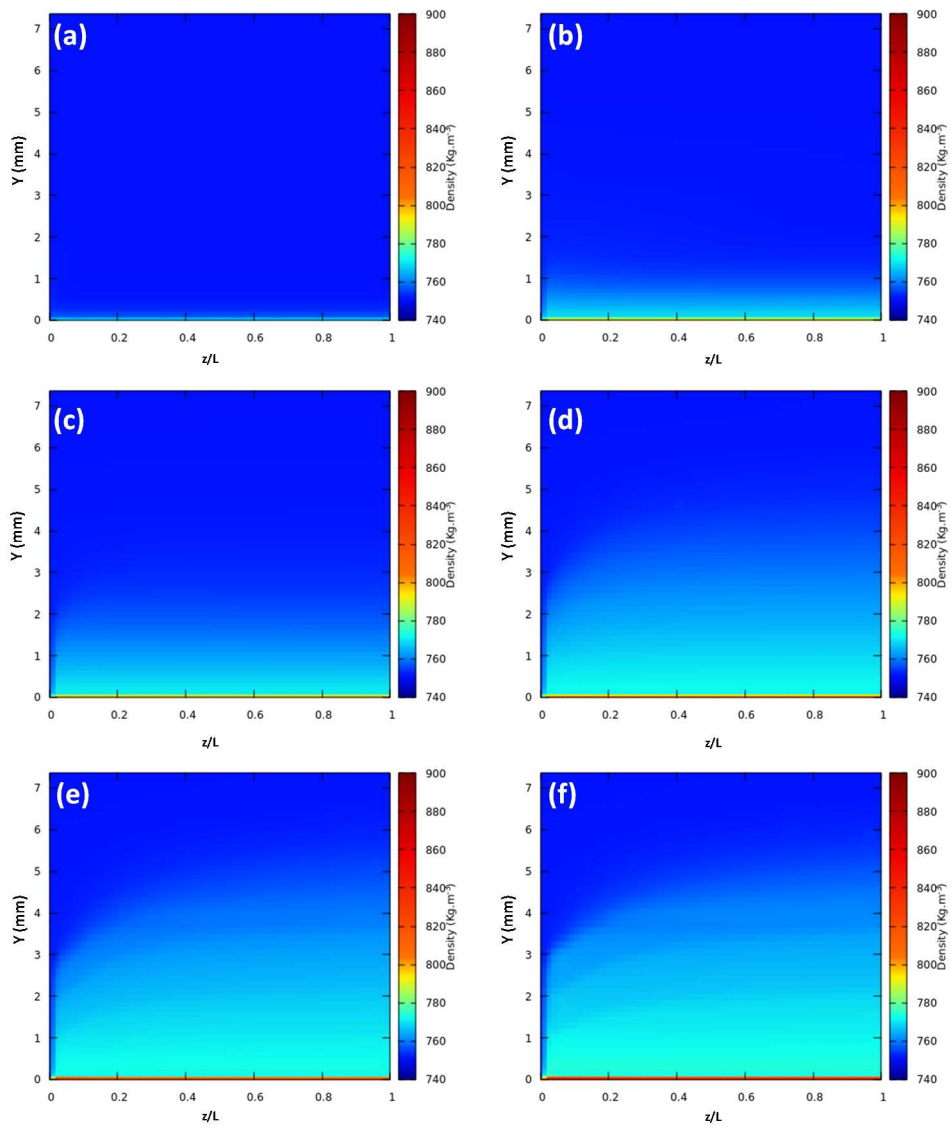


**Figure 7-21.** Mixture density fields in times (a) 10 s, (b) 1 min, (c) 3 min, (d) 10 min, (e) 30 min and (f) 1 h.

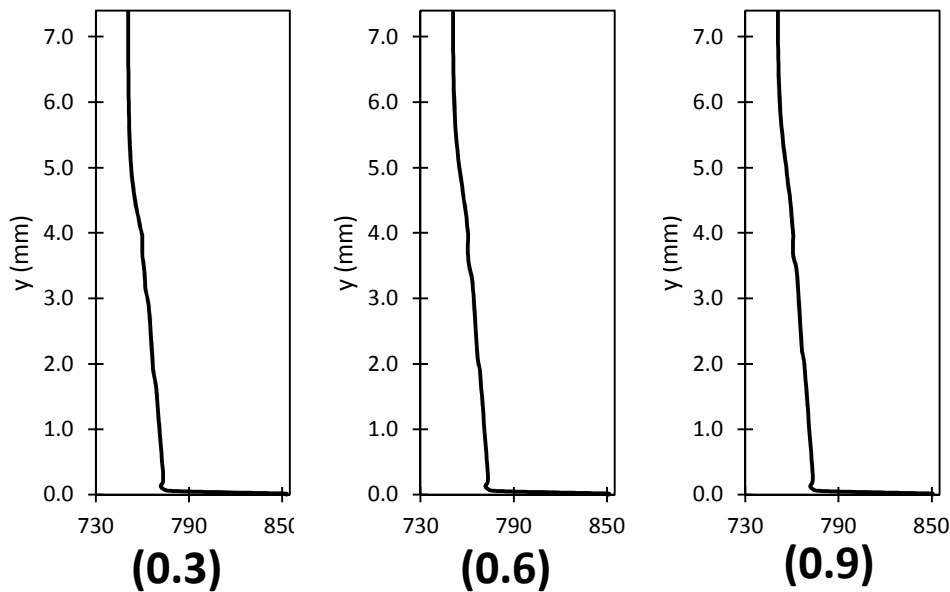


**Figure 7-22.** Mixture density profiles at dimensionless lengths of 0.3, 0.6 and 0.9 in 60 min.

As shown, the viscosity depends strongly on the temperature and solid concentration, and it has a direct impact in the flow velocity. As the viscosity increases, the velocity quickly drops, coming to a complete stop when the viscosity is high enough. The axial mixture velocity field in different times are presented in Figure 7-23.

As a direct result of the increase in the viscosity, the changes in the fluid temperature affect directly the flow velocity. As the viscosity increases, the velocity quickly drops, coming to a complete stop when the viscosity is high enough. In the proposed model, this is the only responsible for the formation of the paraffin deposit. It is defined as a region where the viscosity is high enough so that there is no longer flow. The axial mixture velocity ( $U_m$ ) fields reveal the spontaneous paraffin deposition close to cold wall. As time passes, the open area of the annulus diminishes since the flow near the cold wall starts to slow down until a complete stop. As a result, the flow accelerates towards the outer rim of the annulus.

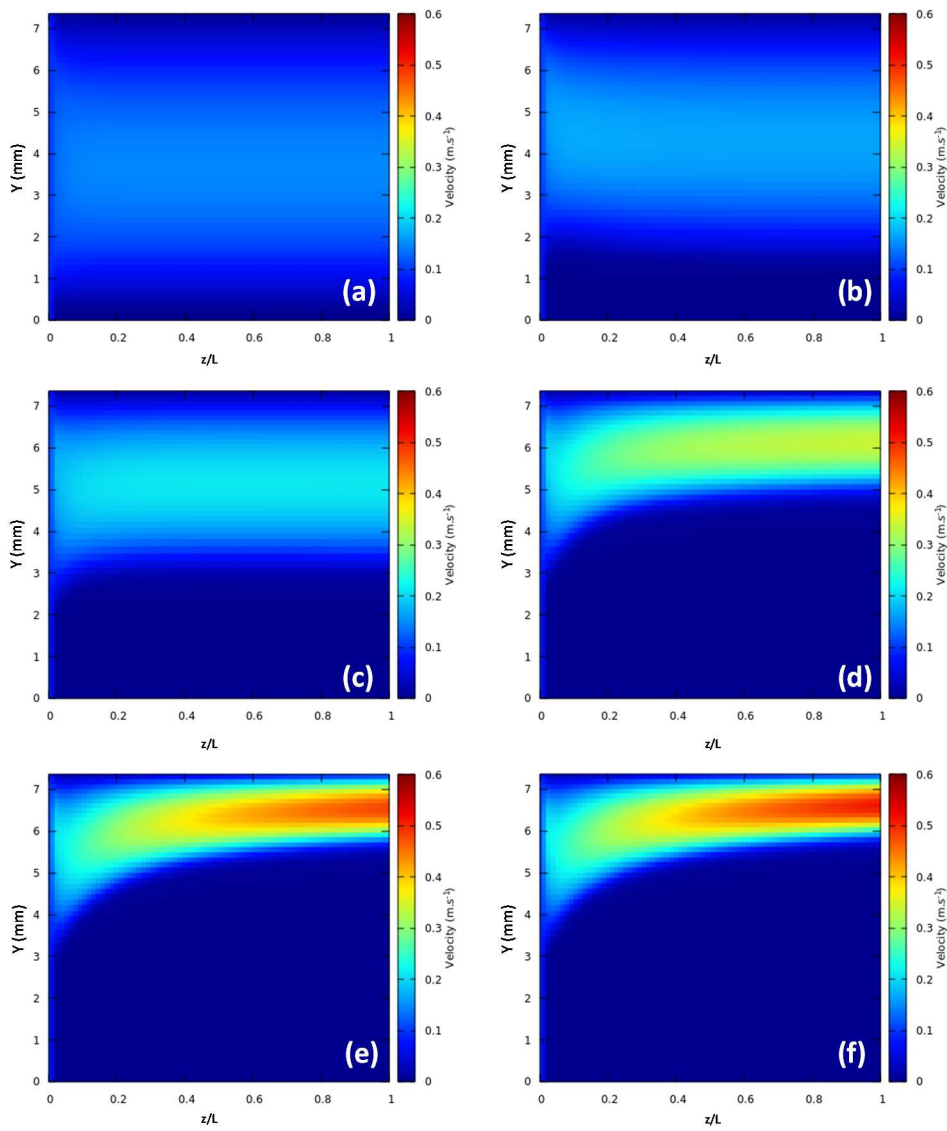


**Figure 7-23.** Axial mixture velocity fields in times (a) 10 s, (b) 1 min, (c) 3 min, (d) 10 min, (e) 30 min and (f) 1 h.

### 7.6.3. Paraffin deposition from the model

In the proposed model, the paraffin deposition is a direct consequence of the decrease in the flow velocity caused by an increase in viscosity. As such, the deposit thickness should be attributed by the point where the velocity is considered to be small enough to cease any transport due to advection. To illustrate the behavior of the velocity as times evolves, the axial mixture velocity (in  $\text{m s}^{-1}$ ) in three different points of the test section (dimensionless lengths of 0.3, 0.6 and 0.9) at different times (10 s, 10 min, 30 min and 1 h) are shown in Figure 7-24. It can be seen that the velocity is zero at the outer cylinder wall and near the inner cylinder, with a maximum value closer to the inner wall, as expected. Further, since the flow is laminar, the velocity profile resembles a parabolic profile. At times passes, the region with negligible velocity near the inner cylinder increases. The region where the velocity is zero is the deposit itself. The resolution of the graph shown in Figure 7-24 is not enough to establish a threshold velocity to define the limit of the deposit region. After the analysis of the results, this threshold was set to be  $1.0 \times 10^{-4}$  m/s. The location of such velocity over the entire length of the test section at different times are shown in Figure 7-25. As such, these profiles coincide with the thickness of the deposit obtained with the proposed model.

To evaluate any correlation between the above set velocity and the amount of solids, in Figures 7-26 and 7-27 the thickness of the deposit is shown together with geometric location along the domain of a few values of solid mass fraction profiles (0.0, 0.02, 0.05 and 0.1, namely) at 10 min and 1 h, respectively. For both cases, the deposit thickness tends to coincide with the location of the 0.05 solid mass fraction.

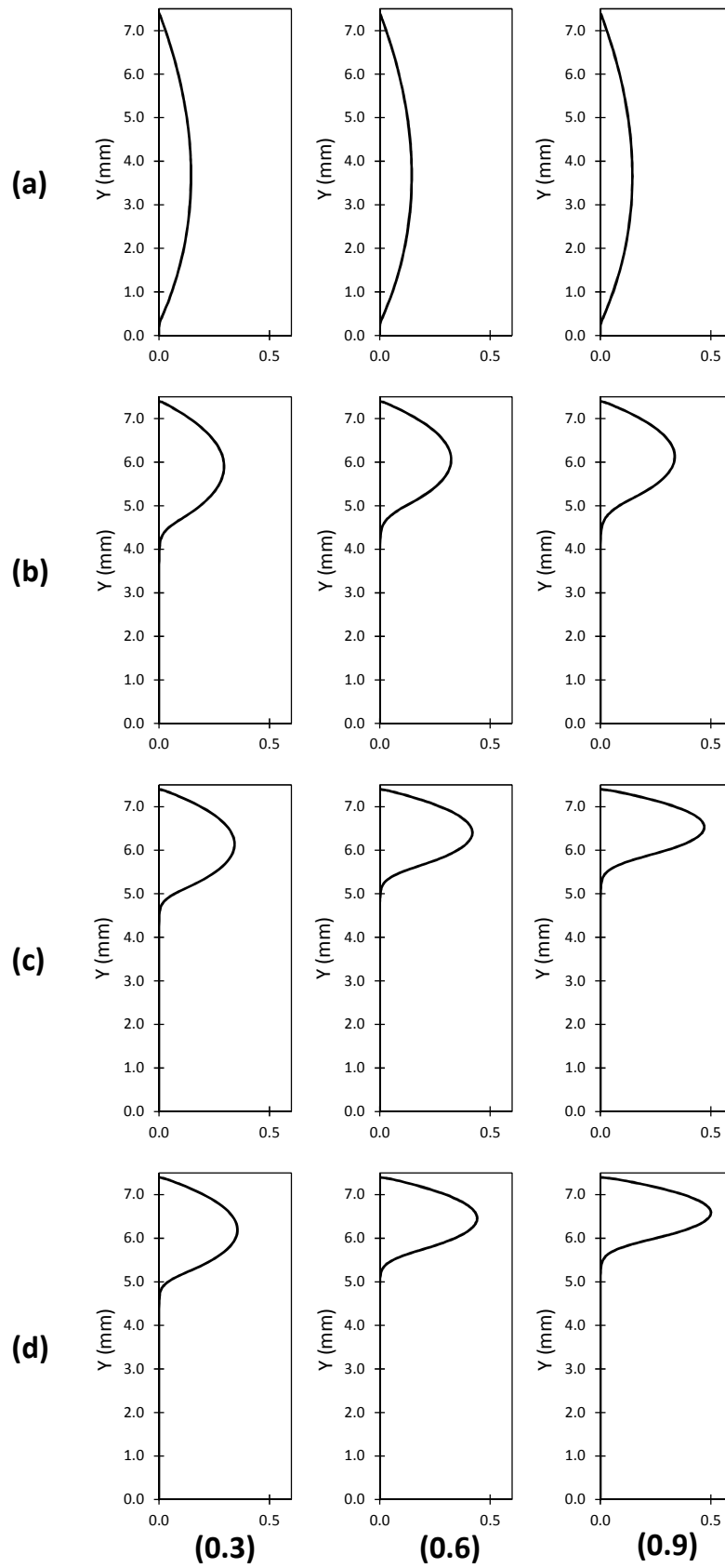


**Figure 7-24.** Axial mixture velocity profiles at dimensionless lengths of 0.3, 0.6 and 0.9 in times (a) 10 s, (b) 10 min, (c) 30 min and (d) 1 h. The velocity is expressed in  $\text{m}\cdot\text{s}^{-1}$ .

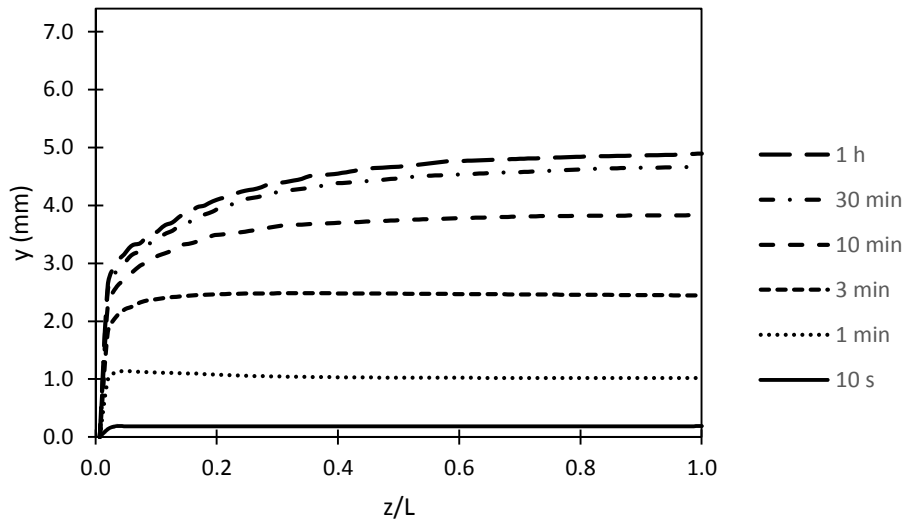


**Figure 7-25.** Profiles of the axial mixture velocity of  $1.0 \times 10^{-4} \text{ m.s}^{-1}$  at different times.

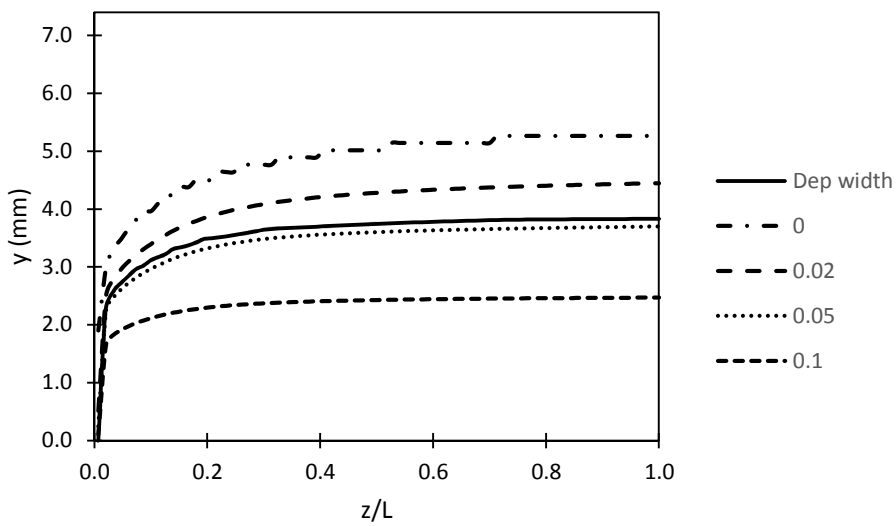


**Figure 7-26.** Thickness of the paraffin deposit at 10 min and the solid mass fraction profile for the values of 0.00, 0.02, 0.05 and 0.10.

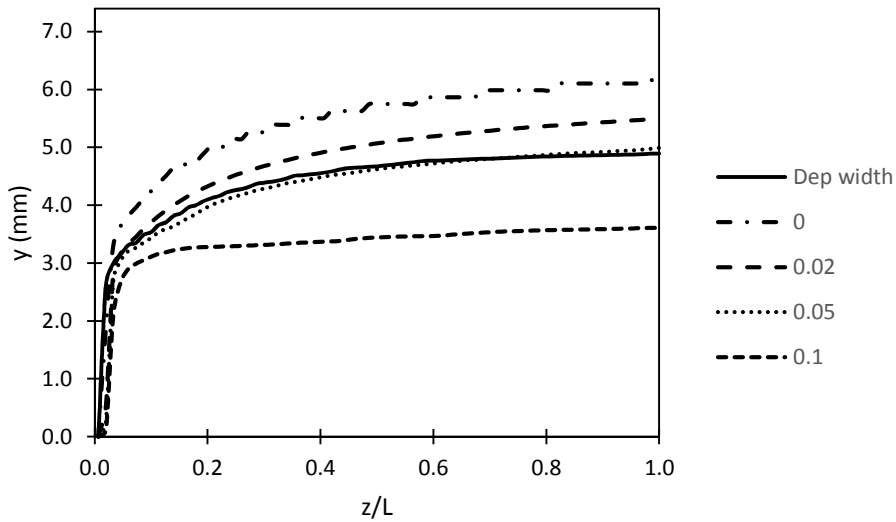


**Figure 7-27.** Thickness of the paraffin deposit at 1 h and the solid mass fraction profile for the values of 0.00, 0.02, 0.05 and 0.10.

#### 7.6.4. Comparison with experimental results

To evaluate the model's ability to reproduce the experimental deposit thickness, the deposit thickness from the model at different times are plotted together with the experimental results of Veiga (2017) in Figure 7-28.

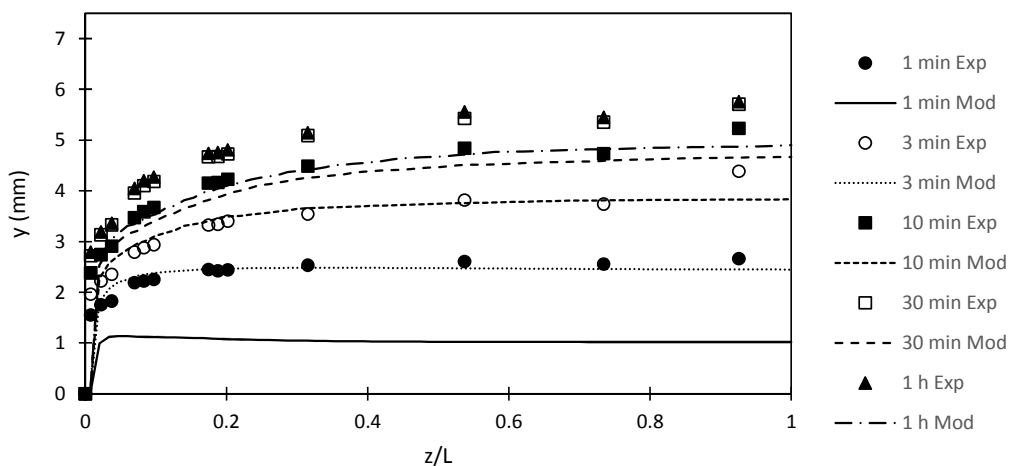


**Figure 7-28.** Experimental thickness of the paraffin deposit (Veiga, 2017) and the thickness obtained from the proposed model at times 1 min, 3 min, 10 min, 30 min and 1 h.

The comparison between the spatial and time evolution of the paraffin deposit thickness obtained with the proposed model with the experimental data reveals that the model systematically underestimates its value. For all cases, especially at early simulation times, the differences are considerable. These differences reduce as the experiment reaches the permanent state, but are still significant.

Although the qualitative deposit thickness profile in time and space was correctly predicted, the fact that it was systematically underestimated is an indication that the model proposed must be improved. One possible improvement could be the introduction of a model to determine the relative solid-liquid velocity, which was set equal to zero for the tests presented. Further, the consideration of the shear rate on the mixture viscosity evaluation might be necessary. The shear rate is expected to be at its maximum value near the walls or, in the presence of a deposit, over the deposit-fluid contact, thus, for a shear-thinning fluid, the viscosity is expected to be reduced. Since this effect was neglected, the results obtained with the mentioned approximations tend to be an upper bound of the achievable deposit thickness caused solely by non-Newtonian behavior of paraffin suspensions.

A common practice found in the literature is tuning the thermophysical properties of the mixture and adjusting them at one's will to in order to reproduce experimental results. It is important to note that this is not the case of the present work. It rather holds dear the ability to reproduce the thermophysical properties of the system under study and by comparing the results obtained from the model to the experimental results. As such, one is then able to evaluate the effectiveness of a given mechanism defined as the main driving force for paraffin deposition. From the results, one is lead to the conclusion that even though a rheological model without shear-thinning effect renders paraffin deposits with an adequate structure and distribution, it solely cannot account for the entire deposit. It is also believed that even if the rheological model is improved, other mechanisms may play an important role to quantitatively reproduce the deposition thickness.

One very good result obtained with the present model is the prediction of the thermal conductivity of the deposit. The results obtained with the proposed model agree well with the experimental results. Recently, Veiga et al. (2017) reported the experimental effective thermal conductivity of these deposits measured under flow conditions. The results indicated values around  $0.22 \text{ W}\cdot\text{m}^{-1}\cdot\text{K}^{-1}$ . In Figure 7-29, the effective mixture thermal conductivity contours of the deposit at different times is

shown, while the profile along the cross section is shown in Figure 7-30 at three position after 1 hour. The results show that deposit exhibit a rather uniform effective thermal conductivity at permanent state and the value is in good agreement with the experimental result. It is noteworthy to remember the reader that, although the Maxwell model is usually applied to combine liquid and solid thermal conductivities in paraffin deposition simulations, the present work proposed the use of a much simpler mixing rule, through the direct combination weighted by the volume fraction of each phase.

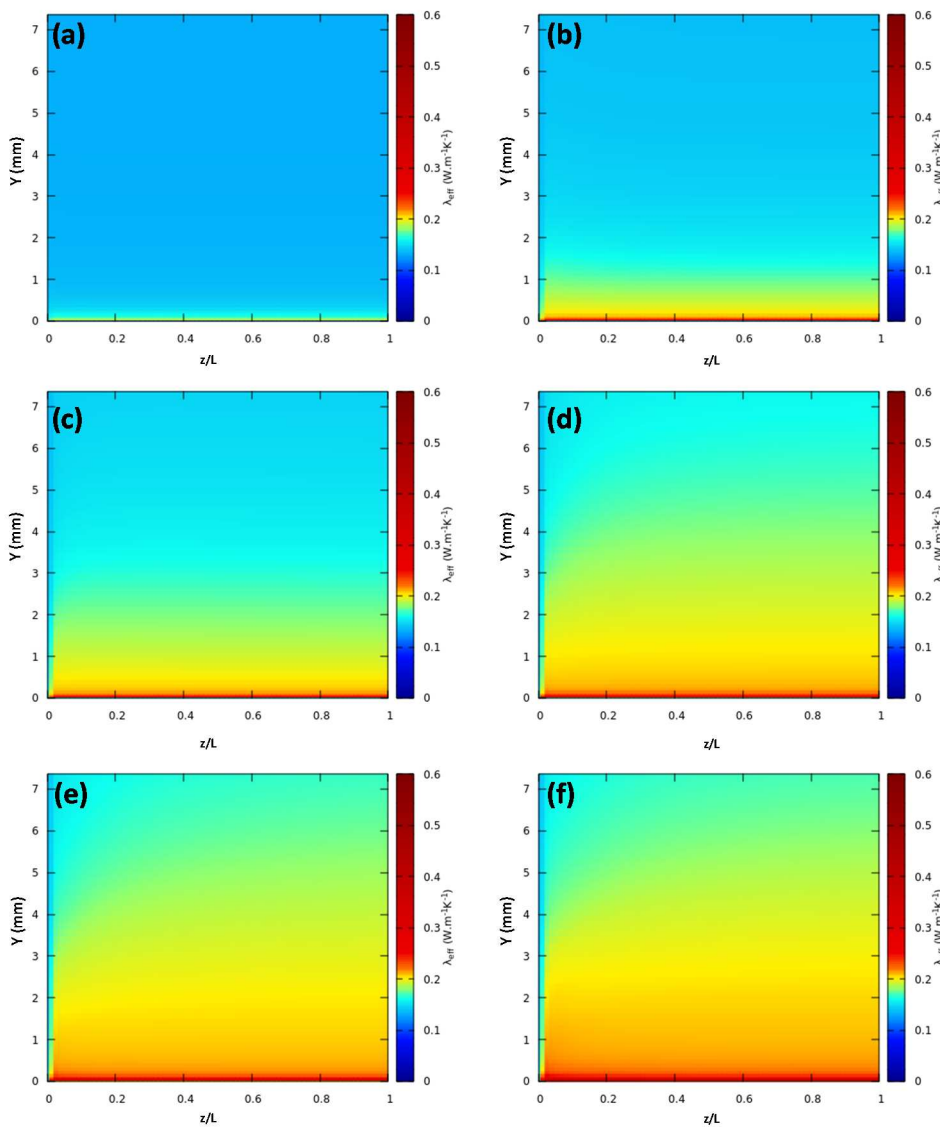


**Figure 7-29.** Effective thermal conductivity profiles in times (a) 10 s, (b) 1 min, (c) 3 min, (d) 10 min, (e) 30 min and (f) 1 h.

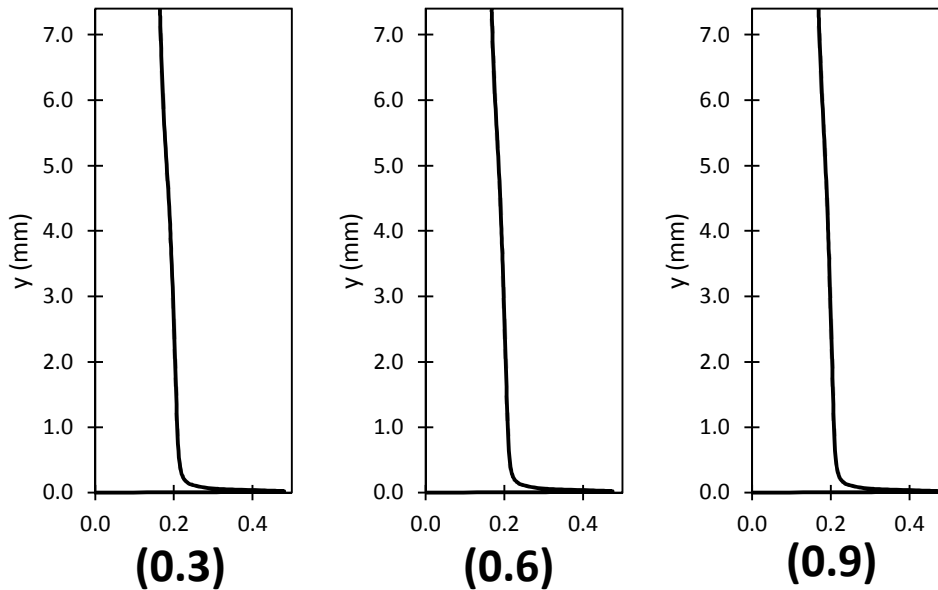


**Figure 7-30.** Effective thermal conductivity profiles at dimensionless lengths of 0.3, 0.6 and 0.9 in 60 min.

## 7.7. Conclusions

To predict paraffin deposition, a drift-flux liquid-solid mixture model was proposed, allowing both liquid and solid to be advected throughout the domain. Although the phases may have different velocities, as a first approximation, the results presented here, were obtained considering the relative velocity null, therefore, the model was simplified to a homogeneous model, and mixture properties were applied.

The thermophysical properties calculated from the different models and correlations were compared to the experimental results and were able to reproduce these to their reported uncertainties. As such, the model carries the closest description of the fluid as possible. To couple the thermodynamic model with the flow solution, the multisolid thermodynamic model was used due to its smaller computing time.

At the present work, the wax deposition mechanism was based on the rheological behavior of the fluid. As temperature decreases, the solid concentration increases resulting in an increase of the mixture viscosity, leading to a reduction in the flow velocity. The deposit region was considered as the region with negligible velocity.

A numerical simulation was performed aiming to reproduce the experimental data. The numerical predictions for the deposit thickness distribution were parallel to the experimental data, but they were underestimated, especially at the beginning of the process, indicating that some additional model improvements are necessary. Among these, the first efforts should be towards substituting the multisolid model used by the modified UNIQUAC. The role played by the drift flux being set to zero should also be investigated. The rheological model should also be improved, including a dependence of the shear rate on the viscosity. One can also argue that the fluid rheology is not the sole mechanism to account for the total paraffin deposition observed in the experiments. Further, a model for the relative liquid-solid velocity must be examined. On the other hand, the model was able to reproduce quite well the effective thermal conductivity, agreeing with the measured values.

## 8 CONCLUSIONS

Wax deposition, a major discipline of Flow Assurance, has been under investigation for decades. Due to its impact in production and the lack of easily applicable contingency strategy, wax deposition has to be dealt with still in the design phase of the production installations. As such, since the early 1980's, efforts have been directed towards modeling the complex wax deposition phenomenon.

Over the years, the critical evaluation of the wax deposition mechanisms proposed initially through a solid physical background start to make room to flexible codes that could be tuned to different experiment scenarios. Although very important to address immediate issues, such a strategy abandons the fundamental search for the underlying physics behind wax deposition.

In an attempt to investigate the phenomenon in a fundamental way, the current work proposed a research strategy that would evaluate every single part of the complex wax deposition model to perform under well-controlled optimal conditions. As such, the results of such a model could then be used to test and evaluate the physical basis of wax deposition.

Most of the effort was directed towards establishing a robust thermodynamic solid-liquid phase behavior model that was able to describe with precision such a behavior for model fluids as well as real complex mixtures. To achieve such a goal, a new strategy to evaluate solid-liquid thermodynamic models was developed. Results showed that the model used throughout Chapters 2, 3, 4 and 5 was robust enough to precisely describe the solid-liquid phase behavior of asymmetric model mixtures at both ordinary and high pressures, as well as describe the behavior of complex mixture like Diesel fuel samples. The unavailability of reliable methods to characterize *n*-alkanes distribution in oil samples hindered the results to be expanded all the way to such systems.

To assure the solid physical basis of the models being employed in this work, the thermal conductivity measurement of heavy *n*-alkanes in both liquid and solid phases was carried out and reported for the first time. The correct modeling of

thermophysical properties and the availability of such data is an imperative necessity in the development of precise models.

At last, a drift flux solid-liquid CFD model was proposed. Coupled with a thermodynamic model to supply the model with phase equilibria and properties data, the model was used to investigate the experimental results obtained by Veiga (2017). As a first approximation, the relative solid-liquid velocity was considered null. The wax deposition mechanism evaluated was based on the assumption that the mixture velocity is a direct function of the solid volume fraction and, thus, the temperature. The results showed that although a qualitative agreement between the model and experimental results were obtained, the model underestimated the thickness of the deposit. As such, the model the proposed should be improved, relaxing some of the simplifications applied. However, one can also argue that the model by itself cannot account for the full wax deposition, an indication that other mechanisms can be playing a role in the total phenomenon. On the other hand, the thermal conductivity of the deposit matched the recently available experimental thermal conductivity of such a deposit measured under real flow conditions. This fact strengthens the presented conclusions that perhaps wax deposition is not a single mechanism phenomenon.

ABRAMS, D. S.; PRAUSNITZ, J. M. Statistical thermodynamics of liquid mixtures: A new expression for the excess Gibbs energy of partly or completely miscible systems. **AIChE Journal**, v. 21, n. 1, p. 116–128, 1975.

AKEIBER, H.; NEJAT, P.; MAJID, M. Z. A.; WAHID, M. A.; JOMEHZADEH, F.; ZEYNALI FAMILI, I.; CALAUTIT, J. K.; HUGHES, B. R.; ZAKI, S. A. A review on phase change material (PCM) for sustainable passive cooling in building envelopes. **Renewable and Sustainable Energy Reviews**, v. 60, p. 1470–1497, 2016.

APTE, M. S. **Investigation of paraffin deposition during multiphase flow in pipelines and wellbores**. Master's Thesis. The University of Tulsa, 1999.

APTE, M. S.; MATZAIN, A.; ZHANG, H.-Q.; VOLK, M.; BRILL, J. P.; CREEK, J. L. Investigation of paraffin deposition during multiphase flow in pipelines and wellbores—part 2: modeling. **Journal of Energy Resources Technology**, v. 123, n. 2, p. 150–157, 2001.

ARCHER, D. G. The enthalpy of fusion of gallium. **Journal of Chemical and Engineering Data**, v. 47, n. 2, p. 304–309, 2002.

ASSAEL, M. J.; CHARITIDOU, E.; NIETO DE CASTRO, C. A.; WAKEHAM, W. A. The thermal conductivity of n-hexane, n-heptane, and n-decane by the transient hot-wire method. **International Journal of Thermophysics**, v. 8, n. 6, p. 663–670, 1987.

ASSAEL, M. J.; DYMOND, J. H.; TSELEKIDOU, V. Correlation of high-pressure thermal conductivity, viscosity, and diffusion coefficients for n-alkanes. **International Journal of Thermophysics**, v. 11, n. 5, p. 863–873, 1990.

ASSAEL, M. J.; DYMOND, J. H.; PAPADAKI, M.; PATTERSON, P. M. Correlation and prediction of dense fluid transport coefficients. I. n-alkanes. **International Journal of Thermophysics**, v. 13, n. 2, p. 269–281, 1992.

ASSAEL, M. J.; ANTONIADIS, K. D.; WU, J. New measurements of the thermal conductivity of PMMA, BK7, and Pyrex 7740 up to 450K. **International Journal of Thermophysics**, v. 29, n. 4, p. 1257–1266, 2008.

ASSAEL, M. J.; BOGDANOU, I.; MYLONA, S. K. Reference correlation of the thermal conductivity of n-heptane from the triple point to 600 K and up to 250 MPa. **Journal of Physical and Chemical Reference Data**, V. 42, n. 2, p. 023101-1-9, 2013a.

ASSAEL, M. J.; MYLONA, S. K.; TSIGLIFISI, C. A.; HUBER, M. L.; PERKINS, R. A. Reference correlation of the thermal conductivity of n-hexane from the triple point to 600 K and up to 500 MPa. **Journal of Physical and Chemical Reference Data**, V. 42, n. 1, p. 013106-1-8, 2013b.

AZEVEDO, L. F. A.; TEIXEIRA, A. M. A Critical review of the modeling of wax deposition mechanisms. **Petroleum Science and Technology**, v. 21, n. 3–4, p. 393–408, 2003.

BANKI, R.; HOTEIT, H.; FIROOZABADI, A. Mathematical formulation and numerical modeling of wax deposition in pipelines from enthalpy-porosity approach and irreversible thermodynamics. **International Journal of Heat and Mass Transfer**, v. 51, n. 13–14, p. 3387–3398, 2008.

BHAT, N. V.; MEHROTRA, A. K. Modeling of deposit formation from “Waxy” mixtures via moving boundary formulation: radial heat transfer under static and laminar flow conditions. **Industrial and Engineering Chemistry Research**, v. 44, n. 17, p. 6948–6962, 2005.

BIDMUS, H. O.; MEHROTRA, A. K. Heat-transfer analogy for wax deposition from paraffinic mixtures. **Industrial & Engineering Chemistry Research**, v. 43, n. 3, p. 791–803, 2004.

BIDMUS, H. O.; MEHROTRA, A. K. Measurement of the liquid-deposit interface temperature during solids deposition from wax-solvent Mixtures under static cooling conditions. **Energy and Fuels**, v. 22, n. 2, p. 1174-1182, 2008a.

BIDMUS, H. O.; MEHROTRA, A. K. Measurement of the liquid-deposit interface temperature during solids deposition from wax-solvent mixtures under sheared cooling. **Energy and Fuels**, v. 22, n. 6, p. 4039–4048, 2008b.

BIPM; IEC; IFCC; ILAC; ISO; IUPAC; IUPAP; OIML. **Evaluation of measurement data - Guide to the expression of uncertainty in measurement**, 2008.

BROADHURST, M. G. An analysis of the solid phase behavior of the normal paraffins. **Physics and Chemistry**, v. 66A, No.3, n. 3, p. 241–249, 1962.

BROWN, T. S.; NIESEN, V. G.; ERICKSON, D. D. Measurement and prediction of the kinetics of paraffin deposition. **Proceedings of SPE Annual Technical Conference and Exhibition**, p. 353–368, 1993.

BURGER, E. D.; PERKINS, T. K.; STRIEGLER, J. H. Studies of wax deposition in the trans alaska pipeline. **Journal of Petroleum Technology**, v. 33, n. 6, p. 1075–1086, 1981.

CALADO, J. C. G.; FARELEIRA, J. M. N. A.; NIETO DE CASTRO, C. A.; WAKEHAM, W. A. Thermal conductivity of five hydrocarbons along the saturation line. **International Journal of Thermophysics**, v. 4, n. 3, p. 193–208, 1983.

CHI, Y.; DARABOINA, N.; SARICA, C. Investigation of inhibitors efficacy in wax deposition mitigation using a laboratory scale flow loop. **AIChE Journal**, v. 62, n. 11, p. 4131–4139, 2016.

CHI, Y.; DARABOINA, N.; SARICA, C. Effect of the flow field on the wax deposition and performance of wax inhibitors: cold finger and flow loop testing. **Energy and Fuels**, v. 31, n. 5, p. 4915–4924, 2017.

CHIAVARO, E. **Differential Scanning Calorimetry - Application in Fat and Oil Technology**. Florida: CRC Press, 2015.

CIVAN, F. A correlation for thermal conductivity of liquid n-alkanes based on the Vogel-Tammann-Fulcher-Hesse equation. **Chemical Engineering Science**, v. 63, n. 24, p. 5883–5886, 2008.

COUTINHO, J. A. P.; ANDERSEN, S. I.; STENBY, E. H. Evaluation of activity coefficient models in prediction of alkane solid-liquid equilibria. **Fluid Phase Equilibria**, v. 103, n. 1, p. 23–39, 1995.

COUTINHO, J. A. P.; KNUDSEN, K.; ANDERSEN, S. I.; STENBY, E. H. A local composition model for paraffinic solid solutions. **Chemical Engineering Science**, v. 51, n. 12, p. 3273–3282, 1996.

COUTINHO, J. A. P., RUFFIER-MÉRAY, V. Experimental measurements and thermodynamic modeling of paraffinic wax formation in undercooled solutions. **Industrial & Engineering Chemistry Research**, v. 36, n. 11, p. 4977–4983, 1997.

COUTINHO, J. A. P. A thermodynamic model for predicting wax formation in jet and diesel fuels. **Energy and Fuels**, v. 14, n. 3, p. 625–631, 2000.

COUTINHO, J. A. P.; DAUPHIN, C.; DARIDON, J.-L. Measurements and modelling of wax formation in diesel fuels. **Fuel**, v. 79, n. 6, p. 607–616, 2000.

COUTINHO, J. A. P.; DARIDON, J.-L. Low-pressure modeling of wax formation in crude oils. **Energy and Fuels**, v. 15, n. 6, p. 1454–1460, 2001.

COUTINHO, J. A. P.; LOPES DA SILVA, J. A.; FERREIRA, A.; SOARES, M. R.; DARIDON, J.-L. Evidence for the aging of wax deposits in crude oils by Ostwald ripening. **Petroleum Science and Technology**, v. 21, n. 3–4, p. 381–391, 2003.

COUTINHO, J. A. P.; DARIDON, J.-L. The limitations of the cloud point measurement techniques and the influence of the oil composition on its detection. **Petroleum Science and Technology**, v. 23, p. 1113–1128, 2005.

COUTINHO, J. A. P., MIRANTE, F., PAULY, J. A new predictive UNIQUAC for modeling of wax formation in hydrocarbon fluids. **Fluid Phase Equilibria**, v. 247, p. 8–17, 2006.

COUTO, G. **Investigation of Two-Phase Oil-Water Paraffin Deposition**. Master's Thesis. The University of Tulsa, 2004.

CREEK, J. L.; LUND, H. J.; BRILL, J. P.; VOLK, M. Wax deposition in single phase flow. **Fluid Phase Equilibria**, v. 158–160, p. 801–811, 1999.

DA SILVA, V. M.; DO CARMO, R. P.; FLEMING, F. P.; DARIDON, J.-L.; PAULY, J.; TAVARES, F. W. Paraffin solubility and calorimetric data calculation using Peng-Robinson EoS and modified UNIQUAC models. **Journal of Petroleum Science and Engineering**, v. 156, p. 945–957, 2017.

DAUPHIN, C.; DARIDON, J.-L.; COUTINHO, J. A. P.; BAYLÈRE, P.; POTIN-GAUTIER, M. Wax content measurements in partially frozen paraffinic systems. **Fluid Phase Equilibria**, v. 161, n. 1, p. 135–151, 1999.

DIRAND, M.; BOUROUKBA, M.; BRIARD, A. J.; CHEVALLIER, V.; PETITJEAN, D.; CORRIOU, J. P. Temperatures and enthalpies of (solid + solid) and (solid + liquid) transitions of n-alkanes. **Journal of Chemical Thermodynamics**, v. 34, n. 8, p. 1255–1277, 2002.

DUMAS, J. P.; GIBOUT, S.; CÉZAC, P.; FRANQUET, E.; HAILLOT, D. Model for the DSC thermograms of the melting of ideal binary solutions **Thermochimica Acta**, v. 571, p. 64-76, 2013.

FANG, X.; FAN, L.-W.; DING, Q.; WANG, X.; YAO, X.-L.; HOU, J.-F.; YU, Z.-T.; CHEN, G.-H.; HU, Y.-C.; CEN, K.-F. Increased thermal conductivity of eicosane-based composite phase change materials in the presence of graphene nanoplatelets. **Energy and Fuels**, v. 27, n. 7, p. 4041–4047, 2013.

FIROOZABADI, A. Chapter 5. In: **Thermodynamics of Hydrocarbon Reservoirs**. New York: McGraw-Hill, 1999.

FLEMING, F. P.; PAULY, J.; DARIDON, J.-L. **Simulation of DSC Curves is Wax Precipitation Evaluation**. 20th European Conference on Thermophysical Properties. Porto, Portugal: 2014.

FLEMING, F. P.; DARIDON, J.-L.; AZEVEDO, L. F. A.; PAULY, J. Direct adjustment of wax thermodynamic model parameter to micro Differential Scanning Calorimetry thermograms. **Fluid Phase Equilibria**, v. 436, p. 20–29, 2017.

FLEMING, F. P.; SILVA, L. A.; LIMA, G. DOS S. V.; HERZOG, I.; ORLANDE, H. R.; DARIDON, J.-L.; PAULY, J.; AZEVEDO, L. F. A. Thermal conductivity of heavy even carbon number n-alkanes (C22 to C32). **IN PRESS**. 2018.

FORSMAN, H.; ANDERSSON, P. Effects of temperature and pressure on the thermal conductivity of solid n-undecane. **Berichte der Bunsengesellschaft für physikalische Chemie**, v. 87, p. 490–495, 1983.

FORSMAN, H.; ANDERSSON, P. Thermal conductivity at high pressure of solid odd-numbered n -alkanes ranging from C9H20 to C19H40. **The Journal of Chemical Physics**, v. 80, n. 6, p. 2804–2807, 1984.

FORSMAN, H.; ANDERSSON, P. Thermal conductivity of solid n-dodecane at high pressure and a comparison with n-undecane and n-tridecane. **Molecular**

**Physics: An International Journal at the Interface Between Chemistry and Physics**, v. 58, n. 3, p. 605–610, 1986.

FRIEND, D. G.; INGHAM, H.; FLY, J. F. Thermophysical properties of ethane. **Journal of Physical and Chemical Reference Data**, v. 20, n. 2, p. 275–347, 1991.

GRIGGS, E. I.; YARBROUGH, D. W. **Thermal Conductivity of solid Unbranched Alkanes from n-hexadecane to n-eicosane**. Proceedings of the 14th Southeastern Seminar on Thermal Science. Raleigh. Fev 1978

HAMOUDA, A. . A.; RAVNØY, J. M. Prediction of wax deposition in pipelines and field experience on the influence of wax on drag-reducer performance. **Offshore Technology Conference (OTC 7060)**, n. 7060, p. 669–679, 1992.

HAN, S.; HUANG, Z.; SENRA, M. J.; HOFFMANN, R.; FOGLER, H. S. Method to determine the wax solubility curve in crude oil from centrifugation and high temperature gas chromatography measurements. **Energy and Fuels**, v. 24, n. 3, p. 1753–1761, 2010.

HANSEN, J. H.; FREDENSLUND, A.; PEDERSEN, K. S.; ROENNINGSSEN, H. P. A thermodynamic model for predicting wax formation in crude oils. **AIChE Journal**, v. 34, n. 12, p. 1937–1942, 1988.

HANSEN, A. B.; LARSEN, E.; PEDERSEN, W. B.; NIELSEN, A. B.; ROENNINGSSEN, H. P. Wax precipitation from North Sea crude oils. 3. Precipitation and dissolution of wax studied by Differential Scanning Calorimetry. **Energy and Fuels**, v. 5, n. 6, p. 914–923, 1991.

HARLOW, F. H.; WELCH, J. E. Numerical calculation of time-dependent viscous incompressible flow of fluid with free surface. **Physics of Fluids**, v. 8, n. 12, p. 2182, 1965.

HARRIS, A.; LEVCHENKO, A. A. **Thermal conductivity measurements on phase change materials**. 40th Annual Conference of The North American Thermal Analysis Society. **Anais...Orlando**: 2012

HARRIS, A.; KAZACHENKO, S.; BATEMAN, R.; NICKERSON, J.; EMANUEL, M. Measuring the thermal conductivity of heat transfer fluids via the modified transient plane source (MTPS). **Journal of Thermal Analysis and Calorimetry**, v. 116, n. 3, p. 1309–1314, 2014.

HAYDUK, W.; MINHAS, B. S. Correlations for prediction of molecular diffusivities in liquids. **The Canadian Journal of Chemical Engineering**, v. 60, p. 295–299, 1982.

HERNANDEZ-PEREZ, O. C.; HENSLEY, H.; SARICA, C.; BRILL, J. P.; VOLK, M.; DELLE-CASE, E. Improvements in single-phase paraffin deposition modeling. **SPE Production & Facilities**, v. 19, n. 4, p. 237–244, 2004.

HOLMEN, R.; LAMVIK, M.; MELHUS, O. Measurements of the thermal conductivities of solid and liquid unbranched alkanes in the C 16 -to-C 19 range

during phase transition 1. **International Journal of Thermophysics**, v. 23, n. 1, p. 27–39, 2002.

HOOKE, R.; JEEVES, T. A. “Direct Search” solution of numerical and statistical problems. **Journal of the ACM**, v. 8, n. 2, p. 212–229, 1961.

HOTEIT, H.; BANKI, R.; FIROOZABADI, A. Wax deposition and aging in flowlines from irreversible thermodynamics. **Energy and Fuels**, v. 22, n. 4, p. 2693–2706, 2008.

HUANG, Z. **Application of the fundamentals of heat and mass transfer to the investigation of wax deposition in subsea pipelines**. Doctorate’s Thesis. University of Michigan, 2011.

HUANG, Z.; LEE, H. S.; SENRA, M. J.; FOGLER, H. S. A fundamental model of wax deposition in subsea oil pipelines. **AIChE Journal**, v. 57, n. 11, p. 2955–2964, 2011.

HUANG, Z.; ZHENG, S.; FOGLER, H. S. **Wax Deposition: Experimental Characterizations, Theoretical Modeling, and Field Practices**. Boca Raton: CRC Press, Taylor & Francis Group, 2015.

HUBER, M. L.; PERKINS, R. A. Thermal conductivity correlations for minor constituent fluids in natural gas: n-octane, n-nonane and n-decane. **Fluid Phase Equilibria**, v. 227, n. 1, p. 47–55, 2005.

IRBY, R. G.; PARSON, J. R.; KESHOK, E. G. An investigation of the thermal properties of octadecane, a material used in thermal energy storage systems. In: YARBROUGH, D. W. (Ed.). **Thermal Conductivity 19**. New York: Plenum Press, 1988. p. 121–143.

ISHII, M.; HIBIKI, T. **Thermo-Fluid Dynamics of Two-Phase Flow**. 2. ed. New York: Springer, 2011.

JI, H.-Y.; TOHIDI, B.; DANESH, A.; TODD, A. C. Wax phase equilibria: developing a thermodynamic model using a systematic approach. **Fluid Phase Equilibria**, v. 216, n. 2, p. 201–217, 2004.

JUYAL, P.; CAO, T.; YEN, A.; VENKATESAN, R. Study of live oil wax precipitation with high-pressure micro-differential scanning calorimetry. **Energy and Fuels**, v. 25, n. 2, p. 568–572, 2011.

KARIZNOVI, M.; NOUROZIEH, H.; ABEDI, J. Phase composition and saturated liquid properties in binary and ternary systems containing carbon dioxide, n-decane, and n-tetradecane. **Journal of Chemical Thermodynamics**, v. 57, p. 189–196, 2013.

KASHIWAGI, H.; OISHI, M.; TANAKA, Y.; KUBOTA, H.; MAKITA, T. Thermal conductivity of fourteen liquids in the temperature range 298–373 K. **International Journal of Thermophysics**, v. 3, n. 2, p. 101–116, 1982.

KATZ, D. L.; FIROOZABADI, A. Predicting phase behavior of condensate/crude-oil systems using methane interaction coefficients. **Journal of Petroleum Technology**, v. 30, n. 11, p. 1649–1655, 1978.

KENISARIN, M. M. Thermophysical properties of some organic phase change materials for latent heat storage. A review. **Solar Energy**, v. 107, p. 553–575, 2014.

KESLER, M. G.; LEE, B. I. Improve prediction of enthalpy of fractions. **Hydrocarbon Processing**, v. 55, n. 3, p. 153–158, 1976.

KONSTANTINOV, V. A.; MANZHELII, V. G.; REVYAKIN, V. P.; SMIRNOV, S. A. Heat transfer in the orientationally disordered phase of SF<sub>6</sub>. **Physica B**, v. 262, n. 4, p. 421–425, 1999.

KONSTANTINOV, V. A.; REVYAKIN, V. P.; SAGAN, V. V. Rotation of the methyl groups and thermal conductivity of molecular crystals: Ethane. **Low Temperature Physics**, v. 32, n. 7, p. 689–694, 2006.

KONSTANTINOV, V. A.; REVYAKIN, V. P.; SAGAN, V. V. The isochoric thermal conductivity of solid n-alkanes: Propane C<sub>3</sub>H<sub>8</sub>. **Low Temperature Physics**, v. 35, p. 577–579, 2009.

KONSTANTINOV, V. A.; REVYAKIN, V. P.; SAGAN, V. V. Isochoric thermal conductivity of solid n-alkanes: Hexane C<sub>6</sub>H<sub>14</sub>. **Low Temperature Physics**, v. 37, n. 5, p. 420–423, 2011.

KONTOGEOORGIS, G. M.; GANI, R. Chapter 10. In: **Computer Aided Property Estimation for Process and Product Design**. Amsterdam: Elsevier B.V., 2004.

LARSEN, B. L.; RASMUSSEN, P.; FREDENSLUND, A. A modified UNIFAC group-contribution model for prediction of phase equilibria and heats of mixing. **Industrial & Engineering Chemistry Research**, v. 26, n. 3, p. 2274–2286, 1987.

LASHKARBOLOOKI, M.; HEZAVE, A. Z.; BAYAT, M.; KHADEMI, M. H.; VAFERI, B. A simple correlation for prediction of thermal conductivity of liquid hydrocarbons and aromatics. **Journal of Theoretical and Computational Chemistry**, v. 15, n. 8, p. 1650065, 2016.

LATINI, G.; DI NICOLA, G.; PIERANTOZZI, M. Liquid thermal conductivity prediction for alkanes, ketones and silanes. **Physics and Chemistry of Liquids**, v. 55, n. 6, p. 747–765, 2017.

LE NEINDRE, B.; GARRABOS, Y.; NIKRAVECH, M. Measurements of the thermal conductivity of propane in the supercritical region. **Journal of Chemical and Engineering Data**, v. 59, n. 11, p. 3422–3433, 2014.

LE NEINDRE, B. Measurements of the thermal conductivity of propane at the approach of the coexistence line. **Fluid Phase Equilibria**, v. 450, p. 1–12, 2017.

LE NEINDRE, B.; DESMAREST, P.; LOMBARDI, G.; KAYSER, M.; CHALVIGNAC, G.; GUMEROV, F.; GARRABOS, Y. Thermal conductivity of gaseous and liquid n-pentane. **Fluid Phase Equilibria**, v. 460, p. 146–154, 2018.

LEE, H. S. **Computational and Rheological Study of Wax Deposition and Gelation in Subsea Pipelines**. Doctorate's Thesis. University of Michigan, 2008.

LÉTOFFÉ, J. M.; CLAUDY, P.; KOK, M. V.; GARCIN, M.; VOLLE, J. L. Crude oils: characterization of waxes precipitated on cooling by d.s.c. and thermomicroscopy. **Fuel**, v. 74, n. 6, p. 810–817, 1995.

LI, S. F. Y.; MAITLAND, G. C.; WAKEHAM, W. A. The thermal conductivity of n-hexane and n-octane at pressures up to 0.64 GPa in the temperature range 34 – 90 °C. **Berichte der Bunsengesellschaft für physikalische Chemi**, v. 88, p. 32–36, 1984.

LIMA, G. DOS S. V. **Estudo comparativo da deposição de parafina em dedo-frio dinâmico e seção tubular, na presença de inibidor químico**. Master's Thesis. Pontifícia Universidade Católica do Rio de Janeiro, 2017.

LINDELOFF, N.; KREJBJERG, K. A compositional model simulating wax deposition in pipeline systems. **Energy and Fuels**, v. 16, n. 4, p. 887–891, 2002.

LIRA-GALEANA, C.; FIROOZABADI, A.; PRAUSNITZ, J. M. Thermodynamics of wax precipitation in petroleum mixtures. **AIChE Journal**, v. 42, n. 1, p. 239–248, 1996.

LUND, H. J. **Investigation of paraffin deposition during single-phase liquid flow in pipelines**. Master's Thesis. The University of Tulsa, 1998.

MACÍAS-SALINAS, R. Modeling the thermal conductivity of n-alkanes via the use of density scaling. **Journal of Chemical Thermodynamics**, v. 116, p. 363–371, 2018.

MAITHUFI, M. N.; JOUBERT, D. J.; KLUMPERMAN, B. Application of gemini surfactants as diesel fuel wax dispersants. **Energy and Fuels**, v. 25, n. 1, p. 162–171, 2011.

MAJEED, A.; BRINGEDAL, B.; OVERA, S. Model calculates wax deposition for N. Sea oils. **Oil and Gas Journal**, v. 88, n. 25, p. 63-69, 1990.

MANABE, R. **A comprehensive mechanistic heat transfer model for the two-phase flow with high-pressure flow pattern validation**. Doctorate's Thesis. The University of Tulsa, 2001.

MARANO, J. J.; HOLDER, G. D. General equation for correlating the thermophysical properties of n-paraffins, n-olefins, and other homologous series. 1. Formalism for developing asymptotic behavior correlations. **Industrial & Engineering Chemistry Research**, v. 36, n. 5, p. 1887–1894, 1997.

MATZAIN, A. **Single Phase Liquid Paraffin**. Master's Thesis. The University of Tulsa, 1996.

MATZAIN, A. **Multiphase Flow Paraffin Deposition Modeling**. Doctorate's Thesis. The University of Tulsa, 1999.

MENASHE, J.; WAKEHAM, W. A. The thermal conductivity of n-nonane and n-undecane at pressures up to 500 MPa in the temperature range 35 – 90 °C. **Berichte der Bunsengesellschaft für physikalische Chemie**, v. 86, n. 6, p. 541–545, 1982.

MENDES, P. R. S.; BRAGA, S. L. Obstruction of pipelines during the flow of waxy crude oils. **Journal of Fluids Engineering**, v. 118, n. 4, p. 722–728, 1996.

MERINO-GARCIA, D.; MARGARONE, M.; CORRERA, S. Kinetics of waxy gel formation from batch experiments. **Energy and Fuels**, v. 21, n. 3, p. 1287–1295, 2007.

MICHELSEN, M. L. The isothermal flash problem. Part I. Stability. **Fluid Phase Equilibria**, v. 9, n. 1, p. 1–19, 1982.

MICHELSEN, M. L.; MOLLERUP, J. M. Chapters 8, 9 and 12. In: **Thermodynamic Models: Fundamentals & Computational Aspects**. 2nd. ed. Holte: Tie-Line Publications, 2007. p. 382.

MORGAN, D. L.; KOBAYASHI, R. Direct vapor pressure measurements of ten n-alkanes in the C-10-C(28) range. **Fluid Phase Equilibria**, v. 97, p. 211–242, 1994a.

MORGAN, D. L.; KOBAYASHI, R. Extension of Pitzer CSP models for vapor pressures and heats of vaporization to long-chain hydrocarbons. **Fluid Phase Equilibria**, v. 94, p. 51–87, 1994b.

MUSTAFA, M.; SAGE, M.; WAKEHAM, W. A. Thermal conductivity of n-tridecane at pressures up to 500 MPa in the temperature range 35-75°C. **International Journal of Thermophysics**, v. 3, n. 3, p. 217–224, 1982.

NABIL, M.; KHODADADI, J. M. Experimental determination of temperature-dependent thermal conductivity of solid eicosane-based nanostructure-enhanced phase change materials. **International Journal of Heat and Mass Transfer**, v. 67, p. 301–310, 2013.

NICHITA, D. V.; GOUAL, L.; FIROOZABADI, A. Wax precipitation in gas condensate mixtures. **SPE Production & Facilities**, v. 16, n. 4, p. 250–259, 2001.

NIETO DE CASTRO, C. A.; TUFEU, R.; LE NEINDRE, B. Thermal conductivity measurement of n-butane over wide temperature and pressure ranges. **International Journal of Thermophysics**, v. 4, n. 1, p. 11–33, 1983.

NIEUWOUDT, I.; RAND, M. Measurement of phase equilibria of supercritical carbon dioxide and paraffins. **Journal of Supercritical Fluids**, v. 22, n. 3, p. 185–199, 2002.

ORÓ, E.; DE GRACIA, A.; CASTELL, A.; FARID, M. M.; CABEZA, L. F. Review on phase change materials (PCMs) for cold thermal energy storage applications. **Applied Energy**, v. 99, p. 513–533, 2012.

PAN, H.; FIROOZABADI, A.; FOTLAND, P. Pressure and composition effect on wax precipitation: experimental data and model results. **SPE Production & Facilities**, v. 12, n. 4, p. 250–258, 1997.

PARADELA, F.; QUEIMADA, A. J.; MARRUCHO, I. M.; NETO, C. P.; COUTINHO, J. A. P. Modeling the thermal conductivity of pure and mixed heavy n-alkanes suitable for the design of phase change materials. **International Journal of Thermophysics**, v. 26, n. 5, p. 1461–1475, 2005.

PASSUT, C. A.; DANNER, R. P. Correlation of ideal gas enthalpy, heat capacity and entropy. **Industrial & Engineering Chemistry Process Design and Development**, v. 11, n. 4, p. 543–546, 1972.

PATANKAR, S. V. **Numerical heat transfer and fluid flow**. New York: Taylor & Francis, 1980.

PAULY, J.; DARIDON, J.-L.; COUTINHO, J. A. P.; LINDELOFF, N.; ANDERSEN, S. I. Prediction of solid-fluid phase diagrams of light gases-heavy paraffin systems up to 200 MPa using an equation of state-G(E) model. **Fluid Phase Equilibria**, v. 167, n. 2, p. 145–159, 2000.

PAULY, J.; COUTINHO, J. A. P.; DARIDON, J.-L. High pressure phase equilibria in methane + waxy systems. 1. Methane + heptadecane. **Fluid Phase Equilibria**, v. 255, n. 2, p. 193–199, 2007.

PAULY, J.; COUTINHO, J. A. P.; DARIDON, J.-L. High pressure phase equilibria in methane + waxy systems. 3. Methane + a synthetic distribution of paraffin ranging from n-C13 to n-C22. **Fluid Phase Equilibria**, v. 313, p. 32–37, 2012.

PEDERSEN, K. S.; SKOVBORG, P.; ROENNINGSSEN, H. P. Wax precipitation from North Sea crude oils. 4. Thermodynamic modeling. **Energy and Fuels**, v. 5, n. 6, p. 924–932, 1991.

PEDERSEN, K. S.; CHRISTENSEN, P. **Phase Behavior of Petroleum Reservoir Fluids**. Boca Raton: CRC Press, Taylor & Francis Group, 2007.

PÉNELOUX, A.; RAUZY, E.; FRÉZE, R. A consistent correction for Redlich-Kwong-Soave volumes. **Fluid Phase Equilibria**, v. 8, n. 1, p. 7–23, 1982.

PENG, D. Y.; ROBINSON, D. B. A New two-constant equation of state. **Industrial and Engineering Chemistry Fundamentals**, v. 15, n. 1, p. 59–64, 1976.

PERKINS, R. A.; RAMIRES, M. L. V.; NIETO DE CASTRO, C. A.; CUSCO, L. Measurement and correlation of the thermal conductivity of butane from 135 K to 600 K at pressures to 70 MPa. **Journal of Chemical and Engineering Data**, v. 47, p. 1263–1271, 2002.

POLING, B. E.; PRAUSNITZ, J. M.; O'CONNEL, J. P. **Properties of Gases and Liquids**. 5th. ed. New York: McGraw-Hill, 2001.

PRASAD, R. C.; VENART, J. E. S. Thermal conductivity of ethane from 290 to 600 K at pressures up to 700 bar, including the critical region. **International Journal of Thermophysics**, v. 5, n. 4, p. 367–385, 1984.

PRASAD, R. C.; WANG, G.; VENART, J. E. S. The thermal conductivity of propane. **International Journal of Thermophysics**, v. 10, n. 5, p. 1013–1027, 1989.

PRAUSNITZ, J. M.; LICHTENTHALER, R. N.; AZEVEDO, E. G. **Molecular Thermodynamics of Fluid-Phase Equilibria**. 3rd. ed. Englewood Cliffs: Prentice Hall, 1999.

QUEIMADA, A. J.; MARRUCHO, I. M.; COUTINHO, J. A. P.; STENBY, E. H. Viscosity and liquid density of asymmetric n-Alkane mixtures: Measurement and modeling. **International Journal of Thermophysics**, v. 26, n. 1, p. 47–61, 2005.

RAMIRES, M. L. V.; NIETO DE CASTRO, C. A.; NAGASAKA, Y.; NAGASHIMA, A.; ASSAEL, M. J.; WAKEHAM, W. A. Standard reference data for thermal conductivity of water. **Journal of Physical and Chemical Reference Data**, v. 24, p. 1377–1381, 1995.

RASTORGUEV, Y. L.; BOGATOV, G. F.; GRIGOR'EV, B. A. Methods of assessing fuel and oil quality. **Chemistry and Technology of Fuels and Oils**, v. 10, n. 9, p. 728–732, 1974.

ROBUSTILLO, M. D.; COTO, B.; MARTOS, C.; ESPADA, J. J. Assessment of different methods to determine the total wax content of crude oils. **Energy and Fuels**, v. 26, n. 10, p. 6352–6357, 2012.

RODRIGUEZ-REARTES, S. B.; CISMONDI, M.; FRANCESCHI, E.; CORAZZA, M. L.; OLIVEIRA, J. V.; ZABALOY, M. S. High-pressure phase equilibria of systems carbon dioxide + n-eicosane and propane + n-eicosane. **Journal of Supercritical Fluids**, v. 50, n. 3, p. 193–202, 2009.

RODRIGUEZ, A. B. **Paraffin Deposition of Crude Oil and Water Dispersions under Flowing Conditions**. Master's Thesis. The University of Tulsa, 2006.

RYGG, O. B.; RYDAHL, A. K.; RØNNINGSEN, H. P. **Wax deposition in offshore pipeline systems**. 1st North American Conference on Multiphase technology. **Anais...Banff**: 1998.

SANSOT, J. M.; PAULY, J.; DARIDON, J.-L.; COUTINHO, J. A. P. Modeling high-pressure wax formation in petroleum fluids. **AIChE Journal**, v. 51, n. 7, p. 2089–2097, 2005.

SENRA, M. J. **Assessing the Role of Polydispersity and Cocrystallization on Crystallizing N-Alkanes in N-Alkane Solutions**. Doctorate's Thesis. University of Michigan, 2009.

SETTARI, A.; AZIZ, K. A generalization of the additive correction methods for the iterative solution of matrix equations. **SIAM Journal on Numerical Analysis**, v. 10, n. 3, p. 506–521, 1973.

SHARMA, A.; TYAGI, V. V.; CHEN, C. R.; BUDDHI, D. Review on thermal energy storage with phase change materials and applications. **Renewable and Sustainable Energy Reviews**, v. 13, n. 2, p. 318–345, 2009.

SHECAIRA, F.; BARROS, D.; RAMACHANDRAN, K.; BONIN, G.; WALTRICH, P.; JENNINGS, D.; NEWBERRY, M.; ZIGLIO, C. The Cottonwood Field Case History: The pig/paraffin obstruction of a long subsea, deepwater tie-back and Its successful remediation. **SPE Annual Technical Conference and Exhibition**, p. 1–10, 2011.

SINGH, P.; VENKATESAN, R.; FOGLER, H. S.; NAGARAJAN, N. Formation and aging of incipient thin film wax-oil gels. **AIChE Journal**, v. 46, n. 5, p. 1059–1074, 2000.

SINGH, P.; YOUYEN, A.; FOGLER, H. S. Existence of critical carbon number in the aging of a wax-oil gel. **AIChE Journal**, v. 47, n. 9, p. 2111–2124, 2001a.

SINGH, P.; VENKATESAN, R.; FOGLER, H. S.; NAGARAJAN, N. Morphological evolution of thick wax deposits during Aging. **AIChE Journal**, v. 47, n. 1, p. 6–18, 2001b.

SINGH, A. **Experimental and Field Verification Study of Wax Deposition in Turbulent Flow Conditions**. Master's Thesis. The University of Tulsa, 2013.

SOUZA, L. B. **Deposição de parafina em linhas de petróleo. Estudo numérico e experimental**. Doctorate's Thesis. Pontifícia Universidade Católica do Rio de Janeiro, 2014.

STROUSE, G. F. **Standard Reference Material 1751: Gallium Melting-Point Standard - NIST Special Publication 260-157**. Washington, 2004.

STRYKER, P. C.; SPARROW, E. M. Application of a spherical thermal conductivity cell to solid n-eicosane paraffin. **International Journal of Heat and Mass Transfer**, v. 33, n. 9, p. 1781–1793, 1990.

SUN, L.; VENART, J. E. S.; PRASAD, R. C. The thermal conductivity , thermal diffusivity , and specific heat of liquid n-pentane 1. **International Journal of Thermophysics**, v. 23, n. 2, p. 391–420, 2002.

TANAKA, Y.; ITANI, Y.; KUBOTA, H.; MAKITA, T. Thermal conductivity of five normal alkanes in the temperature range 283-373K at pressures up to 250MPa. **International Journal of Thermophysics**, v. 9, n. 3, p. 331–350, 1988.

VAN DER KOOI, H. J.; FLÖTER, E.; DE LOOS, T. W. High-pressure phase equilibria of  $\{(1-x)\text{CH}_4+x\text{CH}_3(\text{CH}_2)_{18}\text{CH}_3\}$ . **The Journal of Chemical Thermodynamics**, v. 27, n. 8, p. 847–861, 1995.

VAN DOORMAAL, J. P.; RAITHBY, G. D. Enhancements of the simple method for predicting incompressible fluid flows. **Numerical Heat Transfer**, v. 7, p. 147–163, 1984.

VARGAFTIK, N. B.; FILIPPOV, L. P.; TARZIMANOV, A. A.; TOTSKII, E. E. **Handbook of thermal conductivity of liquids and gases**. Boca Raton: CRC Press, 1994.

VASSILIOU, C. M.; ASSAEL, M. J.; HUBER, M. L.; PERKINS, R. A. Reference correlations of the thermal conductivity of cyclopentane, iso-pentane, and n-pentane. **Journal of Physical and Chemical Reference Data**, v. 44, n. 3, p. 1–16, 2015.

VEIGA, H. M. B. **Study of wax deposits in pipelines**. Doctorate's Thesis. Pontifícia Universidade Católica do Rio de Janeiro, 2017.

VEIGA, H. M. B.; FLEMING, F. P.; AZEVEDO, L. F. A. Wax deposit thermal conductivity measurements under flowing conditions. **Energy and Fuels**, v. 31, n. 11, p. 11532–11547, 2017.

VÉLEZ, C.; KHAYET, M.; ORTIZ DE ZÁRATE, J. M. Temperature-dependent thermal properties of solid/liquid phase change even-numbered n-alkanes: N-Hexadecane, n-octadecane and n-eicosane. **Applied Energy**, v. 143, p. 383–394, 2015a.

VÉLEZ, C.; ORTIZ DE ZÁRATE, J. M.; KHAYET, M. Thermal properties of n-pentadecane, n-heptadecane and n-nonadecane in the solid/liquid phase change region. **International Journal of Thermal Sciences**, v. 94, p. 139–146, 2015b.

VENKATESAN, R. **The Deposition and Rheology of Organic Gels**. Doctorate's Thesis. University of Michigan, 2004.

VENKATESAN, R.; FOGLER, H. S. Comments on analogies for correlated heat and mass transfer in turbulent flow. **AIChE Journal**, v. 50, n. 7, p. 1623–1626, 2004.

VESOVIC, V.; WAKEHAM, W. A.; LUETTNER-STRAHMANN, J.; SENGERS, J. V.; MILLAT, J.; VOGEL, E.; ASSAEL, M. J. The transport properties of ethane. II. Thermal conductivity. **International Journal of Thermophysics**, v. 15, n. 1, p. 33–66, 1994.

WADA, Y.; NAGASAKA, Y.; NAGASHIMA, A. Measurements and correlation of the thermal conductivity of liquid n-paraffin hydrocarbons and their binary and ternary mixtures. **International Journal of Thermophysics**, v. 6, n. 3, p. 251–265, 1985.

WANG, S.; TOZAKI, K. I.; HAYASHI, H.; HOSAKA, S.; INABA, H. Observation of multiple phase transitions in n-C<sub>22</sub>H<sub>46</sub> using a high resolution and super-sensitive DSC. **Thermochimica Acta**, v. 408, p. 31–38, 2003.

WATANABE, H.; SEONG, D. J. The thermal conductivity and thermal diffusivity of liquid n-alkanes: C<sub>n</sub>H<sub>2n+2</sub> (n=5 to 10) and toluene. **International Journal of Thermophysics**, v. 23, n. 2, p. 337–356, 2002.

WEINGARTEN, J. S.; EUCHNER, J. A. Methods for predicting wax precipitation and deposition. **SPE Production Engineering**, v. 3, n. 1, p. 121–126, 1988.

WILKE, C. R.; CHANG, P. Correlation of diffusion coefficients in dilute solutions. **AIChE Journal**, v. 1, n. 2, p. 264–270, 1955.

WON, K. W. Thermodynamics for solid solution-liquid-vapor equilibria: wax phase formation from heavy hydrocarbon mixtures. **Fluid Phase Equilibria**, v. 30, p. 265–279, 1986.

YARBROUGH, D. W.; KUAN, C.-N. The thermal conductivity of solid n-eicosane, n-octadecane, n-heptadecane, n-pentadecane, and n-tetradecane. In: HUST, J. G. (Ed.). . **Proceedings of the 17th International Thermal Conductivity Conference**. New York: Plenum Press, 1983. p. 265–274.

YAWS, C. L. **Yaws' Handbook of Thermodynamic and Physical Properties of Chemical Compounds**. New York: Knovel, 2003.

ZHENG, W.; WANG, S.; LIU, J.; MENG, F.; LI, Y.; MA, H.; LI, T. Synthesis and evaluation of wax dispersant for diesel. **Energy and Fuels**, v. 28, n. 3, p. 1896–1900, 2014.

ZHENG, W.; SAIDOUN, M.; PALERMO, T.; MATEEN, K.; FOGLER, H. S. Wax deposition modeling with considerations of non-Newtonian characteristics: application to field-scale pipeline. **Energy and Fuels**, v. 31, n. 5, p. 5011-5023, 2017.

ZIERVOGEL, R. G.; POLING, B. E. A simple method for constructing phase envelopes for multicomponent mixtures. **Fluid Phase Equilibria**, v. 11, n. 2, p. 127–135, 1983.

# 10 APPENDIX A

In Table 10-1, it is shown a comparison between the compositions of the samples used in the experimental work of Dauphin *et al.* [17] and the samples used in this work for DSC analyses.

**Table 10-1.** Composition differences between samples S1 to S5 and Bim 0 to Bim 13 from Dauphin *et al.* [17] expressed in %.

%	S1	Bim 0	Diff	S2	Bim 3	Diff	S3	Bim 5	Diff	S4	Bim 9	Diff	S5	Bim 13	Diff
C10	63,90	63,84	0,09	64,25	64,25	-0,01	64,65	64,65	0,01	65,63	65,59	0,06	66,40	66,65	-0,38
C18	4,285	4,276	0,21	4,922	4,872	1,02	5,362	5,383	-0,38	6,967	6,958	0,13	10,61	10,57	0,42
C19	3,844	3,871	-0,70	4,419	4,411	0,18	4,874	4,874	-0,01	6,289	6,301	-0,19	9,651	9,571	0,83
C20	3,473	3,494	-0,62	3,944	3,981	-0,95	4,388	4,400	-0,26	5,684	5,688	-0,07	8,717	8,641	0,88
C21	3,116	3,149	-1,06	3,550	3,587	-1,05	4,072	3,963	2,68	5,103	5,124	-0,41	-	-	-
C22	2,789	2,828	-1,40	3,213	3,221	-0,25	3,541	3,561	-0,57	4,601	4,603	-0,04	-	-	-
C23	2,507	2,536	-1,17	2,883	2,889	-0,20	3,172	3,193	-0,67	-	-	-	-	-	-
C24	2,254	2,270	-0,71	2,656	2,586	2,64	2,824	2,858	-1,22	-	-	-	-	-	-
C25	2,001	2,028	-1,34	2,337	2,310	1,16	-	-	-	-	-	-	-	-	-
C26	2,006	1,811	9,73	-	-	-	-	-	-	-	-	-	-	-	-
C27	1,595	1,612	-1,06	-	-	-	-	-	-	-	-	-	-	-	-
C28	1,442	1,441	0,04	-	-	-	-	-	-	-	-	-	-	-	-
C29	1,263	1,274	-0,86	1,436	1,451	-1,03	-	-	-	-	-	-	-	-	-
C30	1,120	1,130	-0,94	1,277	1,290	-1,04	1,442	1,424	1,23	-	-	-	-	-	-
C31	0,991	1,004	-1,34	1,145	1,142	0,30	1,248	1,262	-1,10	-	-	-	-	-	-
C32	0,877	0,887	-1,16	1,000	1,011	-1,09	1,115	1,119	-0,39	1,444	1,444	0,02	-	-	-
C33	0,802	0,788	1,81	0,887	0,895	-0,95	1,002	0,989	1,31	1,279	1,280	-0,06	-	-	-
C34	0,694	0,695	-0,21	0,787	0,790	-0,34	0,865	0,873	-0,92	1,128	1,129	-0,10	1,723	1,716	0,39
C35	0,515	0,522	-1,32	0,681	0,698	-2,51	0,760	0,771	-1,51	0,997	0,998	-0,08	1,521	1,516	0,34
C36	0,530	0,541	-2,07	0,617	0,616	0,17	0,682	0,682	0,03	0,880	0,881	-0,08	1,377	1,337	2,89

To ensure that kinetics effects are kept at a minimum, the DSC thermograms were carried out at a slow enough rate so that the differences between cooling and heating experiments are also a minimum. The resulting curves are displayed in figures 10-1 to 10-5. The heating signal was reciprocated to be directly compared to the cooling signal.

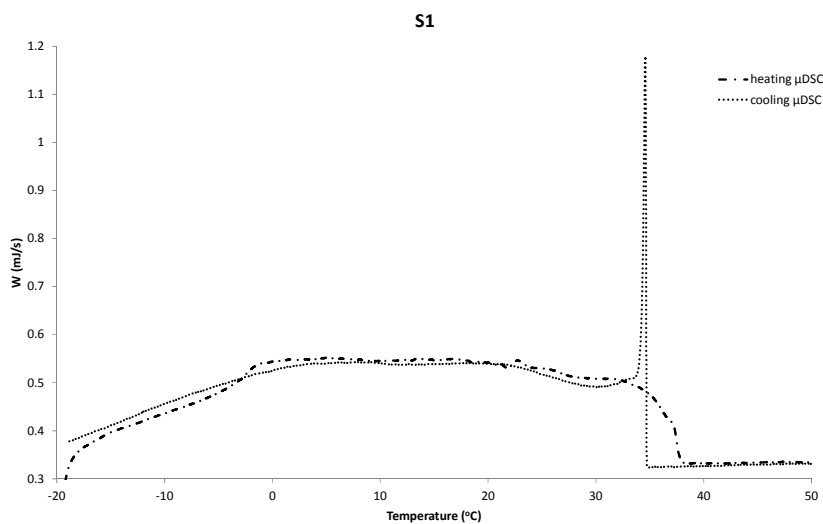


**Figure 10-1.** Heating and cooling curves from 0.2 k/min  $\mu$ DSC for sample S1.

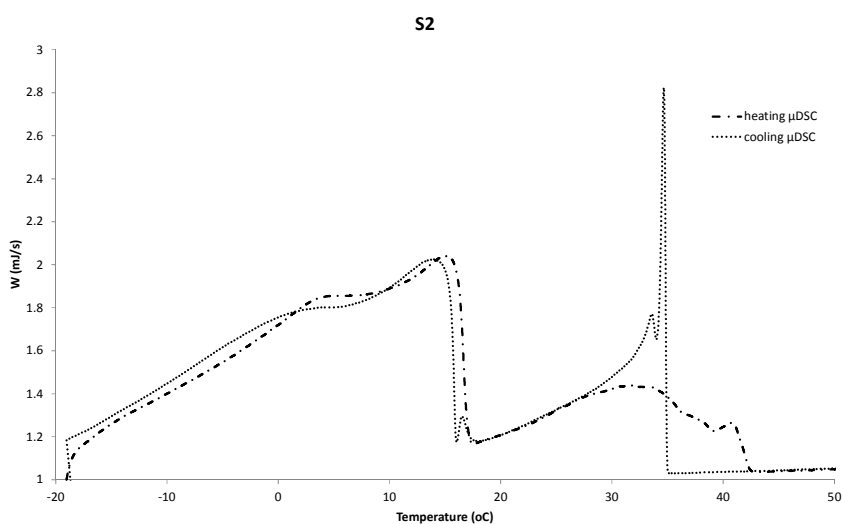


**Figure 10-2.** Heating and cooling curves from 0.2 k/min  $\mu$ DSC for sample S2.

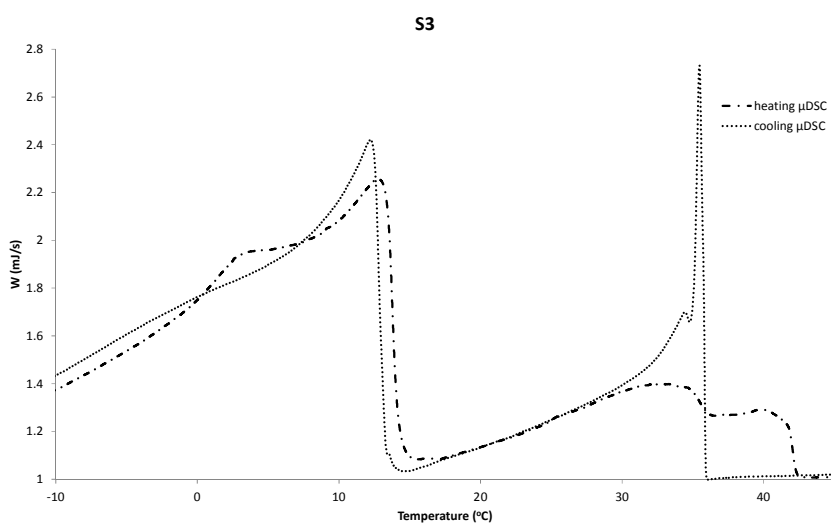


**Figure 10-3.** Heating and cooling curves from 0.2 k/min  $\mu$ DSC for sample S3.

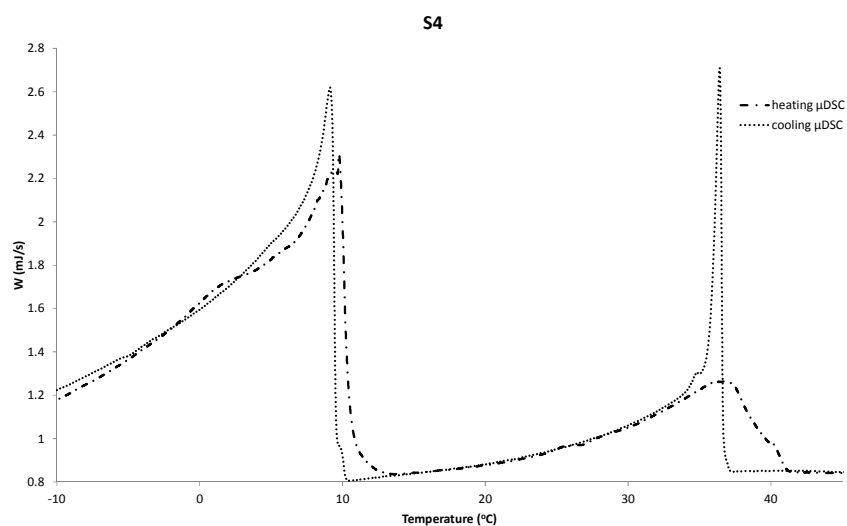


**Figure 10-4.** Heating and cooling curves from 0.2 k/min  $\mu$ DSC for sample S4.

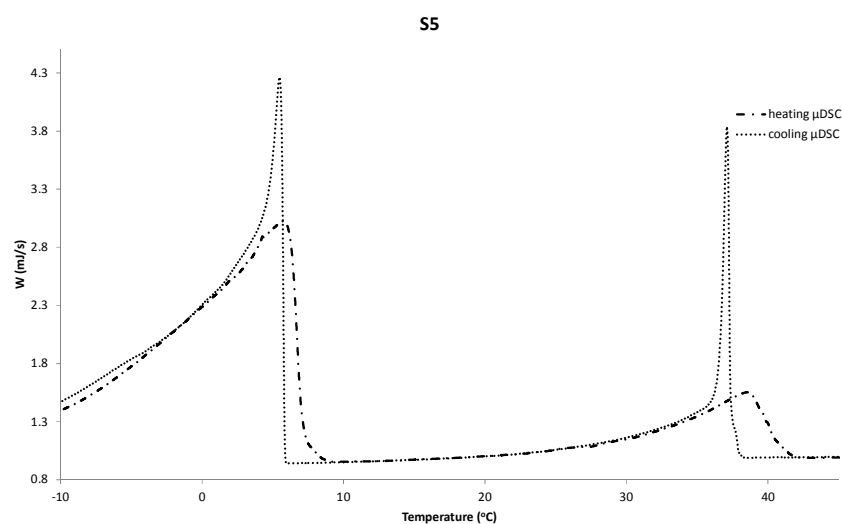


**Figure 10-5.** Heating and cooling curves from 0.2 k/min  $\mu$ DSC for sample S5.

# 11

## APPENDIX B

To express the convective term of the conservation equations in terms of the mixture velocity ( $\mathbf{u}_m$ ) and the mixture properties, it is necessary to carry out a variable transformation over these equations. As a result, a drift flux appears as a source term in the species, linear momentum and heat conservation equations, as shown in section 7.2.6. These transformations are depicted in the following sections.

### 11.1. Drift Flux of Species

The continuity equation for the species for the mixture is a result of the sum of the continuity equation for the species in both phases.

$$\frac{\partial}{\partial t} (c_{i,l} S_l \rho_l + c_{i,s} S_s \rho_s) + \nabla \cdot (c_{i,l} S_l \rho_l \mathbf{u}_l + c_{i,s} S_s \rho_s \mathbf{u}_s) = -\nabla \cdot (c_{i,l} S_l \rho_l \bar{\mathbf{v}}_{i,l}) \quad (\text{B-1})$$

One wishes to express the term  $c_{i,l} S_l \rho_l u_l + c_{i,s} S_s \rho_s u_s$  as a function of  $\rho_m u_m$ . The difference “A” between the terms is:

$$A = (c_{i,l} S_l \rho_l u_l + c_{i,s} S_s \rho_s u_s) - \rho_m u_m$$

$$A = (c_{i,l} S_l \rho_l u_l + c_{i,s} S_s \rho_s u_s) - (c_{i,l} S_l \rho_l + c_{i,s} S_s \rho_s) \left( \frac{S_l \rho_l u_l + S_s \rho_s u_s}{\rho_m} \right)$$

$$\begin{aligned} \rho_m A &= (S_l \rho_l + S_s \rho_s) (c_{i,l} S_l \rho_l u_l + c_{i,s} S_s \rho_s u_s) \\ &\quad - (c_{i,l} S_l \rho_l + c_{i,s} S_s \rho_s) (S_l \rho_l u_l + S_s \rho_s u_s) \end{aligned}$$

$$\begin{aligned} \rho_m A &= (c_{i,l} S_l^2 \rho_l^2 u_l + c_{i,l} S_l \rho_l S_s \rho_s u_l + c_{i,s} S_l \rho_l S_s \rho_s u_s + c_{i,s} S_s^2 \rho_s^2 u_s) \\ &\quad - (c_{i,l} S_l^2 \rho_l^2 u_l + c_{i,l} S_l \rho_l S_s \rho_s u_s + c_{i,s} S_l \rho_l S_s \rho_s u_l + c_{i,s} S_s^2 \rho_s^2 u_s) \end{aligned}$$

$$\rho_m A = c_{i,l} S_l \rho_l S_s \rho_s u_l + c_{i,s} S_l \rho_l S_s \rho_s u_s - c_{i,l} S_l \rho_l S_s \rho_s u_s - c_{i,s} S_l \rho_l S_s \rho_s u_l$$

$$\rho_m A = S_l \rho_l S_s \rho_s (u_l - u_s) (c_{i,l} - c_{i,s}) \rightarrow A = \frac{S_l \rho_l S_s \rho_s}{\rho_m} (u_l - u_s) (c_{i,l} - c_{i,s})$$

It follows that:

$$c_{i,l}S_l\rho_l u_l + c_{i,s}S_s\rho_s u_s = \rho_m u_m + \frac{S_l\rho_l S_s\rho_s}{\rho_m}(u_l - u_s)(c_{i,l} - c_{i,s}) \quad (\text{B-2})$$

## 11.2. Drift Flux of Linear Momentum

The linear momentum conservation equation for the mixture is a result of the sum of the linear momentum conservation equations of both phases.

$$\begin{aligned} \frac{\partial}{\partial t}(S_l\rho_l \mathbf{u}_l + S_s\rho_s \mathbf{u}_s) + \nabla \cdot (S_l\rho_l \mathbf{u}_l \mathbf{u}_l + S_s\rho_s \mathbf{u}_s \mathbf{u}_s) = \\ - \nabla p + \nabla \cdot \boldsymbol{\tau}_m + \rho_m \mathbf{g} \end{aligned} \quad (\text{B-3})$$

One wishes to express the term  $S_l\rho_l u_l u_l + S_s\rho_s u_s u_s$  as a function of  $\rho_m u_m u_m$ . The difference “A” between the terms is:

$$\begin{aligned} A &= (S_l\rho_l u_l u_l + S_s\rho_s u_s u_s) - \rho_m u_m u_m \\ A &= (S_l\rho_l u_l u_l + S_s\rho_s u_s u_s) - \rho_m \left( \frac{S_l\rho_l u_l + S_s\rho_s u_s}{\rho_m} \right) \left( \frac{S_l\rho_l u_l + S_s\rho_s u_s}{\rho_m} \right) \\ \rho_m A &= (S_l\rho_l + S_s\rho_s)(S_l\rho_l u_l u_l + S_s\rho_s u_s u_s) \\ &\quad - (S_l\rho_l u_l + S_s\rho_s u_s)(S_l\rho_l u_l + S_s\rho_s u_s) \\ \rho_m A &= (S_l^2 \rho_l^2 u_l u_l + S_l\rho_l S_s\rho_s u_l u_l + S_l\rho_l S_s\rho_s u_s u_s + S_s^2 \rho_s^2 u_s u_s) \\ &\quad - (S_l^2 \rho_l^2 u_l u_l + S_l\rho_l S_s\rho_s u_l u_s + S_l\rho_l S_s\rho_s u_l u_s + S_s^2 \rho_s^2 u_s u_s) \\ \rho_m A &= S_l\rho_l S_s\rho_s u_l u_l + S_l\rho_l S_s\rho_s u_s u_s - S_l\rho_l S_s\rho_s u_l u_s - S_l\rho_l S_s\rho_s u_l u_s \\ \rho_m A &= S_l\rho_l S_s\rho_s (u_l - u_s)^2 \rightarrow A = \frac{S_l\rho_l S_s\rho_s}{\rho_m} (u_l - u_s)^2 \end{aligned}$$

It follows that:

$$S_l\rho_l u_l u_l + S_s\rho_s u_s u_s = \rho_m u_m u_m + \frac{S_l\rho_l S_s\rho_s}{\rho_m} (u_l - u_s)^2 \quad (\text{B-4})$$

### 11.3. Drift Flux of Energy

The energy conservation equation for the mixture is a result of the sum of the energy conservation equations of both phases.

$$\frac{\partial}{\partial t} (S_l \rho_l h_l + S_s \rho_s h_s) + \nabla \cdot (S_l \rho_l h_l \mathbf{u}_l + S_s \rho_s h_s \mathbf{u}_s) = \frac{Dp}{Dt} + \nabla \cdot (\lambda_m \nabla T) - \nabla \cdot (\sum_{i=1}^N \mathbf{j}_i h_{i,l}) + \Phi \quad (\text{B-5})$$

One wishes to express the term  $S_l \rho_l h_l u_l + S_s \rho_s h_s u_s$  as a function of  $\rho_m h_m u_m$ . The difference “A” between the terms is:

$$\begin{aligned} A &= (S_l \rho_l h_l u_l + S_s \rho_s h_s u_s) - \rho_m h_m u_m \\ A &= (S_l \rho_l h_l u_l + S_s \rho_s h_s u_s) - \rho_m \left( \frac{S_l \rho_l h_l + S_s \rho_s h_s}{\rho_m} \right) \left( \frac{S_l \rho_l u_l + S_s \rho_s u_s}{\rho_m} \right) \\ \rho_m A &= (S_l \rho_l + S_s \rho_s) (S_l \rho_l h_l u_l + S_s \rho_s h_s u_s) \\ &\quad - (S_l \rho_l h_l + S_s \rho_s h_s) (S_l \rho_l u_l + S_s \rho_s u_s) \\ \rho_m A &= (S_l^2 \rho_l^2 h_l u_l + S_l \rho_l S_s \rho_s h_l u_l + S_l \rho_l S_s \rho_s h_s u_s + S_s^2 \rho_s^2 h_s u_s) \\ &\quad - (S_l^2 \rho_l^2 h_l u_l + S_l \rho_l S_s \rho_s h_l u_s + S_l \rho_l S_s \rho_s h_s u_l + S_s^2 \rho_s^2 h_s u_s) \\ \rho_m A &= S_l \rho_l S_s \rho_s h_l u_l + S_l \rho_l S_s \rho_s h_s u_s - S_l \rho_l S_s \rho_s h_s u_l - S_l \rho_l S_s \rho_s h_l u_s \\ \rho_m A &= S_l \rho_l S_s \rho_s (u_l - u_s) (h_l - h_s) \rightarrow A = \frac{S_l \rho_l S_s \rho_s}{\rho_m} (u_l - u_s) (h_l - h_s) \end{aligned}$$

It follows that:

$$S_l \rho_l h_l u_l + S_s \rho_s h_s u_s = \rho_m h_m u_m + \frac{S_l \rho_l S_s \rho_s}{\rho_m} (u_l - u_s) (h_l - h_s) \quad (\text{B-6})$$